University of Pavia
Department of Biology and
Biotechnology “L. Spallanzani”

KU Leuven
Biomedical Sciences Group
Faculty of Medicine
Department of Chronic Diseases,
Metabolism and Ageing

Enteric glial cells: cellular and molecular analysis of an emerging player in intestinal health and disease

Lisa Zanoletti

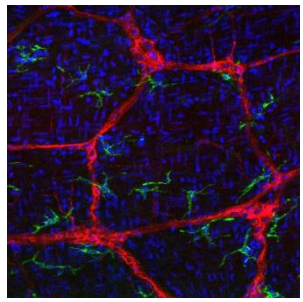

Supervisor University of Pavia: *Prof. Dr. Sergio Comincini*

Supervisor KU Leuven: *Prof. Dr. Gianluca Matteoli*

Co-supervisor: *Dr. Federico Manai, University of Pavia*

KU Leuven jury member: *Bram Verstockt*

Dissertation presented in partial fulfilment of the requirements for the joint/double degree of Doctor in Biomedical Sciences (KU Leuven) and of Dottore di ricerca in Genetica, Biologia Molecolare e Cellulare (University of Pavia)

Part of this Thesis has been adapted from:

Cytological, molecular, cytogenetic, and physiological characterization of a novel immortalized human enteric glial cell line

Zanoletti L, Valdata A, Nehlsen K, Faris P, Casali C, Cacciatore R, Sbarsi I, Carriero F, Arfini D, van Baarle L, De Simone V, Barbieri G, Raimondi E, May T, Moccia F, Bozzola M, Matteoli G, Comincini S, Manai F.

Front Cell Neurosci 17:1170309, 20th of April 2023.

doi: 10.3389/fncel.2023.1170309.

The figure reported in the first page of this manuscript has been collected at KU Leuven, department of Chronic Diseases, Metabolism and Aging. It shows the myenteric plexus in the *muscularis mucosae* of a CX3CR1-CreERT2 CSF1R wt/fl mouse. Enteric glia (red) have been marked with an anti-GFAP antibody, muscularis macrophages (green) with an anti-CX3CR1 antibody and nuclei (blue) have been stained with DAPI.

Table of contents

Abstract

Enteric glia have the unique feature of responding to surrounding cues and acquiring specific states, including a reactive phenotype named “gliosis”. Several studies reported that the EGC phenotype is altered in chronic inflammatory conditions, such as Crohn's disease and ulcerative colitis. However, while the role of EGCs has been well described in inflammatory bowel diseases (IBDs), their involvement in celiac disease (CD) has been poorly investigated so far. CD is a chronic T-cell-mediated enteropathy triggered by the consumption of gluten in genetically susceptible individuals. Once thought to primarily afflict children and provoke gastrointestinal symptoms, CD is now considered a systemic disorder with a broad range of clinical presentations that span all age groups.
Taking into account all common features shared by IBDs and CD and the evidence that EGCs are protagonists in several gut physiological and pathological processes, it is likely that enteric glia might be involved in CD pathogenesis as well.

Considering the lack of available established EGC lines and the technical difficulties related to EGCs’ extraction from sample tissue, the first step of this work was the generation of the first immortalized hEGC line (referred to as hEGC-ClK clone) through a validated lentiviral transgene protocol. Hence, hEGC-ClK cell line was finely characterized and used as an experimental model of hEGCs to test the effects of gluten-derived gliadin and gluten-derived cytotoxic peptide p31-43.
Our results showed that gliadin was able to induce oxidative stress in hEGCs, followed by mitochondrial damage, and finally resulting in caspase-mediated apoptotic cell death. On the other hand, p31-43 exerted milder cytotoxic effects on hEGCs, triggering gliosis and activation of the Nrf2/Keap1-mediated antioxidant defence system. Furthermore, the molecular results were validated by a proteomic analysis and compared with the effects observed in primary murine EGCs. These data highlighted the important but not sufficient contribution of p31-43 in gliadin cytotoxicity toward hEGCs, suggesting the possible involvement of other gliadin-derived peptides.
Altogether, our results might suggest a possible involvement of EGCs in CD pathogenesis, identifying enteric glia as a potential novel therapeutic target for the treatment of CD patients.

Abbreviations

CD = celiac disease
RR= relative risk
TJs = tight junctions
TG2= transglutaminase 2
APCs = antigen-presenting cells
DCs = dendritic cells
LAK = lymphokine-activated killer
IBD = inflammatory bowel diseases
AGA= anti-gliadin antibodies
EMA= anti-endomysial antibodies
IELs= intraepithelial lymphocytes
HR = hazard ratio
SBC = small bowel carcinoma
GFD = gluten-free diet
GI = gastrointestinal
DCs = dendritic cells
GEs = gluten exorphins
DOR = δ opioid receptor
KOR = κ opioid receptor
MOR = μ opioid receptors
ENS = enteric nervous system
ENs = enteric neurons
EGCs = enteric glial cells
IPANs = intrinsic primary afferent neurons
Ach = acetylcholine
NO = nitric oxide
VIP = vasoactive intestinal polypeptide
NPY = neuropeptide Y
ATP = adenosine triphosphate
GABA = γ-aminobutyric acid
NCDCs = neural crest-derived cells
HSCR = Hirschsprung's disease
ENCCs = enteric neural crest-derived cells
EW = embryonic weeks
E = embryonic day
MP = myenteric plexus
SMP = submucosal plexus
GDNF = glial-derived neurotrophic factor
GFAP = glial fibrillary acidic protein
ChAT = choline acetyltransferase

ADP = adenosine diphosphate
CCK = cholecystokinin
PLP-1 = proteolipid protein 1
scRNAseq = single-cell RNA sequencing
LMMP = muscle-myenteric plexus
P = postnatal day
Cx43 = connexin 43
NTPDase2 = nucleoside triphosphate diphosphohydrolase 2
DAMPs = damage-associated molecular patterns
PAMPs = pathogen-associated molecular patterns
TLRs = toll-like receptors
NLRs = nod-like receptors
CDI = *Clostridium difficile* infection
TcdA = Clostridium difficile toxin A
TcdB = Clostridium difficile toxin B
Panx1 = Pannexin-1 channels
TGI = *Toxoplasma gondii* infection
IFNγ = interferon-gamma
TM = tunica muscularis
M-CSF = macrophage colony-stimulating factor
PKC = protein kinase C
POI = post-operative ileus
ME-Macs = muscularis externa macrophages
IL1R1 = IL-1 receptor type 1
NDRG4 = N-Myc downstream-regulated gene4
CRC = colorectal cancer
TME = tumor microenvironment
iDISCO = immunolabeling-enabled imaging of solvent-cleared organs
AOM/DSS = azoxymethane/dextran sodium sulfate
CSC = cancer stem cell
TAMs = tumor-associated macrophages
GEP-NENs = gastroenteropancreatic neoplasms
ÇhD = Crohn's disease
UC = ulcerative colitis
ILCs = innate lymphoid cells
ROS = reactive oxygen species
TEM = transmission electron microscopy
FC = flow cytometry
IF = immunofluorescence
LPS = lipopolysaccharide
$[Ca^{2+}]_i$ = intracellular Ca^{2+} concentration
InsP3 = inositol-1,4,5-trisphosphate
ER = endoplasmic reticulum

SMOCs = second messenger-operated channels
SOCE = store-operated Ca^{2+} entry
InsP3Rs = InsP3 receptors
PLCβ = phospholipase Cβ
2-APB = 2-aminoethyl diphenylborinate
SERCA = Sarco-Endoplasmic Ca^{2+}-ATPase
CPA = cyclopiazonic acid
$[Ca^{2+}]_{ER}$ = endoplasmic reticulum Ca^{2+} concentration
SOCs = store-operated Ca^{2+} channels
PT-gliadin = pepsin-trypsin digested gliadin
PT-albumin = pepsin-trypsin digested albumin
p.t. = post-treatment
DSBs = double-strand breaks
DHE = dihydroethidium
HO-1 = heme oxigenase-1

Introduction

3.1 Celiac disease

Celiac disease (CD), a chronic T-cell-mediated enteropathy triggered by the consumption of gluten in genetically susceptible individuals, has recently become a significant concern in global healthcare [1]. Once thought to primarily afflict children and provoke gastrointestinal symptoms, CD is now understood as a systemic disorder with a broad range of clinical presentations that span all age groups. Due to its wide variability in clinical presentation, CD diagnosis can be delayed or missed, possibly leading to long-term complications.

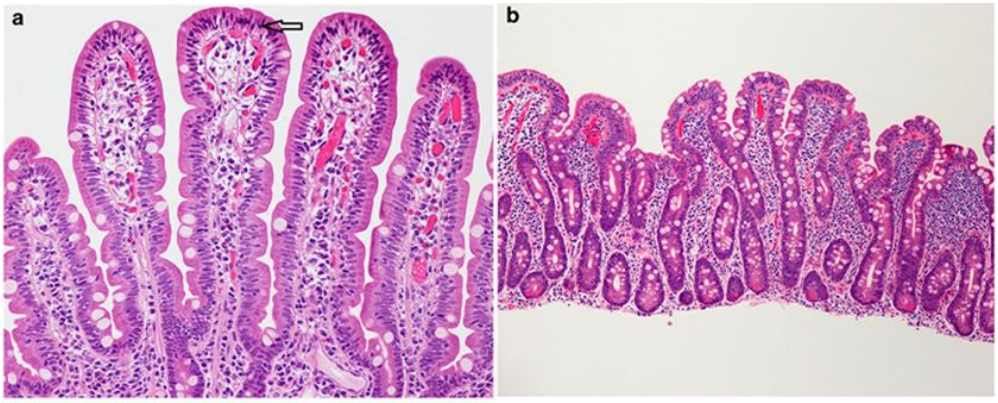

Figure 3.1. ***Histologic features associated with CD.*** ***(A)*** *early phase of CD characterized by a tip-predominant intraepithelial lymphocytosis (arrow).* ***(B)*** *later phase of CD with villous atrophy, crypt hyperplasia, lymphocytosis, and a chronic cell infiltrate in the lamina propria. (A at 200 ×, B 100 × ; Haemotoxylin and Eosin stain)[2] .*

A gluten-free diet (GFD) is the currently available effective treatment for CD. However, considering the emotional and social impact of having to avoid familiar and pleasurable dietary elements over a lifetime, maintaining strict compliance with a gluten-free diet can be challenging. As a result, ongoing research explores novel approaches for both preventing and treating CD.

3.1.1. Prevalence and epidemiology

The prevalence of CD has experienced a significant increase, challenging the notion that it was an uncommon disorder. The global prevalence estimates for CD have ranged widely, from around 0.5% to 2% of the population, with an average of about 1%. Occasionally, elevated percentages have been documented, such as in Sweden (3%) and in the Saharawi population (5.6%). By contrast, CD is less prevalent in regions where gluten-containing grains are not the primary dietary staple and where the prevalence of the major predisposing genes (*HLA-DQ2* and *HLA-DQ8*) for the disease is low. This is particularly notable in parts of East Asia (such as Japan and Vietnam) and some areas of sub-Saharan Africa [3], [4] (**Fig. 3.2**). Additionally, CD is more common in females than in males, according to population screening (relative risk [RR]=1.13-1.79) and clinical studies (female-to-male ratio=1.85) [5].

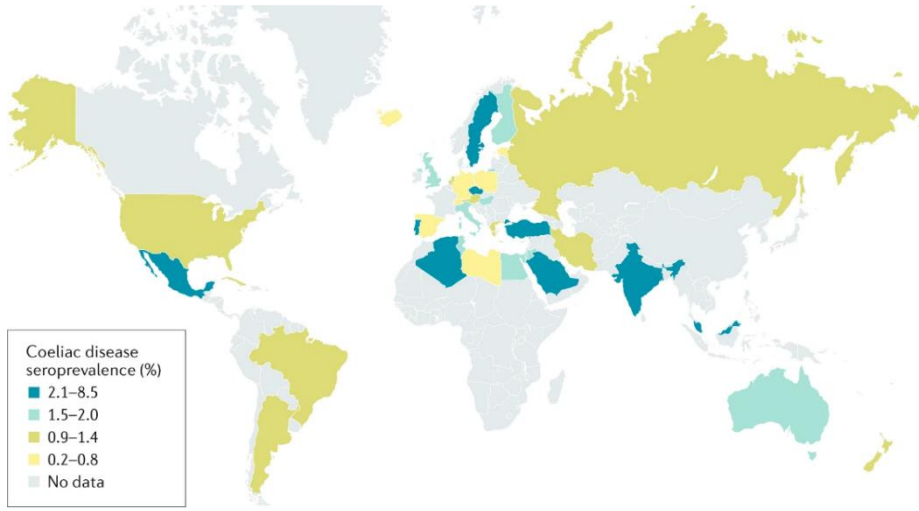

Figure 3.2. ***Celiac disease seroprevalence (%)***. *The map shows coeliac disease seroprevalence as determined by positive serum transglutaminase 2 and/or endomysial autoantibodies. Darker colours indicate higher prevalence. Countries, where no studies on the prevalence of coeliac disease have been conducted, are presented without color [6].*

Overall, the prevalence and epidemiology of CD have evolved from a perception of rarity to a realization of its widespread impact on a global scale. Advances in understanding the genetic basis of the disease, improved diagnostic techniques, and heightened awareness have collectively contributed to a better grasp of its true prevalence. Indeed, the number of newly diagnosed cases of CD has increased exponentially over the past 30-40 years. In countries such as Europe, the USA, Canada, and New Zealand, the incidence of CD was less than two cases per 100,000 individuals annually in the 1980s and 1990s. However, this rate surged to more than 20 cases per 100,000 individuals annually in the 2010s [7].

As CD continues to be unveiled as a significant health concern cutting across demographics and regions, the need for accurate diagnosis, comprehensive management, and increased awareness becomes more pressing.

3.1.2. Pathogenesis

The onset of CD is caused by the ingestion of gluten in genetically predisposed individuals, with the possible involvement of additional factors.
Individuals with a family history of CD carry a risk of 10–15% of developing the condition during their lifetime. Moreover, there is a notable 50–75% concordance rate among monozygotic twins. The main genes involved in the development of CD are located in the *HLA-DQ* locus on the short arm of chromosome 6 [8]. These genes encode Major Histocompatibility Complex (MHC) class II molecules that are involved in the antigen presentation mechanism to $CD4^+$ T-cells. Particularly, 90% of patients carry the variant *HLA-DQ2.5* (alleles: *DQA1*05:01/DQB1*02:01*), while the remaining 10% carry either *HLA-DQ2.2* (alleles: *DQA1*02:01/DQB1*02:02*, 5%) or *HLA-DQ8* variant (alleles *DQA1*03:01/DQB1*03:02*, 5%). Patients with homozygosity for *HLA-DQ2* present a higher risk of developing the disease compared to individuals who are heterozygous [9], [10]. Despite these polymorphisms being associated with the onset of CD, it has been suggested the involvement of other non-HLA genes, since around one-third of the Caucasian population carries the mutated HLA variant. Genome-wide association studies have revealed that an additional 41 non-HLA loci are linked to CD [11].
Considering that only a small percentage of individuals who carry CD-predisposing *HLA-DQ2* and *HLA-DQ8* variants and who eat gluten-containing food develop CD, it is likely that additional environmental co-factors have a role in the onset and development of the disease. Starting from the early 2000s, several longitudinal, multicentric cohort studies focusing on genetically-at-risk newborns have been conducted (e.g., TEDDY in USA, Sweden, Finland, and Germany [12]; Prevent-CD in Spain, Italy, the Netherlands, Poland, Romania, and Croatia [13]; CELIPREV in Italy [14]; MoBa and MIDIA in Norway [15], [16]; and CD-GEMM in USA, Italy, and Spain [17]). These studies provided insights into potential environmental factors influencing CD development beyond gluten, revealing prenatal factors such as maternal smoking [15] and high maternal gluten consumption [18], early introduction of gluten during weaning [19], [20], rotavirus infections [21], use of antibiotics [22] or proton-pump inhibitors in early infancy [23], and shifts in microbiota composition [24] to be positively associated with the development of CD.

3.1.3. Pathophysiology

The intricate mechanism driving intestinal damage in CD (**Fig. 3.3**) stems from the interplay between gluten ingestion, genetic susceptibility, and immune response.

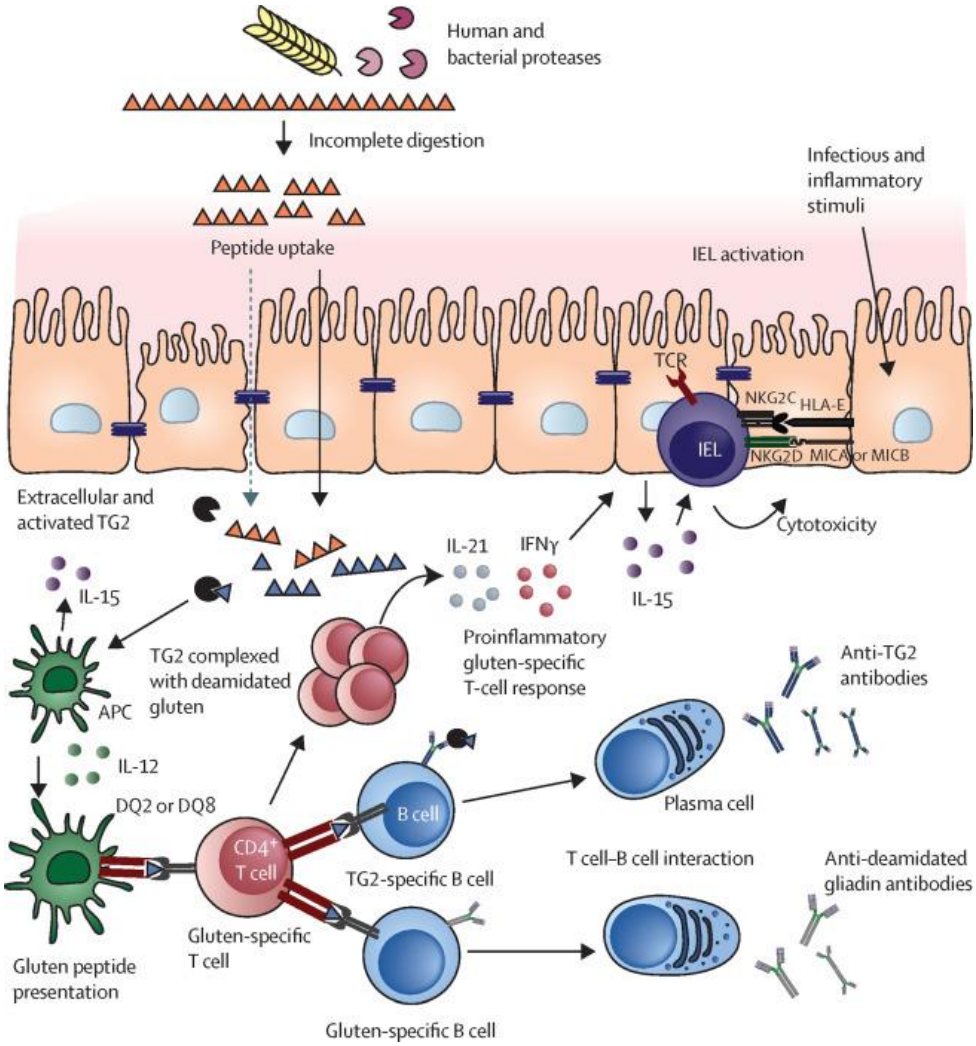

Figure 3.3. ***Celiac disease pathogenesis.*** *Gluten peptides containing T-cell epitopes exhibit resistance to degradation within the gastrointestinal system. TG2 deaminates these peptides, enhancing their ability to bind more effectively to the HLA-DQ molecules on APCs. Gluten-specific activated CD4+ T cells release various pro-inflammatory cytokines, including IFN-γ and IL-21, which contribute to damage in the intestinal lining. This activation also promotes the stimulation of intraepithelial lymphocytes (IELs) and triggers B-cell responses. Activated IELs undergo a transformation into cytolytic NK-like cells, which subsequently lead to the destruction of enterocytes displaying stress signals [25].*

Gluten gets partially digested by a combination of the host (digestive) and microbial (small intestinal microbiota) enzymes, promoting increased intestinal permeability in the epithelial cells and the release of zonulin, a family of molecules that leads to increased paracellular permeability by causing tight junction disassembly [26].

Hence, gluten peptides can cross the intestinal barrier through the paracellular pathway, thus triggering an inflammatory response. In addition, other pathways through which gluten peptides can reach the *lamina propria* have been demonstrated. The main mechanisms include transcytosis, characteristic of the 33-mer peptide, and retro-transcytosis of secretory IgA-gliadin mediated by the overexpression of the transferrin receptor CD71 in the intestinal lumen [27]. Additionally, in the presence of Ca^{2+} and at a temperature of 37°C, gliadin can enter cells without the need for receptors, thanks to the presence of endocytic vesicles [28].

Once in the *lamina propria*, gluten peptides undergo deamination by activated transglutaminase 2 (TG2, also known as tissue transglutaminase), an enzyme that is expressed in many cell types and is secreted during inflammatory conditions to the extracellular matrix. The glutamine residues are converted into glutamic acid, thus imparting negative charges to the peptides structure, which enhances their loading onto HLA-DQ2 and DQ8 molecules present on antigen-presenting cells (APCs) [29]. Then, dendritic cells (DCs) present the gliadin peptides to naive $CD4^+$ T-cells, causing their differentiation into pro-inflammatory Th1/Th7 gluten-specific T-cells. These cells proliferate and release pro-inflammatory molecules such as IFN-γ, TNF-α, IL-18, IL-12, and IL-21. The release of IFN-γ establishes a positive feedback loop, thus leading to the overexpression of HLA-DQ molecules and, consequently, an increase in the presentation of gluten peptides. Additionally, there is an increase in the number of intraepithelial $CD8^+$ lymphocytes, $TCR\alpha\beta^+$ $TCR\gamma\delta^+$ cells with activated lymphokine-activated killer (LAK) cell activity.

Following IL-15 release, stressed epithelial cells overexpress HLA-E and MICA membrane molecules, which are ligands for the CD94/NKG2C and NKG2D receptors on LAK epithelial lymphocytes. The receptor-ligand interaction leads to further release of inflammatory molecules and tissue damage [30], [31], [32].

Finally, the interaction of extracellular TG2 with the gluten peptides induces TG2-specific B-cells, which can interact with $CD4^+$ T-cells and promote the release of anti-TG2 antibodies. B-cells also internalize TG2–gluten complexes, inducing the release of deamidated gluten peptides that bind to HLA-DQ2 or HLA-DQ8 and further activate the gluten-specific T-cells [33].

3.1.4. Clinical manifestation and diagnosis

CD is a so-called "clinical chameleon" and can manifest in three different forms: classical or typical, non-classical or atypical, and subclinical or silent CD. The classical form is more common in children younger than 5 years and it is characterized by typical malabsorption symptoms such as chronic diarrhea, steatorrhea, poor appetite, weight loss, abdominal pain, and muscle wasting [1], [34]. In rare cases, late diagnosis can result in a life-threatening celiac crisis, whose main features are watery diarrhea, marked abdominal distension, dehydration, electrolyte imbalance, hypoalbuminemia, hypotension, and lethargy [35].

Non-classical CD is the most common presentation with non-specific intestinal and extraintestinal symptoms such as iron-deficiency anemia, short stature, osteoporosis, crypt hypertransaminasemia, infertility, dermatitis herpetiformis, and psychiatric and neurological disorders. The main marker of this subtype is iron deficiency anemia due to reduced iron absorption in the duodenum [36], [37], [38], [39], [40]. Lastly, patients with subclinical CD do not experience any symptoms and are usually identified either by screening in the general population or through case-finding in at-risk groups, such as relatives of people with CD.

Notably, CD shows a significant association with various other autoimmune disorders, especially type 1 diabetes, which is associated with CD in 4.5% of cases [41], and Hashimoto's thyroiditis, with an odds ratio of 4.0 for coexisting CD [42]. In addition, other disorders such as autoimmune hepatitis, primary biliary cholangitis [43], Sjögren's syndrome, systemic lupus erythematosus, and systemic sclerosis exhibit association with CD [44].
Although the link between CD and autoimmune comorbidities is mainly attributed to HLA-predisposing genes, the potential role of gluten or other factors in triggering autoimmunity has been suggested [34]. Notably, patients with CD face an increased risk of inflammatory bowel diseases (IBDs) (RR= 9·88), and conversely, individuals with IBDs have a higher susceptibility to CD (RR=3·96) [45]. Additionally, microscopic colitis is also strongly associated with CD, being 50 times more frequent in CD patients compared to the general population [46]. The prevalence of CD is also elevated in individuals affected by genetic and chromosomal disorders, particularly in cases of selective IgA deficiency (15%) [47], Down syndrome (9.8%) [48], Turner syndrome (3.8%) [49], and Williams syndrome (6.9%) [50].

The diverse clinical picture represents the main challenge for accurate diagnosis. It has been estimated that for every diagnosed celiac patient, there are about 7 undiagnosed cases [51]. The diagnostic process involves the use of serological tests to detect IgA/IgG anti-tissue transglutaminase antibodies (anti-tTG), IgA anti-gliadin antibodies (AGA), and IgA anti-endomysial antibodies (EMA). The best first-level screening for CD is the detection of anti-tTG antibodies, along with the measurement of total serum IgA to exclude selective IgA deficiency [52], [53], [54], [55], [56]. Indeed, a high concentration of serum IgA anti-TG2 is strongly linked to the presence of villous atrophy in small intestinal biopsies [57]. Several techniques are currently accessible for detecting anti-TG2 antibodies, including ELISA, fluorescent immunoassay, radioimmunoassay, and chemiluminescence [58].
Once these antibodies are detected in the serum of the patient, a duodenal biopsy is performed to identify the typical histological alterations of CD, such as increased intraepithelial lymphocytes (IELs), crypt hypertrophy and hyperplasia, and villous atrophy. Although different scoring systems can be used to evaluate intestinal damage, the Oberhuber-modified Marsh classification is the most commonly used for this purpose (**Fig. 3.4**) [59].

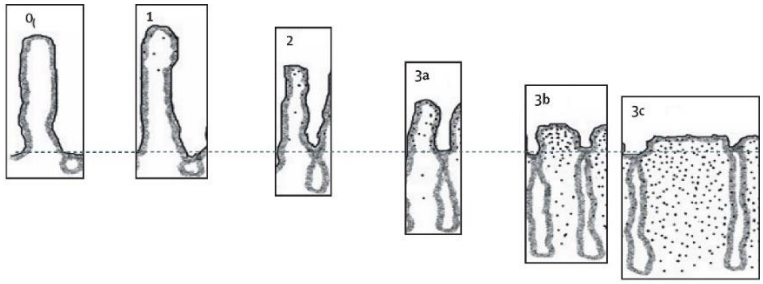

	Marsh-Oberhuber grade					
	0	1	2	3a	3b	3c
Descriptor		Infiltrative	Hyperplastic	Partial villous atrophy	Subtotal villous atrophy	Total villous atrophy
Villous architecture	Normal	Normal	Normal	Shortened, blunt	Clearly atrophic	Complete loss
Crypt architecture	Normal	Normal	Enlarged	Enlarged	Enlarged	Severe hyperplasia
Intraepithelial lymphocytes	Normal (<25 per 100 enterocytes)	Increased	Increased	Increased	Increased	Increased
Vh:Cd ratio	≥3	≥3	≥2 to <3	≥1 to <2	≥0·5 to <1	<0·5

Figure 3.4. ***Small intestinal histology in CD classified according to the Marsh-Oberhuber classification system.*** *Grade 0 is normal small intestinal mucosa, whereas grades 1–3c classify the variable degree of damage found in celiac disease (grades 0–1 are usually found in potential celiac disease, and grades 3a–c reflect the presence of celiac disease-associated villous atrophy) [25].*

3.1.5. Malignancies and mortality risk associated with celiac disease

CD is associated with an elevated risk (RR = 3.1) of non-Hodgkin lymphoma, particularly of the T-cell type, and primarily localized in the gastrointestinal tract [60]. This lymphoma, known as enteropathy-associated T-cell lymphoma, is a rare subtype of non-Hodgkin lymphoma with an incidence of around 0.10 cases per 100,000 individuals per year. It specifically develops in CD patients, either preexisting or concurrently diagnosed, and is more prevalent in older men, with the highest occurrence in the seventh decade of life [61], [62]. Although it is rare in children, cases have also been seen in patients strictly adhering to a gluten-free diet [63]. Enteropathy-associated T-cell lymphoma often represents the final stage of type 2 refractory CD, a complication of adult CD characterized by persistent symptoms and mucosal damage despite following a strict gluten-free diet. This tumor often develops in the jejunum, is multifocal, and is characterized by ulcerative lesions. Moreover, it displays neoplastic cells that are positive for CD3e, CD7, CD103, and cytotoxic markers such as TIA-1, granzyme B, and perforin, while are negative for CD4, CD5, CD8, and CD56. Treating enteropathy-associated T-cell lymphoma becomes challenging as it spreads, resulting in low long-term survival rates (13% at 30 months) [60]. Small bowel carcinoma (SBC) is relatively rare in the general population but has a connection to CD. A retrospective study in Sweden showed that

the risk of SBC was significantly higher (hazard ratio (HR) = 3·05) in CD patients [64]. In some instances, the diagnosis of CD occurs either concurrently with cancer or subsequently. The majority of SBCs are located in the jejunum or duodenum and often exhibit clinical symptoms including pain, persistent iron deficiency anemia, occult or overt bleeding, and signs of obstruction. Non-compliance with a gluten-free diet is considered a risk factor for small bowel carcinoma. Early diagnosis improves prognosis, with studies indicating a high five-year survival rate (80%) based on clinical, molecular, and histological subtypes [65].
Complications and the risk of associated malignancies contribute to increased overall mortality in CD (77). A Swedish cohort study identified a slight but significant rise in mortality risk (HR = 1·21 [95% CI, 1·17–1·25]) among nearly 50,000 CD patients compared to healthy controls. Those with celiac disease faced an elevated risk of mortality from cancer, respiratory issues, and cardiovascular diseases [61].

3.1.6. Treatment

Currently, the only effective treatment for CD is strict adherence to GFD. In line with directives established by international regulatory agencies, commercially sold gluten-free products need to maintain a gluten content of below 20 mg/kg (20 parts per million) to meet the established safety criteria [66], [67].
GFD is a nutritionally safe approach that enables disease remission, including mucosal healing, with minimal associated risks. However, effectively removing gluten from the diet is more difficult than it appears. Labelled gluten-free items, such as oats and lentils [68], can be contaminated with gluten during various stages of food processing. Additionally, gluten serves as a common ingredient for its binding and stabilizing properties, and it is often found in unexpected foods like hamburgers, soy sauce, canned soups, dressings, and ice cream [66]. Moreover, considering that wheat is a dietary staple in numerous countries, eliminating gluten may have negative psychosocial impacts and adversely affect quality of life [69]. The necessity to consistently consider dietary restrictions might contribute to psychological disturbances, particularly in patients in vulnerable life stages like adolescence [70].
Moreover, research indicates that GFD may lead to insufficient long-term intake of specific nutrients, particularly fiber, calcium, iron, folate, and other vitamins [71]. While commercial gluten-free products might contain higher amounts of simple sugars and fats compared to gluten-containing products, most studies have not shown an increased risk of obesity or dyslipidemia linked to GFD [72]. Considering these premises, new dietary and pharmacological therapies that could improve the health and quality of life of patients with CD are currently under investigation.

3.2. Gluten

Grains such as wheat, rice, and corn are the main components of the Mediterranean diet, forming the base of the food pyramid, and should be consumed at every meal. Gluten is the primary protein component of some grains, particularly those belonging to the *Triticeae* tribe and its hybrids. i.e., wheat, rye, barley, and spelt. It is a complex mixture of protein storage linked by interchain disulfide bonds and it is rich in proline and glutamine residues (called prolamins). This protein complex, together with starch and lipids, is accumulated in the endosperm of grain seeds during the maturation phase and plays a key role in the subsequent germination phase [73].
The hexaploid *Triticum aestivum* (2n=42, AABBDD genome) is the most common and well-known wheat species; its kernel contains 8 to 15% protein, of which 10-15% is albumin/globulin and 85-90% is gluten [74]. Gluten, in turn, consists of two main groups of proteins - gliadins and glutenins - classified based on their solubility in alcohol. Alcohol-soluble gliadins, which constitute the prolamin fraction of wheat, have been divided into four groups based on their molecular weight and amino acid composition: ω5-, ω1,2-, α/β-, and γ-gliadins. The prolamins present in other cereals include zeins in corn, hordeins in barley, secalins in rye, and avenalins in oats. On the other hand, glutenins can be classified into two main groups: low molecular weight glutenins (LMW) and high molecular weight glutenins (HMW), which further have two subgroups, X and Y [73], [75] (**Table 3.1**).

Type	MW (kDa)	Proportion (%)	Classification
ωGliadins (ω5, ω1,2)	39-55	3-7	S-poor
α/β-Gliadins	28-35	28-33	S-rich
γ-Gliadin	31-35	23-31	S-rich
x-HMW-GS	83-88	4-9	HMW
y-HMW-GS	67-74	3-4	HMW
LMW-GS	30-39	19-25	Type B – S-rich Type C – S-rich Type D – S-poor

Table 3.1. ***Gluten protein types.*** *S-poor and S-rich indicate the Sulphur content of gluten proteins. Table modified from Wieser et al. 1996 [75] and Shewry et al. 2002 [76].*

Wheat (*Triticum aestivum L.*) prolamins are encoded by multiple copy genes mapped in distinct genomic regions on the short and long arms of chromosomes 1 (1L) and short arms of chromosomes 6 (6S). Gliadins are encoded by six different loci: *Gli-A1*, *Gli-B1*, and *Gli-D1* localized on the short arms of chromosomes 1 and *Gli-A2*, *Gli-B2* and *Gli-D2* on the short arms of chromosomes 6. Specifically, α-gliadin is encoded by *Gli-2* loci whereas γ- and ω-gliadins by *Gli-1* loci. Conversely, glutelins are encoded by six loci localized on the short and long arms of chromosomes 1. Particularly, HMW-GS are encoded by *Glu-A1*, *Glu-B1*, and *Glu-D1* loci on the long

arms of chromosomes 1 whereas LMW-GS are encoded by *Glu-A3*, *Glu-B3*, and *Glu-D3* loci strictly associated with *Gli-1* [76] (**Fig. 3.5**).

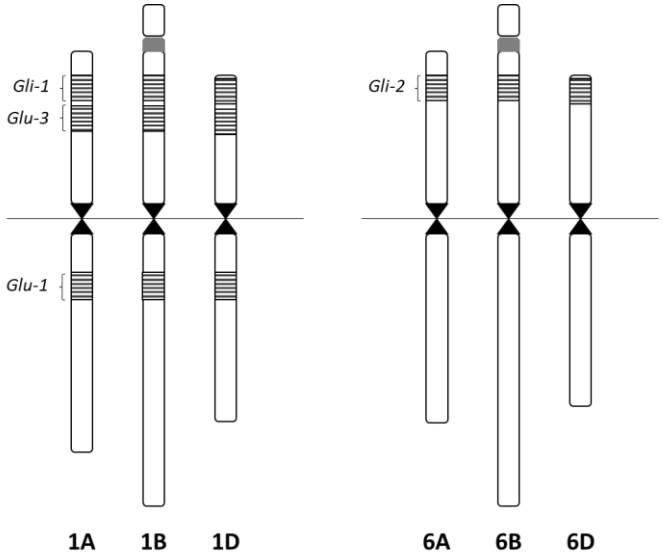

Figure 3.5. ***Prolamins loci in Triticum aestivum L.*** *(genome AABBDD). "Gli" indicates gliadin loci whereas "Glu" indicates the glutenin loci.*

3.2.1. Gluten peptides

The digestion of gliadins and glutenins in the gastrointestinal (GI) tract results in the release of cytotoxic and immunogenic peptides, which lead to epithelial damage and the initiation of the T-cell mediated immune response, respectively. CD and other gluten-related disorders are primarily caused by peptides derived from gliadin, the toxic component of gluten [77] (**Table 3.2**).

Sequence	Position	Toxicity	Immunogenicity
VPVPQLQPQNPSQQQPQEQ	α3-21	+	-
VRVPVPQLQPQNPSQQQPQ	α1-29	-	+
QNPSQQQPQEQVPLVQQQ	α11-28	-	+
QVPLVQQQQFPGQQQPFPPQ	α21-40	-	+
PGQQQPFPPQQPY	α31-43	+	-
PGQQQPFPPQQPYPQPQPF	α31-49	+	+
FPGQQQPFPPQQPYPQPQPF	α30-49	-	+
PGQQQPFPPQQPYPQPQPFPSQQPY	α31-55	+	-
QPYPQPQPFPSQQPYLQL	α41-58	-	+
PQPQPFPSQQPY	α44-55	+	-
PQPFPSQQPYLQLQPFPQ	α46-63	-	+
SQQPYLQLQPFPQPQLPY	α51-70	+	-
LQLQPFPQPQLPYPQPQLPY	α56-75	+	-
PQPQLPYPQPQLPY	α62-75*	-	+/+++
QLQPFPQ	α57-63*	-	+++
QLQPFPQPQLPY	α57-68*	-	+/+++
LQLQPFPQPQLPYPQPQLPYPQPQLPYPQPQPF	α57-89*	-	+/+++
QLQPFPQPQLPY	α58-69*	-	+/+++
PQPQLPYPQPQLPY	α63-76*	-	+/+++
PFRPQQPYPQPQPQ	α93-106*	-	+
LIFCMDVVLQ	α123-132	-	+
QQPLQQYPLGQGSFRPSQQNPQAQG	α198-222	-	+
QQYPLGQGSFRPSQQNPQA	α202-220	+	-
QYPLGQGSFRPSQQNPQA	α203-220*	-	+
LGQGSFRPSQQN	α206-217	+	+ (if *)
PSGQGSFQPSQQ	α205-216*	-	+/+++
QGSFQPSQQN	α208-217*	-	-/+++
LQPQQPFPQQPQQPYPQQPQ	γ60-79	-	+
FPQQPQQPYPQQPQ	γ66-78	-	+
FSQPQQQFPQPQ	γ102-113*	-	-/+
OQPQQSFPEQQ	γ134-153*	-	+/+++
VQGQGIIQPQQPAQL	γ222-236*	-	+/+

Table 3.2. ***List of toxic and immunogenic peptides derived by gliadins.*** *Asterisks indicate deamination by TG2. Table modified by [78].*

3.2.2. 33-mer peptide

The 33-mer peptide, whose sequence is LQLQPFPQPQLPYPQPQLPYPQPQLPYPQPQPF (residues 57-89), is the most gliadin-derived immunogenic peptide. This peptide is present only in the α2-gliadin coded by the D-genome of *Triticum aestivum* [79] and consists of six overlapping copies of three distinct epitopes [80], [81]:

· DQ2.5-glia-α1a (originally called DQ2-α-I), whose sequence is PFPQPQLPY
· DQ2.5-glia-α2 (originally called DQ2-α-II), whose sequence is PQPQLPYPQ
· DQ2.5-glia-α1b (originally called DQ2-α-III), whose sequence is PYPQPQLPY

The DQ2.5-glia-α2 epitope is primarily responsible for the interaction between 33-mer and HLA-DQ2 molecules (1:1 stoichiometry). Before its interaction with HLA-DQ2, the only modification occurring on 33-mer is its deamination mediated by TG2 at a pH close to that in the extracellular space (pH = 6) [82].
In vitro and *in vivo* studies showed that 33-mer is resistant to the activity of different gastrointestinal enzymes, such as gastric and pancreatic proteases as well as other intestinal enzymes [83]. As other cytotoxic peptides (i.e., p31-43), this peptide can induce pro-inflammatory genes in primary murine macrophages in a way that resembles the action of LPS, thus leading to the over-expression of TNF-α, IL-12, and other molecules such as IP-10 and MCP-5, essential for monocytes and T-cells recruitment in the inflammation sites [84].
Recent studies also demonstrated that 33-mer peptide can undergo self-assembly processes due to hydrophobic effect, intramolecular hydrogen bonding, and electrostatic complementarity. Aggregation can lead to supramolecular structures of more than 220 nm that can induce the over-expression of NF-kB via TLR2 and TLR4 pathways in macrophages, thus promoting the release of IP-10, CXCL10, and TNF-α [85], [86], [87], [88], [89], [90]. Additionally, the 33-mer peptide is able to increase the gut-homing $CCR9^{+}$ expression onto autologous T-cells in dendritic cells (DCs) [91].
Other peptides with similar characteristics to 33-mer have been discovered in other gliadin proteins, such as γ-gliadin. Specifically, the 26-mer peptide identified in γ5-gliadin, whose sequence is FLQPQQPFPQQPQQPYPQQPQQPFPQ, presents three epitopes (DQ-γ-III, DQ-γ-VI, and DQ-γ-VII) and shows resistance to the gastrointestinal enzymes [92].

3.2.3. p31-43 peptide

The p31-43 is the most well-known and extensively studied cytotoxic peptide. Its sequence is LGQQQPFPPQQPY, and it is a part of the longer p31-55 peptide (LGQQQPFPPQQPYPQPQPFPSQQPY) [93].
One of the primary effects of p31-43 is the stimulation of cytoskeletal rearrangement. Specifically, the activation of PKC leads to the zonulin signal transduction pathway, ultimately promoting an increase in intestinal permeability [94].
Several studies demonstrate that the administration of p31-43 to CD patients leads to increased IL-15 levels and apoptosis in intestinal enterocytes [95]. This peptide is also capable of interacting with the epidermal growth factor receptor (EGFR) and the IL-15/IL-15R complex [96], [97], inducing proliferation, oxidative stress, and endosomal maturation in enterocytes [98]. Additionally, in murine tissues, p31-43 induces the production of pro-inflammatory cytokines by macrophages [84]. All these data support the hypothesis that the p31-43 peptide can stimulate the innate immune response.
Further experiments conducted in mice have confirmed the ability of p31-43 to induce a local inflammatory response in the cells of the small intestine. This occurs through the activation of the NLRP3 inflammasome, which can sense signals derived from cellular damage caused by nanostructures [99]. In this context, similar to the 33-mer peptide, p31-43 can also self-assemble into oligomeric complexes under certain physiological conditions. Since a specific membrane receptor for p31-43 has never been identified [100], it can be hypothesized that the structural organization into oligomers is crucial for inducing the various biological effects exerted by this peptide [101]. Moreover, the poly-proline II secondary structure of p31-43 leads to nanostructures, which act as a reserve that protects the peptide from degradation [99].
Nowadays, the structure of p31-43 was solved by Calvanese and colleagues (2019) [102]. Additionally, it seems that there is no p31-43 receptor on the cell surface, suggesting that p31-43 could be the prototype of a new class of cell-penetrating peptides (CPPs), small peptides able to establish an interaction as direct contact with the cell membrane or by escaping endocytic vesicles [103], [100].

3.2.4. Gluten Exorphins

In addition to the immunogenic and cytotoxic peptides, gluten digestion generates other small peptides that might contribute to the development of CD. Gluten exorphins (GEs) are a family of small peptides (four to five amino acids) derived from the GI digestion of gluten. These peptides can bind to opioid receptors (ORs) and exert actions similar to those of morphine. They were first described by Zioudrou and colleagues in 1979 [104]. The isolation and characterization of GEs was performed in 1992 and 1993 by Fukudome and colleagues. Gluten was digested with

different enzymes and tested using the MVD assay in presence or absence of naloxone [105], [106], [107].
They identified five classes of gluten exorphins: A4, A5, B4, B5, and C5.

A4: Gly-Tyr-Tyr-Pro
A5: Gly-Tyr-Tyr-Pro-Thr
B4: Tyr-Gly-Gly-Trp
B5: Tyr-Gly-Gly-Trp-Leu
C5: Tyr-Pro-Ile-Ser-Leu

A4 and A5 are selective ligands for the δ opioid receptor (DOR) but show no affinity for the κ opioid receptor (KOR). Their opioid activity is mediated by the N-terminal glycine residue. B4 and B5, on the other hand, exhibit high affinity for both the δ (DOR) and μ (MOR) opioid receptors, but not for the κ receptor. The exorphin C, finally, is selective for the μ receptors.
B5 is the most potent exorphin, with an EC_{50} of 0.05 μM in the GPI assay and 0.017 μM in the MVD assay. The EC_{50} represents the concentration of a ligand needed to saturate half of the receptors. The amino acid residue conferring these characteristics to B5 is the C-terminal leucine [105], [106].
Several studies suggest that food-derived peptides with opioid-like actions have various physiological and pathological effects. Gluten-derived exorphins have been shown to carry out actions that can mimic those of endogenous opioids. For example, exorphins are capable of increasing intestinal transit time [108], and especially exorphins A5 and B5 can stimulate insulin production after a meal [109]. Additionally, a study on murine models demonstrated that oral administration of exorphin A5 can have anti-nociceptive effects, and influence learning and behaviors associated with anxiety [110]. The accumulation of food-derived peptides with opioid-like action has also recently been associated with nervous system disorders, such as schizophrenia and autism [111]. Recently, our laboratory described the molecular effects triggered by gluten exorphins in SUP-T1 and Caco-2 cells. Particularly, all the gluten exorphins can promote phosphorylation of Erk1/2 in both cell lines and activation of Akt in SUP-T1. Moreover, in Caco-2 cells exorphin B5 was able to inhibit STAT3 activation. Experiments on primary $CD3^+$ and $CD8^+$ T-cells derived from healthy individuals using exorphins B4 and B5 showed the inhibition of cell metabolism soon [112].

3.3. Enteric glial cells

3.3.1. The Enteric Nervous System

The enteric nervous system (ENS) is an extensive neural network of the GI tract, extending from the esophagus, through the stomach and small intestine (duodenum, jejunum, and ileum) to the end of the large intestine (cecum, colon and rectum) [113]. It is comprised primarily of two cell types: enteric neurons (ENs) and enteric glial cells (EGCs). These cells are organized into ganglia located in two concentric and interconnected enteric nerve plexuses embedded in the gut wall, which locally regulate the functioning of nearby tissues and cells such as smooth muscle, glands, blood vessels, and immune cells [114], [115].
Between the longitudinal and circular muscle layers there is the myenteric plexus, while the submucosal plexus lies within the connective tissues of the submucosa. In mice, rats, and guinea pigs, the submucosal plexus is composed of a single layer of small ganglia, whereas in larger animals it is organized in two layers of ganglia, called the inner and the outer submucosal plexus. [116], [117], [118]. The neurons of the myenteric plexus control GI motility by regulating the activity of the gut's smooth muscle [119], [120], [121]. In contrast, the submucosal plexus regulates mucosal secretion, absorption, and blood flow. In bigger animals, additional control of the circular and longitudinal muscles is provided by the outer submucosal plexus [122], [123].

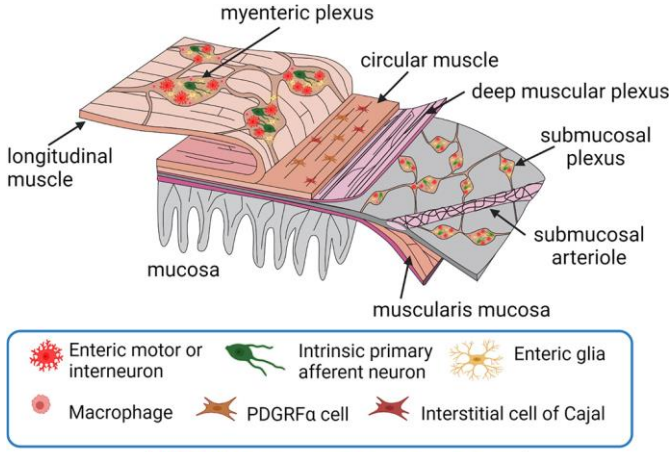

Figure 3.6. ***General organization of the ENS*** [114].

ENs are classified into different categories based on their histochemical, electrophysiologic, and functional properties. They include intrinsic primary afferent neurons (IPANs), secretomotor neurons, interneurons, motor neurons, and vasomotor neurons [124]. ENS neurons are synaptically interconnected, forming parallel reflex

circuits. ENs are synaptically interconnected, and forms parallel reflex circuits. For the complex neurochemical signaling within the ENS, most ENs use acetylcholine (Ach), and others use nitric oxide (NO), substance P, vasoactive intestinal polypeptide (VIP), neuropeptide Y (NPY), and adenosine triphosphate (ATP), in different combinations [125]. Moreover, a small fraction of neurons in the ENS synthesizes dopamine [125], serotonin [126], [127], or γ-aminobutyric acid (GABA) [128].

Enteric glia are a group of peripheral neuroglia associated with the bodies and neurites of ENs throughout the whole GI tract. These glial cells are found in high concentrations within the ganglia of the ENS, where they surround enteric synapses and outnumber neurons by three to five times [129]. Since their discovery, numerous studies have demonstrated that EGCs plays a crucial role in digestive physiology. They support myenteric and submucosal neurons and regulate the activity of neural circuits of intestine [130], [131]. However, recent research, partly inspired by the recognition that EGCs are not confined solely to the ganglia but are also dispersed throughout the intestinal wall, have revealed that they have additional functions that go beyond their conventional neuroprotective and regulatory roles. Specifically, EGCs display neurotransmitter, immune, and homeostatic functions, and contribute to maintaining the integrity of the intestinal epithelial barrier, promoting the proliferation and differentiation of epithelial cells, and supporting the defence mechanisms of the intestine [132].

3.3.2. Enteric glia development

The ENS arise from neural crest-derived cells (NCDCs) that migrate along the length of the developing intestine [133], [134]. These cells have high migratory potential that relies on specialized mechanisms, which when disrupted, result in intestinal colonization and ENS formation failure. In extreme cases, the failure of neural progenitors to colonize the entire gut cause aganglionosis. In this case, the most distal part of the large intestine lacks innervation. This leads to a life-threatening disease called Hirschsprung's disease (HSCR), that has an occurrence in about one in 5000 live births [135]. Nonetheless, despite the development of enteric ganglia, errors occurring in their assembly can still lead to severe consequences, such as chronic idiopathic intestinal pseudo-obstruction [134].
Murine and chick models are commonly used to study ENS development [136], [137] because in humans it occurs through a similar process, in which enteric neural crest-derived cells (ENCCs) take a similar migratory route between Embryonic Weeks (EW) 4-7 [137], [138], [139]. As the gut undergoes rapid growth and elongation during the initial phases of development, extensive migration, and proliferation are required for vagal and sacral neural crest-derived progenitors to successfully colonize it.

Vagal ENCCs invade the foregut at Embryonic Day (E) 9.5 and migrate rostrocaudally, to proliferate and differentiate into neurons and glia as they trail behind the migratory wavefront. Between E11 and E12, some ENCCs cross the mesentery from the midgut to the hindgut, contributing to at least the distal two-thirds of the hindgut ENS [140]. Subsequently, a smaller group of sacral ENCCs enters the hindgut and migrates caudorostrally, while Vagal ENCCs reach the end of the gut by E14.5 [141].

Finally, from E15.5, a subpopulation of ENCCs migrates from the Myenteric Plexus (MP) inwards to begin forming the Submucosal Plexus (SMP) [142], [143]. From E18.5, enteric neurons start to show neurogenic motor activity but the formation of synaptic connections mainly occurs postnatally [144], [145].

ENS development is orchestrated by several signaling pathways, whose timing and fine regulation are crucial to establish a fully functional neural and glial network. While significant progress has been made in understanding the differentiation mechanism of ENs and EGCs in mice, there remains a limitation in information and knowledge regarding the decision making of bipotent ENCCs to become either neurons or glia [146].

Sox10 is a key transcription factor in neural crest and enteric glial development, whose dual role in maintaining pluripotency and promoting glial differentiation is not yet well understood [147]. During early embryogenesis, Sox10 regulates the expression of several key genes, including *Ret* [148], [149], [150] and *Ednrb* [151], which are critical for early ENS development, promoting ENCC proliferation and migration. As ENCCs differentiate, ENs decreases Sox10 expression, whereas it is maintained by the majority of adult enteric glia [152]. During the development of the ENS, the expression of Sox10 is extremely fine-tuned in time and space and is orchestrated by an interplay of several signaling pathways [153]. For example, the Notch signaling pathway, which is activated by the Delta ligand, indirectly promotes Sox10 expression via the transcription factor Hes1, which can repress the pro-neural gene *Ascl1* [154], [155]. In addition, the glial-derived neurotrophic factor (GDNF)-Ret and Sox10 pathways act synergistically to regulate neural crest migration and proliferation during early ENS development [156], [157], [158]. However, similar to Sox10, the role of GDNF-Ret signaling changes over time, and the timing and location of increased GDNF can have different effects on the ENS. Indeed, Ret becomes upregulated in neurons and downregulated in enteric glia [159]. Overall, the GDNF-ret signaling pathway is essential for the development and function of enteric glia, and its dysregulation has been implicated in a range of gastrointestinal disorders, including Hirschsprung's disease [158].

Finally, studies have demonstrated that the transcription factors Foxd3 and the orphan nuclear receptor Nr2f1 are necessary for the differentiation of neural crest cells into glial cells. In particular, they regulate the expression of genes involved in the development and function of enteric glial cells, such as glial fibrillary acidic protein (GFAP) and choline acetyltransferase (ChAT) [160], [161], [162].

3.3.3. Glia diversity

Recently, there has been growing interest in enteric glia heterogeneity and plasticity. Indeed, it has been demonstrated that specific intestinal environmental cues drive EGC's phenotype and functions, resulting in subpopulations of glia with unique characteristics within the different intestinal regions. However, there is still limited knowledge regarding regional or local glial heterogeneity and the role of glial specializations in contributing to the various digestive functions.
The current classification includes six EGC subtypes, depending on their morphology and anatomical location within the intestinal wall and the enteric ganglia [163], [164]. Type I_{MP} and $_{SMP}$ EGCs surround neuron cell bodies with short and irregularly branched processes within the myenteric and submucosal plexuses, respectively. Fibrous glia (Type II) present long processes that connect myenteric ganglia, whereas multipolar Type III EGCs are associated with the mucosa (Type III_{MUCOSA}) and the myenteric and submucosal plexuses (Type III_{MP} and $_{SMP}$). Finally, elongated Type IV resides in the smooth muscle layers (Type IV) [130]. Interestingly, in a recent study Scavuzzo and colleagues identified two additional populations with triad and bipolar shape [165].

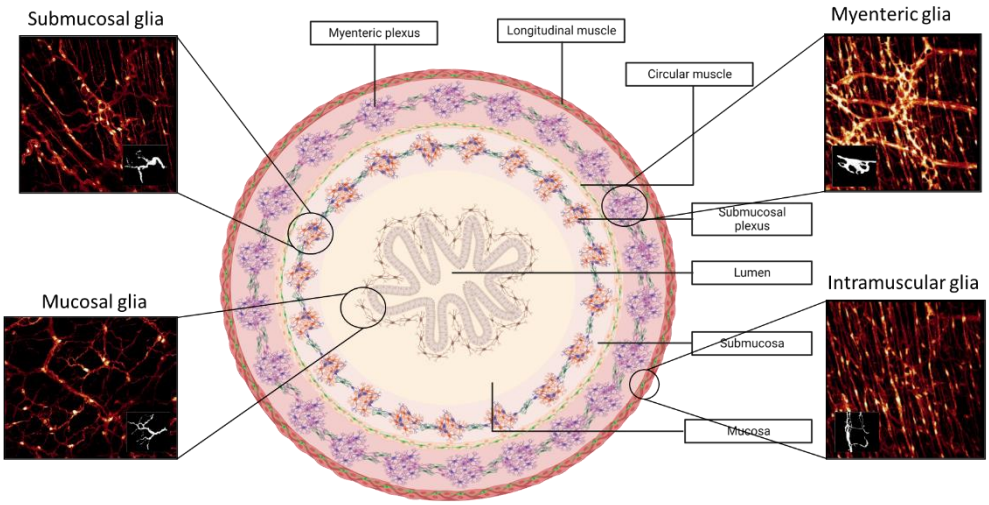

Figure 3.7. ***EGC populations.*** *Local subpopulations of glia are defined based on their morphology, anatomical location in the intestinal wall, and localization within or outside of the enteric ganglia (figure adapted from Seguella and Gulbransen, 2021[130].*

Nevertheless, this classification is not exhaustive to encompass the functional heterogeneity between intestinal regions or even within the major subtypes themselves. For instance, a recent study conducted by Seguella and colleagues reported distinct responses to neuromodulators among glial cells in the duodenum and colon, suggesting functional diversity across intestinal regions. This

classification based on the functional response profile to adenosine diphosphate (ADP) and cholecystokinin (CCK) delineates 4 unique subpopulations, whose heterogeneity is associated with differing mechanisms of communication with neurons [166].
Moreover, molecular and functional data suggest added complexity within and between the major glial subtypes. Although enteric glial markers such as GFAP, the Ca2+ binding protein S100β, proteolipid protein 1 (PLP-1), and the transcription factor Sox10 have been identified, none is sufficient to label all EGCs in the gut [164], [167], [168], [169]. For example, the expression of GFAP is dynamic and varies depending on the glial state [170], and subtype [164]. Additionally, the detection and distribution of GFAP+ cells in immunolabeling experiments may be limited by the antibody's ability to recognize one or more GFAP isoforms [171], [172], [173], [174].
To better delineate and functionally characterize unique enteric glial populations in the gut, emerging techniques such as single-cell RNA sequencing (scRNAseq) have been employed. In a study of 2018, Zeisel and colleagues performed scRNAseq of neural crest-derived cells isolated from the small intestinal myenteric plexus of Wnt1Cre;R26Tomato transgenic mice and identified seven distinct EGC sub-types, including one proliferative [167]. Also, more recently Guyer and colleagues reported 9 transcriptionally different EGC clusters in GFP+ cells isolated from the small intestine longitudinal muscle-myenteric plexus (LMMP) of Plp1::GFP mice at postnatal day 14 (P14) [175]. By contrast, in human embryos, six clusters of enteric glial cells have been identified [168]. Finally, Scavuzzo and colleagues demonstrated that EGCs share many genes with their homologus in CNS and PNS, but in unusual combinations that impart them with a distinctive identity compared to all other glia in the body. Hence, they made use of single-nucleus RNA-sequencing and identified 7 distinct molecular classes of enteric glia with different signatures between duodenal and colonic enteric glia [165].

3.3.4. Enteric glia in gastrointestinal physiology

The initial evidence of communication from neuron to glia was collected in 1972, when Gabella observed presynaptic specialization in nerve processes that made contact with enteric glia in the myenteric plexus of the ileum of guinea pig [176]. Only 40 years later did Ca^{2+} imaging experiments prove EGC's ability to functionally respond to endogenous and exogenous neurotransmitters *in vitro*, registering increased intracellular Ca^{2+} concentration as a response [177], [178], [179], [180], [181], [182]. To date, it is well known that, like astrocytes, EGCs can be activated by various neurotransmitters, resulting in increased intracellular Ca^{2+} levels, followed by the release of gliotransmitters such as ATP through membrane channels composed of connexin 43 (Cx43 or GJA1) [183]. A study conducted by McClain and colleagues demonstrated the role of Cx43 hemichannels in the propagation of "calcium waves" through the enteric glial network, revealing that glial "calcium waves" triggered by

extracellular ATP or ADP were disrupted when Cx43 was specifically lost in glial cells, resulting in abnormal activity within the ENS network and GI dysmotility [184].

Although it has been demonstrated that EGCs bidirectionally communicate with enteric neurons and non-neuronal cells, the necessity of glial support in the enteric network is not fully understood. Particularly, considering that EGC and astrocytes exhibit molecular similarities, their role in supporting neural networks might be compared [185]. Nevertheless, while the supportive role of astrocytes has been widely demonstrated [186], research studies supporting the notion that enteric glia share similar functions are still in progress. The limited available evidence suggests that EGCs maintain homeostasis in the microenvironment surrounding neurons. By participating in the uptake, metabolism, storage, enzymatic conversion, and release of gliotransmitters, EGCs contribute to the regulation of neurotransmitter availability in the enteric nervous system, thereby influencing neuronal signaling [187], [188], [189], [190], [191]. Indeed, EGCs can actively take up neurotransmitters from the extracellular space using specific transporters. For instance, the action of GAT2 in enteric glia allows for the reuptake and regulation of GABA, contributing to the precise control of GABAergic signaling in the enteric nervous system [192], [188]. Hence, once inside the EGCs, these neurotransmitters can undergo metabolism through enzymatic processes. Indeed, EGCs express enzymes such as nucleoside triphosphate diphosphohydrolase 2 (NTPDase2) [189], [190], [191] and glutamine synthetase [187], which catalyse the hydrolysis of ATP and ADP and the conversion from glutamate into glutamine, respectively. Their activity in EGC influences these molecules' availability and signaling properties, contributing to the fine-tuning of neurotransmitter balance and modulation of neuronal activity in the enteric nervous system. Additionally, recent in vitro studies showed that Ach, the key neurotransmitter that stimulates smooth muscle contraction in the gut, is detected by EGCs, which in turn get activated and may contribute to control GI motility [193].

Gut motility is controlled by the ENS, which coordinates gastrointestinal movement by sensory, inter, and motor neurons. Intrinsic sensory neurons detect luminal stimuli and activate ascending interneurons, which evoke contraction by synapsing with excitatory neurons, or relaxation by connecting with inhibitory motor neurons [194]. Considering that EGCs intermingle with enteric neurons, smooth muscle, and intestinal epithelium within the intestinal walls, their role in gut motility has been suggested but not finely investigated. Recently, Scavuzzo and colleagues made use of single nucleus RNA-sequencing to identify distinct molecular populations of EGCs and define their morphological and spatial diversity. They identified a functionally specialized biosensor subtype of enteric glia, called “hub cells”, which can influence the function of enteric neurons to regulate intestinal contractions and gut physiology through the mechanosensory ion channel PIEZO2 [165].

Finally, in vitro studies suggest that enteric glia may also play a role in to neurogenesis and maturation of neuronal networks, as they have the capability to generate trophic compounds such as pro-epidermal growth factor, nerve growth

factor, and vascular endothelial growth factor. EGCs also release GDNF, which is known to promote the survival, growth, and development of neurons within the ENS. It supports the survival of enteric neurons during development and plays a crucial role in maintaining the integrity and functionality of mature enteric neurons. GDNF released by EGCs provides essential trophic support to neurons, ensuring their proper functioning and preventing cell death [195].

In vivo data demonstrating the necessity of glial support in the enteric network are controversial, as different mouse models of enteric glial depletion present different outcomes. For instance, models involving glial-targeted CD8+ and CD4+ T-cells [196], [197] transgenic mice expressing herpes simplex virus thymidine kinase (GFAPHSV-TK) [198], and the use of gliotoxin 6-aminonicotinamide [199], [200] lead to severe intestinal issues and even death. However, depleting glia in mice using the PLPCreER;Rosa26DTA model, which employs diphtheria toxin under the control of Cre recombinase directed to glia, has shown minimal changes, except for an increase in colonic migrating motor complex frequency in female mice [201]. The reasons for these discrepancies between models are not fully understood but may involve factors such as different penetrance, effects on specific glial subtypes, and compensatory responses from surrounding cells [201]. It should be noted that the specific effects of glial depletion on neuronal signaling have not been extensively assessed in these models. Data from the PLPCreER;Rosa26DTA mouse model suggest that glial depletion does not significantly impact enteric neuron survival under steady-state conditions, challenging the notion that glia are necessary for maintaining enteric neuron survival and ongoing neurogenesis [201], [202]. However, gliogenesis is consistently detected in the adult mouse gut under steady-state conditions and increases in response to certain types of ENS injury, including inflammation, irradiation, benzalkonium chloride treatment, and partial gut stenosis [203], [204]. The neurogenic potential of glia may be only enacted under conditions that disrupt the normal homeostatic state of the enteric nervous system.

3.3.5. Enteric glia in gastrointestinal diseases

Given EGC's contribution to maintaining intestinal homeostasis together with other cells, it is likely that glia also play a critical role during neuropathology [205], [206]. Especially, this is important in disorders concerning the gut-brain axis (previously named functional gastrointestinal and motility disorders), whose main features are abnormal motility, pain, and age-associated decline in gastrointestinal neuromuscular function [207], [208], [209], [210]. However, EGCs influence pathological mechanisms in intestinal diseases of various nature, by modulating neuroplasticity and immune responses [170], [211], [212]. Considering their similarities to immune cells in terms of molecular composition and observed responses, EGC have been recognized for their immunoregulatory properties in intestinal inflammatory

conditions. Indeed, EGCs can detect microorganisms, damage-associated molecular patterns (DAMPs), pathogen-associated molecular patterns (PAMPS), and signals originating from immune cells. This is acquired through the expression of functional pattern recognition receptors, such as toll-like receptors (TLRs), nod-like receptors (NLRs), cytokine receptors (e.g., IFNγR), and the necessary machinery to respond to inflammatory triggers (e.g., NF-κB, MYD88, STAT1, STAT3, etc.). Moreover, when stimulated, EGCs release cytokines and chemokines that play roles in either pro- or anti-inflammatory conditions [213], [214], [215], [216]. While the diverse reactions of EGCs to inflammatory stimuli have primarily been studied *in vitro* [213], [214], it is becoming increasingly evident that EGCs can respond to challenges within the tissue *in vivo* [217], [170], [212], [218]. During this response, EGCs acquire a distinct molecular state similar to astrogliosis [219], which involves cell cycle entry and GFAP upregulation, enabling them to exert local immunomodulatory effects on surrounding cells [218], [220], [221], [222].

3.3.5.1. Infections

Clostridium difficile (C. difficile) infection (CDI) has been reported as the most common cause of antibiotic-associated colitis. Indeed, this bacterium is a common inhabitant of the gut microbiota in 1–3% of adults and, after treatment with a broad spectrum of antibiotics, it can exploit the lack of commensal bacteria and colonize the large intestine. It is well known that *C. difficile* toxin A (TcdA) and toxin B (TcdB) affect various cell types in the intestine, including enterocytes, colonocytes, and ENs. Indeed, several studies highlighted that *C. difficile* TcdA and TcdB induce glucosylation of Rho GTPases, cytopathic/cytotoxic effects, and inflammation. Recently, Fettucciari and colleagues demonstrated that EGCs are susceptible to TcdB. Specifically, they treated rat-transformed EGCs with TcdB and reported its early cytopathic effects, such as cell rounding, glucosylation of Rac1, and cell cycle arrest [223]. Subsequently, they demonstrated that TcdB induces apoptosis in EGCs *in vitro* by activating three signaling pathways mediated by caspases, calpains, and cathepsin B and that the activation of apoptosis was enhanced in the presence of the pro-inflammatory cytokines TNF-α and IFN-γ. Notably, the ability to activate three different apoptotic signaling pathways could be an advantageous strategy adopted by *C. difficile* in order to bypass cell resistance to one or two specific apoptotic pathways [224], [225]. Moreover, a recent study reported that Pannexin-1 (Panx1) channel, whose involvement in intestinal inflammation and inflammatory bowel disease (IBD) is well-known, is increased in the intestinal tissue of mice during CDI. In addition, it plays an important role in the effects of *C. difficile* toxins in EGCs, contributing to caspase-3/7-mediated cell death and IL-6 over-expression [226]. Finally, a recent work from Costa and colleagues identified adenosine receptors as key regulators of EGC response to TcdA and TcdB, pointing out A2B activation as an important mechanism in inducing glial apoptosis [227].

On the other side, *in vivo* studies detected an increase of S100β in colon tissues and fecal samples of patients with CDI, as well as in colon tissues from *C. difficile*-infected mice. Costa and colleagues showed that S100β modulates the inflammatory response during CDI, upregulating proinflammatory mediators such as IL-1β, IL-18, IL-6, GMCSF, TNF-α, IL-17, IL-23, and IL-2, and downregulating protective mediators, including SOCS2, IL-22, and Bcl-2. In EGCs, S100β upregulation induced IL-6 expression via activation of the RAGE/PI3K/NFκB signaling pathway. Inhibition of S100β activity has been shown to mitigate intestinal damage and diarrhea caused by *C. difficile* toxins, suggesting that targeting S100β could be a potential therapeutic strategy for managing the effects of CDI on the GI system [228].

Toxoplasma gondii (T. gondii) affects up to one-third of people worldwide and is contracted by consuming raw meat containing tissue cysts or food that contains oocysts. Once in the GI tract, *T. gondii* rapidly proliferates and crosses the intestinal barrier, initiating a local immune response. It has been shown that infection with different strains of *T. gondii* causes changes in the neuronal subpopulations and epithelial cells in different segments of the GI tract [229]. Recently, a study conducted by Trevizan and colleagues made use of Wistar rats to evaluate the kinetics of neuronal and glial responses after orally receiving sporulated oocysts of the parasite. Following *T. gondii* infection (TGI), they observed a decrease in ENs and an increase in the EGC/neuron ratio, with major alterations beginning 72 hours post-infection. The highest EGC/neuron ratio was observed in the MP 24 hours post-infection and SMP 48 hours post-infection, suggesting a possible protective factor for neurons in the presence of acute TGI [230].

Finally, a study by Progatzky et. al demonstrated that helminthic infection in mice induces the reactive glia phenotype and the upregulation of an IFN-γ gene signature. They performed single cell RNA sequencing on the *tunica muscularis* (TM) of mice infected with third-stage *Heligmosomoides polygyrus* larvae, which settle in the TM of the duodenum and induce local tissue inflammation and multicellular granulomatous infiltrates. The single-cell transcriptomics analysis highlighted that glia-specific abrogation of IFNγ signaling results in tissue-wide activation of pro-inflammatory transcriptional programs, identifying this pathway as fundamental in restoring tissue integrity after helminth infection. Moreover, CXCL10 has been pointed out as a critical mediator of tissue repair downstream of the IFNγ-induced activation of EGCs, showing that IFNγ–EGC–CXCL10 axis plays a fundamental role in immune response and tissue repair after infectious challenge [218].

3.3.5.2. Intestinal inflammation

Intestinal inflammation induces the recruitment of immune cells, such as neutrophils, macrophages, and lymphocytes, triggering a dynamic and highly coordinated immune response within the GI tract. EGCs have been recognized for their immunoregulatory role in intestinal inflammatory conditions, being able to interact both with innate [218], [231], [221] and adaptive immune cells [232], [222].
By eliciting intestinal inflammation in a mouse model lacking glial Cx43 (Sox10CreERT2;Cx43f/f), Grubišić et al. demonstrated that EGCs exert an immunomodulatory role by activating muscularis macrophages through mechanisms that require glial connexin-43 (Cx43) and macrophage colony-stimulating factor (M-CSF) production. *In vitro* experiments with mouse and human enteric glia showed that glial Cx43-dependent M-CSF production is induced by pro-inflammatory signals through protein kinase C (PKC) and TNFα converting enzyme (TACE), an enzyme that cleaves membrane-bound M-CSF. Together, these data underscore a mechanism by which enteric glia impact visceral sensitivity through interactions with muscularis macrophages, highlighting the significance of EGCs as an crucial intermediary in the neuroimmune crosstalk in the GI system [221].

EGCs have the unique feature of responding to surrounding cues and acquiring specific states, including a reactive phenotype named “gliosis”. Glial differentiation into reactive EGC includes changes in molecular composition, structure, and functions, which seems to be influenced by several factors, including type and severity of the injury, and glial subtype [170]. Gliosis is also shown to be part of an intestinal immune response that occurs upon abdominal surgery that leads to impaired motility in post-operative ileus (POI). A study performed by Schneider and team, which involves *in vivo*, *ex vivo*, and *in vitro* analysis in mice and human specimens, suggests that the activation of EGCs in this process is induced by ATP released during abdominal surgery and the following ATP-triggered purinergic P2X2 signaling in glial cells. In addition, they identified the glial P2X2 antagonist drug ambroxol as a possible novel therapy in reducing gliosis, ameliorating inflammation, and improving dysmotility during POI [233].

Considering that EGCs, ENs, and muscularis externa macrophages (ME-Macs) are closely associated cells in the gut wall, it is likely that they interact during intestinal inflammation. However, the precise mechanisms of EGC-ME-Macs communication and their impact on intestinal inflammation are poorly understood and are objects of investigation in the field of GI physiology and pathology. Previous studies showed that the blocking of IL-1 receptor type 1 (IL1R1) protects from POI in mice, suggesting that IL-1 is a crucial cytokine in the development of this disorder [234]. Since EGCs express IL1R and the activation of this receptor results in the release of important mediators in POI such as IL-6 and CCL2 [235], Schneider and colleagues conducted a study to demonstrate the role of enteric glia in this disorder. They showed

that IL1R1-signaling induces the reactive phenotype in murine and human EGCs, which then release chemokines, cytokines, and CSF-1 and -3. Making use of ribosomal tagging, they discovered that enteric gliosis plays an early role in the pathogenesis of POI. Interestingly, the specific ablation of glial IL1R1 did not induce the reactive phenotype in EGC and decreased immune cell infiltration, protecting mice from developing POI. Moreover, the alterations in surgery-induced glial activation in IL1R-lacking mice affected ME-Mac functions, including phagocytosis, migration, and accumulation around enteric ganglia. In patients, bowel surgery also induced IL-1 signaling and macrophage activation, further confirming the data obtained in the murine model [236]. In line with these findings, Stakenborg et.al reported that EGCs were activated during muscularis inflammation. This resulted in monocyte infiltration and differentiation of anti-inflammatory CD206+ Mφs via CCL2 and CSF1, respectively. Furthermore, they also show that CSF1-CSF1R signaling is crucial for the differentiation of monocytes into CD206+ Mφs and EGC proliferation during muscularis inflammation [231]. Taken together, these studies indicate the inevitable role of EGCs in inflammation and their potential to contribute to novel therapeutic strategies for inflammation-related disorders.

3.3.5.3. Cancer

A well-known prognostic marker in colon cancer is tumoral infiltration of neural structures, i.e., perineural invasion [237], [238], which is associated with a reduced 5-year disease-free survival rate [239], presence of metastasis at the time of resection [240], and increased risk of recurrence [241]. As tumor cells invade the bowel wall, neurochemical alterations [242] and an increase in neural element density occur, positively correlating with tumor grading [243]. Considering these premises, it is likely that tumoral and neural cells make close interactions and play a key role in carcinogenesis. In line, it has been shown that the enteric neuronal network guides tumor cell migration, with tumor epithelial cells establishing direct interactions with ENs via N-cadherin and L1CAM [244]. Additionally, a recent study demonstrated that neuronal loss of the N-Myc downstream-regulated Gene4 (NDRG4), an important biomarker for colorectal cancer (CRC) expressed by ENs, is correlated with enlarged adenoma development and the release of pro-carcinogenic extracellular matrix molecules, nidogen 1 and fibulin 2, in the tumoral microenvironment [245]. However, further studies in human cohorts are needed to translate these findings to a clinical level.

Limited attention has been dedicated to exploring whether and how enteric glia may affect the development and progression of CRC. Although previous research yielded conflicting results regarding the increase or decrease in enteric glia expression in CRC [246], [247], [248], [249], in 2019 Vales and colleagues definitely identified EGCs as a key component of the tumor microenvironment (TME). Particularly, by three-dimensional imaging on full-thickness human colon adenocarcinomas using the

iDISCO (immunolabeling-enabled imaging of solvent-cleared organs) staining, they showed that S100β^{+}- GFAP^{+}- positive enteric glial cell bodies and projections massively infiltrate the whole tumor [250].

Notably, a study conducted by Yuan and team showed a significant tumor burden reduction following EGC depletion in azoxymethane/dextran sodium sulfate (AOM/DSS)-induced CRC mouse model and in Apc$^{Min/+}$ mouse model of familial adenomatous polyposis, suggesting that enteric glia promote tumor development at an early premalignant stage. In line, they also found that the properties of established malignant tumors were not affected by glial depletion, which instead slowed down the development of precancerous dysplastic lesions [248]. Similarly, Valès et al. showed that EGC react to tumor epithelial cells-derived ligands IL-1 α/β, acquiring an activated phenotype. Hence, enteric glia elicit cancer stem cell (CSC) expansion and promote tumorigenesis via a PGE2/EP4/EGFR-dependent pathway [250]. Anyway, during carcinogenesis IL-1 α/β can be produced by several cell types, including infiltrating myeloid cells, colon epithelial cells, and stromal cells. In line, in a recent study van Baarle and colleagues reported that tumor-infiltrating monocytes-derived IL-1 influences the phenotype and function of tumoral EGC in the CRC TME. Hence, IL-1-activated enteric glia produce IL-6, directly enhancing the differentiation of tumor-infiltrating monocytes towards pro-tumorigenic SPP1+ TAMs. Additionally, they demonstrated that tumor EGCs present a unique reactive phenotype, with increased expression of genes correlated with astrogliosis (e.g. Lcn2 and Timp1) and immunomodulatory functions (e.g. Ccl2 and Il6). Notably, this EGC tumoral phenotype is associated with worse disease outcomes, as observed in both pre-clinical CRC mouse models and in patients with CRC [251] Finally, in cultured biopsy samples, the expression of glial S100β increases in CRC compared to healthy tissue and induces the downstream activation of the proliferative signaling pathway RAGE/MAPK/NF-kappaB, resulting in a decreased expression of the pro-apoptotic protein wtp53. Moreover, the higher expression of S100β was also associated with the up-regulation of proinflammatory and proangiogenic factors, including VEGF, IL-6, and AQP4 [249].

The glial contribution to carcinogenic progression has also been suggested in other intestinal tumors, such as duodenal gastrinomas. For example, a study performed by Sundaresan and team suggested that the development of MEN1-associated gastrinoma in the submucosa might arise from EGCs through hormone-dependent PKA signaling [252]. Similarly, Duan and colleagues reported that in the context of gastroenteropancreatic neoplasms (GEP-NENs), the deletion of Men1 in GFAP+ cells led to glial cell reprogramming toward a neuroendocrine phenotype, resulting in gastric neuroendocrine hyperplasia and neuroendocrine tumors in the pituitary and pancreas [253].

3.3.5.4. Inflammatory bowel disease

IBD refers to chronic inflammatory disorders affecting the gastrointestinal (GI) tract, whose prevalence is rapidly increasing in Western countries, affecting more than 2 million Europeans and 1,5 million North Americans [254]. Crohn's disease (ChD) and ulcerative colitis (UC) are the main disorders belonging to IBDs, affecting different segments of the GI tract but sharing common features, mainly chronic inflammation and abnormal intestinal immune response. Common symptoms include abdominal pain, diarrhea, rectal bleeding, weight loss, and fatigue, leading to reduced quality of life [255]. Although the ethiology of IBD is still not completely understood, a central player in the development and progression of IBD is the immune system, which mistakenly triggers an exaggerated inflammatory response against harmless substances (i.e., food and bacteria) in genetically predisposed individuals. This abnormal immune response involves various immune cells, including T-cells, B-cells, and macrophages. The chronic inflammation damages the intestinal tissues and disrupts their normal functions, leading to the characteristic symptoms of IBDs [255].
Notably, 70% of IBD patients do not respond properly to the first-line therapy, implying that the immune cells are not the only players in the pathogenesis of this disease. Moreover, the course of IBD is unpredictable, with periods of active inflammation known as flare-ups and remission, when symptoms subside. Psychological stress exerts a profound impact on IBD, with numerous studies suggesting that stressful life events can exacerbate IBD flares [256], [257], [258]. In line, recent research identified the ENS as a relay between psychological stress and inflammation in the gut, highlighting the importance of the gut-brain axis [259]. Altogether these data suggest that ENs play a critical role in the development and progression of IBD pathogenesis.

Recent studies have investigated the role of EGCs in the context of IBD and showed that enteric glia in IBD patients present molecular abnormalities. By making use of western blotting and ELISA, Von Boyen and colleagues observed increased expression of GFAP in inflamed colonic biopsies from CD and UC patients [260]. In line, when the expression of another glial marker, S100β was quantified, it was found that the expression profile was roughly the same, with elevated levels of S100β in inflamed colonic biopsies compared to those from healthy controls [261], [262], [263], [264]. Additionally, gliomediators and proteins involved in glial cell signalling, such as GDNF and TLR4, are upregulated in IBD patients [260], [262]. Considering that molecular abnormalities lead to functional alteration, it is likely that even the crosstalk between EGCs and other intestinal cell types is defective in the context of IBD. It has been shown that during DSS-induced colitis enteric glia and neurons are exposed to inflammatory stimuli, once intraganglionic macrophages induce degradation of the membrane surrounding the myenteric plexus [265]. In chronic inflammation, EGCs also interact with innate lymphoid cells (ILCs), which

make part of the innate immune system and are regulated by numerous inflammatory mediators, such as neuropeptides, hormones, eicosanoids, and cytokines [266]. Ibiza et al. showed that EGCs regulate a group of ILC3, which express the neuroregulatory receptor tyrosine kinase RET and provide protection against DSS-induced colitis. During chronic inflammation GDNF-derived $GFAP^+$ cells activate RET, leading to IL-22 induction in ILC3 and protection against inflammation [220]. EGCs have also been suggested to interact with mast cells. Some *in vitro* experiments showed that GNDF regulates enteric mast cells and improves the disease outcome of DSS-induced experimental colitis via JNK pathway activation.

Additionally, few studies describing glia-T-cell interaction in IBD showed that enteric glia isolated from ChD patients inhibit the proliferation of activated T lymphocytes [232].

Altogether, these data identify EGCs as a new potential target for treating IBD. A recent study by Li and colleagues studied the effect of the isoquinoline alkaloid berberine, which has anti-inflammatory and therapeutic effects in experimental colitis, regulating neuroimmune interactions in UC. When berberine was administered, disease severity was decreased and the mucosal barrier homeostasis in UC was restored. Moreover, in the in vitro experiments using monoculture and simulated inflammatory conditions, berberine exhibited direct protective effects on EGCs, bone marrow-derived dendritic cells (BMDCs), T cells, and intestinal epithelial cells (IECs). Furthermore, berberine could also regulate the cell-cell interactions of EGCs, IECs, and immune cells in co-culture systems [267]. The research conducted so far gives us an understanding of the complexity of the role of EGCs in IBD. However, further studies are to be performed for a deeper understanding of EGC's role in the context of IBD.

Aims

Although for many years EGCs have been solely known for their role in supporting neuronal functions by shielding and supplying neurotrophic factors to the enteric neurons, in the last decades, their contribution to intestinal homeostasis, maintenance of the epithelial barrier integrity, mucosal inflammation, and immunity has been disclosed.
Several studies reported that the EGC phenotype is altered in chronic inflammatory conditions, such as ChD and UC. However, while the role of EGCs has been well described in IBD, their involvement in CD, which is also an immune-mediated inflammatory disorder of the GI tract, has been poorly investigated so far [268].
Taking into account all common features shared by IBD and CD and the evidence that EGCs are protagonists in several gut physiological and pathological processes, they might be involved in CD pathogenesis as well.

Therefore, the aim of this Ph.D. project is to study the possible role of EGCs in CD pathogenesis. To achieve this main goal, the first immortalized human normal EGC line has been generated, finely characterized, and used as an experimental model. Then, the effects of gluten-derived gliadin and the gluten-derived cytotoxic peptide p31-43 on EGCs have been assessed.

Materials and methods

5.1. Isolation of human and murine EGCs

Primary human EGCs (hEGCs) were extracted from the colon of a 75-year-old female donor. The tissue was acquired from Tissue Solutions, in compliance with ethical approvals and donor consent (Declaration of Helsinki from 1964 and its later amendments). Approximately 2 cm^3 of tissue was collected and preserved in HypoThermosol medium (BioLife Solutions). The myenteric plexus (MP) was subsequently isolated, as described by Soret *et al*. (2013) [269]. The MP was cut into 1–2 mm fragments and incubated at 37°C for 20 minutes. These fragments were homogenized through repeated pipetting in pre-warmed Digest Medium (6 mL/g of bioptic material) composed of Liver Digest Medium (Thermo Fisher Scientific), supplemented with 2000 U of DNAse I, 10 mg of Liberase (Sigma-Aldrich), 1 mL of trypsin 2.5%, and 30 µL (stock solution 100 U/mL) of collagenase type I (Thermo Fisher Scientific). Following incubation, the cell/tissue suspension was passed through a 100 µm nylon mesh and centrifuged twice for 5 minutes at 200 x g.

Embryonic neurosphere-derived mEGCs were obtained following previously established protocols [231]. In summary, total intestines extracted from E13.5 C57BL/6J mice were subjected to enzymatic digestion using collagenase D (0.5 mg/mL; Roche) and DNase I (0.1 mg/mL; Roche) in DMEM/F-12 medium (Gibco, ThermoFisher Scientific) for 1 hour at 37°C with gentle agitation. After enzymatic digestion, the tissue was filtered through a 70-µm cell strainer, and the isolated cells were maintained at 37°C in a 5% CO_2 atmosphere in DMEM/F-12 medium (100 µg/mL Penicillin and Streptomycin, 2 mM L-glutamine, 10 mM HEPES, 1 mM sodium pyruvate, 50 µM 2-Mercaptoethanol, 1x B27 (Gibco, ThermoFisher Scientific), 40 ng/mL epidermal growth factor (EGF) (Stemcell Technologies) and 20 ng/mL fibroblast growth factor (FGF) (Invitrogen, ThermoFisher Scientific). Following a minimum of 1 week in culture, neurospheres were dissociated with the NeuroCult™ Chemical Dissociation Kit (Stemcell Technologies), following the manufacturer's instructions, and then filtered through a 70-µm cell strainer. Subsequently, single cell suspension was seeded onto pre-coated plates with Poly-D-Lysine (PDL solution, 1.0 mg/mL, Sigma Aldrich) and differentiated in DMEM medium (10% FBS, 100 µg/mL Penicillin and Streptomycin, 2 mM L-glutamine, 10 mM HEPES, 1 mM sodium pyruvate, and 50 µM 2-Mercaptoethanol) until reaching confluence for a duration of 5 days, resulting in the generation of primary EGCs.

5.2. hEGC lentiviral transduction and identification of integrated genes

To immortalize hEGCs, the method described by Lipps *et al*. in 2018 [270] was employed. Specifically, several rounds of lentiviral infection with a MOI between 1 and 5 using self-inactivating lentiviral vectors were performed once hEGCs reached 80% of confluence. The list of lentiviral transduced genes is provided in **Supplementary Table T1**. Cells were incubated with lentiviral vectors overnight at 37°C/5% CO_2 in culture medium supplemented with Polybrene (8 µg/mL). Subsequent to medium removal, 30 clones were selected for their growth characteristics. Among them, Clone K (hereafter referred to as hEGC-ClK) was chosen for further analysis and characterization. The integration of lentiviral genes was then confirmed by PCR, using a consensus forward primer (5`: GGAGGCCTAGGCTTTTGCAA) located within the SV40 promoter sequence coupled with genes-specific reverse primers (**Supplementary Table T1**). Genomic DNA was extracted using DNAzol reagent (Gibco Fisher Scientific) following the manufacturer's protocol. 0.5 µg of template DNA and Mango-Taq Polymerase Kit (PJK-Biotech) were used during PCR. The amplification process consisted of 40 cycles: 94°C (30 seconds)/55°C (45 seconds)/72°C (45 seconds). The presence or absence of the targeted genes was assessed by agarose gel electrophoresis (2% *w/v*).

5.3. Established human cell line culture conditions and treatments with digested gliadin and gluten-derived peptide p41-43

hEGC-ClK were cultured in plates pre-coated with hAEC Coating solution from InSCREENeX in an appropriate hEGCs medium at 37°C with a 5% CO2 atmosphere.

Human established cell lines - the low-grade astrocytoma Res186 [271], high-grade astrocytoma T98G cells, and BJ hTERT human fibroblasts (ATCC) - were cultivated in DMEM medium supplemented with 10% FBS, 100 units/mL penicillin, 0.1 mg/mL streptomycin, and 1% L-glutamine (Euroclone). Cell cultures were maintained at 37°C in a 5% CO_2 atmosphere.

According to the experimental setup, cells were treated with 0.05 µg/µL, 0.1 µg/µL, 0.25 µg/µL, 0.5 µg/µL, 1 µg/µL of whole digested gliadin (peptic-tryptic gliadin, PT-gliadin) or with 10 µg/mL, 20 µg/mL, 40 µg/mL, 50 µg/mL, 100 µg/mL, 200 µg/mL, and 400 µg/mL of gluten-derived peptide p31-43 (ThermoFisher Scientific). Bright microscopy observations were performed with the Nikon Eclipse TS-100 phase-contrast microscope.

5.4. Cumulative Population Doubling Level

The Cumulative Population Doubling Level (cPDL) was determined following ATCC guidelines, using the formula n= 3.32 (logUCY - logI) + X, where 'n' represents the final PDL number, 'UCY' represents the cell yield at that point, 'I' is the initial inoculum cell number, and 'X' is the doubling level of the initial inoculum.

5.5. Immunofluorescence

hEGC-ClK cells (2×10^4) were cultured on 2 hours-precoated coverslips (huAEC Coating Solution (InSCREENeX) for 24 hours at 37°C/5% CO_2. After a first wash with PBS, cells were fixed with 4% paraformaldehyde (PFA) at room temperature (RT) for 15 minutes, followed by three PBS washes. Cells were then incubated for 1 hour at RT with primary antibodies anti-GFAP (1:30), anti-S100β (1:30), anti-SOX10 (1:30) (Immunological Sciences), anti-HLA-DQA1 (1:30) (Abcam), anti-γH2Ax (1:30), anti-IL-1β (1:30), anti-Nrf2 (1:30), Anti-HO-1 (1:30) (Cell Signalling), anti-catalase (1:30) (Santa Cruz). Following three TBS+Tween20 0.1% washes, species-specific AlexaFluor633- and AlexaFluor488-labeled secondary antibodies (Thermo Fisher Scientific) were used at a 1:30 final dilution for 30 minutes at RT. Subsequently, slides were stained with DAPI (0.4 µg/mL) (Sigma-Aldrich) for 8 minutes at RT, followed by a wash with distilled water. Slides were mounted with Dako Fluorescence Mounting Medium (DAKO) and sealed. Fluorescence signals were observed using a LEICA TCS SP8 STED 3X confocal microscope (Leica). Negative controls were implemented to confirm the specificity of the signal, e.g., anti-Naspin antibody (Immunological Sciences).

5.6. Flow cytometry analysis

The expression of CD31, CD45, CD271, and CD326 proteins was assessed by flow cytometry. hEGC-ClK cells (5×10^4) were seeded in a pre-coated multiwell-6 plate up to 100% confluence, which typically occurred 48 hours post-seeding. Subsequently, cells were detached and centrifuged at 500 x g for 3 minutes at 4°C. After removing the supernatant, cells were stained with L/D efluor (Thermo Fisher Scientific) at a 1:400 dilution in PBS for 30 minutes at 4°C in the dark. Cells were then centrifuged 500 x g for 3 minutes at 4°C and Fc block (diluted at 1:100 in FACS buffer) was added for 15 minutes at 4°C. After this step, cells were centrifuged at 500 x g for 3 minutes and incubated with an extracellular staining mix with primary antibodies CD31-PE (1:300), CD45-PE-Cy5 (1:300), CD271-PE (1:100), CD326-PE-Cy7 (1:300) (BioLegend) for 20 minutes at 4°C in the dark. Cells were then centrifuged as above-described, washed, and resuspended in 200 µL of FACS buffer. The analysis was then performed using a BD FACSymphony A5 flow cytometer (BD), setting Forward Scatter (FSC) > 200 to exclude cellular debris.

Mitochondrial membrane potential, intracellular ROS, cell proliferation, and caspase 3/7 activation indexes were determined using flow cytometry and dedicated kits

(MitoPotential, Oxidative Stress, Ki-67, and Capase 3/7 Assays, Luminex) following Carriero *et al*., 2021 [272] and Slivinschi *et al*., 2022 [273]. The analysis was performed with Muse Cell Analyzer (Merck).

For the MitoPotential analysis, hEGC-ClK cells were trypsinized, collected, and washed with Assay Buffer 1X. Next, cells were incubated for 25 minutes at 37°C with 100 µL of Assay Buffer 1X and 95 µL of pre-diluted MitoPotential Reagent (1:1000). Finally, 5 µL of 7-AAD were added, and the samples were analysed after a 5-minute incubation in the dark at RT.

For the oxidative stress analysis, hEGC-ClK cells were trypsinized, collected, and washed in Assay Buffer 1X. Next, cells were incubated for 30 minutes at 37°C in 10 µL of Assay Buffer 1X and 190 µL of pre-diluted Oxidative Stress Reagent (diluted at 1:800) before analysis. Oxidative stress was also evaluated using the fluorescent dye dihydroethidium (DHE) at the final dilution of 1 µL/mL through fluorescent microscope observations, according to manufacturer's instruction.

For proliferation analysis, hEGC-ClK cells were trypsinized, collected, and washed with PBS. Cells were then resuspended in 1X Fixation solution for 15 minutes at RT. Subsequently, the permeabilization solution was added and cells were incubated for 15 minutes at RT. Subsequently, cells were incubated with Assay Buffer 1X for the same time interval. Finally, Muse Hu IgG1-PE (isotypic control) or Hu Ki67-PE antibodies were added, mixed, and incubated for 30 min at RT before analysis.

For Caspase 3/7 activation analysis, cells were trypsinized, and collected. Next, cells were incubated for 30 minutes at 37°C in 50 µL of Assay Buffer 1X and 5 µL of Muse Caspase Reagent (1:8). Finally, 150 µL of 7-AAD working solution (1:75) was added, mixed, and incubated for 5 minutes at RT before analysis.

5.7. Real-time PCR expression analysis

RNeasy Plus Micro Kit (QIAGEN) was used to extract total RNA from hEGC-ClK cells, following the manufacturer's instructions. RNA quantification was carried out using Nanodrop (ThermoFisher Scientific). *GFAP*, *SOX10*, *S100β*, *PLP1*, *CCL2*, *IL-6*, *GDNF*, *RPLP0*, and *GAPDH* cDNAs were obtained using random hexamers primers (Applied Biosystems), consistent with Comincini *et al*., 2013 [274]. The sequence of forward and reverse primers for the targeted genes is listed in **Supplementary Table T2**. The following amplification was performed using the LightCycler 480 SYBR Green I Master kit (Roche). Real-time PCR was performed using 2 µg of each cDNA amplified making use of Step-One PCR instrument (Applied Biosystems), with the following thermal profile: incubation of 95°C for 30 seconds, followed by 45 cycles of denaturation at 95°C for 10 seconds, annealing at 58-60°C for 15 seconds and elongation at 72°C for 15 seconds with fluorescence collection. Subsequently, a melting curve analysis was conducted, ranging from 60 to 95°C, with data collected at each degree (5 readings/°C). The data were normalized

to *GAPDH* or *RPLP0* according to the specific aim of the experiment. Relative quantification, following the method of Schmittgen and Livak (2008)- [275], was used to calculate the relative changes in gene expression.

5.8. HLA genotyping

Genomic DNA extraction from hEGC-ClK cells ($1x10^6$) was performed using the Maxwell CSC Blood DNA automated Purification System (Promega), following the manufacturer's guidelines. For HLA class I and II genotyping, a sequence-specific oligonucleotide-primed polymerase chain reaction (PCR-SSO) method was employed, using the LABScan3D system (One Lambda Inc) based on the Luminex xMAP technology (Luminex). LABType commercial kits (One Lambda Inc.) were used for class I HLA-A, B, C, and class II HLA-DRB1, DQA1, DQB1 genotyping, CWD (Common and Well-Documented alleles) and XR (High Resolution). The amplification protocol consisted of 5 cycles (96°C for 20 seconds/70°C for 20 seconds/62°C for 20 seconds) followed by an additional 30 cycles (96°C for 10 seconds/70°C for 15 seconds/62°C for 20 seconds). Amplifications were subsequently evaluated using 2% agarose pre-casting electrophoresis.

5.9. Metaphase spread preparation

6 x 10^5 hEGC-ClK cells at passage 21 (p21) were seeded in 10 cm diameter Petri dishes. After 24 hours, nocodazole (Sigma-Aldrich) was added to the culture medium at a final concentration of 1.34 µM for 2 hours at 37°C and 5% CO_2, in order to accumulate metaphase-blocked cells. Following this treatment, cells were detached using 0.5 mL of trypsin–EDTA (Thermo Fisher Scientific) and resuspended in PBS. Samples were then centrifuged at 2200 x g for 10 minutes and resuspended in 10 mL of pre-warmed hypotonic solution (75 mM KCl) for 15 minutes at 37°C. After centrifugation at 2200 x g for 10 minutes, the pellet was resuspended in 10 mL of fixative solution (methanol and acetic acid, 3:1) for 45 minutes at −20°C. This fixation process was repeated once using fresh fixative solution. The cells were then centrifuged as before and resuspended in an appropriate volume of fresh fixative solution based on the pellet size. Subsequently, the cell suspension was dropped onto microscope slides pre-treated with fixative solution, and the slides were left to air-dry. Next, the slides were stained with DAPI (0.4 µg/mL) (Sigma-Aldrich) for 8 minutes at room temperature. After washing with distilled water, the slides were mounted with a drop of Dako Fluorescence Mounting Medium (DAKO) and sealed. Visualization and analysis of 100 images were conducted using Axioplan microscope (Zeiss) equipped with a Charged-Couple Device (CCD) camera (Photometrics).

5.10. BAC extraction

Specific human BAC probes - RP11-160F8 (5q11.2, coordinates: 54.033.661–54.188.673) and RP11-69A18 (5q35.1, coordinates: 171.790.208–171.957.002) (BACPAC Human Resources in Emeryville, CA) - with pBACe3.6 backbone, were

employed in Fluorescence *in Situ* Hybridization (FISH) experiments. Purified *E. coli* LB stabs were initially propagated on LB agar plates containing chloramphenicol (12.5 µg/mL). Single colonies were isolated from these plates and expanded overnight in LB medium with antibiotics at 37°C with agitation. The obtained cultures were then collected, centrifuged at 9600 x g for 30 minutes, and resuspended in 5 mL of P1 buffer (Tris–HCl 50 mM, pH 8; RNase A 100 µg/mL; EDTA 10 mM) before adding 10 mL of P2 buffer (NaOH 200 mM; SDS 1%). The tubes were gently mixed and incubated for 5 minutes. Subsequently, 10 mL of P3 buffer (K-acetate 3 M) was added, and the tubes were incubated for 15 minutes at 4°C. Afterward, the tubes were centrifuged at 9600 x g for 1 hour and subsequently for 45 minutes at 9600 x g. A step of purification was performed, using a QIAGEN-tip 100 column from the Qiagen Plasmid Mini Kit (QIAGEN), following the manufacturer's instructions. The final elution was centrifuged at 9600 x g for 45 minutes after the addition of 3.5 mL of isopropanol. The resulting pellet was then resuspended in 70% ethanol and centrifuged again at 9600 x g for 20 minutes. After air-drying, the pellet was resuspended in an appropriate volume of sterile water. To verify the presence of inserts, the purified BACs were digested using the EcoRI enzyme and loaded onto a 1% agarose gel. DNA quantification of BACs was carried out using a NanoDrop 1,000 spectrophotometer (Thermo Fisher Scientific).

5.11. Fluorescence *in situ* hybridization

To label the probes, a total of 4 µL of Biotin/Digoxigenin-Nick Translation Mix (Roche), 1 µg of BAC probes, and sterile water were added to reach a final volume of 20 µL. After incubation at 15°C for 3 hours, the nick translation reaction was blocked by adding 1 µL of EDTA (25 mM, pH 8). Then, 10 µL of salmon sperm DNA (1 µg/µL), 2 µL of dextran blue (stock solution 1.8%, filtered), 151 µL of pre-refrigerated 100% ethanol, 10 µL of Roche human COT DNA (1 µg/µL), and 17.2 µL of ammonium acetate (2.14 M, pH 8) was added. The samples were then incubated for 2 hours at -20°C and subsequently centrifuged at 1100 x g for 20 minutes at room temperature (RT). After removing the supernatant, the pellets were dried, resuspended in 35 µL of hybridization solution (25% formamide, 10% dextran sulfate, 1% tween-20, and 2X SSC), and stored at -20°C. After overnight incubation at 37°C, the slides were denatured for 2.5 minutes at 78°C after adding 150 µL of 70% formamide (Sigma-Aldrich), 2X saline sodium citrate (SSC, Sigma-Aldrich), and sterile water. Following the denaturation step, slides were treated with 2X SSC (4°C) for 2.5 minutes and then dehydrated through an ethanol series (75–95-100%), with each step lasting 3 minutes. Probes were denatured at 80°C for 8 minutes and then stored on ice to halt the reaction. 15 µL of the labeled probe were added to each slide for *in situ* hybridization and probe detection. The slides were stored overnight at 37°C in a moisture chamber. Six washes of 5 minutes were performed using 50% formamide and 2X SSC at 45°C. Permeabilization was immediately performed with 60 µL of 3% BSA in 0.1% Tween-20 and 4X SSC at 37°C for 30 minutes. Then,

probes were incubated at 37°C for 30 minutes with anti-DIG and anti-BIO antibodies (Abcam), respectively conjugated to rhodamine and FITC fluorophores, and diluted in 1% BSA, 0.1% Tween20, and 4X SSC. Three washes, each lasting 5 minutes, in 4X SSC and 0.1% Tween20 were performed at 42°C. Slides were subsequently treated with 60 µL of species-specific secondary antibodies labelled with rhodamine and FITC (1% BSA, 0.1% Tween 20, 4X SSC) and further incubated at 37°C for 30 minutes. Two washes were performed as previously described, followed by a third one in 4X SSC at RT. Slides were covered with DAPI (0.4 µg/mL) (Sigma-Aldrich) and incubated for 8 minutes at RT. After washing with distilled water, slides were mounted by adding a drop of Dako Fluorescence Mounting Medium (DAKO) and sealed. Finally, probe detection was carried out using an Axioplan fluorescent microscope from Carl Zeiss equipped with a Charged-Couple Device (CCD) camera (Photometrics).

5.12. Electron microscopy analysis

For the ultrastructure analysis of hEGC-ClK cells, transmission electron microscopy (TEM) was employed. After centrifugation at 800 x g for 5 min, 1x 10^6 cells (p21) were fixed with 2.5% glutaraldehyde in PBS for 2 hours (RT). Then, cells were washed and rinsed in PBS (pH 7.2) overnight and post-fixated by incubating 1% aqueous OsO4 (Sigma-Aldrich) for 1 hour at RT. Cells were pre-embedded in 2% agarose in water, dehydrated in acetone, and finally embedded in epoxy resin (Electron Microscopy Sciences, EM-bed812). Ultrathin sections with a thickness of 60–80 nm were collected on nickel grids and stained with uranyl acetate and lead citrate. The specimens were observed using a JEM 1200 EX II electron microscope (JEOL) equipped with the MegaView G2 CCD camera (Olympus OSIS) and operating at 120 kV. The morphology of organelles (a minimum of 20 for each type) was subsequently analysed by two independent evaluators.

For immunolabeling with colloidal gold and subsequent visualization by TEM, the established protocol by Casali *et al*. 2023 [276] was followed. For immunocytochemistry, cells were fixed with 4% paraformaldehyde (PFA) in culture medium for 2 hours at 4°C. The cell pellet was rinsed three times in PBS for 10 minutes each, pre-embedded in 2% agarose in water, incubated in NH4Cl 0.5 M for 30 minutes and dehydrated in graded ethanol (2 x 5' 30%, 2 x 10' 50%, 2 x 10' 70%, 2 x 15' 90%, and 3 x 10' 100%) and then embedded in acrylic resin (LR White). Ultrathin sections (60-80 nm) were cut on a Reichert OM-U3 ultramicrotome and collected on nickel grids (200 Mesh). The specimens were observed with a JEM 1200 EX II (JEOL) electron microscope operating at 100 kV and equipped with a MegaView G2 CCD camera (Olympus OSIS). Grids for immunocytochemical analyses were first incubated in a drop of normal goat serum (NGS) diluted in PBS and then incubated over-night (ON) in a drop of primary antibody (1:30). Then, grids were rinsed twice in PBS/Tween20 for 5 minutes and twice in PBS for 5 minutes, incubated in NGS and finally in a proper colloidal gold-particle conjugated-

secondary antibodies (1:20) for 30 minutes at room temperature. Grids were rinsed twice in PBS for 5 minutes and twice in dH2O for 5 minutes

5.13. Ca^{2+} signals measurements

Ca^{2+} imaging was carried out following the procedures outlined in previous studies (33187307, 32535721). In brief, 2 x 10^4 cells were seeded onto round glass coverslips (8 mm) pre-coated with huAEC Coating Solution (In-SCREENeX) for 2 hours. The following day, the cells were exposed to fura-2 acetoxymethyl ester at a final concentration of 4 µM (Fura-2/AM, 1 mM stock solution in DMSO) in PSS for 30 minutes at 37°C and 5% CO_2. After a 15-minute de-esterification period in PSS, the coverslip was mounted in a small Petri dish, and the cells were observed using an upright epifluorescence Axiolab microscope (Carl Zeiss) equipped with a Zeiss 40X Achroplan objective (water-immersion, 2.0 mm working distance, 0.9 numerical aperture). Excitation of cells was alternated between 340 and 380 nm using a filter wheel (Lambda 10, Sutter Instrument), and the emitted fluorescent signal at 510 nm was detected with an Extended-ISIS CCD camera (Photonic Science). The fluorescent signals were continuously recorded and graphed on-line for 10 to 40 selected regions of interest (ROIs), each corresponding to a specific individual cell. The intracellular Ca^{2+} concentration ($[Ca^{2+}]i$) was tracked by measuring the ratio of mean fluorescence emitted at 510 nm during alternate excitation at 340 and 380 nm (Ratio F340/F380) for each ROI. An increase in $[Ca^{2+}]i$ results in an increase in this ratio (33187307, 32535721). Ratio measurements were made and displayed on-line every 3 seconds. All experiments were conducted at RT (22–24°C).

5.14. Multispectral Imaging Flow Cytometry Analysis

An Amnis ImageStream MkII instrument (Luminex) equipped with 3 lasers (100 mW 488 nm, 150 mW 642 nm, and 70 mW 785 nm (SSC) was used to assay the autophagic flux. After trypsinization, hEGC-ClK cells were labelled using the Autophagy LC3 Antibody-based Kit (Merck), according to the manufacturer's instructions. Finally, 1 × 10^6 cells were resuspended in 200 µL of D-PBS for the analysis and 10000 events were collected for every sample. Data acquisition was performed by INSPIRE software v0.3, while data analysis using the following IDEAS v6.2.

5.15. Gliadin digestion

Digestion of gliadin from wheat (Sigma) was performed following the protocol of Drago *et al*., with slight modifications [277]. Particularly, gliadin (1 g/mL) was suspended in 500 mL of 0.2 N HCl and incubated for 2 hours at 37°C with the addition of 1 g of pepsin (Sigma). The pH of the solution was then adjusted to 7.4 using 2 N NaOH. Subsequently, 1 g of trypsin (Sigma) was added, and the solution was incubated at 37°C for 4 hours under agitation. To stop the enzymatic reaction, the solution was then boiled for 30 minutes. The resulting preparation (referred to as

PT-gliadin) was stored at -80°C. Albumin (Sigma) was digested following the same protocol (PT-albumin) and was used as a negative control.

5.16. Viability and cytotoxicity assays

Cell viability was assessed using the CellTiter 96 AQueous One Solution Cell Proliferation Assay kit (Promega, Madison, WI, USA) according to manufacturer's instructions. Cells (2-3 x 10^3) were seeded in a multiwell-96 plate in 100 µL of growth medium. Digested gliadin or p31-43 was added and cell viability was tested at 6, 12, and 24 hours after treatment by adding 20 µL of MTS reagent. Each replicate was performed using 8 wells/condition. The release of LDH was carried out of the culture medium of cells in the presence/absence of p31-43. Briefly, 50 µL of culture medium was collected in a fresh multiweek-96, and 50 µL of CytoTox96 reagent (Promega) was added. After an incubation of 30 minutes in the dark, the reaction was blocked by adding 50 µL of Stop solution. Cells treated with Lysis buffer and completely lysed were used as a positive control. Absorbance (490 nm) was detected using the microplate reader TECAN Sunrise (Männedorf, Switzerland).

5.17. Immunoblotting analysis

hEGC-ClK cells were cultured in a multiwell-6 plate in the presence/absence of digested gliadin or gluten-derived peptide p31-43. Immunoblotting was performed as described (21478678). For sample preparation, cells were collected and lysed in ice-cold Triton X-100 buffer (150 mM NaCl, 50 mM Tris-HCl pH 7.4, 1% Triton X-100), supplemented with Complete Mini protease inhibitor cocktail 7X (Roche) and 1 mM sodium orthovanadate (Sigma). Protein quantification was performed using the Quant-It Protein Assay Kit (Invitrogen). Subsequently, proteins (20–30 µg) were mixed with Laemmli sample buffer (6% glycerol, 2% SDS, 150 mM β-mercaptoethanol, 0.02% bromophenol blue, and 0.5 M Tris-HCl, pH 6.8), and denatured at 95 °C for 5 minutes. They were then separated on a 12% SDS-PAGE gel based on their size. Following electrophoresis, the proteins were transferred onto a nitrocellulose membrane using the Trans-Blot Turbo Transfer System (Biorad) according to the manufacturer's instructions. The membranes were subsequently blocked for 1 hour at RT with 5% (*w/v*) non-fat milk in TBS (138 mM NaCl, 20 mM Tris-HCl, pH 7.6) containing 0.1% Tween 20. Overnight incubation at 4 °C followed, during which the membranes were probed with polyclonal primary antibodies against GFAP, caspase-3, cleaved caspase-3, Nrf2, phosphor-Erk1/2 (Tyr204/Tyr187, #5726), Erk1/2, S100β, LC3-II (Cell Signalling), and catalase (Santa Cruz) diluted at 1:2000 in 5% non-fat milk in TBS. Additionally, a monoclonal primary antibody against β-actin (BACT) and α-tubulin was diluted at 1:4000 (Cell Signalling). Subsequently, species-specific peroxidase-labelled ECL secondary antibodies (Cell Signaling, 1:2000) were used in 5% non-fat milk in TBS. Protein signals were detected using the Westar Hypernova Western Blotting Detection Kit (Cyanagen,

Bologna, Italy) with the Chemidoc MP system (Biorad). Densitometric analysis was performed using ImageJ software (http://rsbweb.nih.gov/ij).

5.18. JC-1 Mitochondrial potential assay

hEGC-ClK cells were cultured in multiwell-6 plates for 24 hours and then treated with digested gliadin or p31-43. After 3 and 6 hours p.t. JC-1 dye was added to the culture media at the final concentration of 2 μg/mL and incubated for 30 minutes. Then, fluorescence microscope observation at 490 nm was performed using a Nikon Eclipse TS-100 fluorescent microscope.

5.19. Caspase-3 activation assay

hEGC-ClK cells (2 x 10^5) were seeded in a multiwell-6 in presence/absence of p31-43. Analysis of caspase-3 activation was performed at 4 hours p.t. using the NucView 488 Caspase-3 assay kit (Biotium) according to manufacturer's instructions. Briefly, the culture medium was replaced with a fresh one containing 5 μM of the substrate. After an incubation of 30 minutes, cells were visualized using a Nikon Eclipse TS-100 fluorescent microscope.

5.20. Proteomics analysis

hEGC-ClK cells (2x10^5) were seeded in a multiwell-6 plate and cultured for 24 hours. Following p31-43 treatment, cells were trypsinized and collected. For sample preparation, cells were collected and lysed in ice-cold Triton X-100 buffer (50 mM Tris-HCl pH 7.4, 150 mM NaCl, 1% Triton X-100), supplemented with Complete Mini protease inhibitor cocktail 7X (Roche, Basel, Switzerland) and 1 mM sodium orthovanadate (Sigma). Protein quantification was performed using the Quant-It Protein Assay Kit (Invitrogen, Carlsbad, CA, USA). All samples have been analysed at UNITECH OMICs (University of Milano, Italy) using: Dionex Ultimate 3000 nano-LC system connected to Orbitrap FusionTM TribridTM Mass Spectrometer (Thermo Scientific) equipped with nanoelectrospray ion source. Peptide mixtures were pre-concentrated onto an Acclaim PepMap 100 – 100μm x 2cm C18 (Thermo Scientific) and separated on EASY- Spray column ES802A, 25 cm x 75 μm ID packed with Thermo Scientific Acclaim PepMap RSLC C18, 3 μm, 100 Å using mobile phase A (0.1 % formic acid in water) and mobile phase B (0.1% formic acid in acetonitrile 20/80, v/v) at a flow rate of 0.3 μL/minute. The temperature was set to 35°C and the samples were injected in triplicates. The sample injection volume is 4 μL. All the data were elaborated with the Proteome Discoverer 2.5 software setting the *Homo sapiens* (sp_incl_isoformsTaxID=9606_and_subtaxonomies) (v2022-12-14) and trypsin as the used enzyme. The applied filters for the LFQ analysis were:

- Protein level: peptides ≥ 2
- Peptide level: Xcorr ≥ 2.2, Rank = 1, Confidence = High
- PSMs levels: Xcorr ≥ 2.2

Data analysis was performed with a double-blind approach by two independent operators. The differentially expressed proteins (DEP) with an adjusted p-value < 0.05 were studied through the STRING software for a GO Ontology and Reactome analyses.

5.21. Statistical analysis

Data analysis was performed using GraphPad Prism 9.1.2.1. Data derived from flow cytometry experiments are displayed as the mean ± SE. Statistical significance was determined when $p \leq 0.05$. Specific details regarding the statistical tests employed for each experiment can be found in the figure legends. All the data related to Ca^{2+} signaling were collected from a minimum of three separate batches of hEGC-ClK cells. Each trace presented represents the average Ca^{2+} activity recorded from multiple cells exhibiting similar Ca^{2+} behavior within the same field of view. The peak amplitude of ATP-induced intracellular Ca^{2+} release and entry was quantified by assessing the disparity between the F340/F380 ratio at the peak of the Ca^{2+} response and the mean F340/F380 ratio during a 1-minute baseline recording taken before the introduction of the agonist. The combined data is displayed as the mean ± SE, and statistical significance ($p \leq 0.05$) was determined through One-Way ANOVA analysis. The number of cells measured for each experimental condition is either indicated in or above the corresponding bar histogram**.**

Results

6.1. Generation of immortalized EGCs

So far, several technical difficulties can affect enteric glia *in vitro*, *ex vivo*, and *in vivo* studies [212], [278], [279], [280], [281], [282], [283], [284]. Although it is possible to isolate EGCs using various techniques from guinea pig-, mouse-, rat-, and human- specimens for *in vitro* experiments, these protocols involve multiple steps that can compromise the overall quality [269]. Indeed, potential contamination events with other cell types and de-differentiation of glial cells can frequently occur. Considering these premises, the development of novel standardized EGC models is required to investigate EGCs' role in health and disease.

In my Ph.D. project, a well-established lentiviral transduction protocol was employed [270] to create a novel immortalized human EGC line originating from the MP, which may represent a valuable tool to bridge the gap in *in vitro* EGC studies.

Lentiviral transduction was performed on primary human enteric glial cells (hEGCs) extracted from a human normal duodenal biopsy. It was performed by making use of lentiviral vectors carrying 33 distinct genes (**Supplementary Table T1**), as previously described by Lipps and colleagues [270]. Out of the resulting 30 cell clones, a specific one, hereafter referred to as hEGC-ClK, was selected for further investigation based on its growth rate and morphological features. PCR analysis performed on hEGC-ClK cells confirmed the integration of eight specific transgenes: *Core*, *BMI1*, *E6*, *E7*, *ID1*, *MYC*, *Nanog*, and *REX* (**Supplementary Fig. S1; Supplementary Table T2**).

As shown in **Fig. 1A**, the morphology of hEGC-ClK cells closely resembles that of primary mEGCs and hEGCs. We then calculated the cumulative population doubling per day (cPDL) for hEGC-ClK cells and compared it to the cPDL of primary hEGCs. As illustrated in **Fig. 1B**, hEGC-ClK cells showed a higher cPDL and kept on growing up to 40 days. By contrast, primary hEGCs reached a growth plateau after 19 days and became senescent after 29 days, ultimately leading to cell death. Notably, hEGC-ClK cells have been successfully expanded up to passage 35 (p35), and preliminary analyses have confirmed their maintaining of both morphological features as well as the expression of glial markers GFAP and S100β. Furthermore, flow cytometry assays demonstrated that hEGC-ClK cells at p35 do not present increased levels of intracellular reactive oxygen species (ROS) or depolarized mitochondria (**Supplementary Fig. S2**).

According to the cell proliferation rate and the guidelines provided by Lipps *et al*. in 2018 [270], hEGC-ClK cells, at an early culture passage (p21), were utilized for characterization analysis. We investigated proliferation levels of the hEGC-ClK clone using flow cytometry analysis of Ki-67 expression levels. Specifically, hEGC-ClK cells were seeded at different concentrations for 24 hours ($2 – 5 – 8x10^5$ in a multiwell-6 plate) and their proliferation rate was compared to that of two established glioma cell lines, i.e., low-grade astrocytoma Res186 (WHO grade I) and

glioblastoma T98G (grade IV). As reported in **Fig. 1C**, the percentage of Ki-67 positive cells exhibited a significant reduction in a concentration-dependent manner. Additionally, the number of Ki-67-positive cells in hEGC-ClK population was comparable to that observed in Res186, but significantly lower when compared to T98G ones (**Fig. 1D, Supplementary Fig. S3**). Notably the percentage of Ki-67-positive cells in the T98G cell line remained consistent regardless of cell confluence, as shown in **Supplementary Fig. S3**.

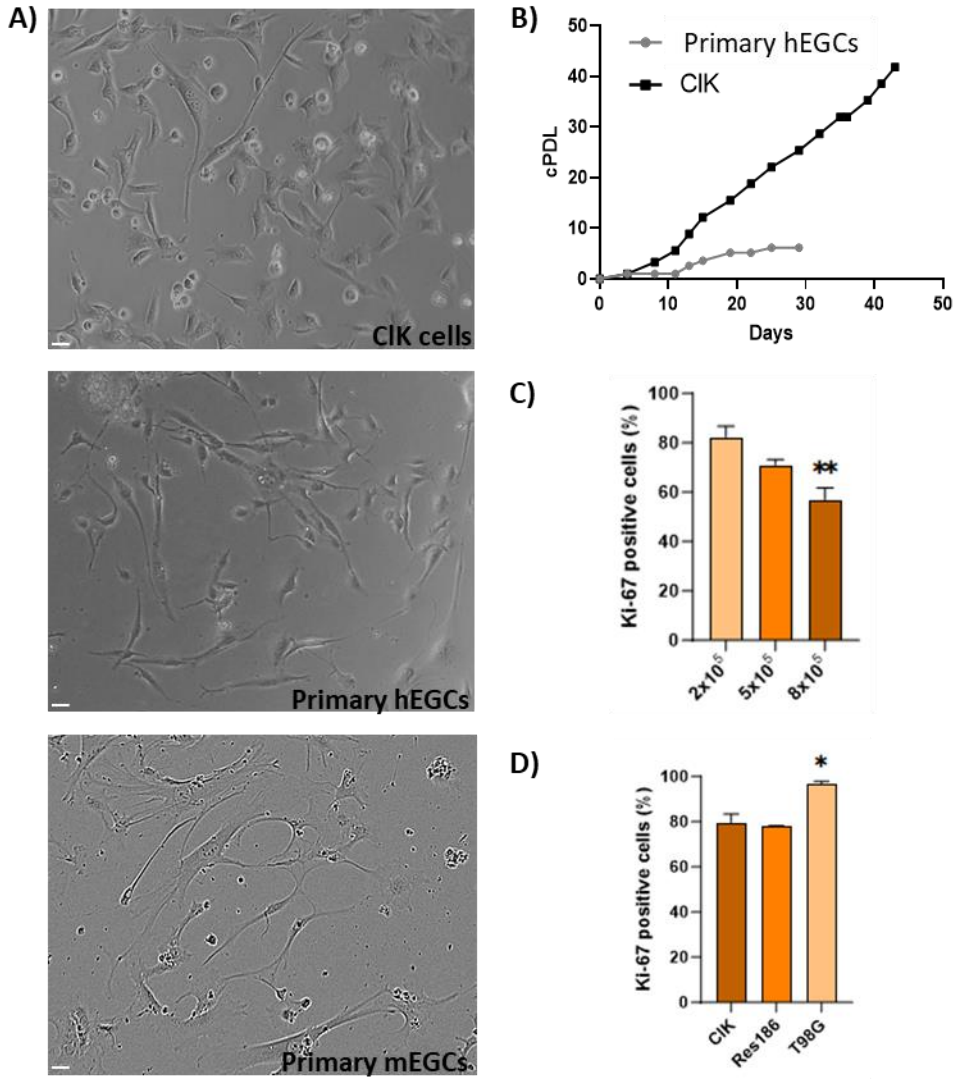

Figure 1. *hEGC-ClK morphology and proliferation analysis.* ***(A)*** *Optical microscope analysis (brightfield) of hEGC-ClK cells (p21), primary hEGCs (2 days post-isolation), and primary mEGCs (2 days post-isolation)). Size bars (= 10 μm) are reported.* ***(B)*** *Cumulative population doublings (cPDL) of primary hEGCs and hEGC-ClK cells. Mock-infected control cells died 10 days after infection (data not shown). cPDL values are reported in* ***Supplementary Table T3***. ***(C)*** *Percentage of Ki-67 positive hEGC-ClK cells at different cell concentrations (i.e., 2–5-8×10^5). On the X-axis is reported the number of cells and on the Y-axis the percentage of cells positive to Ki-67. (**) indicates p < 0.01, ANOVA One-Way compared with the lower concentration.* ***(D)*** *Comparison of the percentages of Ki-67 hEGC-ClK positive cells with human low- (Res186) and high-grade astrocytoma (T98G) established cell lines, all at 2×105. (*) indicates p < 0.05, ANOVA One-Way, compared with hEGC-ClK cells. Experiments were performed on three independent biological replicas. Corresponding cytofluorimetric plots are reported in* ***Supplementary Fig. S3***.

6.2. Ultrastructural analysis and mitochondrial membrane potential (ΔΨm) measurement

To study the cellular and organelle morphology, an ultrastructural analysis was performed by making use of transmission electron microscopy (TEM). Specifically, as illustrated in **Fig. 2A**, no alteration in mitochondrial shape was detected and the integrity of internal membrane cristae was assessed. Additionally, the lentiviral transduction process did not affect other cellular organelles, such as the Golgi apparatus and endoplasmic reticulum.

Considering that mitochondrial functionality can affect mitochondrial membrane potential (ΔΨm) and subsequently cell viability [285], the mitochondrial depolarization of hEGC-CIK cells was evaluated by flow cytometry, as shown in **Fig. 2B**. Our findings revealed a statistically significant low percentage of cells displaying depolarization events (i.e., depolarized live cells = 2.90%; depolarized dead cells = 1.90%) within the overall cell population. Furthermore, basal intracellular ROS levels were examined by flow cytometry analysis, considering that elevated ROS levels are a typical feature of transformed or pathological cells, arising from various internal and environmental factors [286]. As highlighted in **Fig. 2C**, hEGC-ClK cells exhibited relatively low intracellular levels of ROS (i.e., 5.57%). Furthermore, as demonstrated in **Supplementary Fig. S4**, the intracellular ROS levels were similar to those of human primary fibroblasts, while human primary retinal endothelial cells and glioma cell lines (specifically, HREC and T98G) exhibited higher basal ROS levels when compared to hEGC-ClK cells.

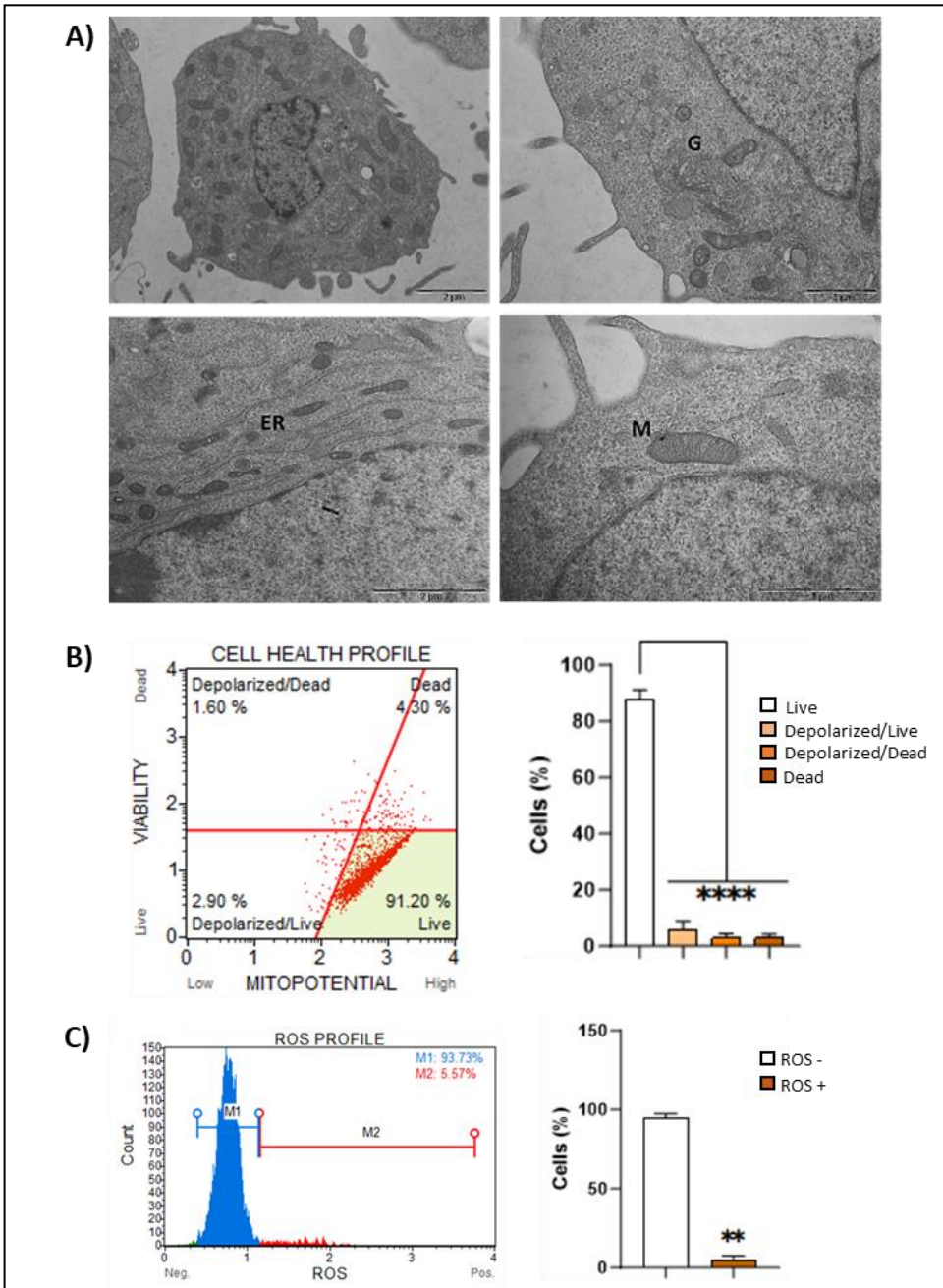

Figure 2. ***Ultrastructural and functional characterization of hEGC-ClK cells.*** ***(A)*** *TEM analysis of hEGC-ClK cells (p21). M: mitochondria; G: Golgi apparatus; ER: endoplasmic reticulum. Scale bars (1–2 μm) are reported.* ***(B)*** *Cytofluorimetric plot and relative histogram reporting the mitochondrial depolarization percentages of hEGC-ClK cells. Events collected: 2000 cells. Experiments were performed on three independent biological replicates. Data are reported as mean ± SE. On the Y-axis is reported the number of cells expressed as percentages (%). (****) indicate $p \leq 0.0001$, ANOVA One-Way.* ***(C)*** *Cytofluorimetric ROS profile plot (M1 gate: ROS-; M2 gate: ROS+) of hEGC-ClK cells and relative histograms. Events collected: 2,000 cells. Experiments were performed on three independent biological replicates. Histogram data are represented as mean ± SE. On the Y-axis is reported the number of cells expressed as percentages (%). (**) indicates $p \leq 0.01$, t-test.*

6.3. Cytogenetic analysis

Considering the transgenes integration events, cytogenetic analysis of hEGC-ClK cells was performed to assess genome integrity and the presence of chromosomal rearrangements. The chromosome count was determined in a sample of 100 metaphase spreads. As shown in **Fig. 3A**, heteroploidy was observed within the analysed cell population. Notably, one near-diploid population was detected, comprising 31% of the cells, with a chromosome number of 2n = 44, and a near-tetraploid population, constituting 9% of the cells, with a chromosome number of 2n = 86.

In the most prevalent cell population (2n= 44), karyotype reconstruction using reverse DAPI banding was conducted on a sample of 20 metaphase spreads (**Fig. 3B**). The cytogenetic analysis of the karyotype revealed monosomy of chromosomes 5, 13, and 15, as well as the presence of a large metacentric derivative chromosome, similar in size to chromosome 1. Additionally, a small chromosome fragment (marker M1) in a single copy in 39% of the analysed metaphase spreads was identified. Specifically, 19% of both cell populations (2n=44 and 2n=86) were positive for the M1 marker (**Supplementary Fig. S5**).

Following a deeper examination, a striking similarity in banding patterns was observed between the large metacentric derivative chromosome and the long arm of chromosome 5. Hence, we hypothesized that the rearranged chromosome resulted from a translocation event involving the 5q arm and an unidentified chromosome fragment, leading to a partial monosomy of chromosome 5. This newly formed large metacentric chromosome was subsequently designated as der5.

Two-colour FISH (Fluorescence *In Situ* Hybridization) experiments were carried out to verify the involvement of the long arm of chromosome 5 in the formation of the large derivative chromosome. Specifically, DNA probes targeting the sub-centromeric region (RP11-160F8, band: q11.2, red) and the sub-telomeric region (RP11-69A18, band: q35.1, green) of chromosome 5 were used. The chromosomal localization of the two probes was first verified by FISH on control human metaphase spreads (data not shown). Subsequently, we differently labelled the probes and co-hybridized them to hEGC-ClK metaphase cells at p21. Clear fluorescence signals were observed on both the normal chromosome 5 (**Fig. 3C**) and the derivative marker chromosome (**Fig. 3D**), providing confirmation that the region between bands 5q11.2 and 5q35.1 was indeed implicated in the translocation that formed der5. Furthermore, the FISH signals precisely showed that the orientation of the translocated 5q fragment mirrors the canonical arrangement seen on the original chromosome 5 (**Fig. 3D**).

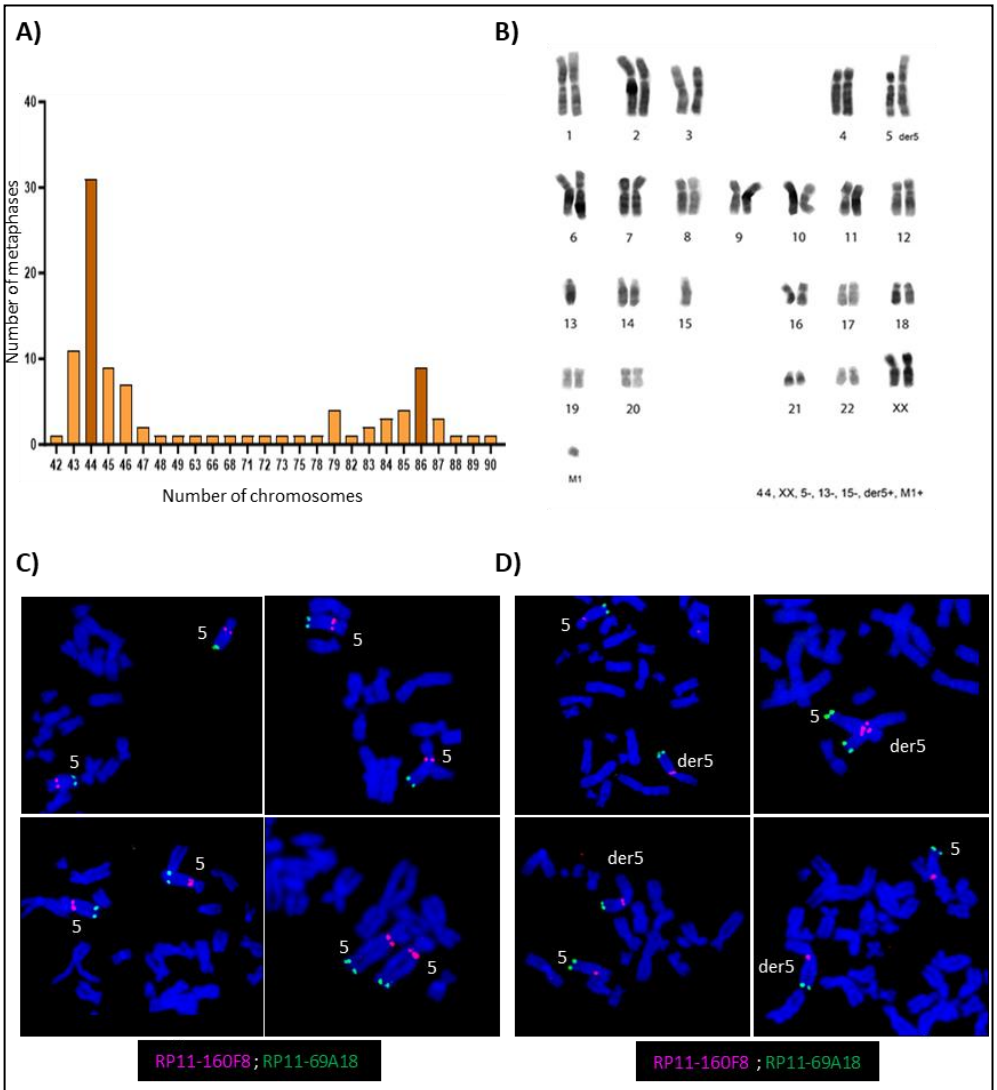

Figure 3. ***Chromosomes' distribution and karyotype reconstruction of hEGC-ClK clone***. ***(A)*** *Distribution of the number of chromosomes counted in 100 metaphases and* ***(B)*** *consensus karyotype of the hEGC-ClK clone. The related values are reported in* ***Supplementary Table T4***. ***(C-D)*** *FISH experiments on hEGC-ClK clone (p21) metaphases lacking* ***(A)*** *or presenting* ***(B)*** *the der5 chromosome. The panel reports two-color FISH experiments performed using a sub-centromeric (RP11-160F8, red) and a sub-telomeric (RP11-69A18, green) DNA probe specific for the long arm of chromosome 5.*

6.4. Enteric glial specific-markers analysis

Flow cytometry analysis was then performed to examine the cellular composition of the hEGC-ClK clone and to exclude the presence of other cell types. Specific markers, such as CD31 for endothelial [287], CD45 for hematopoietic [288], and CD326 for epithelial cells [289] were assayed. As reported in **Fig. 4A**, flow cytometry analysis did not detect the expression of these markers on hEGC-ClK cells. Moreover, there was no detectable positivity for CD271, a marker associated with mesenchymal stem cells [290], as the signal closely overlapped with the mock unstained control (**Supplementary Fig. S6)**. Then, immunofluorescence analysis was perfumed to assess the expression of enteric glial-specific markers GFAP, Sox10, and S100β (26689598) in hEGC-ClK cells (**Fig. 4B**). Notably, immunofluorescence analysis highlighted the nuclear localization of the nucleoplasmic shuttle protein Sox10.

Given that enteric glial cells (EGCs) express both class I and II HLA molecules on their plasma membranes [291], [292], the basal expression of HLA epitopes in untreated hEGC-ClK cells was examined by immunofluorescence, using a specific anti-HLA antibody. Initially, the expression levels of HLA-DQA1, which is associated with intestinal disorders (e.g., CD), and the development of anti-drug antibodies in IBDs were investigated [293], [294]. As shown in **Supplementary Fig. S7**, the expression of HLA-DQA1 was confirmed by the detection of specific fluorescence signals in hEGC-ClK cells, although with variations in intensity among cells. Fluorescent signal specificity was verified through negative control staining. Subsequently, HLA genotyping on hEGC-ClK cells was performed, and the PCR-SSO results revealed the HLA molecules expressed in the hEGC-ClK clone, as detailed in **Supplementary Table T5**.

Inflammatory stimuli have been reported to activate enteric glia both *in vitro* and *in vivo*, resulting in EGC activation and increase in glial markers (14724154, 27416040, 26964064, 28063977, 35533467). Hence, Real-Time PCR analysis was performed to assess the mRNA expression levels of *GFAP*, *SOX10*, *S100β*, *CCL2*, and *PLP1* genes following treatment with lipopolysaccharide (LPS) and/or IFN-γ.

hEGC-ClK cells were exposed to different concentrations of LPS (0.1 and 1 μg/mL), IFN-γ (5 ng/mL), or a combination of both (LPS 0.1 μg/mL + IFN-γ 5 ng/mL). As shown in **Fig. 4C**, at 24 hours post-treatment, *GFAP* mRNA levels displayed an increasing trend in all treatments, with statistically significant increases observed only in IFN-γ treatment or in the case of LPS + IFN-γ, compared to non-treated (NT) cells. *SOX10* expression did not exhibit significant variations. Conversely, a statistically significant increase in *S100β* mRNA levels was observed in samples treated with LPS 1 μg/mL and IFN-γ. An increasing trend in *PLP1* mRNA expression was also observed, with a statistically significant increase only in the LPS + IFN-γ treated sample. Lastly, *CCL2* expression levels showed a statistically significant increase in all treatments except for IFN-γ.

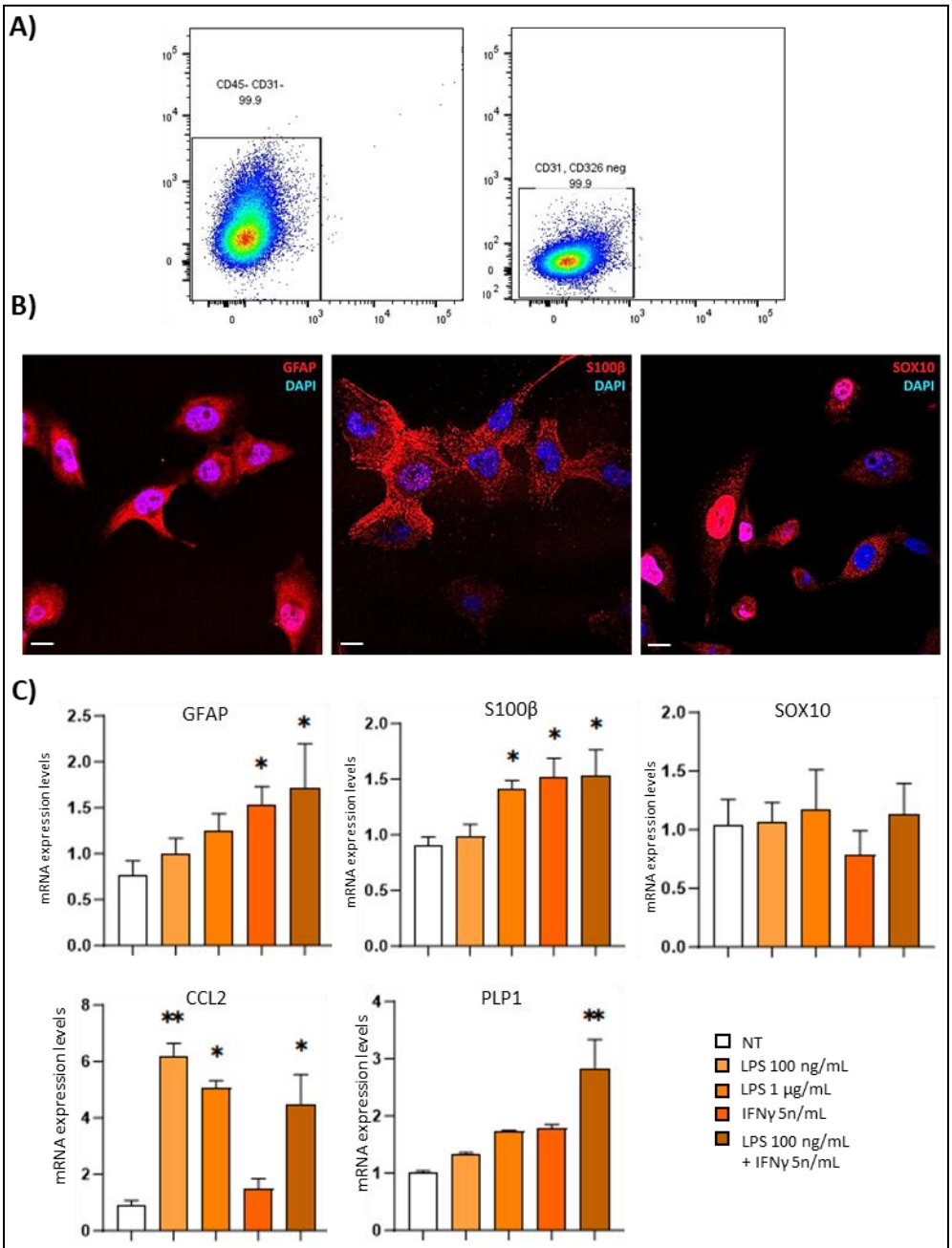

Figure 4. ***Molecular characterization of hEGC-ClK cells****. **(A)** Cytofluorimetric pseudocolor plots of CD31, CD45, and CD326 expression in hEGC-ClK cells. Event collected: 10,000 cells. **(B)** Immunofluorescence of GFAP, SOX10, and S100β. The analysis was performed using specific anti-GFAP, anti-SOX10, and anti-S100β IgG antibodies conjugated with AlexaFluor633. Nuclei were stained with DAPI. Scale bars (=10 µm) are reported. **(C)** GFAP, SOX10, S100β, PLP1, and CCL2 mRNA expression level analysis in hEGC-ClK cells treated with inflammatory stimuli for 24 h. The expression levels of the genes in treated cells were compared with those of non-treated (NT) cells. In the Y-axis, relative quantification values are reported. Data are reported as mean ± SE. (*) indicate $p \leq 0.05$, (**) indicate $p \leq 0.01$, ANOVA One-Way. Experiments were performed on three independent biological replicas.*

6.5. ATP triggers intracellular Ca2+ signaling in hEGC-ClK cells

It has been widely reported that EGCs respond to extracellular stimuli by increasing intracellular Ca^{2+} concentration ($[Ca^{2+}]_i$) (23279281, 33731961). Communication between neurons and glia relies on the neuronal release of ATP, which subsequently binds to postsynaptic Gq/11 coupled P2Y1 receptors, leading to $[Ca^{2+}]_i$ increase (19368656, 26771001, 30730592, 33731961). Therefore, assessing ATP-induced intracellular Ca^{2+} signalling is a valuable strategy to validate the functionality of the hEGC-ClK cells (23279281, 23991747).

Our findings reported that ATP (100 μM) evoked intracellular Ca^{2+} signals in the majority of hEGC-ClK cells (97.3%, n = 147). These signals manifested as either a transient $[Ca^{2+}]_i$ spike - observed in 69.2% of the cells(n = 99) - or a biphasic increase in $[Ca^{2+}]_i$ - seen in 30.8% of the cells,(n = 44) - characterized by an initial Ca^{2+} peak followed by a prolonged plateau above the resting Ca^{2+} levels (**Fig. 5A**). Importantly, the Ca^{2+} response to ATP was effectively blocked by suramin (**Fig. 5B**), a non-selective P2Y receptor antagonist [295], [177], as well as by MRS-2179 (10 μM) (**Fig. 5C**), a selective P2Y1 receptor inhibitor (23279281, 27775719) [295], [296]. Notably, the Ca^{2+} response to ATP resumed upon removal of MRS-2179 (**Fig. 5C**), but not suramin (not shown). Detailed statistical analysis of these findings is presented in **Fig. 5D**. Collectively, these results demonstrate the ability of ATP to consistently trigger intracellular Ca^{2+} signals in hEGC-ClK cells.

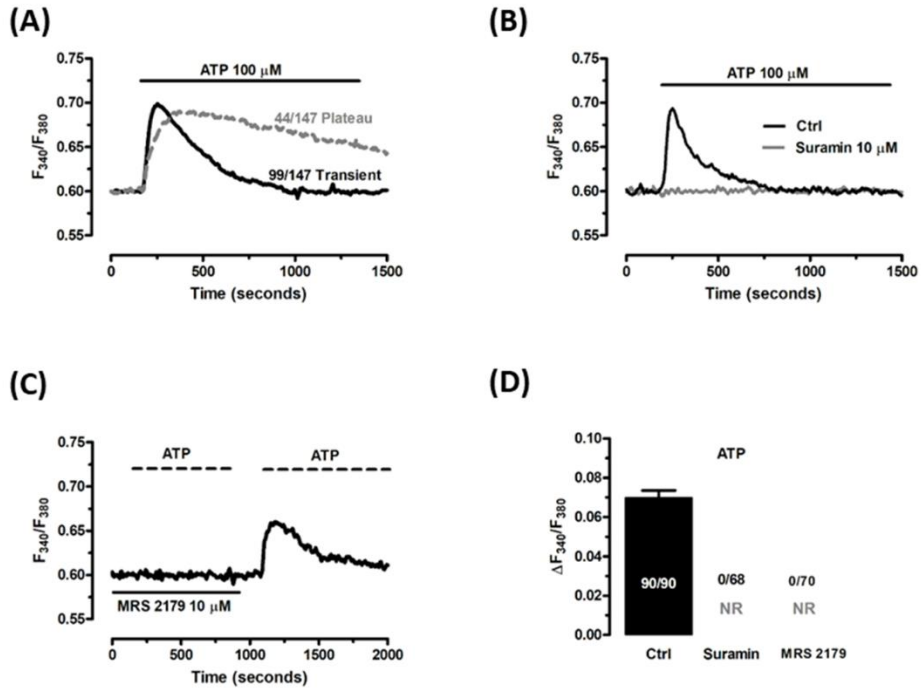

Figure 5. ***ATP induces P2Y1 receptor-mediated increase in [Ca^{2+}]' in hEGC-ClK cells.*** ***(A)*** *ATP (100 μM) triggered heterogeneous Ca2+ signals in hEGC-ClK cells.* ***(B)*** *The Ca^{2+} response to ATP (100 μM) was abolished after preincubation with suramin (10 μM, 30 min), a non-specific P2Y receptor inhibitor.* ***(C)*** *Pretreating the hEGC-ClK cells with MRS-2179 (10 μM, 30 min), a competitive antagonist of the P2Y1 receptor abolished the Ca^{2+} response to ATP (100 μM), whereas the signals resumed upon washout of the inhibitor.* ***(D)*** *Mean ± SE. Ca^{2+} response amplitude to ATP in the absence (Ctrl) and presence of P2Y receptor blockers. In panel (D); NR: no response. The Ca^{2+} response to ATP requires InsP3-induced ER Ca^{2+} release and SOCE activation.*

Evidence obtained from EGCs isolated from different animal species reported that EGCs' response to ATP $[Ca^{2+}]_i$ is mediated by inositol-1,4,5-trisphosphate (InsP3)-dependent Ca^{2+} release from the endoplasmic reticulum (ER) [297]. Accordingly, in the absence of extracellular Ca^{2+} (0 Ca^{2+}), ATP at a concentration of 100 μM triggered a transient increase in $[Ca^{2+}]_i$ in hEGC-ClK cells, consistent with the depletion of endogenous Ca^{2+} stores (**Fig. 6A**). The magnitude of the peak increase in $[Ca^{2+}]_i$ was significantly lower ($p < 0.001$) compared to the Ca^{2+} response induced by ATP in the presence of extracellular Ca^{2+} (0.078 ± 0.004, n = 220, vs. 0.093 ± 0.004, n = 179). Interestingly, the subsequent reintroduction of extracellular Ca^{2+} into the perfusate elicited a second significant peak in $[Ca^{2+}]_i$, resulting from extracellular Ca^{2+} entry in 167 out of 227 cells (**Fig. 6A**). ATP was removed 100s before the restoration of external Ca^{2+} (**Fig. 6A**). Therefore, the ATP-induced extracellular Ca^{2+} entry did not occur through ionotropic P2X receptors or second messenger-operated channels (SMOCs), but rather, it was likely mediated by store-operated Ca^{2+} entry (SOCE). SOCE is a ubiquitous Ca^{2+} entry pathway, which is activated after depletion of the

ER Ca^{2+} pool and does not depend on a specific agonist (18929662, 31473770). Moreover, SOCE has been shown to sustain the Ca^{2+} response to ATP in enteric glia (9724268).

To confirm these data, a pharmacological approach to inhibit InsP3-induced ER Ca^{2+} release and SOCE was used. The inhibition of phospholipase Cβ (PLCβ) with U73122 (10 μM, 20 min) (**Fig. 6B, 6D**; [298]) and the blockade of InsP3 receptors (InsP3Rs) with 2-Aminoethyl diphenylborinate (2-APB; 50 μM, 20 min) (**Fig. 6B, 6D**) effectively suppressed ATP-induced ER Ca^{2+} mobilization (28677119, 32535721)Additionally, the use of cyclopiazonic acid (CPA) to interfere with the activity of the Sarco-Endoplasmic Ca^{2+}-ATPase (SERCA) ([299]; **Fig. 6C, 6D**), led to the abolition of the intracellular Ca^{2+} response to ATP. SERCA is responsible for sequestering cytosolic Ca^{2+} into the ER lumen and maintaining ER Ca^{2+} concentration ($[Ca^{2+}]_{ER}$) (23677809). CPA inhibits SERCA activity, leading to a transient increase in $[Ca^{2+}]_i$ due to the passive leakage of Ca^{2+} from the ER, followed by a return to baseline levels through the coordinated action of the Na^+/Ca^{2+} exchanger, plasma membrane Ca^{2+}-ATPase, and mitochondria (18929662, 31473770). As shown in **Fig. 6C**, under 0 Ca^{2+} conditions, CPA (30 μM) induced a transient rise in $[Ca^{2+}]_i$, reflecting ER Ca^{2+} depletion. After 20 min in the presence of CPA, ATP failed to elevate $[Ca^{2+}]_i$, confirming that InsP3-induced ER Ca^{2+} release was responsible for the initial Ca^{2+} peak.

SOCE is the Ca^{2+} entry pathway activated in response to InsP3-induced reduction in $[Ca^{2+}]_{ER}$, serving to refill the endogenous Ca^{2+} reservoir and extend the Ca^{2+} response to extracellular stimuli in non-excitable cells [300], including glial cells (23677809). To investigate the role of SOCE in ATP-induced extracellular Ca^{2+} entry in hEGC-ClK cells, we employed the "Ca^{2+} add-back" protocol described in **Fig. 6A** in both the absence and presence of two established blockers of Orai1 (12673831), the pore-forming subunit of SOCs in glial cells [301]. ATP-induced extracellular Ca^{2+} entry in hEGC-ClK cells was significantly reduced ($p < 0.005$) when the cells were pre-treated with BTP-2 (20 μM, 20 min) or Pyr6 (10 μM, 20 min) (**Fig. 6E, 6F**), while ER Ca^{2+} release remained unaffected (**Fig. 6E, 6F**). This observation confirmed the selectivity of each drug towards SOCE. In summary, these findings provide strong evidence that ATP, the primary mediator of neuron-to-glia communication in the enteric nervous system, activates hEGC-ClK cells by inducing an increase in $[Ca^{2+}]_i$. This increase is mediated by P2Y1 receptors, and it depends on InsP3-dependent ER Ca^{2+} release and subsequent SOCE.

Finally, the ability of other neurotransmitters to activate hEGC-ClK cells by increasing $[Ca^{2+}]_i$ was assessed. As shown in **Supplementary Fig. S8,** acetylcholine (Ach, 10 μM), serotonin (5-hydroxytryptamine or 5-HT, 10 μM), and glutamate

(100 μM) evoked intracellular Ca^{2+} signals, which had either a transient or an oscillator pattern.

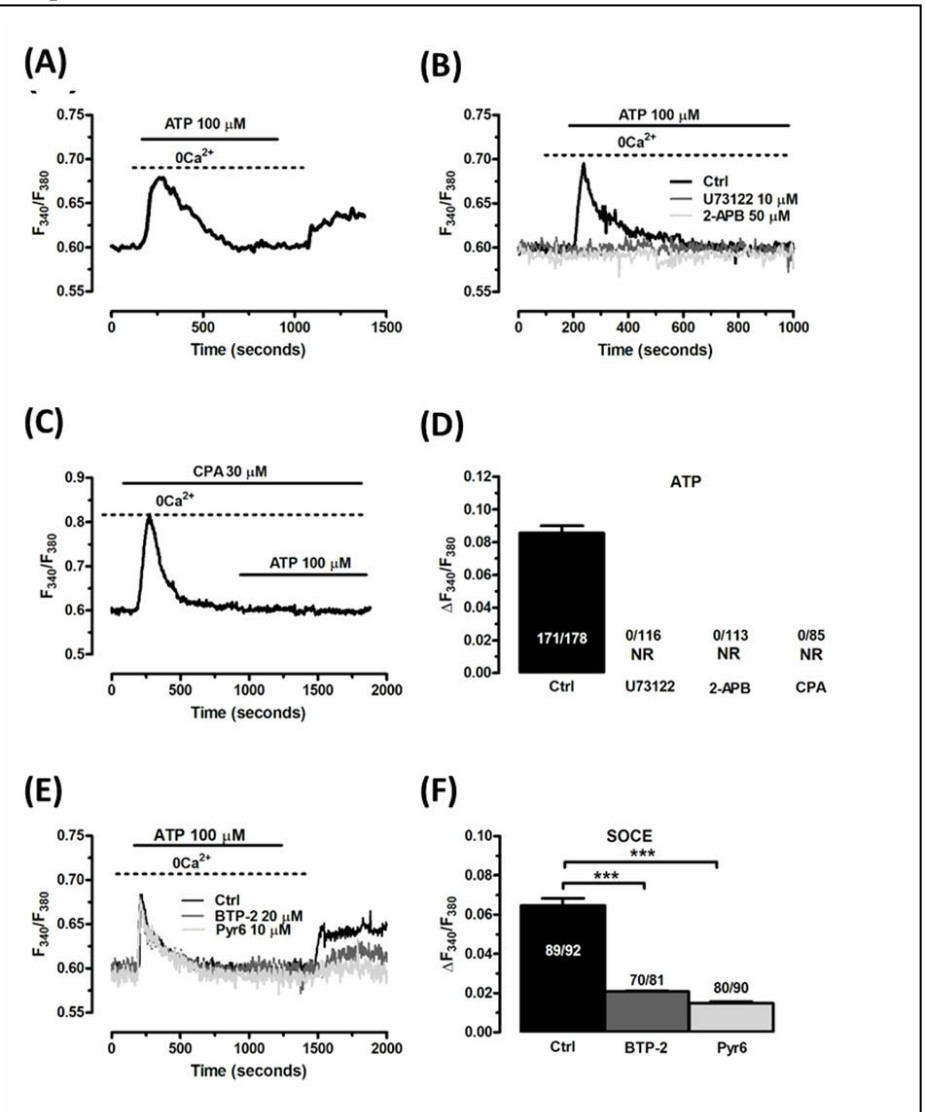

Figure 6. ***(A)*** *Cells perfused with ATP (100 μM) in the absence of extracellular Ca^{2+} responded with a transient increase in $[Ca^{2+}]_i$, whereas restoration of extracellular Ca^{2+} caused a second elevation in $[Ca^{2+}]_i$. ATP was removed 100 s before the re-addition of extracellular Ca^{2+}.* ***(B)*** *ATP-induced transient Ca2+ release was blocked upon hEGC-ClK preincubation with U73122 (10 μM, 30 min) and 2-APB (50 μM, 30 min). ATP was administered at 100 μM.* ***(C)*** *Pharmacological depletion of the ER Ca^{2+} pool with CPA (30 μM) in the absence of extracellular Ca^{2+} (0 Ca^{2+}) inhibits the Ca^{2+} release evoked by ATP (100 μM).* ***(D)*** *Mean ± SE of the amplitude of ATP-induced intracellular Ca^{2+} release under the designated treatments.* ***(E)*** *ATP-induced extracellular Ca^{2+} entry was dramatically reduced by selectively blocking SOCE with BTP-2 (20 μM, 20 min) or Pyr6 (10 μM, 10 min).* ***(F)*** *mean ± SE of the amplitude of the peak Ca^{2+} entry by ATP under the designated treatments. In panel d; NR: no response. One-way ANOVA analysis was used for statistical comparison. In Panel F: (***) $p \leq 0.005$.*

6.6. Enzymatically digested gliadin leads to cytotoxicity in hEGC-ClK cells

So far, several studies employing both 2D- and 3D-cell cultures demonstrated that gluten-derived gliadin induces cellular cytotoxicity. Particularly, gliadin has been shown to induce cytoskeleton rearrangements, alter cellular metabolism, reduce cell viability, and induce apoptosis in Caco-2 cells, the *in vitro* gold-standard epithelial cell line for CD studies [302]. These data confirmed Weiser's hypothesis, which suggested that damage to epithelial cells might constitute the initial stage in the development of CD [261]. Additionally, gliadin has been described to induce cellular stress in other intestinal cell lines, including immune cells [303]. Considering these premises, it is likely that gluten-derived gliadin exerts its cytotoxic effect even on EGCs during CD pathogenesis.

Firstly, different concentrations (0.05, 0.1, 0.25, 0.5, and 1 μg/μL) of pepsin-trypsin digested gliadin (PT-gliadin) were added to hEGC-ClK cells and cell viability was assessed at different time points (i.e., 6, 12, 24 hours p.t.) by MTS assay. To test whether cell confluence might affect the cellular response, we compared two different subculturing confluences, i.e., 2000 and 3000 cells/well in a multiwell-96 microplate (diameter: 7,15 mm/well). Additionally, pepsin-trypsin digested albumin (PT-albumin) at the same concentrations was used as a negative control. A significant decrease in cellular viability was observed in 0.5 and 1 μg/uL treatments after 12 (**Supplementary Fig. S9**) and 24 hours (**Fig. 7A**), while cytotoxicity at 6 post-treatment (p.t.) was not scored (**Fig. 7A**) compared with non-treated (NT) cells and the negative control with albumin. Moreover, cell confluence did not significantly affect the response to treatments. Similarly, the cytotoxic effect of whole digested gliadin treatment (0.5 and 1 μg/μL) was observed by making use of optical microscopy, as shown in **Fig. 7B.** Again, cell confluence did not influence the hEGC-ClK cells response to digested gliadin treatment **(Supplementary Fig. S10)**

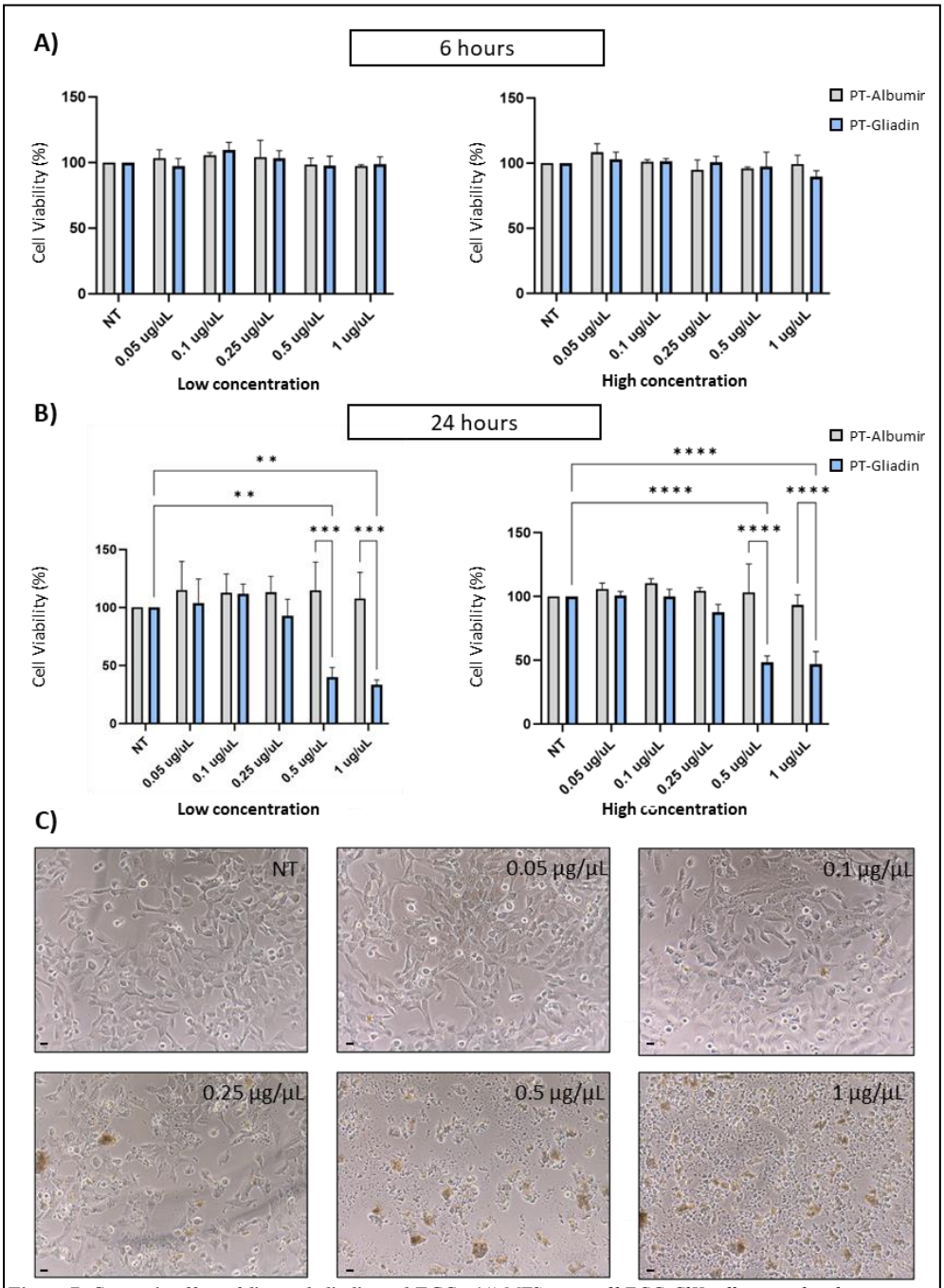

Figure 7. ***Cytotoxic effect of digested gliadin on hEGCs***. ***(A)*** *MTS assay of hECG-ClK cells treated with increasing concentration of digested gliadin. Analysis was performed at 6 and 24 hours p.t. The values on the Y-axis, reported as mean ± SD, indicate cell viability (%) normalized with that of control cells. The asterisks indicate p<0.05 (*), p<0.01 (**) or p<0.001 (***), p<0.0001(****) Two-Way ANOVA, compared with relative control cells. The experiments were performed in three independent biological replicas.* ***(B)***. *Bright microscopy analysis of hEGC-ClK cells treated with increasing concentration of PT-gliadin. Cells were seeded at "high confluence", i.e., 100.000 cells/well in a 6-well microplate and cultured per 24 hours. Images were visualized through the Nikon Eclipse TS-100 phase-contrast microscope. Cells were analyzed 24 hours p.t. Images were collected at 10X magnification. Size bars (= 10 µm) are reported.*

6.7. Whole digested gliadin treatment leads to mitochondrial damage

Gliadin intake induces oxidative stress in intestinal epithelial cells (IECs), impairing intracellular oxidative balance and affecting cell viability and metabolism [304]. Accordingly, intracellular ROS levels in hEGC-ClK cells following enzymatically digested gliadin treatment were analysed. Cells were treated with two different concentrations of digested gliadin (i.e., 0.25 and 1 μg/μL), accordingly with MTS results. Intracellular ROS levels were then measured at 3 and 6 hours p.t. by cytofluorimetric analysis. As shown in **Fig. 8A**, a statistically significant increase in ROS levels was observed in both treatments with a concentration-dependent trend (cytofluorimetric plots are reported in **Supplementary Fig. S11**). Oxidative stress caused by ROS induces rapid depolarization of inner mitochondrial membrane potential (ΔΨm) and subsequent impairment of oxidative phosphorylation. Coherently, ΔΨm analysis by flow cytometry in hEGC-ClK cells revealed a significant increase in the percentage of cells with ΔΨm alterations 6 hours after 0.25 and 1 μg/μL gliadin treatments (**Supplementary Fig. S12**). Additionally, gliadin-induced mitochondrial damage by fluorescence microscopy analysis using the JC-1 dye was assessed. This cationic dye, once accumulated in healthy mitochondria, exhibits an emission spectrum at ~ 590 nm (red). Conversely, depolarized and/or damaged mitochondria do not lead to JC-1 aggregation, which in turn remains in its soluble form that emits at ~525 nm (green). As shown in **Fig. 8B**, nearly red fluorescence spots, which correspond to healthy mitochondria, decreased in their number after digested-gliadin administration in a concentration-dependent manner at 6 hours after treatment. The same trend was observed at 3 hours p.t. (**Supplementary Fig. S13**). By making use of TEM, we then performed ultrastructural analysis of gliadin-treated hEGC-ClK cells and detected mitochondrial engulfment and cristae loss events starting from 12 hours p.t., further highlighting the presence of mitochondrial damage (**Fig. 8C**).

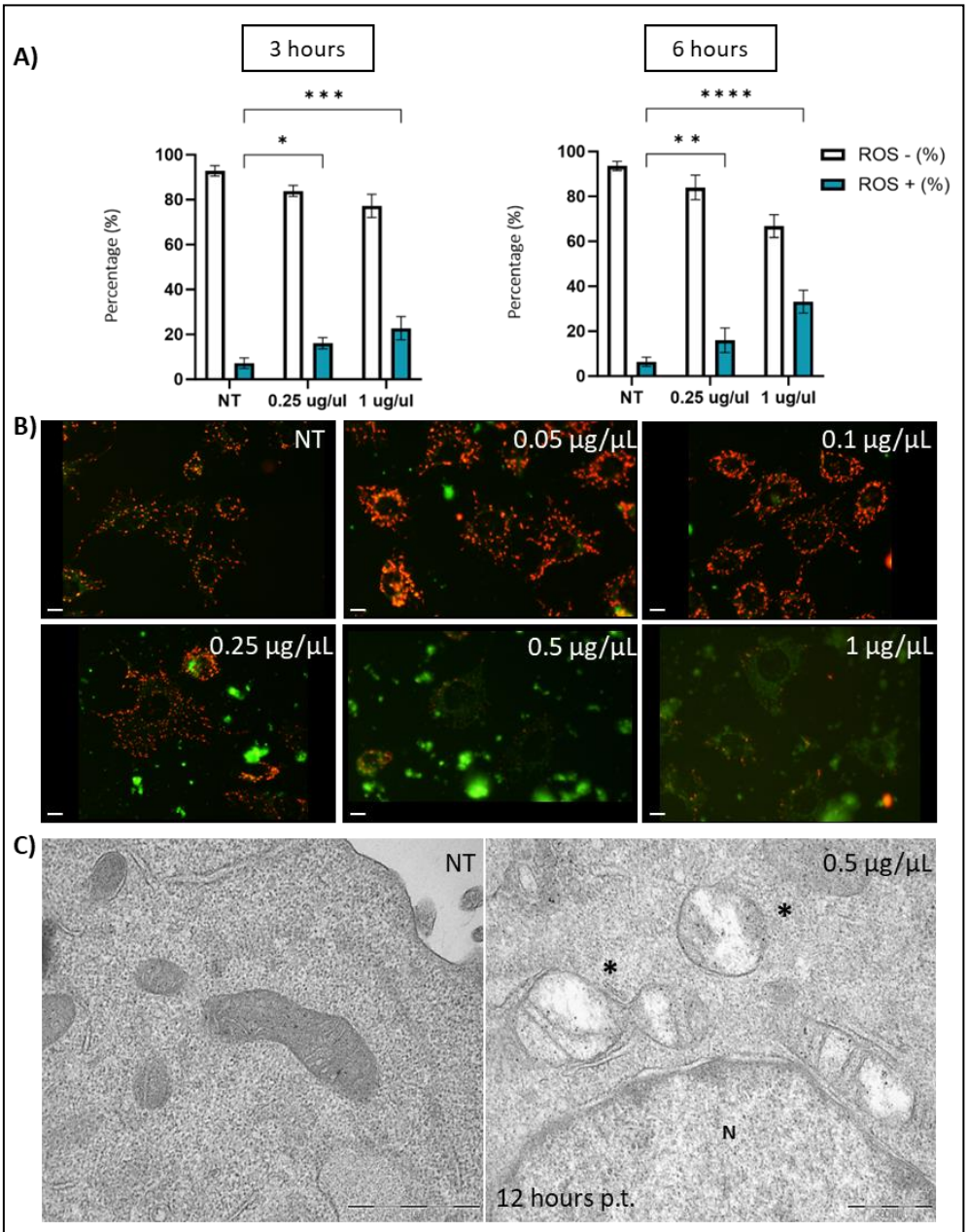

Figure 8. ***PT-gliadin induces mitochondrial damage in hEGCs***. ***(A)*** *Analysis of intracellular ROS levels in hEGC-ClK cells treated with digested gliadin. Analysis was performed at 3 and 6 hours p.t. (gliadin concentration: 0.25 µg/µL, 1 µg/µL). Cytofluorimetric plots are reported in* ***Supplementary Fig. S11****. Events collected: 2000. Histogram data are represented as mean ± SD. On the Y-axis is reported the number of cells expressed as percentages (%). The asterisks indicate p<0.05 (*), p<0.01 (**) or p<0.001 (***), p<0.0001(****) Two-Way ANOVA, compared with relative control cells. Experiments were performed in triplicate.* ***(B)*** *Analysis of mitochondrial membrane potential (ΔΨm) in EGCs cells treated with Pt-gliadin (0.25 µg/µl and 1 µg/µl). Pictures were collected 3 and 6 hours after the treatment. Fluorescence microscope observation at 490 nM following JC-1 administration. Orange-red spots indicated healthy mitochondria. Size bars (= 10 µM) are reported.* ***(C)*** *Electron microscopy analysis of EGCs treated with digested gliadin (0.5 µg/µL). Pictures were collected 12 hours p.t. Asterisks indicate damaged mitochondria. N: nucleus. Scale bars (1µM left; 500nM right) are reported.*

6.8. Whole digested gliadin treatment induces impairment in the autophagic pathway and caspase-mediated apoptosis in hEGCs

By making use of a well-established *in vitro* model of CD based on Caco-2 cells [305], [306], [307], we previously demonstrated that digested gliadin can block autophagy, a self-degradative mechanism that plays a cell protective function in removing misfolded or aggregated proteins, clearing damaged organelles, as well as eliminating intracellular pathogens [308]. To assess gliadin effects on autophagic mechanism in hEGC-ClK cells, immunoblotting analysis to quantify the expression of LC3-II and SQSTM1/p62 proteins, the main hallmarks of the autophagy process [309], was performed. hEGC-ClK cells were treated with 0.25 and 0.5 ug/μL of whole digested gliadin in the presence or absence of Bafilomycin A1 (BAF, 50nM), an autophagy inhibitor commonly used to evaluate the autophagic flux [309]. As reported in **Fig. 9A**, enzymatically digested gliadin induced a statistically significant decrease in LC3-II expression levels at 6 hours p.t., suggesting a block in the autophagy pathway. Moreover, a similar trend, even if not significant, was also observed in SQSTM1/p62 protein expression. The ability of digested gliadin to block autophagy was confirmed by Multispectral Imaging Flow Cytometry (MIFC) analysis using the same experimental approach. The samples, identically treated with BAF, showed an increase in LC3-II-associated fluorescence intensity in the NT sample. Conversely, no significant increase was scored between digested gliadin (PT-gliadin) and PT-gliadin + Bafilomycin A1 treated cells (**Fig. 9B**). Moreover, multivesicular bodies (MVBs) and autophagic vesicles were detected starting from 6 hours p.t. in hEGC-ClK cells treated with whole digested gliadin (**Supplementary Fig. S14)**.

It has been widely suggested that the impairment of the autophagy pathway could also induce apoptotic cell death [310]. Considering that hEGC-ClK cell viability is decreased after gliadin administration and that mitochondrial functional alterations are highly associated with apoptosis, we performed a caspase-specific cytofluorimetric assay to detect the activation of effector caspase-3 and -7 in hEGC-ClK cells treated with digested gliadin. As reported in **Fig. 9C**, a significantly increased expression of cleaved caspases 3 and 7 was detected with 0.25, 0.5, and 1 μg/μL treatments after 6 hours, suggesting that gliadin was able to induce caspase-mediated apoptosis. Accordingly, the immunoblotting analysis revealed an increased cleaved caspase-3/uncleaved caspase-3 ratio, suggesting the activation of the apoptotic process (**Supplementary Fig. S15**). Finally, ultrastructural analysis by TEM confirmed apoptotic morphological features at 24 hours p.t. (**Fig. 9D**).

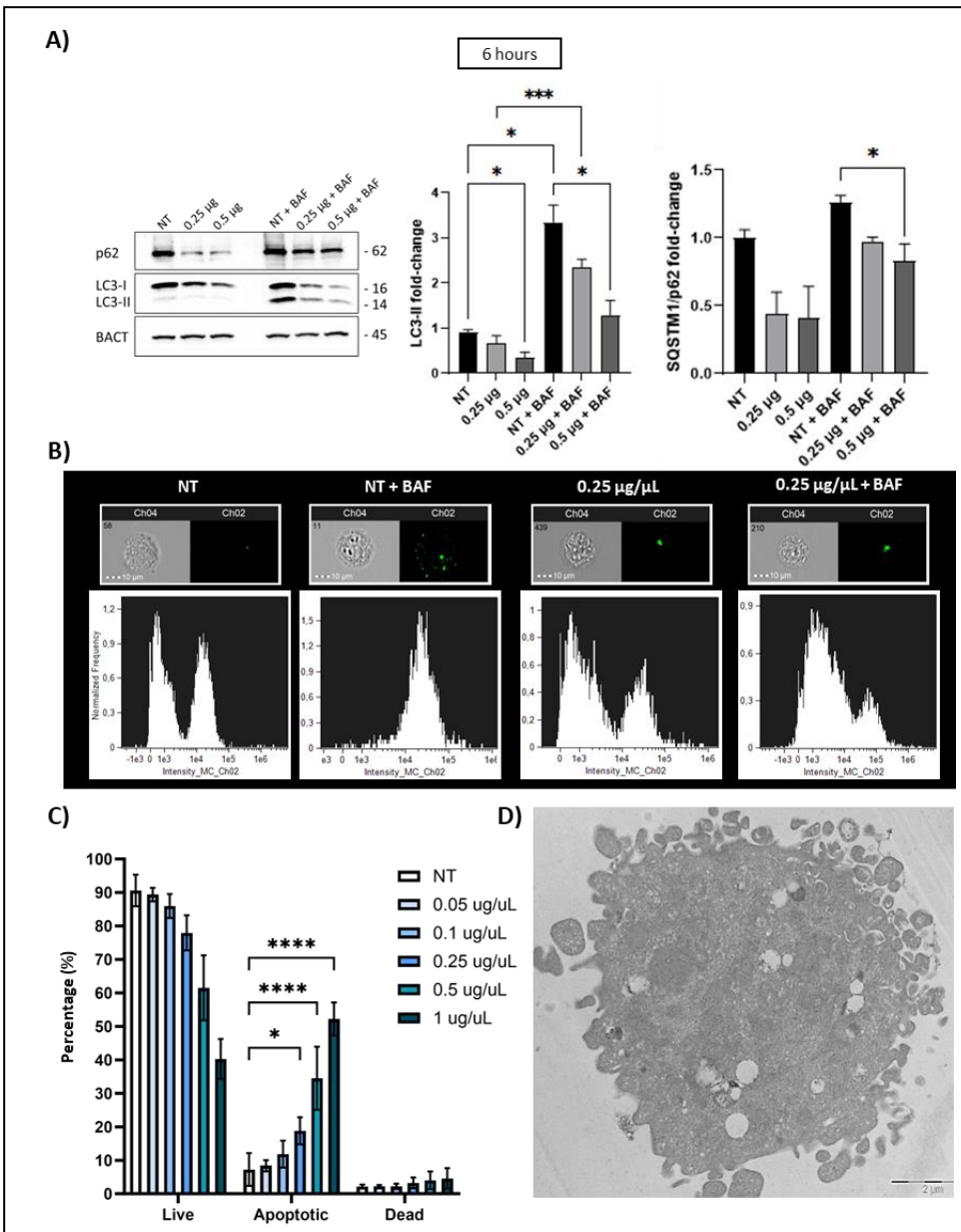

Figure 9. ***PT-gliadin induces autophagy block and caspase-mediated apoptosis in hEGC-ClK cells***. ***(A)*** *Immunoblotting of SQSTM1/p62 and cleaved LC3-I/II levels and relative densitometric analysis in hEGCs at 6 p.t. (0.25 µg/µL and 0.5 µg/µL). β-actin expression was used as housekeeping control. Experiments were performed in triplicate. Data are reported as mean ± SD. The asterisks indicate p<0.05 (*), p<0.01 (**) or p<0.001 (***), p<0.0001(****) One-Way ANOVA, compared with relative control cells.* ***(B)*** *Multispectral imaging flow cytometry (MIFC) analysis. Cells were treated with 0,25 µg/µl gliadin in the presence or absence of Bafilomycin A1. Brightfield (BF) and LC3-AF555 (yellow) images of the cells are shown for NT, NT + BAF, GL 0,25 µg/µl, and GL 0, 25 µg/µl + BAF. Event collected: 2000.* ***(C)*** *Analysis of Caspase 3 and 7 activations in EGCs treated with PT-gliadin. Analysis was performed at 6 hours p.t. (0.05 µg/µL, 0.1 µg/µL, 0.25 µg/µL, 0.5 µg/µL, 1 µg/µL). Histogram data are represented as mean ± SD. On the Y-axis is reported the number of cells expressed as percentages (%). The asterisks indicate p<0.05 (*), p<0.01 (**) or p<0.001 (***), p<0.0001(****) Two-Way ANOVA, compared with relative control cells. Experiments were performed in triplicate.* ***(D)*** *Electron microscopy analysis of EGCs treated with digested gliadin (0.5 µg/µl). Pictures were collected 24 hours p.t. Scale bars (2µM) are reported.*

6.9. p31-43 exerts mild cytotoxic effects on hEGCs through reactive oxygen species production

Considering that p31-43 peptide was investigated in several cell lines ranging from 20 to 100 μg/mL [95], [311], [312], [313], cell viability was preliminary assessed in hEGC-ClK cells by MTS assay using increasing concentrations of p31-43 (i.e., 10, 20, 40, 50, 100, 200, and 400 μg/mL) at 24 hours p.t. While a statistically significant increase in cell viability was observed in hEGC-ClK cells treated with 10 μg/mL of the peptide, a decreasing trend was detected for higher concentrations, although not statistically significant (**Fig. 10A**). Interestingly, no effects on cell viability were observed on normal primary rat astrocytes (**Supplementary Figure S16**). In line with the data present in the literature [99], [96], we selected two representative concentrations (i.e., 10 and 100 μg/mL) for further investigations. Notably, p31-43-mediated morphological alterations were observed starting from one hour p.t. and in a concentration-dependent manner by making use of optical microscopy, as shown in **Supplementary Fig. S17.**

Considering the previous results with whole digested gliadin and the ability of p31-43 to induce the formation of reactive oxygen and nitrogen species (ROS and RNS) [98], flow cytometry and fluorescence microscopy were used to measure the intracellular ROS levels after p31-43 treatment. In line with the previous experiments with enzymatically digested gliadin, the analysis was performed at 4 hours after treatment. As reported in **Fig. 10B,** flow cytometry analysis showed a slight but statistically significant increase in intracellular ROS after the treatment (cytofluorimetric plots are reported in **Supplementary Fig. S18**). This result was then corroborated by fluorescence microscopy, which detected increased red fluorescence signals due to dihydroethidium (DHE) internalization in hEGC-ClK cells treated with p31-43 compared with the relative control (**Supplementary Fig. S19**). As known, ROS can have genotoxic effects and promote the expression of the histone γ-H2Ax [314], a marker associated with DNA double-strand breaks (DSBs). Furthermore, as described by Monguzzi and colleagues [304], gliadin can induce DNA damage and the consequent increase in the abovementioned histone in Caco-2 cells. Considering these premises, an immunofluorescence assay was carried out to study the expression of γ-H2Ax in hEGC-ClK cells after p31-43 treatment (i.e., 100 μg/mL). The results highlighted that the peptide was able to induce the expression of histone γ-H2Ax inside the nuclei, as suggested by the accumulation of the associated green fluorescence signals (**Figure 10C**). To better characterize the cytotoxic effect of p31-43, a LDH assay was preliminary performed, showing that p31-43 treatment led to an increasing trend in LDH release compared to non-treated (NT) cells at 6 hours p.t., with a significant increase for 100 μg/mL concentration (**Supplementary Fig. S20**).

Moreover, ultrastructural analysis by TEM was performed at 24 hours p.t. to study organelles integrity as well as cytosolic composition. Similarily to the results obtained with whole digested gliadin, the presence of mitochondrial mild alterations

(i.e., partial loss of mitochondrial cristae and matrix engulfment) was observed in treated cells compared to untreated cells. Moreover, after p31-43 administration, an increase in intracellular vesicles and multivesicular bodies (MVBs), which were not present after treatment with peptic-tryptic gliadin (**Fig 10D**) was scored.
Considering the induction of caspase3/7-mediated apoptosis triggered by whole-digested gliadin, caspase-3 activation was evaluated by fluorescent microscope observations. Briefly, a high-affinity DNA-binding dye linked to the DEVD peptide (a caspase-3 substrate) was added to the hEGC-ClK culture medium with the p31-43 peptide, and images were collected after 4 hours. Differently from digested gliadin, no apoptotic events were detected as a consequence of p31-43 treatment (results also confirmed by flow cytometry, data not shown) (**Supplementary Fig. S21**).

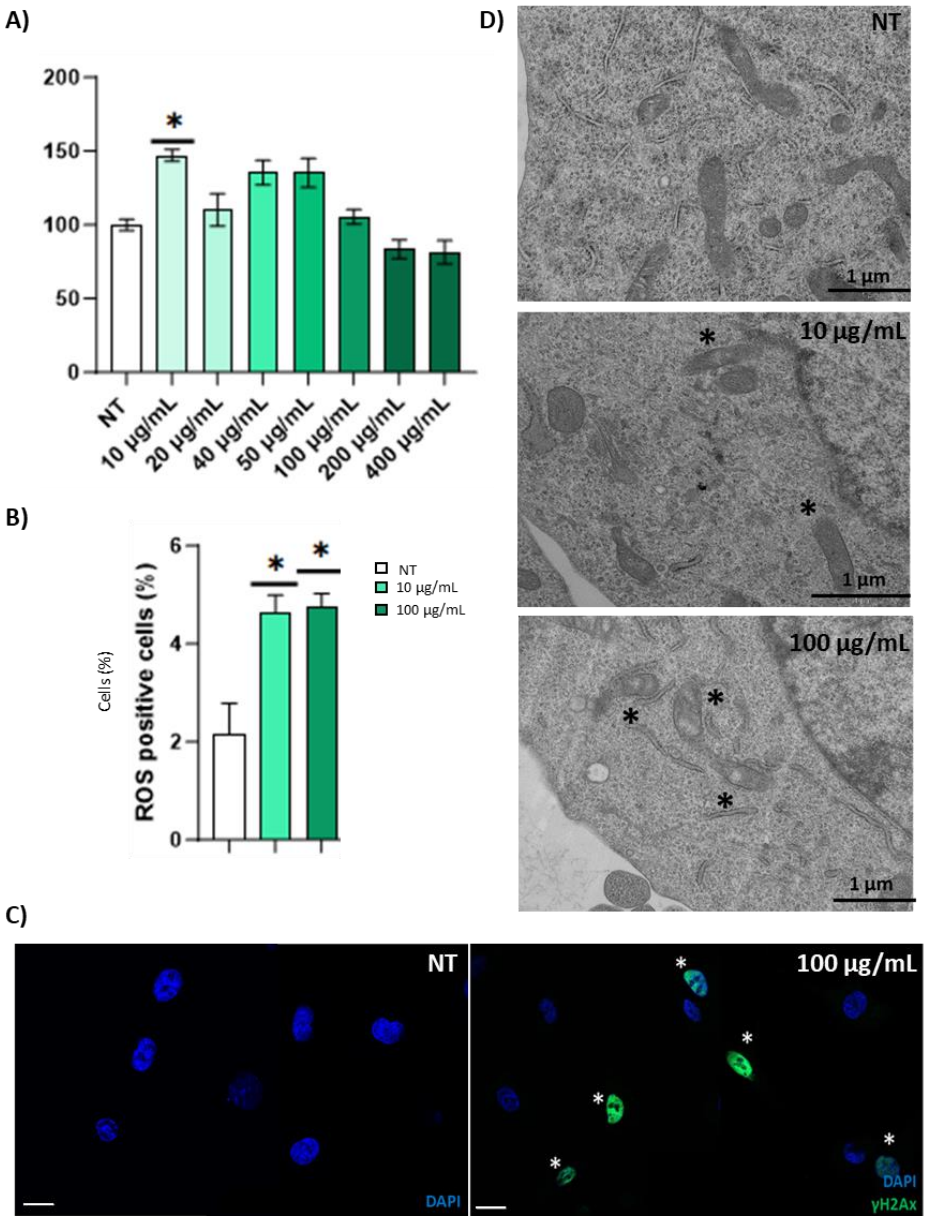

Figure 10. ***Cytotoxic effect of gluten-derived peptide p31-43 on hEGCs.*** ***(A)*** *MTS assay of hECG-ClKs treated with increasing concentration of p31-43 (10, 20, 40, 50, 100, 200, and 400 µg/mL). Analysis was performed 24 hours p.t. The values on the Y-axis, reported as mean ± SD, indicate cell viability (%) normalized with that of control cells. (B) Analysis of intracellular ROS levels in EGCs treated with p31-43. Analysis was performed at 4 hours p.t. (10 and 100 µg/mL). Cytofluorimetric plots are reported in* ***Supplementary Fig. S18****. Events collected: 2000. Histogram data are represented as mean ± SD. On the Y-axis is reported the number of cells expressed as percentages (%).* ***(A, B)*** *The asterisk indicate p<0.05, One-Way ANOVA, compared with relative control cells. Experiments were performed on at least three independent biological triplicates.* ***(C)*** *Immunofluorescence of histone γ-H2Ax in hEGC-ClKs cells treated with p31-43 (100 µg/mL). The analysis was performed using a specific anti-γ-H2Ax antibody conjugated with AlexaFluor488. Nuclei were stained with DAPI. Scale bars (=10 µm) are reported. Pictures were collected at 6 hours p.t.* ***(D)*** *Electron microscopy analysis of hEGC-ClK cells treated with p31-43 (100 µg/mL). Pictures were collected 24 hours p.t. Asterisks indicate damaged mitochondria. Scale bars are reported.*

6.10. p31-43 induces reactive glia-associated markers expression

Since the "reactive glia" is a cellular response against pathological alterations and/or exogenous harmful insults [315], [316], [170], we preliminarily investigated whether p31-43 administration led to increased expression of reactive phenotype-associated glial markers S100β and GFAP. Immunoblotting analysis showed that S100β protein levels significantly increased in a concentration-dependent manner at 4 hours and 24 hours p.t., although statistically significant only for 100 μg/mL of p31-43 (**Fig. 11A**). Conversely, GFAP protein levels did show significant difference only at 4 hours compared to non-treated (NT) cells (**Supplementary Fig. S22**). Accordingly, results obtained by immunofluorescence at 24 hours with the same experimental setup further confirmed enhanced induction only for S100β (**Fig 11B and Supplementary Fig. S23**).

As reported by several studies, "reactive glia" is associated with the secretion of pro-inflammatory molecules, including IL-1β, IL-6, and CCL2 [132]. Hence, immunofluorescence was preliminary performed in hEGC-ClK cells 24 hours after treatment with p31-43 (i.e., 100 μg/mL) to investigate the expression of total IL-1β. Interestingly, the fluorescence intensity associated with total IL-1β in treated cells was reduced compared to control cells (**Fig. 11C**). Subsequently, other molecules associated with inflamed states of the gut were investigated. Specifically, *GDNF*, *IL-6*, and *CCL2* mRNA expression were studied through Real-Time PCR in hEGCs at 24 hours after p31-43 treatment (i.e., 10 and 100 μg/mL). As reported (**Fig. 11D**), the mRNA of all the analysed target genes increased in a concentration-dependent manner resulting in statistical significance for *GDNF* and *IL-6* only in the presence of 100 μg/mL of p31-43. Conversely, *CCL2* increase was significant at both the tested concentrations of the peptide.

Considering the results collected in hEGC-ClK cells, mRNA expression levels of *GFAP* and *S100β* were analyzed through Real-Time PCR in primary murine EGCs (pmEGCs) at 24 hours after treatment (i.e., 10 and 100 μg/mL p31-43). No differences were detected for both the analysed markers, although a decreasing trend was observed for GFAP levels and an increasing one for S100β (**Supplementary Fig. S24**). A similar trend was observed also for *CCL2* mRNA expression levels at 24 hours p.t. (**Supplementary Fig. S24**). Despite these evidence, *IL-6* mRNA expression levels were investigated at different time intervals (i.e., 6, 12, and 24 hours p.t.). As shown (**Supplementary Fig. S24**), a concentration-dependent increasing trend in *IL-6* mRNA was observed at all the investigated time intervals, although statistically significant only at 12 hours after treatment for both the concentrations of p31-43.

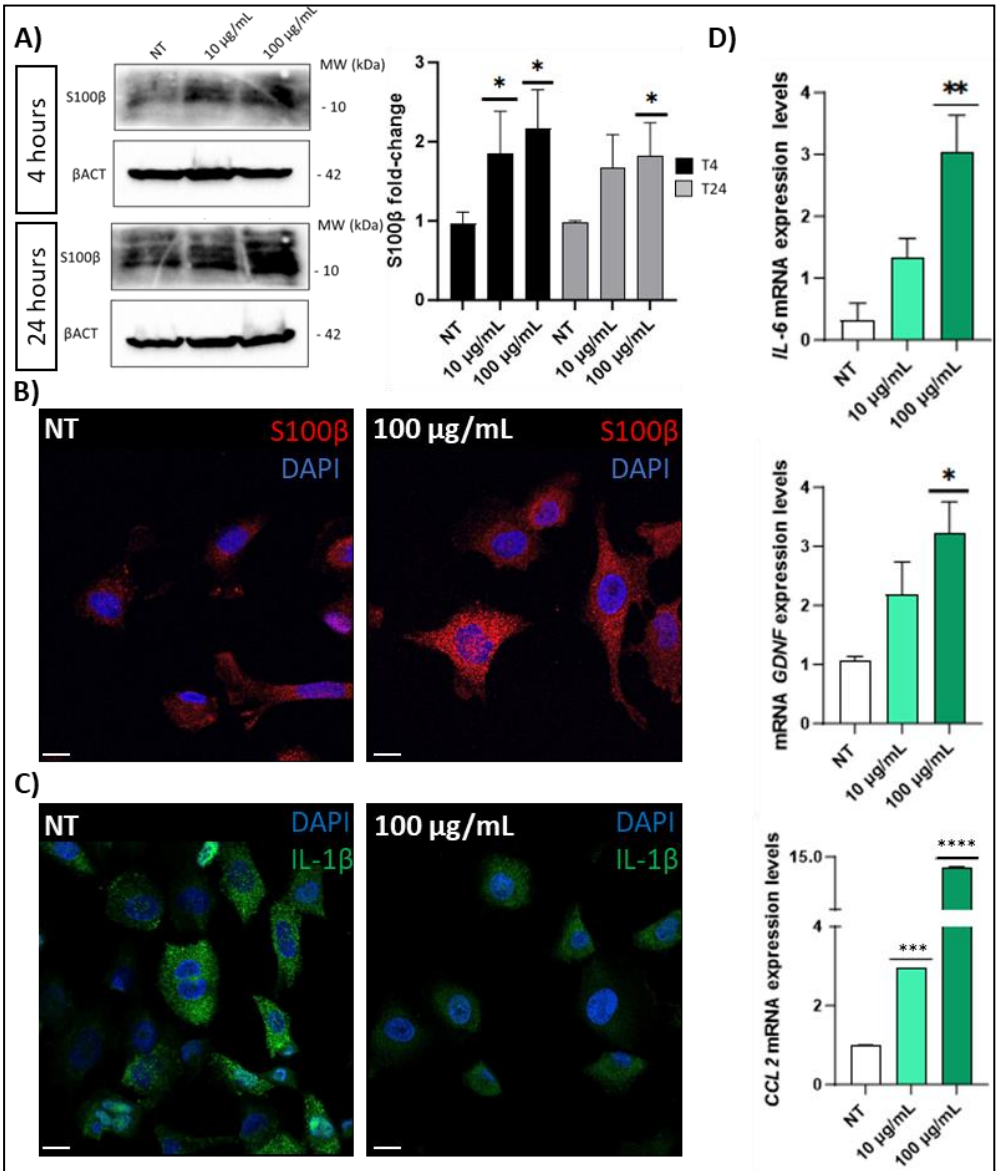

Figure 11. ***Reactive glial phenotype analysis*** ***(A)*** *Immunoblotting of S100β levels and relative densitometric analysis in hEGC-ClK cells at 4 and 24 p.t. (10 µg/mL and 100 µg/mL). β-actin expression was used as housekeeping control. Experiments were performed in triplicate. Data are reported as mean ± SD. The asterisks indicate p ≤ 0.05 (*), One-Way ANOVA, compared with relative control cells.* ***(B)*** *Immunofluorescence of S100β in hEGC-ClK cells treated with p31-43 (100 µg/mL). The analysis was performed using a specific anti-S100β antibody conjugated with AlexaFluor633. Nuclei were stained with DAPI. Scale bars (=10 µm) are reported. Pictures were collected at 24 hours p.t.* ***(C)*** *Immunofluorescence of IL-1β in hEGC-ClK cells treated with p31-43 (100 µg/mL). The analysis was performed using a specific anti-IL1β antibody conjugated with AlexaFluor488. Nuclei were stained with DAPI. Scale bars (=10 µm) are reported. Pictures were collected at 24 hours p.t.* ***(D)*** *IL-6, GFND, and CCL2 mRNA expression level analysis in hEGC-ClK cells treated with p31-43 (100 µg/mL). The expression levels of the selected genes in treated cells were compared with those of non-treated (NT) cells. In the Y-axis, relative quantification values are reported. Data are reported as mean ± SE. The asterisks indicate p<0.05 (*), p<0.01 (**) or p<0.001 (***), p<0.0001(****), ANOVA One-Way. Experiments were performed on three independent biological replicas.*

6.11. p31-43 triggers the antioxidant defense system in hEGCs

Considering that gliadin peptides can induce the antioxidant defence system regulated by Nrf2/Keap1 [317], protein expression levels of Nrf2 were analysed by immunoblotting at 4 and 24 hours after treatment. As reported in **Fig. 12A**, at 4 hours p.t. a statistically significant increase in Nrf2 protein expression was observed compared with control cells. Accordingly, the immunoblotting analysis revealed an increased Erk1/2 phosphorylation, which has been associated with Nrf2 induction [318], [319], [320], and immune cell activation after gliadin administration [321]. Conversely, at 24 hours the levels of the investigated proteins returned at basal levels (**Fig. 12A**). Under oxidative stress, Nrf2 is phosphorylated and moves from the cytoplasm to the nucleus by disrupting the complex with Keap1 [322], [323]. Thereby, Nrf2 translocation was assessed by immunofluorescence at 4 hours p.t. using 100 μg/mL p31-43 (**Figure 12B**).

Once in the nucleus, Nrf2 promotes transcriptional activation of antioxidant genes, including *Heme Oxygenase-1* (*HO-1*) and *Catalase* (*CAT*), by binding to the antioxidant response element (ARE) in the promoter regions of the target genes [324]. Hence, HO-1 and catalase protein expression was finely evaluated at 24 hours p.t., considering that preliminary results at 4 hours did not show any difference in HO-1 expression (**Fig. 12C**). Hence, immunoblotting and immunofluorescence analysis at 24 hours p.t. (i.e., 100 μg/mL) revealed a statistically significant increase in HO-1**(Fig. 12C, Fig. 12D)** protein levels.

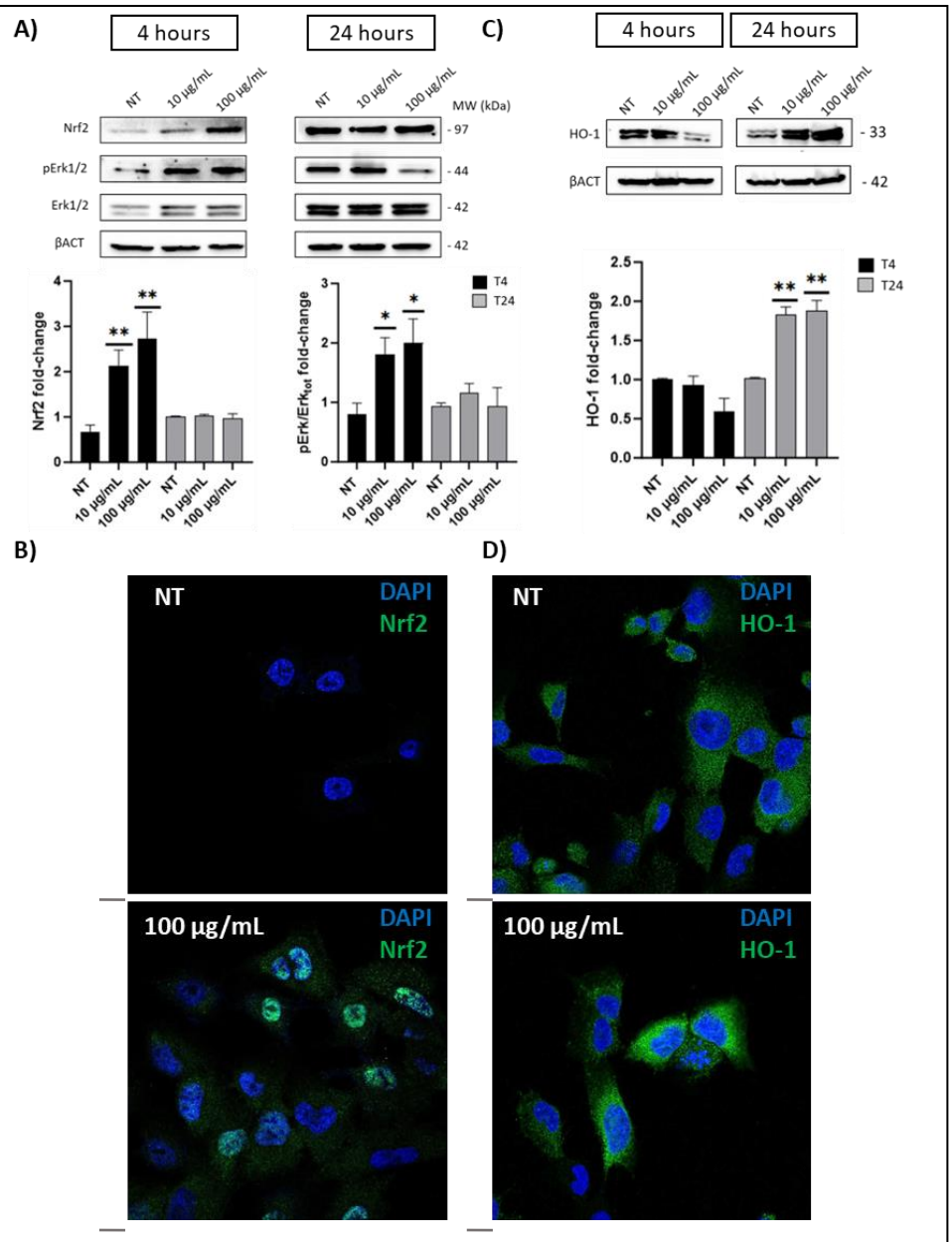

Figure 12. ***p31-43 induces antioxidant defense response in hEGCs.*** ***(A)*** *Immunoblotting of Nrf2 and pErk1/2 levels and relative densitometric analysis in hEGC-ClK cells at 4 and 24 p.t.(10 µg/ml and 100 µg/ml). β-actin expression was used as housekeeping control. Experiments were performed in triplicate.* ***(B)*** *Immunofluorescence of Nrf2 in hEGC-ClK cells treated with p31-43 (100 µg/mL). The analysis was performed using a specific anti-Nrf2 antibody conjugated with AlexaFluor488. Nuclei were stained with DAPI. Scale bars (=10 µm) are reported. Pictures were collected at 4 hours p.t.* ***(C)*** *Immunoblotting of HO-1 levels and relative densitometric analysis in hEGC-ClK cells at 4 and 24 p.t.(10 µg/ml and 100 µg/ml). β-actin expression was used as housekeeping control. Experiments were performed in triplicate.* ***(A, C)*** *Data are reported as mean ± SD. The asterisks indicate $p<0.05$ (*), $p<0.01$ (**) One-Way ANOVA, compared with relative control cells.* ***(D)*** *Immunofluorescence of HO-1 in hEGC-ClK cells treated with p31-43 (100 µg/mL). The analysis was performed using a specific anti-HO-1 antibody conjugated with AlexaFluor488. Nuclei were stained with DAPI. Scale bars (=10 µm) are reported. Pictures were collected at 24 hours p.t.*

Accordingly, an increased catalase expression was observed (**Fig. 13A**) and the translocation of the enzyme into the nucleus, with 44.2% of translocation events in treated cells *vs*. 29.1% in control cells (**Fig. 13B**). Moreover, catalase nuclear translocation was better investigated through immunolabelling at TEM using colloidal gold. As reported in **Fig. 13C**, catalase localization in non-treated (NT) cells is both in the cytosol and the nucleus, particularly associated with heterochromatic regions (e.g., along the nuclear membrane). Differently, after p31-43 treatment, catalase increases its presence in the nucleus and its localization along the nuclear membrane is almost abolished.

Finally, taking into account the interplay between the Nrf2 pathway and autophagy [325] as well as autophagy involvement in cellular response against gliadin [326], [327], [308], [328], [329], the protein expression levels of LC3-II were investigated using immunoblotting at the same time points previously analysed. Alterations in LC3-II expression levels were observed at 4 hours p.t., although not significant; at 24 hours p.t. no differences were detected (**Supplementary Fig. S25**).

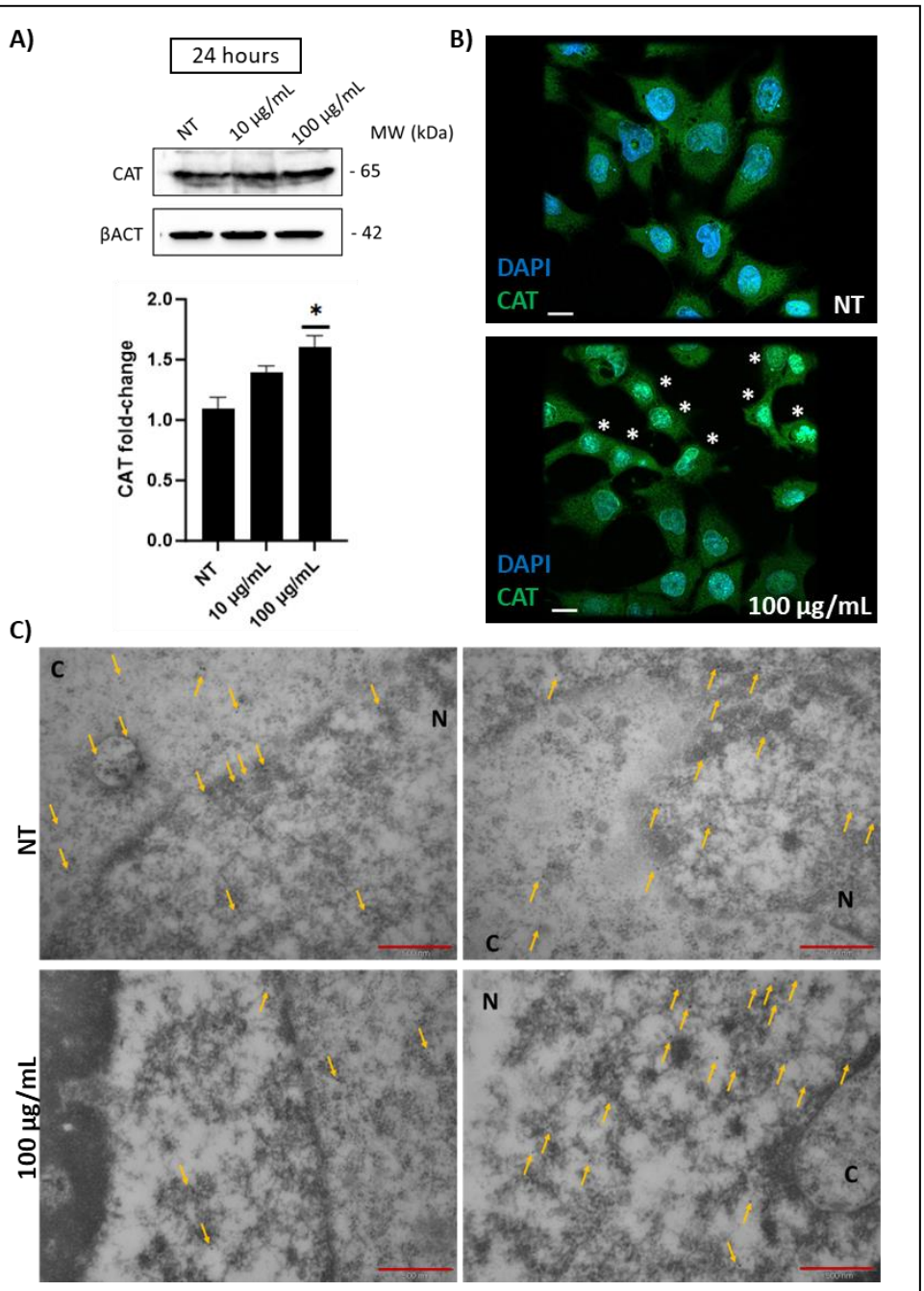

Figure 13. ***p31-43 induces antioxidant defence response in hEGCs. (A)*** *Immunoblotting of catalase levels and relative densitometric analysis in hEGC-ClK cells at 24 p.t. (10 µg/ml and 100 µg/ml). β-actin expression was used as housekeeping control. Experiments were performed in triplicate. Data are reported as mean ± SD. The asterisks indicate p<0.05 (*), One-Way ANOVA, compared with relative control cells.* ***(B)*** *Immunofluorescence of catalase in hEGC-ClK cells treated with p31-43 (100 µg/mL). The analysis was performed using a specific anti-catalase antibody conjugated with AlexaFluor488. Nuclei were stained with DAPI. Scale bars (=10 µm) are reported. Pictures were collected at 24 hours p.t.* ***(C)*** *Catalase nuclear translocation analysis by immunolabeling at electron microscopy using colloidal gold of hEGCs treated with p31-43 (100 µg/ml). Yellow arrows indicate the colloidal gold-linked catalase. Scale bars(500 nM) are reported.*

6.12. Proteomics analysis highlighted that p31-43 induces stress conditions in hEGCs

In order to corroborate the abovementioned results, a proteomics analysis based on nLC-HRMS was performed in hEGC-ClK p31-43 treated cells treated at 24 hours p.t. Among 2161 identified proteins, 241 resulted differentially expressed between treated and the relative control (NT) cells in a significant manner (Adj p-value ≤ 0.05). The volcano plot reported in **Fig. 14** showed the distribution of up- and down-regulated proteins.

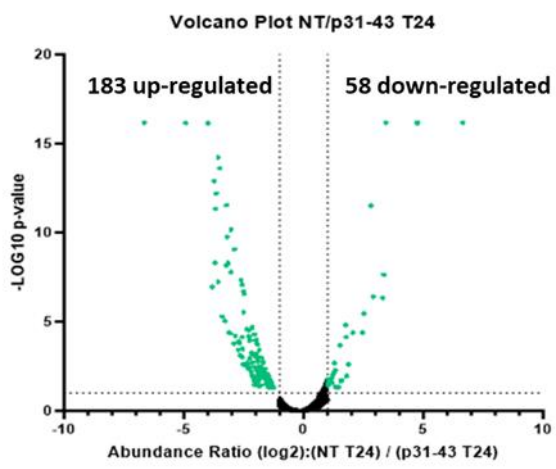

Figure 14. ***Volcano plot of the differentially expressed proteins in hEGC-ClK after p31-43 treatment.*** *On Y-axis is reported the -LOG 10 of the p-value, whereas on X-axis the Abundance Ratio expressed as (log2): NT/treated. The light blue spots indicate proteins that resulted statistically significant expressed in treated cells compared with NT cells. The number of the up- and down-regulated proteins is reported.*

Then, a GO enrichment analysis was carried out and the significant differentially expressed proteins were categorized into onthological groups (i.e., biological function, BP, cellular component, CC, and molecular function, MF). In **Fig. 15**, the heatmap for the statistically significant items in BP, CC, and MF (False Discovery Rate ≤ 0.05, Benjamini-Hochberg procedure), is reported (the complete lists are shown in **Appendix A**). The analysis led to a PPI enrichment p-value < 1.0e-16, underlined that the obtained network had significantly more interactions that expected. For BP, the identified proteins were mainly involved in cellular metabolism (particularly regarding nitrogen compounds), cellular component organization and localization (e.g., organelles, macromolecules, membranes and proteins), cellular stress response, and DNA repair. Similarly, the GO analysis for CC showed that the proteins were mainly cytoplasmic and associated with the maintenance of intracellular anatomical structure. Another important fraction resulted to be associated with extracellular exosomes and vesicles. The MF analysis revealed that most of the proteins were involved in RNA and protein binding as well as in

heterocyclic and organic cyclic compounds. The GO enrichment analysis conducted on up- and down-regulated proteins separately, showed that the latter are only associated with the term RNA binding for MF and only involved in organelle organization for BP.

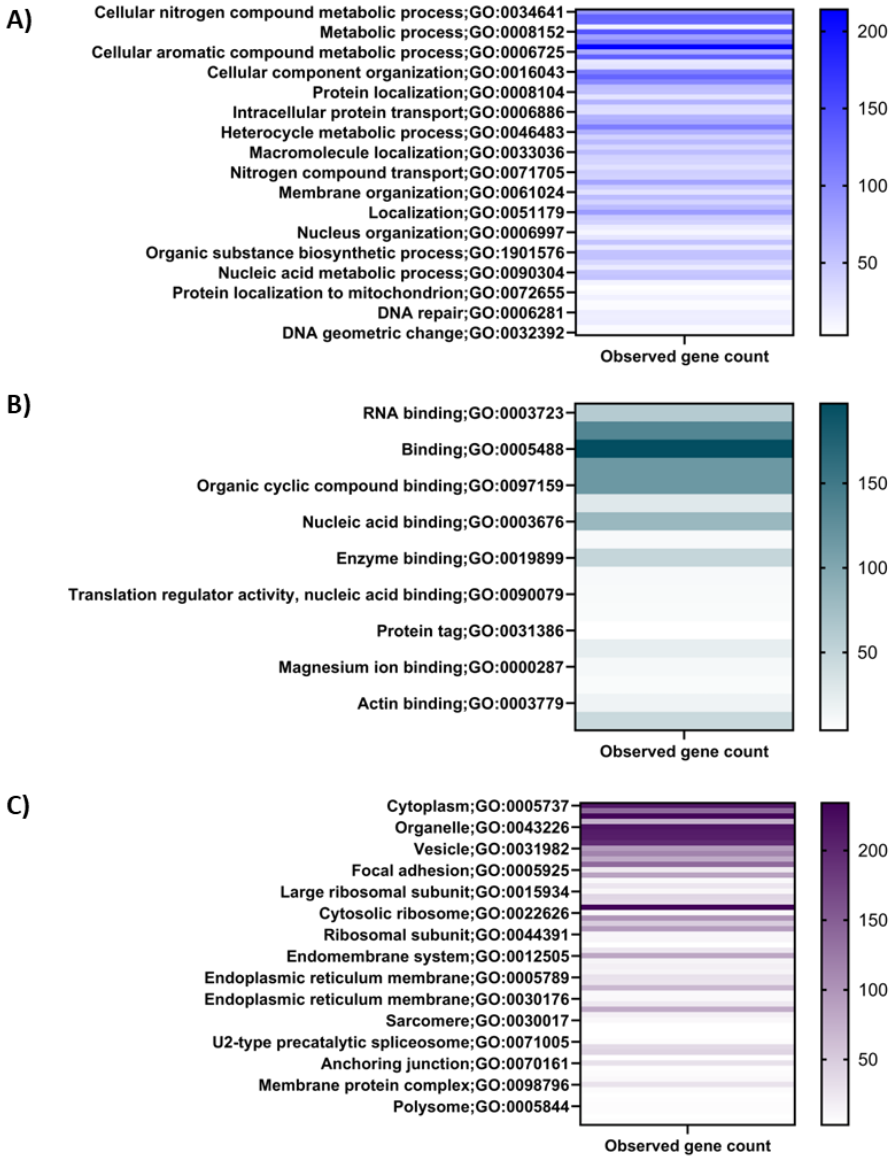

Figure 15. ***Heatmap reporting the results of the GO enrichment analysis***. *Biological Process* ***(A)****, Molecular Function* ***(B)*** *and Cellular Component* ***(C)*** *were used to classify the differentially expressed proteins. The complete lists of GO terms are reported in* ***Appendix A****.*

Subsequently, the differentially expressed proteins were investigated through a Reactome analysis in order to identify the pathways mainly enriched. As reported in **Appendix B**, several proteins are involved in pathways associated to cellular response to stress, apoptosis, membrane trafficking, nuclear excision repair (NER), p53-mediated response, innate immune system, autophagy/mitophagy, DNA damage, and endocytosis. Notably, this result was obtained investigating the up-regulated proteins, since the down-regulated ones produced different categorization results (data not shown). A list of up- and down-regulated protein of interest was then extrapolated and reported below **(Fig.16**).

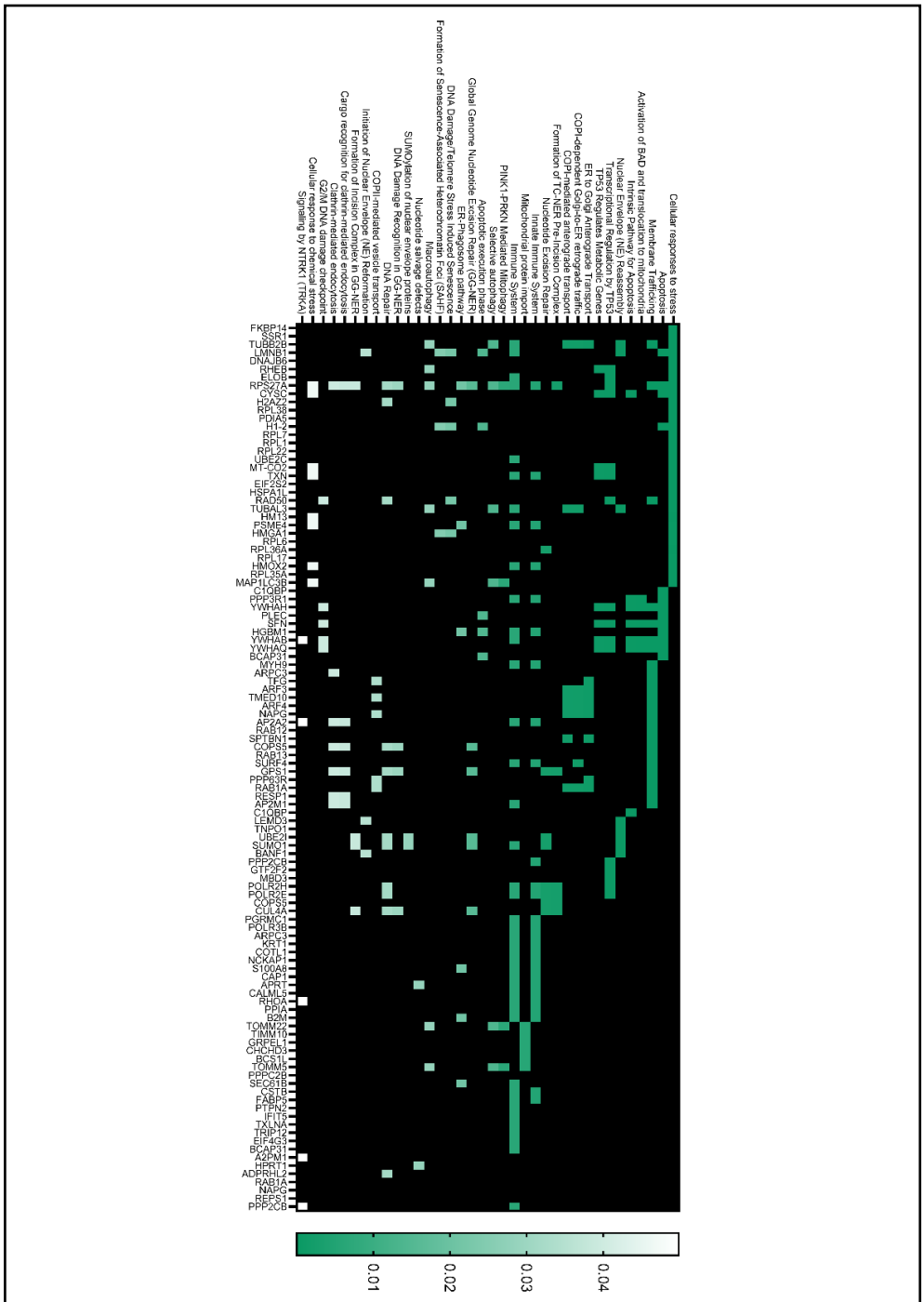

Figure 16. ***Heatmap of up- and down-regulated proteins of interest in hEGC-ClK after p31-43 treatment.*** *Reactome analysis of the differentially up-regulated proteins (adj p-value <0.05) identified in treated hEGC-ClK cells compared with non treated (NT) cells at 24 hours p.t. On Y-axis are reported the pathways whereas on the X axis the classified proteins (FDR < 0.05). The different levels of significance are represented by the reported colored scale (see legend) from white (FDR = 0.05) to green (FDR < 0.01).*

Discussion

Interest in EGCs has recently grown due to their key role in maintaining intestinal homeostasis and their involvement in intestinal inflammation and disease. Particularly, EGCs gained attention because of their plasticity and their ability to shape phenotype and function after specific cues, such as cytokines and chemokines released during intestinal inflammation in pathological contexts.

In this Thesis, it has been investigated the role of EGCs in the context of CD, particularly in the response against whole-digested gliadin (PT-gliadin) and the gluten-derived cytotoxic peptide p31-43. Considering the lack of available established EGC lines and the technical difficulties related to EGC isolation from sample tissue, with the consequent limitation in performing *in vitro*, *in vivo*, and *ex vivo* studies, the first step of this work was the generation of a novel immortalized human EGC line (hEGC). Indeed, EGCs pose a challenge for biological research because they constitute a heterogeneous population *in vivo*, depending on their location within the GI tract. Additionally, the absence of an appropriate human model is a significant limitation for studying EGCs' functions. Although enteric glial cells can be isolated from various species (e.g., guinea pigs, mice, rats, and humans), the isolation protocol presents technical challenges [269]. Furthermore, EGCs have a tendency to revert to undifferentiated states when cultured in vitro, differentiating into both neurons and non-myelinating Schwann cells [330]. A validated protocol based on lentiviral transduction [331] was selected, considering its advantages compared with other techniques. Especially, in comparison to other methodologies (e.g., iPS differentiation, transdifferentiation, or reactivation of hTERT), this approach can be virtually applied to every cell type, thus leading to the production of homogeneous cell lines with a high proliferation rate [331]. Hence, we successfully generated hEGC-ClK cells, an immortalized EGC line, from human intestinal tissue obtained during surgery. Notably, hEGC-ClK cells demonstrated an actively proliferating phenotype with increasing cPDL compared with primary cells, which reached a growth plateau 19 days post-isolation and stopped their growth after 29 days. Additionally, the analysis of the cell proliferation marker Ki-67 revealed a lower expression in hEGC-ClK cells compared to the high-grade astrocytoma T98G cell line. This finding suggested a potential contact inhibition of proliferation in hEGC-ClK, a feature typically retained by noncancerous cells and often lost in transformed cells (Pavel et al., 2018). This hypothesis was further corroborated by the evidence collected on other developed immortalized cell lines derived with the same transduction protocol, which did not show the ability to develop tumors *in vivo* (Lipps et al., 2018). Furthermore, detailed analyses using TEM and flow cytometry showed no significant structural or morphological differences in the hEGC-ClK cells compared to their original counterparts, as well as no disturbances in mitochondrial membrane potential. Additionally, less than 6% of the analysed cells displayed

elevated levels of ROS. Subsequent flow cytometry and immunofluorescence analyses confirmed that hEGC-ClK cells expressed specific markers associated with mature EGCs, such as GFAP, SOX10, and S100β [332], [333] while showing no expression of markers specific to endothelial, hematopoietic, or epithelial cells [287], [290], [289], [288]. This demonstrated the absence of marked contamination by other cell types in the isolated EGCs. Importantly, mRNA expression analysis of GFAP, SOX10, S100β, PLP1, and CCL2 [334], [217], [212], [335], [336] genes after LPS and IFN-γ treatment, showed the hEGC-ClK cells' capability to respond to inflammatory stimuli, consistent with expectations for EGCs. Additionally, immunofluorescence and genotyping experiments revealed the expression of HLA-DQA1 on the hEGC-ClK plasma membrane and the identification of an HLA-DQB1*0602 allele, which is associated with narcolepsy-cataplexy. By contrast, no alleles linked to intestinal diseases (e.g., CD, IBDs) or co-morbidities (e.g., diabetes) were found [337], [291], [338], [292].

Considering that *in vitro* immortalization processes can induce structural and numerical chromosome alterations (Goymer, 2008), an accurate cytogenetic analysis of the hEGC-ClK clone was performed to evaluate potential genetic changes. The results highlighted that hEGC-ClK cells predominantly had a modal karyotype of 44 chromosomes (2n = 44) with a recurrent chromosomal rearrangement, consistent with observations in other cell lines generated using the same technology [270]. Notably, the distribution of the chromosome number showed a tendency to acquire a near-tetraploid arrangement (4n), as suggested by the second modal value detected (2n = 86). Moreover, a large metacentric derivative chromosome (der5) and a small chromosome fragment (M1) were detected in a significant proportion of metaphases. Approximately 38% of the metaphases manifested M1 with a potentially functional centromere, although additional verification is necessary. The large metacentric rearranged chromosome was hypothesized to contain the entire 5q arm, as confirmed by fluorescence in situ hybridization (FISH) experiments using DNA BAC probes specific for the sub-centromeric and sub-telomeric regions of the long arm of chromosome 5. So far, the origin of the other translocated arm remains unidentified, and additional FISH experiments may be required to clarify its composition. It is likely that the rearrangement involves the missing homolog of the long arm of chromosomes 13 and 15, considering their complete monosomy in the modal karyotype. Future studies may involve the analysis of hEGC-ClK 's karyotype at higher culture passages to gain insights into its evolution over time.

ATP is a crucial mediator of intercellular communication between ENs and EGCs [130], being released by direct stimulation of intrinsic nerves or extrinsic cholinergic nerve fibers [182], [339], [340], [339], which may co-release acetylcholine and ATP. ATP-triggered intracellular Ca^{2+} signals in EGCs integrate neuronal activity in the myenteric plexus and help to coordinate patterns of contractile activity in the GI tract [182], [130]. The EGC response to ATP involves Gq/11-coupled P2Y1 receptors [180], [183], [177], [130], InsP3-induced endoplasmic reticulum (ER) Ca^{2+} mobilization [341], and store-operated Ca^{2+} entry (SOCE) [342]. In our study, hEGC-

ClK cells exhibited two distinct patterns of intracellular Ca^{2+} signals in response to ATP: a transient increase in $[Ca^{2+}]_i$ followed by a return to baseline and a biphasic signal that persisted as long as ATP was present in the perfusate. Prolonged exposure to ATP has previously been demonstrated to elicit a two-phase increase in $[Ca^{2+}]_i$ in guinea pig EGCs [179], [182]. In contrast, ATP induced varying Ca^{2+} waveforms (transient vs. sustained) in mouse glia [177] and multiple Ca^{2+} spikes in human EGCs [295]. Similarly, ATP evoked different kinetics of intracellular Ca^{2+} signals in mouse brain astrocytes as well [343], [344], [345]. Hence, the diversity in ATP-induced intracellular Ca^{2+} signals observed in hEGC-ClK cells reflects the variability previously reported in both enteric and brain glial cells. The following evidence suggests that the response to ATP-evoked Ca^{2+} in the hEGC-ClK clone is mediated by P2Y1 receptors, initiated by InsP3-induced ER Ca^{2+} release, and sustained by SOCE. Firstly, blocking P2Y1 receptors with suramin or MRS-2179 abolished the onset of the Ca^{2+} signal. Secondly, although the plateau phase was eliminated and the duration of the Ca^{2+} signal was significantly shorter when extracellular Ca^{2+} was absent, the Ca^{2+} response to ATP still occurred, as compared to hEGC-ClK cells displaying a transient rise in $[Ca^{2+}]_i$ in PSS. Therefore, mobilization of the endogenous Ca^{2+} store is necessary to initiate ATP-induced intracellular Ca^{2+} signals in these cells. Thirdly, inhibiting InsP3 production with U73122 and directly blocking InsP3Rs with 2-APB prevented ATP-induced intracellular Ca^{2+} release [298], [346]. Additionally, ATP failed to elicit a significant increase in $[Ca^{2+}]_i$ when the ER Ca^{2+} store was depleted with the SERCA inhibitor, CPA, which is a common pharmacological tool to reduce $[Ca^{2+}]_{ER}$ in EGCs. Fourthly, achieving the full Ca^{2+} peak and sustaining the plateau in hEGC-ClK cells with a long-lasting Ca^{2+} response required extracellular Ca^{2+} entry. The "Ca^{2+} add-back" protocol demonstrated that, after depleting the InsP3-sensitive ER Ca^{2+} pool, ATP induced the influx of extracellular Ca^{2+}. As extensively discussed [347], [348], Ca^{2+} entry did not necessitate the presence of the agonist in the perfusate, indicating the activation of SOCE. In line with this hypothesis, ATP-induced extracellular Ca^{2+} was significantly reduced by BTP-2 and Pyr6, two pyrazole derivatives that selectively block Orai1, the pore-forming subunits of SOCs in glial cells [301]. Prior studies have demonstrated that SOCE prolonged the Ca^{2+} response induced by ATP in guinea pig EGCs [342] and endothelin-1 [349], whereas this is the first time that SOCE activation is reported in a human-derived EGCs. Although a full characterization of the Ca^{2+} handling machinery is required, this preliminary evidence illustrates that hEGC-ClK cells are capable of generating a functional Ca^{2+} signal in response to ATP, a key mediator of neuron-to-glia communication in the ENS. Furthermore, hEGC-ClK cells display intracellular $[Ca^{2+}]$ signals in response to other enteric neurotransmitters, such as 5-HT, Ach, and glutamate, which are known to activate EGCs by increasing $[Ca^{2+}]_i$ [295], [177], [130].

Since there are few data regarding the involvement of EGCs in CD, this cell line was employed as an *in vitro* model to investigate the effects of gliadin peptides on enteric

glia. As reported in literature [268], duodenal biopsies derived from CD patients showed increased levels of S100β, iNOS, and NO compared to patients under a GFD and healthy controls. To our knowledge, this is the only evidence present in literature regarding the involvement of EGCs in this pathology. Initially, the effects of enzymatically digested (peptic-tryptic, PT) gliadin were studied. The treatment with these peptides (i.e., 0.5 and 1 μg/μL) led to cytotoxicity in hEGC-ClK cells starting from 12 hours, as demonstrated by MTS assay and optical microscope observation. Moreover, cell confluence did not significantly affect the cellular response to the treatments. The data collected by flow cytometry revealed increased levels of intracellular ROS after digested gliadin treatment, confirming the results obtained by Monguzzi and colleagues in Caco-2 cells [304], which demonstrated that gliadin is able to induce oxidative stress and DNA damage. Although it is well known that mitochondria are main targets of elevated ROS exposure [350] and that an increase in ROS levels associated with oxidative mtDNA damage plays a major role in apoptosis, the mechanism whereby mtDNA damage mediates apoptotic signaling is not properly understood [351], [352]. Cytotoxic agents, including radiations and several chemical compounds, produce apoptotic signals that lead to the formation of pores in the mitochondrial membrane. These events alter the integrity of the mitochondrial membrane, resulting in a decrease in ΔΨm and the release of two main groups of pro-apoptotic proteins, which normally are sequestered in the inter-membrane space [353], [354]. Cytochrome c - a soluble protein implicated in the electron transport chain - is the most important protein released after the formation of mitochondrial permeability transition pores (mPTPs) [355]. Several studies suggest that oxidative stress could be a key player in the release of cytochrome c in the cytosol. Indeed, the oxidation of cardiolipin (CL) decreases its affinity to cytochrome c, thus facilitating its mobilization [356], [355] and its consequent binding with apoptotic protease activating factor-1 (Apaf-1), ATP and pro-caspase 9. This complex, known as apoptosome, cleaves the pro-caspase 9 to its active form, which in turn cleaves and activates pro-caspase 3 into the effector caspase-3 [354].

Considering these premises, the impact of digested gliadin on ΔΨm in hEGC-ClK cells was analysed. The results revealed that a significant increase in mitochondrial depolarization was only observed after 1 μg/μL treatment, whereas no alterations in ΔΨm were detected for 0.25 μg/μL treatment. Mitochondrial damage was also corroborated by JC-1 and ultrastructural analysis, which highlighted alterations in ΔΨm as well as architectural aberrations, represented by the loss of mitochondrial internal cristae and matrix engulfment. Notably, the damage to these organelles is also underlined by events of mitophagy; furthermore, autophagic vesicles together with MVBs were detected, suggesting the activation of defence mechanisms and the secretion of inflammatory mediators. A study conducted by our lab previously demonstrated that digested gliadin can block the autophagic pathway in Caco-2 cells [308]. Hence, the expression of the autophagy markers LC3-II and SQSTM1/p62 [309] was studied by immunoblotting and MIFC to evaluate the autophagic flux.

Whole digested gliadin was able to significantly reduce the level of both markers in hEGC-ClK cells starting from 6 hours p.t., thus compromising the correct autophagic flux, as demonstrated by the addition of Bafilomycin A1. These results confirmed the autophagic impairment in hEGC-ClK cells triggered by digested gliadin, underlying the ability of these peptides to alter the homeostasis of this pro-survival pathway. It has been widely suggested that the impairment of the autophagic mechanism can induce apoptotic cell death [310]. As reported, the activation of the pro-survival mechanism in hEGC-ClK cells after digested gliadin treatment (i.e., autophagy) is not sufficient to counteract the apoptotic induction, which is here mediated by the activation of the effector caspase-3 and caspase-7, as demonstrated by flow cytometry and immunoblotting analysis.

Starting from this evidence, we studied the effects of p31-43 (LGQQQPFPPQQPY), a widely investigated gluten-derived peptide, in the same hEGC line. Thanks to its poly-proline II secondary structure, p31-43 is able to spontaneously generate oligomeric nanostructures, that protect this peptide from enzymatic digestion, thus amplifying its cytotoxic effects [99], [101], [102]. Due to its biochemical properties, p31-43 can induce cellular damage and trigger innate immunity response in a variety of immune and non-immune cell types [357], [303]. The results reported in this Thesis demonstrated that p31-43 significantly contributes to gliadin toxicity. Firstly, a cell viability assay was performed to evaluate p31-43 cytotoxicity in hEGC-ClK cells. Contrary to gliadin, p31-43 did not significantly affect cell viability but showed a decreasing trend at higher concentrations. However, flow cytometry, immunofluorescence, and histone γ-H2Ax translocation analysis highlighted the presence of oxidative stress in hEGC-ClK cells starting from 4 hours after p31-43 treatment. Notably, the amount of intracellular ROS levels at 4 hours p.t. was lower compared with that detected by enzymatically digested gliadin. Interestingly, at 24 hours after treatment the basal levels of intracellular ROS were partially rescued, pointing out that p31-43 treatment constitutes an acute stress and that hEGC-ClK cells are able to partially counteract this condition. Notably, observations by TEM were consistent with the previous results: mitochondrial alterations after p31-43 treatment were milder compared with those observed after digest gliadin administration. Altogether, these data suggest that p31-43 alone can slightly affect hEGC viability and other gliadin peptides might contribute to inducing oxidative stress and cytotoxicity. Finally, analysis of the induction of caspase 3/7-mediated apoptosis by immunofluorescence and flow cytometry did not detect any apoptotic event, further corroborating our hypothesis. Since the “reactive glia” is a cellular response against pathological alterations and/or exogenous harmful insults [315], [316], [170], we preliminarily investigated whether p31-43 treatment led to increased expression of reactive phenotype-associated glial markers, i.e., S100β and GFAP. As shown by immunoblotting and immunofluorescence analysis, p31-43 was able to induce the expression of both the reactive glial markers. Specifically, in line with the results collected by Esposito and colleagues [268], GFAP induction seemed to be

transient compared to S100β. The pro-inflammatory response was subsequently investigated through immunofluorescence of total IL-1β and Real-Time PCR of other representative pro-inflammatory genes, i.e., *IL-6* and *CCL2*. The fluorescence signal associated with total IL-1β suggested its massive cleavage and release after p31-43 treatment; the inflammatory response operated by hEGC-ClK cells was also supported by increased levels of *IL-6* and *CCL2* mRNAs. Another up-regulated protein during inflammatory processes of both CNS and ENS is GDNF [213], [358], whose mRNA expression was also induced after p31-43 treatment in hEGC-ClK cells. The role of GDNF is still controversial since its levels are enhanced in the inflamed mucosa of IBDs [213], but other studies revealed that its up-regulation is responsible for rescuing normal tissue homeostasis [260]. In this specific context, it is not clear whether GDNF expression acted as a compensatory mechanism. Further studies are needed to deeply investigate this aspect. The abovementioned results were partially confirmed on primary murine EGCs. Indeed, in these cells, p31-43 was not able to induce *GFAP* and *S100β* but an increase in *IL-6* mRNA levels was observed at 12 hours p.t. The discrepancy in the cellular response against p31-43 in human and primary murine EGCs could be explained by the lack of spontaneous mouse models of CD, as the case for dogs (Irish setters) or monkeys (Rhesus macaques). Indeed, rats and mice have to be induced to develop the classical hallmarks of CD: nowadays, different models based on rodents are available, e.g., germ-free Wistar AVN rats (in which gliadin is administered immediately after birth), sensitized Rag1-/-, NOD, and CD19-/- CVID mice, "dietary"-induced BALB/c mice, and transgenic mice [359], [360], [361]. Further experiments might focus on studying the cellular and molecular response in primary murine EGCs derived from a CD mouse model.

The activation of cellular defence mechanisms could explain the ability of EGCs to prevent cell death events and implement an inflammatory response after p31-43 treatment, as well as determine the increase in cell viability observed at the lowest concentration of the peptide. According to the collected results indicating oxidative stress after p31-43 treatment and considering that gliadin peptides can induce the antioxidant defence system regulated by Nrf2/Keap1 [317], the activation of the Nrf2 pathway was evaluated. This transcription factor is the master regulator of the antioxidant defence system and, under particular stimuli, is able to induce the expression of target genes, such as *HO-1*, *CAT*, *GST*, and *TXN*, which contain the antioxidant response element (ARE) in their promoter. Moreover, the involvement of this pathway in gut disorders was already discussed by our laboratory, suggesting that its modulation could represent a valuable therapeutic approach for IBDs and CD [362]. The ability of wheat-derived peptides to induce the Nrf2/Keap1 signaling pathway was already demonstrated by Wang and colleagues in Caco-2 cells [317]. The collected results confirmed the ability of p31-43 to activate Nrf2 in hECG-ClK cells and induce its translocation into the nucleus at 4 hours after treatment. Then, HO-1 and catalase protein expression was finely evaluated at 24 hours p.t.,

considering that preliminary results at 4 hours did not show any difference in HO-1 expression, thus suggesting a delay between Nrf2 activation and HO-1 induction. Immunoblotting and immunofluorescence analysis at 24 hours p.t. revealed an increase in HO-1 protein levels. Interestingly, catalase translocation to the nucleus and its role in nuclear protection after oxidative damage was described in the literature, which reports its involvement in the so-called "nuclear shield" together with other enzymes, e.g., glutathione peroxidase, and glutathione transferase [363], [364]. Accordingly, immunoblotting and immunofluorescence analysis revealed increased catalase expression after p31-43 administration and its translocation. Moreover, immunolabelling followed by TEM analysis using colloidal gold particles, showed that after p31-43 treatment catalase increases its presence in the nucleus. Finally, taking into account the interplay between the Nrf2 pathway and autophagy [325] as well as autophagy involvement in cellular response against gliadin [308], [326], [327], [328], [329], the protein expression levels of LC3-II were investigated. We observed alterations in LC3-II expression levels at 4 hours p.t., even if not significant; at 24 hours after treatment, no differences were detected. Further experiments using Bafilomycin A1 are needed to better understand the autophagic response against p31-43. Notably, proteomic analysis at 24 hours p.t. revealed an accumulation of LC3 compared with the relative control. The functional meaning of this increased expression requires further investigation. The proteomic analysis confirmed also the activation of protective mechanisms against oxidative stress: specifically, at 24 hours p.t. an enhancement in the levels of several anti-oxidant enzymes was observed (i.e., glutaredoxin-3, glutathione-S-transferase Mu 3, heme oxygenase-2, thioredoxin). The Reactome Enrichment analysis highlighted the up-regulation of proteins involved in cellular responses to stress, DNA repair (principally mediated by NER), and membrane trafficking. Mitochondrial damage was further underlined by the same analysis; particularly, p31-43 treatment led to the production of several mitochondrial chaperones, e.g., MICOS complex subunit MIC19, which play a key role in maintenance of mitochondrial crests [365], mitochondrial import inner membrane translocase subunit Tim10, a chaperon-like protein [366], mitochondrial import receptor subunit TOM22 homolog, a molecular shuttle together with TOM20 for P450 cytocrome [367], and mitochondrial chaperone BCS1, which is involved in the organelle homeostasis and in the formation of LETM1 complex [368], [369].

In conclusion, in this Thesis the first human enteric glial cell line was successfully generated and characterized, which may represent a valuable tool to bridge the gap in *in vitro* EGC knowledge. Hence, hEGC-ClK cells were used as an experimental model to test the effects of gluten-derived peptides (i.e., gliadin and p31-43) and assess their cytotoxicity. The collected results showed that gliadin induces oxidative stress in hEGCs, followed by mitochondrial damage, and finally resulting in caspase-mediated apoptosis. By contrast, p31-43 exerted milder cytotoxic effects on hEGCs, triggering gliosis and activation of the Nrf2/Keap1-mediated antioxidant defense

system. According with the evidence collected in literature, the p31-43 treatment was effective for the comprehension of EGCs' loss of homeostasis in CD in *in vitro* studies; indeed, the detrimental effect of whole digested gliadin could be due by the lack of the tissue microenvironment, thus pushing for further *in vivo* studies to validate these evidence. Considering the collected results, it is likely that EGCs interaction with cytotoxic peptides might induce shift into reactive glia phenotype during CD. Altogether our results might suggest a possible involvement of EGCs in CD pathogenesis, identifying enteric glia as a potential novel therapeutic target for the treatment of CD patients. However, further investigation is required to deeply elucidate the role of EGCs in CD onset and progression. Firstly, as *in vitro* analysis, the effects of other gliadin-derived peptides (i.e., the immunogenic peptide 33mer) will be tested on hEGC-ClK cells in order to elucidate their relative contribution to CD. Secondarily, as a translational approach, duodenal biopsies from CD patients at the time of diagnosis, CD patients following a GFD, and healthy related controls will be collected. Then, a quantification and characterization EGCs will be performed in order to identify differences in morphology, and tissue distribution in celiac patients versus healthy controls, further comparing the resultus obtained in *in vitro* experiments.

References

1. Ludvigsson, J.F., et al., *The Oslo definitions for coeliac disease and related terms.* Gut, 2013. **62**(1): p. 43-52.
2. Kamboj, A.K. and A.S. Oxentenko, *Clinical and Histologic Mimickers of Celiac Disease.* Clin Transl Gastroenterol, 2017. **8**(8): p. e114.
3. Singh, P., et al., *Global Prevalence of Celiac Disease: Systematic Review and Meta-analysis.* Clin Gastroenterol Hepatol, 2018. **16**(6): p. 823-836.e2.
4. Fukunaga, M., et al., *Serological screening for celiac disease in adults in Japan: Shimane CoHRE study.* JGH Open, 2020. **4**(4): p. 558-560.
5. Jansson-Knodell, C.L., et al., *Sex Difference in Celiac Disease in Undiagnosed Populations: A Systematic Review and Meta-analysis.* Clin Gastroenterol Hepatol, 2019. **17**(10): p. 1954-1968.e13.
6. Lindfors, K., et al., *Coeliac disease.* Nat Rev Dis Primers, 2019. **5**(1): p. 3.
7. King, J.A., et al., *Incidence of Celiac Disease Is Increasing Over Time: A Systematic Review and Meta-analysis.* Am J Gastroenterol, 2020. **115**(4): p. 507-525.
8. Sollid, L.M. and E. Thorsby, *HLA susceptibility genes in celiac disease: genetic mapping and role in pathogenesis.* Gastroenterology, 1993. **105**(3): p. 910-22.
9. Karell, K., et al., *HLA types in celiac disease patients not carrying the DQA1*05-DQB1*02 (DQ2) heterodimer: results from the European Genetics Cluster on Celiac Disease.* Hum Immunol, 2003. **64**(4): p. 469-77.
10. Kuja-Halkola, R., et al., *Heritability of non-HLA genetics in coeliac disease: a population-based study in 107 000 twins.* Gut, 2016. **65**(11): p. 1793-1798.
11. Ricano-Ponce, I., et al., *Immunochip meta-analysis in European and Argentinian populations identifies two novel genetic loci associated with celiac disease.* Eur J Hum Genet, 2020. **28**(3): p. 313-323.
12. Koletzko, S., et al., *Cesarean Section on the Risk of Celiac Disease in the Offspring: The Teddy Study.* J Pediatr Gastroenterol Nutr, 2018. **66**(3): p. 417-424.
13. Vriezinga, S.L., et al., *Randomized feeding intervention in infants at high risk for celiac disease.* N Engl J Med, 2014. **371**(14): p. 1304-15.
14. Lionetti, E., et al., *Introduction of gluten, HLA status, and the risk of celiac disease in children.* N Engl J Med, 2014. **371**(14): p. 1295-303.
15. Marild, K., et al., *Smoking in pregnancy, cord blood cotinine and risk of celiac disease diagnosis in offspring.* Eur J Epidemiol, 2019. **34**(7): p. 637-649.
16. Tapia, G., et al., *Parechovirus Infection in Early Childhood and Association With Subsequent Celiac Disease.* Am J Gastroenterol, 2021. **116**(4): p. 788-795.
17. Leonard, M.M., et al., *Multi-omics analysis reveals the influence of genetic and environmental risk factors on developing gut microbiota in infants at risk of celiac disease.* Microbiome, 2020. **8**(1): p. 130.
18. Lund-Blix, N.A., et al., *Maternal fibre and gluten intake during pregnancy and risk of childhood celiac disease: the MoBa study.* Sci Rep, 2020. **10**(1): p. 16439.
19. Andren Aronsson, C., et al., *Association of Gluten Intake During the First 5 Years of Life With Incidence of Celiac Disease Autoimmunity and Celiac Disease Among Children at Increased Risk.* JAMA, 2019. **322**(6): p. 514-523.
20. Lindfors, K., et al., *Metagenomics of the faecal virome indicate a cumulative effect of enterovirus and gluten amount on the risk of coeliac disease autoimmunity in genetically at risk children: the TEDDY study.* Gut, 2020. **69**(8): p. 1416-1422.
21. Stene, L.C., et al., *Rotavirus infection frequency and risk of celiac disease autoimmunity in early childhood: a longitudinal study.* Am J Gastroenterol, 2006. **101**(10): p. 2333-40.
22. Dydensborg Sander, S., et al., *Association Between Antibiotics in the First Year of Life and Celiac Disease.* Gastroenterology, 2019. **156**(8): p. 2217-2229.

23. Lebwohl, B., et al., *Use of proton pump inhibitors and subsequent risk of celiac disease.* Dig Liver Dis, 2014. **46**(1): p. 36-40.
24. Leonard, M.M., et al., *Microbiome signatures of progression toward celiac disease onset in at-risk children in a longitudinal prospective cohort study.* Proc Natl Acad Sci U S A, 2021. **118**(29).
25. Catassi, C., et al., *Coeliac disease.* Lancet, 2022. **399**(10344): p. 2413-2426.
26. Dieli-Crimi, R., M.C. Cenit, and C. Nunez, *The genetics of celiac disease: A comprehensive review of clinical implications.* J Autoimmun, 2015. **64**: p. 26-41.
27. Schumann, M., et al., *Mechanisms of epithelial translocation of the alpha(2)-gliadin-33mer in coeliac sprue.* Gut, 2008. **57**(6): p. 747-54.
28. Barone, M.V. and K.P. Zimmer, *Endocytosis and transcytosis of gliadin peptides.* Mol Cell Pediatr, 2016. **3**(1): p. 8.
29. Di Sabatino, A. and G.R. Corazza, *Coeliac disease.* Lancet, 2009. **373**(9673): p. 1480-93.
30. Mention, J.J., et al., *Interleukin 15: a key to disrupted intraepithelial lymphocyte homeostasis and lymphomagenesis in celiac disease.* Gastroenterology, 2003. **125**(3): p. 730-45.
31. Meresse, B., et al., *Reprogramming of CTLs into natural killer-like cells in celiac disease.* J Exp Med, 2006. **203**(5): p. 1343-55.
32. Meresse, B., et al., *Coordinated induction by IL15 of a TCR-independent NKG2D signaling pathway converts CTL into lymphokine-activated killer cells in celiac disease.* Immunity, 2004. **21**(3): p. 357-66.
33. Jabri, B. and L.M. Sollid, *T Cells in Celiac Disease.* J Immunol, 2017. **198**(8): p. 3005-3014.
34. Fasano, A. and C. Catassi, *Clinical practice. Celiac disease.* N Engl J Med, 2012. **367**(25): p. 2419-26.
35. Catassi, G.N., et al., *A negative fallout of COVID-19 lockdown in Italy: Life-threatening delay in the diagnosis of celiac disease.* Dig Liver Dis, 2020. **52**(10): p. 1092-1093.
36. Therrien, A., C.P. Kelly, and J.A. Silvester, *Celiac Disease: Extraintestinal Manifestations and Associated Conditions.* J Clin Gastroenterol, 2020. **54**(1): p. 8-21.
37. Stefanelli, G., et al., *Persistent Iron Deficiency Anemia in Patients with Celiac Disease Despite a Gluten-Free Diet.* Nutrients, 2020. **12**(8).
38. Mearns, E.S., et al., *Neurological Manifestations of Neuropathy and Ataxia in Celiac Disease: A Systematic Review.* Nutrients, 2019. **11**(2).
39. Reunala, T., K. Hervonen, and T. Salmi, *Dermatitis Herpetiformis: An Update on Diagnosis and Management.* Am J Clin Dermatol, 2021. **22**(3): p. 329-338.
40. Di Sabatino, A., et al., *Splenic hypofunction and the spectrum of autoimmune and malignant complications in celiac disease.* Clin Gastroenterol Hepatol, 2006. **4**(2): p. 179-86.
41. Taczanowska, A., et al., *Celiac disease in children with type 1 diabetes varies around the world: An international, cross-sectional study of 57 375 patients from the SWEET registry.* J Diabetes, 2021. **13**(6): p. 448-457.
42. Elfstrom, P., et al., *Risk of thyroid disease in individuals with celiac disease.* J Clin Endocrinol Metab, 2008. **93**(10): p. 3915-21.
43. Efe, C., et al., *Extrahepatic autoimmune diseases in primary biliary cholangitis: Prevalence and significance for clinical presentation and disease outcome.* J Gastroenterol Hepatol, 2021. **36**(4): p. 936-942.
44. Bartoloni, E., et al., *Celiac Disease Prevalence is Increased in Primary Sjogren's Syndrome and Diffuse Systemic Sclerosis: Lessons from a Large Multi-Center Study.* J Clin Med, 2019. **8**(4).
45. Pinto-Sanchez, M.I., et al., *Association Between Inflammatory Bowel Diseases and Celiac Disease: A Systematic Review and Meta-Analysis.* Gastroenterology, 2020. **159**(3): p. 884-903 e31.
46. Stewart, M., et al., *The association of coeliac disease and microscopic colitis: a large population-based study.* Aliment Pharmacol Ther, 2011. **33**(12): p. 1340-9.

47. Wang, N., et al., *Serological assessment for celiac disease in IgA deficient adults.* PLoS One, 2014. **9**(4): p. e93180.
48. Liu, E., et al., *Routine Screening for Celiac Disease in Children With Down Syndrome Improves Case Finding.* J Pediatr Gastroenterol Nutr, 2020. **71**(2): p. 252-256.
49. Al-Bluwi, G.S.M., et al., *Prevalence of Celiac Disease in Patients With Turner Syndrome: Systematic Review and Meta-Analysis.* Front Med (Lausanne), 2021. **8**: p. 674896.
50. Pangallo, E., et al., *Williams-Beuren Syndrome and celiac disease: A real association?* Eur J Med Genet, 2020. **63**(9): p. 103999.
51. Gatti, S., et al., *Increased Prevalence of Celiac Disease in School-age Children in Italy.* Clin Gastroenterol Hepatol, 2020. **18**(3): p. 596-603.
52. Husby, S., et al., *European Society Paediatric Gastroenterology, Hepatology and Nutrition Guidelines for Diagnosing Coeliac Disease 2020.* J Pediatr Gastroenterol Nutr, 2020. **70**(1): p. 141-156.
53. Husby, S., J.A. Murray, and D.A. Katzka, *AGA Clinical Practice Update on Diagnosis and Monitoring of Celiac Disease-Changing Utility of Serology and Histologic Measures: Expert Review.* Gastroenterology, 2019. **156**(4): p. 885-889.
54. Al-Toma, A., et al., *European Society for the Study of Coeliac Disease (ESsCD) guideline for coeliac disease and other gluten-related disorders.* United European Gastroenterol J, 2019. **7**(5): p. 583-613.
55. Bai, J.C., et al., *World Gastroenterology Organisation global guidelines on celiac disease.* J Clin Gastroenterol, 2013. **47**(2): p. 121-6.
56. Hill, I.D., et al., *NASPGHAN Clinical Report on the Diagnosis and Treatment of Gluten-related Disorders.* J Pediatr Gastroenterol Nutr, 2016. **63**(1): p. 156-65.
57. Holmes, G. and C. Ciacci, *The serological diagnosis of coeliac disease - a step forward.* Gastroenterol Hepatol Bed Bench, 2018. **11**(3): p. 209-215.
58. Previtali, G., et al., *Celiac Disease Diagnosis Without Biopsy: Is a 10x ULN Antitransglutaminase Result Suitable for a Chemiluminescence Method?* J Pediatr Gastroenterol Nutr, 2018. **66**(4): p. 645-650.
59. Oberhuber, G., *Histopathology of celiac disease.* Biomed Pharmacother, 2000. **54**(7): p. 368-72.
60. Catassi, C., I. Bearzi, and G.K. Holmes, *Association of celiac disease and intestinal lymphomas and other cancers.* Gastroenterology, 2005. **128**(4 Suppl 1): p. S79-86.
61. Lebwohl, B., et al., *Association Between Celiac Disease and Mortality Risk in a Swedish Population.* JAMA, 2020. **323**(13): p. 1277-1285.
62. Lebwohl, B., et al., *Cancer Risk in 47,241 Individuals With Celiac Disease: A Nationwide Cohort Study.* Clin Gastroenterol Hepatol, 2022. **20**(2): p. e111-e131.
63. Ludvigsson, J.F., *Mortality and malignancy in celiac disease.* Gastrointest Endosc Clin N Am, 2012. **22**(4): p. 705-22.
64. Emilsson, L., et al., *Risk of Small Bowel Adenocarcinoma, Adenomas, and Carcinoids in a Nationwide Cohort of Individuals With Celiac Disease.* Gastroenterology, 2020. **159**(5): p. 1686-1694 e2.
65. Caio, G., et al., *Small bowel adenocarcinoma as a complication of celiac disease: clinical and diagnostic features.* BMC Gastroenterol, 2019. **19**(1): p. 45.
66. Wieser, H., et al., *Food Safety and Cross-Contamination of Gluten-Free Products: A Narrative Review.* Nutrients, 2021. **13**(7).
67. Catassi, C., et al., *A prospective, double-blind, placebo-controlled trial to establish a safe gluten threshold for patients with celiac disease.* Am J Clin Nutr, 2007. **85**(1): p. 160-6.
68. Verma, A.K., et al., *Gluten Contamination in Naturally or Labeled Gluten-Free Products Marketed in Italy.* Nutrients, 2017. **9**(2).
69. Moller, S.P., et al., *Systematic review: Exploration of the impact of psychosocial factors on quality of life in adults living with coeliac disease.* J Psychosom Res, 2021. **147**: p. 110537.

70. White, L.E., E. Bannerman, and P.M. Gillett, *Coeliac disease and the gluten-free diet: a review of the burdens; factors associated with adherence and impact on health-related quality of life, with specific focus on adolescence.* J Hum Nutr Diet, 2016. **29**(5): p. 593-606.
71. Vici, G., et al., *Gluten free diet and nutrient deficiencies: A review.* Clin Nutr, 2016. **35**(6): p. 1236-1241.
72. Stein, A.C., et al., *Obesity and Cardiovascular Risk in Adults With Celiac Disease.* J Clin Gastroenterol, 2016. **50**(7): p. 545-50.
73. Shewry, P.R. and N.G. Halford, *Cereal seed storage proteins: structures, properties and role in grain utilization.* J Exp Bot, 2002. **53**(370): p. 947-58.
74. Wieser, H., *Chemistry of gluten proteins.* Food Microbiol, 2007. **24**(2): p. 115-9.
75. Wieser, H., *Relation between gliadin structure and coeliac toxicity.* Acta Paediatr Suppl, 1996. **412**: p. 3-9.
76. Shewry, P.R., N.G. Halford, and D. Lafiandra, *Genetics of wheat gluten proteins.* Adv Genet, 2003. **49**: p. 111-84.
77. Matsuo, H., T. Yokooji, and T. Taogoshi, *Common food allergens and their IgE-binding epitopes.* Allergol Int, 2015. **64**(4): p. 332-43.
78. Ciccocioppo, R., A. Di Sabatino, and G.R. Corazza, *The immune recognition of gluten in coeliac disease.* Clin Exp Immunol, 2005. **140**(3): p. 408-16.
79. Molberg, O., et al., *Mapping of gluten T-cell epitopes in the bread wheat ancestors: implications for celiac disease.* Gastroenterology, 2005. **128**(2): p. 393-401.
80. Arentz-Hansen, H., et al., *The intestinal T cell response to alpha-gliadin in adult celiac disease is focused on a single deamidated glutamine targeted by tissue transglutaminase.* J Exp Med, 2000. **191**(4): p. 603-12.
81. Sollid, L.M., et al., *Nomenclature and listing of celiac disease relevant gluten T-cell epitopes restricted by HLA-DQ molecules.* Immunogenetics, 2012. **64**(6): p. 455-60.
82. Xia, J., et al., *Inhibition of HLA-DQ2-mediated antigen presentation by analogues of a high affinity 33-residue peptide from alpha2-gliadin.* J Am Chem Soc, 2006. **128**(6): p. 1859-67.
83. Shan, L., et al., *Structural basis for gluten intolerance in celiac sprue.* Science, 2002. **297**(5590): p. 2275-9.
84. Thomas, K.E., et al., *Gliadin stimulation of murine macrophage inflammatory gene expression and intestinal permeability are MyD88-dependent: role of the innate immune response in Celiac disease.* J Immunol, 2006. **176**(4): p. 2512-21.
85. Herrera, M.G., et al., *Circular dichroism and electron microscopy studies in vitro of 33-mer gliadin peptide revealed secondary structure transition and supramolecular organization.* Biopolymers, 2014. **101**(1): p. 96-106.
86. Herrera, M.G., et al., *Self-assembly of 33-mer gliadin peptide oligomers.* Soft Matter, 2015. **11**(44): p. 8648-60.
87. Herrera, M.G., T.V. Veuthey, and V.I. Dodero, *Self-organization of gliadin in aqueous media under physiological digestive pHs.* Colloids Surf B Biointerfaces, 2016. **141**: p. 565-575.
88. Herrera, M.G., et al., *Insights into gliadin supramolecular organization at digestive pH 3.0.* Colloids Surf B Biointerfaces, 2018. **165**: p. 363-370.
89. Herrera, M.G., et al., *Large supramolecular structures of 33-mer gliadin peptide activate toll-like receptors in macrophages.* Nanomedicine, 2018. **14**(4): p. 1417-1427.
90. Amundarain, M.J., et al., *Molecular mechanisms of 33-mer gliadin peptide oligomerisation.* Phys Chem Chem Phys, 2019. **21**(40): p. 22539-22552.
91. Escudero-Hernandez, C., et al., *Circulating Dendritic Cells from Celiac Disease Patients Display a Gut-Homing Profile and are Differentially Modulated by Different Gliadin-Derived Peptides.* Mol Nutr Food Res, 2020. **64**(6): p. e1900989.
92. Shan, L., et al., *Identification and analysis of multivalent proteolytically resistant peptides from gluten: implications for celiac sprue.* J Proteome Res, 2005. **4**(5): p. 1732-41.
93. Mamone, G., et al., *Identification of a peptide from alpha-gliadin resistant to digestive enzymes: implications for celiac disease.* J Chromatogr B Analyt Technol Biomed Life Sci, 2007. **855**(2): p. 236-41.

94. Clemente, M.G., et al., *Early effects of gliadin on enterocyte intracellular signalling involved in intestinal barrier function.* Gut, 2003. **52**(2): p. 218-23.
95. Maiuri, L., et al., *Association between innate response to gliadin and activation of pathogenic T cells in coeliac disease.* Lancet, 2003. **362**(9377): p. 30-7.
96. Barone, M.V., et al., *Growth factor-like activity of gliadin, an alimentary protein: implications for coeliac disease.* Gut, 2007. **56**(4): p. 480-8.
97. Barone, M.V., et al., *Gliadin-mediated proliferation and innate immune activation in celiac disease are due to alterations in vesicular trafficking.* PLoS One, 2011. **6**(2): p. e17039.
98. Luciani, A., et al., *Lysosomal accumulation of gliadin p31-43 peptide induces oxidative stress and tissue transglutaminase-mediated PPARgamma downregulation in intestinal epithelial cells and coeliac mucosa.* Gut, 2010. **59**(3): p. 311-9.
99. Gomez Castro, M.F., et al., *p31-43 Gliadin Peptide Forms Oligomers and Induces NLRP3 Inflammasome/Caspase 1- Dependent Mucosal Damage in Small Intestine.* Front Immunol, 2019. **10**: p. 31.
100. Paolella, G., et al., *The toxic alpha-gliadin peptide 31-43 enters cells without a surface membrane receptor.* Cell Biol Int, 2018. **42**(1): p. 112-120.
101. Herrera, M.G., et al., *Structural conformation and self-assembly process of p31-43 gliadin peptide in aqueous solution. Implications for celiac disease.* FEBS J, 2020. **287**(10): p. 2134-2149.
102. Calvanese, L., et al., *Structural insights on P31-43, a gliadin peptide able to promote an innate but not an adaptive response in celiac disease.* J Pept Sci, 2019. **25**(5): p. e3161.
103. Martucciello, S., et al., *Interplay between Type 2 Transglutaminase (TG2), Gliadin Peptide 31-43 and Anti-TG2 Antibodies in Celiac Disease.* Int J Mol Sci, 2020. **21**(10).
104. Zioudrou, C., R.A. Streaty, and W.A. Klee, *Opioid peptides derived from food proteins. The exorphins.* J Biol Chem, 1979. **254**(7): p. 2446-9.
105. Fukudome, S. and M. Yoshikawa, *Opioid peptides derived from wheat gluten: their isolation and characterization.* FEBS Lett, 1992. **296**(1): p. 107-11.
106. Fukudome, S. and M. Yoshikawa, *Gluten exorphin C. A novel opioid peptide derived from wheat gluten.* FEBS Lett, 1993. **316**(1): p. 17-9.
107. Fukudome, S., et al., *Release of opioid peptides, gluten exorphins by the action of pancreatic elastase.* FEBS Lett, 1997. **412**(3): p. 475-9.
108. Tovoli, F., et al., *Clinical and diagnostic aspects of gluten related disorders.* World J Clin Cases, 2015. **3**(3): p. 275-84.
109. Fukudome, S., et al., *Effect of gluten exorphins A5 and B5 on the postprandial plasma insulin level in conscious rats.* Life Sci, 1995. **57**(7): p. 729-34.
110. Takahashi, M., et al., *Behavioral and pharmacological studies on gluten exorphin A5, a newly isolated bioactive food protein fragment, in mice.* Jpn J Pharmacol, 2000. **84**(3): p. 259-65.
111. Pruimboom, L. and K. de Punder, *The opioid effects of gluten exorphins: asymptomatic celiac disease.* J Health Popul Nutr, 2015. **33**: p. 24.
112. Manai, F., et al., *Gluten Exorphins Promote Cell Proliferation through the Activation of Mitogenic and Pro-Survival Pathways.* Int J Mol Sci, 2023. **24**(4).
113. Kang, Y.N., C. Fung, and P. Vanden Berghe, *Gut innervation and enteric nervous system development: a spatial, temporal and molecular tour de force.* Development, 2021. **148**(3).
114. Sharkey, K.A. and G.M. Mawe, *The enteric nervous system.* Physiol Rev, 2023. **103**(2): p. 1487-1564.
115. Grundy, D. and M. Schemann, *Enteric nervous system.* Curr Opin Gastroenterol, 2007. **23**(2): p. 121-6.
116. Christensen, J. and G.A. Rick, *Intrinsic nerves in the mammalian colon: confirmation of a plexus at the circular muscle-submucosal interface.* J Auton Nerv Syst, 1987. **21**(2-3): p. 223-31.
117. Fang, S., R. Wu, and J. Christensen, *Intramucosal nerve cells in human small intestine.* J Auton Nerv Syst, 1993. **44**(2-3): p. 129-36.

118. Brehmer, A., H. Rupprecht, and W. Neuhuber, *Two submucosal nerve plexus in human intestines.* Histochem Cell Biol, 2010. **133**(2): p. 149-61.
119. Sanders, K.M., S.J. Hwang, and S.M. Ward, *Neuroeffector apparatus in gastrointestinal smooth muscle organs.* J Physiol, 2010. **588**(Pt 23): p. 4621-39.
120. Spencer, N.J., et al., *Insights into the mechanisms underlying colonic motor patterns.* J Physiol, 2016. **594**(15): p. 4099-116.
121. Smith, T.K. and S.D. Koh, *A model of the enteric neural circuitry underlying the generation of rhythmic motor patterns in the colon: the role of serotonin.* Am J Physiol Gastrointest Liver Physiol, 2017. **312**(1): p. G1-G14.
122. Furness, J.B., et al., *The enteric nervous system and gastrointestinal innervation: integrated local and central control.* Adv Exp Med Biol, 2014. **817**: p. 39-71.
123. Vanner, S. and W.K. Macnaughton, *Submucosal secretomotor and vasodilator reflexes.* Neurogastroenterol Motil, 2004. **16 Suppl 1**: p. 39-43.
124. Furness, J.B., *Types of neurons in the enteric nervous system.* J Auton Nerv Syst, 2000. **81**(1-3): p. 87-96.
125. Anlauf, M., et al., *Chemical coding of the human gastrointestinal nervous system: cholinergic, VIPergic, and catecholaminergic phenotypes.* J Comp Neurol, 2003. **459**(1): p. 90-111.
126. Gershon, M.D. and J. Tack, *The serotonin signaling system: from basic understanding to drug development for functional GI disorders.* Gastroenterology, 2007. **132**(1): p. 397-414.
127. McLean, P.G., R.A. Borman, and K. Lee, *5-HT in the enteric nervous system: gut function and neuropharmacology.* Trends Neurosci, 2007. **30**(1): p. 9-13.
128. Auteri, M., M.G. Zizzo, and R. Serio, *GABA and GABA receptors in the gastrointestinal tract: from motility to inflammation.* Pharmacol Res, 2015. **93**: p. 11-21.
129. Michel, K., et al., *How big is the little brain in the gut? Neuronal numbers in the enteric nervous system of mice, Guinea pig, and human.* Neurogastroenterol Motil, 2022. **34**(12): p. e14440.
130. Seguella, L. and B.D. Gulbransen, *Enteric glial biology, intercellular signalling and roles in gastrointestinal disease.* Nat Rev Gastroenterol Hepatol, 2021. **18**(8): p. 571-587.
131. Boesmans, W., et al., *Development, Diversity, and Neurogenic Capacity of Enteric Glia.* Front Cell Dev Biol, 2021. **9**: p. 775102.
132. Liu, C. and J. Yang, *Enteric Glial Cells in Immunological Disorders of the Gut.* Front Cell Neurosci, 2022. **16**: p. 895871.
133. Xu, Q., T. Heanue, and V. Pachnis, *Travelling within the fetal gut: simple rules for an arduous journey.* BMC Biol, 2014. **12**: p. 50.
134. Rao, M. and M.D. Gershon, *Enteric nervous system development: what could possibly go wrong?* Nat Rev Neurosci, 2018. **19**(9): p. 552-565.
135. Heuckeroth, R.O., *Hirschsprung disease - integrating basic science and clinical medicine to improve outcomes.* Nat Rev Gastroenterol Hepatol, 2018. **15**(3): p. 152-167.
136. Goldstein, A.M. and N. Nagy, *A bird's eye view of enteric nervous system development: lessons from the avian embryo.* Pediatr Res, 2008. **64**(4): p. 326-33.
137. Wallace, A.S. and A.J. Burns, *Development of the enteric nervous system, smooth muscle and interstitial cells of Cajal in the human gastrointestinal tract.* Cell Tissue Res, 2005. **319**(3): p. 367-82.
138. Fu, M., et al., *HOXB5 expression is spatially and temporarily regulated in human embryonic gut during neural crest cell colonization and differentiation of enteric neuroblasts.* Dev Dyn, 2003. **228**(1): p. 1-10.
139. Obermayr, F., et al., *Development and developmental disorders of the enteric nervous system.* Nat Rev Gastroenterol Hepatol, 2013. **10**(1): p. 43-57.
140. Nishiyama, C., et al., *Trans-mesenteric neural crest cells are the principal source of the colonic enteric nervous system.* Nat Neurosci, 2012. **15**(9): p. 1211-8.
141. Wang, X., et al., *Analysis of the sacral neural crest cell contribution to the hindgut enteric nervous system in the mouse embryo.* Gastroenterology, 2011. **141**(3): p. 992-1002 e1-6.

142. Hao, M.M., et al., *Development of the intrinsic innervation of the small bowel mucosa and villi.* Am J Physiol Gastrointest Liver Physiol, 2020. **318**(1): p. G53-G65.
143. Uesaka, T., M. Nagashimada, and H. Enomoto, *GDNF signaling levels control migration and neuronal differentiation of enteric ganglion precursors.* J Neurosci, 2013. **33**(41): p. 16372-82.
144. Roberts, R.R., et al., *The first intestinal motility patterns in fetal mice are not mediated by neurons or interstitial cells of Cajal.* J Physiol, 2010. **588**(Pt 7): p. 1153-69.
145. Foong, J.P., et al., *Myenteric neurons of the mouse small intestine undergo significant electrophysiological and morphological changes during postnatal development.* J Physiol, 2012. **590**(10): p. 2375-90.
146. Pawolski, V. and M.H.H. Schmidt, *Neuron-Glia Interaction in the Developing and Adult Enteric Nervous System.* Cells, 2020. **10**(1).
147. Southard-Smith, E.M., L. Kos, and W.J. Pavan, *Sox10 mutation disrupts neural crest development in Dom Hirschsprung mouse model.* Nat Genet, 1998. **18**(1): p. 60-4.
148. Lang, D., et al., *Pax3 is required for enteric ganglia formation and functions with Sox10 to modulate expression of c-ret.* J Clin Invest, 2000. **106**(8): p. 963-71.
149. Lang, D. and J.A. Epstein, *Sox10 and Pax3 physically interact to mediate activation of a conserved c-RET enhancer.* Hum Mol Genet, 2003. **12**(8): p. 937-45.
150. Chatterjee, S., et al., *A multi-enhancer RET regulatory code is disrupted in Hirschsprung disease.* Genome Res, 2021. **31**(12): p. 2199-208.
151. Zhu, L., et al., *Spatiotemporal regulation of endothelin receptor-B by SOX10 in neural crest-derived enteric neuron precursors.* Nat Genet, 2004. **36**(7): p. 732-7.
152. Mollaaghababa, R. and W.J. Pavan, *The importance of having your SOX on: role of SOX10 in the development of neural crest-derived melanocytes and glia.* Oncogene, 2003. **22**(20): p. 3024-34.
153. Pan, S.F., et al., *Trisomy of chromosome 20.* Clin Genet, 1976. **9**(5): p. 449-53.
154. Okamura, Y. and Y. Saga, *Notch signaling is required for the maintenance of enteric neural crest progenitors.* Development, 2008. **135**(21): p. 3555-65.
155. Bray, S.J., *Notch signalling in context.* Nat Rev Mol Cell Biol, 2016. **17**(11): p. 722-735.
156. Heanue, T.A. and V. Pachnis, *Enteric nervous system development and Hirschsprung's disease: advances in genetic and stem cell studies.* Nat Rev Neurosci, 2007. **8**(6): p. 466-79.
157. Avetisyan, M., E.M. Schill, and R.O. Heuckeroth, *Building a second brain in the bowel.* J Clin Invest, 2015. **125**(3): p. 899-907.
158. Angrist, M., et al., *Germline mutations in glial cell line-derived neurotrophic factor (GDNF) and RET in a Hirschsprung disease patient.* Nat Genet, 1996. **14**(3): p. 341-4.
159. Wang, H., et al., *The timing and location of glial cell line-derived neurotrophic factor expression determine enteric nervous system structure and function.* J Neurosci, 2010. **30**(4): p. 1523-38.
160. Mundell, N.A. and P.A. Labosky, *Neural crest stem cell multipotency requires Foxd3 to maintain neural potential and repress mesenchymal fates.* Development, 2011. **138**(4): p. 641-52.
161. Mundell, N.A., et al., *Enteric nervous system specific deletion of Foxd3 disrupts glial cell differentiation and activates compensatory enteric progenitors.* Dev Biol, 2012. **363**(2): p. 373-87.
162. Bergeron, K.F., et al., *Upregulation of the Nr2f1-A830082K12Rik gene pair in murine neural crest cells results in a complex phenotype reminiscent of Waardenburg syndrome type 4.* Dis Model Mech, 2016. **9**(11): p. 1283-1293.
163. Hanani, M. and A. Reichenbach, *Morphology of horseradish peroxidase (HRP)-injected glial cells in the myenteric plexus of the guinea-pig.* Cell Tissue Res, 1994. **278**(1): p. 153-60.
164. Boesmans, W., et al., *Heterogeneity and phenotypic plasticity of glial cells in the mammalian enteric nervous system.* Glia, 2015. **63**(2): p. 229-41.
165. Scavuzzo, M.A., et al., *Enteric glial hub cells coordinate intestinal motility.* bioRxiv, 2023.

166. Seguella, L., et al., *Functional Intraregional and Interregional Heterogeneity between Myenteric Glial Cells of the Colon and Duodenum in Mice.* J Neurosci, 2022. **42**(46): p. 8694-8708.
167. Zeisel, A., et al., *Molecular Architecture of the Mouse Nervous System.* Cell, 2018. **174**(4): p. 999-1014 e22.
168. Drokhlyansky, E., et al., *The Human and Mouse Enteric Nervous System at Single-Cell Resolution.* Cell, 2020. **182**(6): p. 1606-1622 e23.
169. Rao, M., et al., *Enteric glia express proteolipid protein 1 and are a transcriptionally unique population of glia in the mammalian nervous system.* Glia, 2015. **63**(11): p. 2040-2057.
170. Delvalle, N.M., et al., *Communication Between Enteric Neurons, Glia, and Nociceptors Underlies the Effects of Tachykinins on Neuroinflammation.* Cell Mol Gastroenterol Hepatol, 2018. **6**(3): p. 321-344.
171. Jessen, K.R., R. Thorpe, and R. Mirsky, *Molecular identity, distribution and heterogeneity of glial fibrillary acidic protein: an immunoblotting and immunohistochemical study of Schwann cells, satellite cells, enteric glia and astrocytes.* J Neurocytol, 1984. **13**(2): p. 187-200.
172. Park, Y.M., et al., *Astrocyte Specificity and Coverage of hGFAP-CreERT2 [Tg(GFAP-Cre/ERT2)13Kdmc] Mouse Line in Various Brain Regions.* Exp Neurobiol, 2018. **27**(6): p. 508-525.
173. Zhang, Z., et al., *The Appropriate Marker for Astrocytes: Comparing the Distribution and Expression of Three Astrocytic Markers in Different Mouse Cerebral Regions.* Biomed Res Int, 2019. **2019**: p. 9605265.
174. Jessen, K.R. and R. Mirsky, *Glial fibrillary acidic polypeptides in peripheral glia. Molecular weight, heterogeneity and distribution.* J Neuroimmunol, 1985. **8**(4-6): p. 377-93.
175. Guyer, R.A., et al., *Single-cell multiome sequencing clarifies enteric glial diversity and identifies an intraganglionic population poised for neurogenesis.* Cell Rep, 2023. **42**(3): p. 112194.
176. Gabella, G., *Fine structure of the myenteric plexus in the guinea-pig ileum.* J Anat, 1972. **111**(Pt 1): p. 69-97.
177. Boesmans, W., et al., *Structurally defined signaling in neuro-glia units in the enteric nervous system.* Glia, 2019. **67**(6): p. 1167-1178.
178. Broadhead, M.J., et al., *Ca2+ transients in myenteric glial cells during the colonic migrating motor complex in the isolated murine large intestine.* J Physiol, 2012. **590**(2): p. 335-50.
179. Kimball, B.C. and M.W. Mulholland, *Enteric glia exhibit P2U receptors that increase cytosolic calcium by a phospholipase C-dependent mechanism.* J Neurochem, 1996. **66**(2): p. 604-12.
180. Gomes, P., et al., *ATP-dependent paracrine communication between enteric neurons and glia in a primary cell culture derived from embryonic mice.* Neurogastroenterol Motil, 2009. **21**(8): p. 870-e62.
181. Boesmans, W., M.M. Hao, and P. Vanden Berghe, *Optical Tools to Investigate Cellular Activity in the Intestinal Wall.* J Neurogastroenterol Motil, 2015. **21**(3): p. 337-51.
182. Gulbransen, B.D. and K.A. Sharkey, *Purinergic neuron-to-glia signaling in the enteric nervous system.* Gastroenterology, 2009. **136**(4): p. 1349-58.
183. Brown, I.A., et al., *Enteric glia mediate neuron death in colitis through purinergic pathways that require connexin-43 and nitric oxide.* Cell Mol Gastroenterol Hepatol, 2016. **2**(1): p. 77-91.
184. McClain, J., et al., *Ca2+ responses in enteric glia are mediated by connexin-43 hemichannels and modulate colonic transit in mice.* Gastroenterology, 2014. **146**(2): p. 497-507 e1.
185. Cabarrocas, J., T.C. Savidge, and R.S. Liblau, *Role of enteric glial cells in inflammatory bowel disease.* Glia, 2003. **41**(1): p. 81-93.
186. Verkhratsky, A. and M. Nedergaard, *Physiology of Astroglia.* Physiol Rev, 2018. **98**(1): p. 239-389.

187. Ruhl, A., et al., *Functional expression of the peptide transporter PEPT2 in the mammalian enteric nervous system.* J Comp Neurol, 2005. **490**(1): p. 1-11.
188. Fletcher, E.L., M.J. Clark, and J.B. Furness, *Neuronal and glial localization of GABA transporter immunoreactivity in the myenteric plexus.* Cell Tissue Res, 2002. **308**(3): p. 339-46.
189. Lavoie, E.G., et al., *Ectonucleotidases in the digestive system: focus on NTPDase3 localization.* Am J Physiol Gastrointest Liver Physiol, 2011. **300**(4): p. G608-20.
190. Grubisic, V., et al., *NTPDase1 and -2 are expressed by distinct cellular compartments in the mouse colon and differentially impact colonic physiology and function after DSS colitis.* Am J Physiol Gastrointest Liver Physiol, 2019. **317**(3): p. G314-G332.
191. Braun, N., et al., *Association of the ecto-ATPase NTPDase2 with glial cells of the peripheral nervous system.* Glia, 2004. **45**(2): p. 124-32.
192. Fried, D.E., et al., *Ammonia modifies enteric neuromuscular transmission through glial gamma-aminobutyric acid signaling.* Am J Physiol Gastrointest Liver Physiol, 2017. **313**(6): p. G570-G580.
193. Puchalski, Z., *[Anxiety pattern in patients with alopecia areata, rosacea and lichen planus].* Przegl Dermatol, 1983. **70**(5-6): p. 521-6.
194. Spencer, N.J. and H. Hu, *Enteric nervous system: sensory transduction, neural circuits and gastrointestinal motility.* Nat Rev Gastroenterol Hepatol, 2020. **17**(6): p. 338-351.
195. Soret, R., et al., *Glial Cell-Derived Neurotrophic Factor Induces Enteric Neurogenesis and Improves Colon Structure and Function in Mouse Models of Hirschsprung Disease.* Gastroenterology, 2020. **159**(5): p. 1824-1838 e17.
196. Magnusson, F.C., et al., *Direct presentation of antigen by lymph node stromal cells protects against CD8 T-cell-mediated intestinal autoimmunity.* Gastroenterology, 2008. **134**(4): p. 1028-37.
197. Cornet, A., et al., *Enterocolitis induced by autoimmune targeting of enteric glial cells: a possible mechanism in Crohn's disease?* Proc Natl Acad Sci U S A, 2001. **98**(23): p. 13306-11.
198. Bush, T.G., et al., *Fulminant jejuno-ileitis following ablation of enteric glia in adult transgenic mice.* Cell, 1998. **93**(2): p. 189-201.
199. Aikawa, H. and K. Suzuki, *Lesions in the skin, intestine, and central nervous system induced by an antimetabolite of niacin.* Am J Pathol, 1986. **122**(2): p. 335-42.
200. Aikawa, H. and K. Suzuki, *Enteric gliopathy in niacin-deficiency induced by CNS glio-toxin.* Brain Res, 1985. **334**(2): p. 354-6.
201. Rao, M., et al., *Enteric Glia Regulate Gastrointestinal Motility but Are Not Required for Maintenance of the Epithelium in Mice.* Gastroenterology, 2017. **153**(4): p. 1068-1081 e7.
202. Matheis, F., et al., *Adrenergic Signaling in Muscularis Macrophages Limits Infection-Induced Neuronal Loss.* Cell, 2020. **180**(1): p. 64-78 e16.
203. Joseph, N.M., et al., *Enteric glia are multipotent in culture but primarily form glia in the adult rodent gut.* J Clin Invest, 2011. **121**(9): p. 3398-411.
204. Laranjeira, C., et al., *Glial cells in the mouse enteric nervous system can undergo neurogenesis in response to injury.* J Clin Invest, 2011. **121**(9): p. 3412-24.
205. De Schepper, S., et al., *Self-Maintaining Gut Macrophages Are Essential for Intestinal Homeostasis.* Cell, 2018. **175**(2): p. 400-415 e13.
206. Obata, Y., et al., *Neuronal programming by microbiota regulates intestinal physiology.* Nature, 2020. **578**(7794): p. 284-289.
207. Drossman, D.A., *Functional Gastrointestinal Disorders: History, Pathophysiology, Clinical Features and Rome IV.* Gastroenterology, 2016.
208. Phillips, R.J., E.J. Kieffer, and T.L. Powley, *Loss of glia and neurons in the myenteric plexus of the aged Fischer 344 rat.* Anat Embryol (Berl), 2004. **209**(1): p. 19-30.
209. Camilleri, M., T. Cowen, and T.R. Koch, *Enteric neurodegeneration in ageing.* Neurogastroenterol Motil, 2008. **20**(4): p. 418-29.
210. Saffrey, M.J., *Aging of the mammalian gastrointestinal tract: a complex organ system.* Age (Dordr), 2014. **36**(3): p. 9603.

211. Bon-Frauches, A.C. and W. Boesmans, *The enteric nervous system: the hub in a star network.* Nat Rev Gastroenterol Hepatol, 2020. **17**(12): p. 717-718.
212. Rosenbaum, C., et al., *Activation of Myenteric Glia during Acute Inflammation In Vitro and In Vivo.* PLoS One, 2016. **11**(3): p. e0151335.
213. Pochard, C., et al., *The multiple faces of inflammatory enteric glial cells: is Crohn's disease a gliopathy?* Am J Physiol Gastrointest Liver Physiol, 2018. **315**(1): p. G1-G11.
214. Scott, N.A., et al., *Carcinoma of the anal canal and flow cytometric DNA analysis.* Br J Cancer, 1989. **60**(1): p. 56-8.
215. Rosenberg, H.J. and M. Rao, *Enteric glia in homeostasis and disease: From fundamental biology to human pathology.* iScience, 2021. **24**(8): p. 102863.
216. Grubisic, V. and B.D. Gulbransen, *Enteric glia: the most alimentary of all glia.* J Physiol, 2017. **595**(2): p. 557-570.
217. Linan-Rico, A., et al., *Molecular Signaling and Dysfunction of the Human Reactive Enteric Glial Cell Phenotype: Implications for GI Infection, IBD, POI, Neurological, Motility, and GI Disorders.* Inflamm Bowel Dis, 2016. **22**(8): p. 1812-34.
218. Progatzky, F., et al., *Regulation of intestinal immunity and tissue repair by enteric glia.* Nature, 2021. **599**(7883): p. 125-130.
219. Escartin, C., et al., *Reactive astrocyte nomenclature, definitions, and future directions.* Nat Neurosci, 2021. **24**(3): p. 312-325.
220. Ibiza, S., et al., *Glial-cell-derived neuroregulators control type 3 innate lymphoid cells and gut defence.* Nature, 2016. **535**(7612): p. 440-443.
221. Grubisic, V., et al., *Enteric Glia Modulate Macrophage Phenotype and Visceral Sensitivity following Inflammation.* Cell Rep, 2020. **32**(10): p. 108100.
222. Chow, A.K., V. Grubisic, and B.D. Gulbransen, *Enteric Glia Regulate Lymphocyte Activation via Autophagy-Mediated MHC-II Expression.* Cell Mol Gastroenterol Hepatol, 2021. **12**(4): p. 1215-1237.
223. Fettucciari, K., et al., *Enteric glial cells are susceptible to Clostridium difficile toxin B.* Cell Mol Life Sci, 2017. **74**(8): p. 1527-1551.
224. Macchioni, L., et al., *Enteric glial cells counteract Clostridium difficile Toxin B through a NADPH oxidase/ROS/JNK/caspase-3 axis, without involving mitochondrial pathways.* Sci Rep, 2017. **7**: p. 45569.
225. Fettucciari, K., et al., *Clostridioides difficile toxin B alone and with pro-inflammatory cytokines induces apoptosis in enteric glial cells by activating three different signalling pathways mediated by caspases, calpains and cathepsin B.* Cell Mol Life Sci, 2022. **79**(8): p. 442.
226. Loureiro, A.V., et al., *Role of Pannexin-1-P2X7R signaling on cell death and pro-inflammatory mediator expression induced by Clostridioides difficile toxins in enteric glia.* Front Immunol, 2022. **13**: p. 956340.
227. Costa, D.V.S., et al., *Adenosine receptors differentially mediate enteric glial cell death induced by Clostridioides difficile Toxins A and B.* Front Immunol, 2022. **13**: p. 956326.
228. Costa, D.V.S., et al., *S100B Inhibition Attenuates Intestinal Damage and Diarrhea Severity During Clostridioides difficile Infection by Modulating Inflammatory Response.* Front Cell Infect Microbiol, 2021. **11**: p. 739874.
229. Schneider, L.C.L., et al., *Toxoplasma gondii promotes changes in VIPergic submucosal neurons, mucosal intraepithelial lymphocytes, and goblet cells during acute infection in the ileum of rats.* Neurogastroenterol Motil, 2018. **30**(5): p. e13264.
230. Trevizan, A.R., et al., *Acute Toxoplasma gondii infection alters the number of neurons and the proportion of enteric glial cells in the duodenum in Wistar rats.* Neurogastroenterol Motil, 2019. **31**(3): p. e13523.
231. Stakenborg, M., et al., *Enteric glial cells favor accumulation of anti-inflammatory macrophages during the resolution of muscularis inflammation.* Mucosal Immunol, 2022. **15**(6): p. 1296-1308.

232. Kermarrec, L., et al., *Enteric glial cells have specific immunosuppressive properties.* J Neuroimmunol, 2016. **295-296**: p. 79-83.
233. Schneider, R., et al., *A novel P2X2-dependent purinergic mechanism of enteric gliosis in intestinal inflammation.* EMBO Mol Med, 2021. **13**(1): p. e12724.
234. Stoffels, B., et al., *Postoperative ileus involves interleukin-1 receptor signaling in enteric glia.* Gastroenterology, 2014. **146**(1): p. 176-87 e1.
235. Hupa, K.J., et al., *AIM2 inflammasome-derived IL-1beta induces postoperative ileus in mice.* Sci Rep, 2019. **9**(1): p. 10602.
236. Schneider, R., et al., *IL-1-dependent enteric gliosis guides intestinal inflammation and dysmotility and modulates macrophage function.* Commun Biol, 2022. **5**(1): p. 811.
237. Liebig, C., et al., *Perineural invasion in cancer: a review of the literature.* Cancer, 2009. **115**(15): p. 3379-91.
238. Knijn, N., et al., *Perineural Invasion is a Strong Prognostic Factor in Colorectal Cancer: A Systematic Review.* Am J Surg Pathol, 2016. **40**(1): p. 103-12.
239. Liebig, C., et al., *Perineural invasion is an independent predictor of outcome in colorectal cancer.* J Clin Oncol, 2009. **27**(31): p. 5131-7.
240. Krasna, M.J., et al., *Vascular and neural invasion in colorectal carcinoma. Incidence and prognostic significance.* Cancer, 1988. **61**(5): p. 1018-23.
241. Horn, A., O. Dahl, and I. Morild, *Venous and neural invasion as predictors of recurrence in rectal adenocarcinoma.* Dis Colon Rectum, 1991. **34**(9): p. 798-804.
242. Godlewski, J. and Z. Kmiec, *Colorectal Cancer Invasion and Atrophy of the Enteric Nervous System: Potential Feedback and Impact on Cancer Progression.* Int J Mol Sci, 2020. **21**(9).
243. Ciurea, R.N., et al., *B2 adrenergic receptors and morphological changes of the enteric nervous system in colorectal adenocarcinoma.* World J Gastroenterol, 2017. **23**(7): p. 1250-1261.
244. Duchalais, E., et al., *Colorectal Cancer Cells Adhere to and Migrate Along the Neurons of the Enteric Nervous System.* Cell Mol Gastroenterol Hepatol, 2018. **5**(1): p. 31-49.
245. Vaes, N., et al., *Loss of enteric neuronal Ndrg4 promotes colorectal cancer via increased release of Nid1 and Fbln2.* EMBO Rep, 2021. **22**(6): p. e51913.
246. Neunlist, M., et al., *Neuro-glial crosstalk in inflammatory bowel disease.* J Intern Med, 2008. **263**(6): p. 577-83.
247. Neunlist, M., et al., *Enteric glia inhibit intestinal epithelial cell proliferation partly through a TGF-beta1-dependent pathway.* Am J Physiol Gastrointest Liver Physiol, 2007. **292**(1): p. G231-41.
248. Yuan, R., et al., *Enteric Glia Play a Critical Role in Promoting the Development of Colorectal Cancer.* Front Oncol, 2020. **10**: p. 595892.
249. Seguella, L., et al., *Pentamidine niosomes thwart S100B effects in human colon carcinoma biopsies favouring wtp53 rescue.* J Cell Mol Med, 2020. **24**(5): p. 3053-3063.
250. Vales, S., et al., *Tumor cells hijack enteric glia to activate colon cancer stem cells and stimulate tumorigenesis.* EBioMedicine, 2019. **49**: p. 172-188.
251. Baarle, L.v., et al., *IL-1R signaling drives enteric glia-macrophage interactions in colorectal cancer.* bioRxiv, 2023: p. 2023.06.01.543246.
252. Sundaresan, S., et al., *Gastrin Induces Nuclear Export and Proteasome Degradation of Menin in Enteric Glial Cells.* Gastroenterology, 2017. **153**(6): p. 1555-1567 e15.
253. Duan, S., et al., *GFAP-directed Inactivation of Men1 Exploits Glial Cell Plasticity in Favor of Neuroendocrine Reprogramming.* Cell Mol Gastroenterol Hepatol, 2022. **14**(5): p. 1025-1051.
254. Collaborators, G.B.D.I.B.D., *The global, regional, and national burden of inflammatory bowel disease in 195 countries and territories, 1990-2017: a systematic analysis for the Global Burden of Disease Study 2017.* Lancet Gastroenterol Hepatol, 2020. **5**(1): p. 17-30.
255. Baumgart, D.C. and S.R. Carding, *Inflammatory bowel disease: cause and immunobiology.* Lancet, 2007. **369**(9573): p. 1627-40.

256. Sgambato, D., et al., *The Role of Stress in Inflammatory Bowel Diseases.* Curr Pharm Des, 2017. **23**(27): p. 3997-4002.
257. Sun, Y., et al., *Stress Triggers Flare of Inflammatory Bowel Disease in Children and Adults.* Front Pediatr, 2019. **7**: p. 432.
258. Araki, M., et al., *Psychologic stress and disease activity in patients with inflammatory bowel disease: A multicenter cross-sectional study.* PLoS One, 2020. **15**(5): p. e0233365.
259. Schneider, K.M., et al., *The enteric nervous system relays psychological stress to intestinal inflammation.* Cell, 2023. **186**(13): p. 2823-2838 e20.
260. von Boyen, G.B., et al., *Distribution of enteric glia and GDNF during gut inflammation.* BMC Gastroenterol, 2011. **11**: p. 3.
261. Cirillo, C., et al., *Increased mucosal nitric oxide production in ulcerative colitis is mediated in part by the enteroglial-derived S100B protein.* Neurogastroenterol Motil, 2009. **21**(11): p. 1209-e112.
262. Esposito, G., et al., *Palmitoylethanolamide improves colon inflammation through an enteric glia/toll like receptor 4-dependent PPAR-alpha activation.* Gut, 2014. **63**(8): p. 1300-12.
263. Villanacci, V., et al., *Enteric nervous system abnormalities in inflammatory bowel diseases.* Neurogastroenterol Motil, 2008. **20**(9): p. 1009-16.
264. Cirillo, C., et al., *S100B protein in the gut: the evidence for enteroglial-sustained intestinal inflammation.* World J Gastroenterol, 2011. **17**(10): p. 1261-6.
265. Dora, D., et al., *Evidence of a Myenteric Plexus Barrier and Its Macrophage-Dependent Degradation During Murine Colitis: Implications in Enteric Neuroinflammation.* Cell Mol Gastroenterol Hepatol, 2021. **12**(5): p. 1617-1641.
266. Artis, D. and H. Spits, *The biology of innate lymphoid cells.* Nature, 2015. **517**(7534): p. 293-301.
267. Li, H., et al., *Protective role of berberine on ulcerative colitis through modulating enteric glial cells-intestinal epithelial cells-immune cells interactions.* Acta Pharm Sin B, 2020. **10**(3): p. 447-461.
268. Esposito, G., et al., *Enteric glial-derived S100B protein stimulates nitric oxide production in celiac disease.* Gastroenterology, 2007. **133**(3): p. 918-25.
269. Soret, R., et al., *Characterization of human, mouse, and rat cultures of enteric glial cells and their effect on intestinal epithelial cells.* Neurogastroenterol Motil, 2013. **25**(11): p. e755-64.
270. Lipps, C., et al., *Expansion of functional personalized cells with specific transgene combinations.* Nat Commun, 2018. **9**(1): p. 994.
271. Bobola, M.S., et al., *O6-methylguanine-DNA methyltransferase, O6-benzylguanine, and resistance to clinical alkylators in pediatric primary brain tumor cell lines.* Clin Cancer Res, 2005. **11**(7): p. 2747-55.
272. Carriero, F., et al., *Berberine Photo-Activation Potentiates Cytotoxicity in Human Astrocytoma Cells through Apoptosis Induction.* J Pers Med, 2021. **11**(10).
273. Slivinschi, B., et al., *Enhanced Delivery of Rose Bengal by Amino Acids Starvation and Exosomes Inhibition in Human Astrocytoma Cells to Potentiate Anticancer Photodynamic Therapy Effects.* Cells, 2022. **11**(16).
274. Comincini, S., et al., *microRNA-17 regulates the expression of ATG7 and modulates the autophagy process, improving the sensitivity to temozolomide and low-dose ionizing radiation treatments in human glioblastoma cells.* Cancer Biol Ther, 2013. **14**(7): p. 574-86.
275. Schmittgen, T.D. and K.J. Livak, *Analyzing real-time PCR data by the comparative C(T) method.* Nat Protoc, 2008. **3**(6): p. 1101-8.
276. Casali, C., et al., *Oxidative Stress and Nuclear Reprogramming: A Pilot Study of the Effects of Reactive Oxygen Species on Architectural and Epigenetic Landscapes.* Int J Mol Sci, 2022. **24**(1).
277. Drago, S., et al., *Gliadin, zonulin and gut permeability: Effects on celiac and non-celiac intestinal mucosa and intestinal cell lines.* Scand J Gastroenterol, 2006. **41**(4): p. 408-19.

278. Ruhl, A., S. Franzke, and W. Stremmel, *IL-1beta and IL-10 have dual effects on enteric glial cell proliferation.* Neurogastroenterol Motil, 2001. **13**(1): p. 89-94.
279. Middlemiss, P.J., et al., *A method for purifying enteric glia from rat myenteric plexus.* In Vitro Cell Dev Biol Anim, 2002. **38**(4): p. 188-90.
280. Grundmann, D., et al., *Isolation of high-purity myenteric plexus from adult human and mouse gastrointestinal tract.* Sci Rep, 2015. **5**: p. 9226.
281. Le Berre-Scoul, C., et al., *A novel enteric neuron-glia coculture system reveals the role of glia in neuronal development.* J Physiol, 2017. **595**(2): p. 583-598.
282. D'Errico, F., et al., *Estrogen receptor beta controls proliferation of enteric glia and differentiation of neurons in the myenteric plexus after damage.* Proc Natl Acad Sci U S A, 2018. **115**(22): p. 5798-5803.
283. Wang, Z., et al., *Isolation of Enteric Glial Cells from the Submucosa and Lamina Propria of the Adult Mouse.* J Vis Exp, 2018(138).
284. Cerantola, S., et al., *Involvement of Enteric Glia in Small Intestine Neuromuscular Dysfunction of Toll-Like Receptor 4-Deficient Mice.* Cells, 2020. **9**(4).
285. Kroemer, G. and J.C. Reed, *Mitochondrial control of cell death.* Nat Med, 2000. **6**(5): p. 513-9.
286. Yang, H., et al., *The role of cellular reactive oxygen species in cancer chemotherapy.* J Exp Clin Cancer Res, 2018. **37**(1): p. 266.
287. Woodfin, A., M.B. Voisin, and S. Nourshargh, *PECAM-1: a multi-functional molecule in inflammation and vascular biology.* Arterioscler Thromb Vasc Biol, 2007. **27**(12): p. 2514-23.
288. Al Barashdi, M.A., et al., *Protein tyrosine phosphatase receptor type C (PTPRC or CD45).* J Clin Pathol, 2021. **74**(9): p. 548-552.
289. Keller, L., S. Werner, and K. Pantel, *Biology and clinical relevance of EpCAM.* Cell Stress, 2019. **3**(6): p. 165-180.
290. Alvarez-Viejo, M., Y. Menendez-Menendez, and J. Otero-Hernandez, *CD271 as a marker to identify mesenchymal stem cells from diverse sources before culture.* World J Stem Cells, 2015. **7**(2): p. 470-6.
291. Geboes, K., et al., *Major histocompatibility class II expression on the small intestinal nervous system in Crohn's disease.* Gastroenterology, 1992. **103**(2): p. 439-47.
292. da Silveira, A.B., et al., *Enteroglial cells act as antigen-presenting cells in chagasic megacolon.* Hum Pathol, 2011. **42**(4): p. 522-32.
293. Murray, J.A., et al., *HLA DQ gene dosage and risk and severity of celiac disease.* Clin Gastroenterol Hepatol, 2007. **5**(12): p. 1406-12.
294. Sazonovs, A., et al., *HLA-DQA1*05 Carriage Associated With Development of Anti-Drug Antibodies to Infliximab and Adalimumab in Patients With Crohn's Disease.* Gastroenterology, 2020. **158**(1): p. 189-199.
295. Boesmans, W., et al., *Neurotransmitters involved in fast excitatory neurotransmission directly activate enteric glial cells.* Neurogastroenterol Motil, 2013. **25**(2): p. e151-60.
296. Mishra, A., et al., *Astrocytes mediate neurovascular signaling to capillary pericytes but not to arterioles.* Nat Neurosci, 2016. **19**(12): p. 1619-1627.
297. Verkhratsky, A. and V. Parpura, *Store-operated calcium entry in neuroglia.* Neurosci Bull, 2014. **30**(1): p. 125-33.
298. Zhang, W., et al., *Intercellular calcium waves in cultured enteric glia from neonatal guinea pig.* Glia, 2003. **42**(3): p. 252-62.
299. Dragoni, S., et al., *Enhanced expression of Stim, Orai, and TRPC transcripts and proteins in endothelial progenitor cells isolated from patients with primary myelofibrosis.* PLoS One, 2014. **9**(3): p. e91099.
300. Prakriya, M. and R.S. Lewis, *Store-Operated Calcium Channels.* Physiol Rev, 2015. **95**(4): p. 1383-436.
301. Toth, A.B., et al., *CRAC channels regulate astrocyte Ca(2+) signaling and gliotransmitter release to modulate hippocampal GABAergic transmission.* Sci Signal, 2019. **12**(582).

302. Elli, L., E. Dolfini, and M.T. Bardella, *Gliadin cytotoxicity and in vitro cell cultures.* Toxicol Lett, 2003. **146**(1): p. 1-8.
303. Barone, M.V., R. Troncone, and S. Auricchio, *Gliadin peptides as triggers of the proliferative and stress/innate immune response of the celiac small intestinal mucosa.* Int J Mol Sci, 2014. **15**(11): p. 20518-37.
304. Monguzzi, E., et al., *Gliadin effect on the oxidative balance and DNA damage: An in-vitro, ex-vivo study.* Dig Liver Dis, 2019. **51**(1): p. 47-54.
305. Iacomino, G., et al., *Structural analysis and Caco-2 cell permeability of the celiac-toxic A-gliadin peptide 31-55.* J Agric Food Chem, 2013. **61**(5): p. 1088-96.
306. Freire, R., et al., *Human gut derived-organoids provide model to study gluten response and effects of microbiota-derived molecules in celiac disease.* Sci Rep, 2019. **9**(1): p. 7029.
307. Stoven, S., J.A. Murray, and E.V. Marietta, *Latest in vitro and in vivo models of celiac disease.* Expert Opin Drug Discov, 2013. **8**(4): p. 445-57.
308. Manai, F., et al., *The In Vitro Effects of Enzymatic Digested Gliadin on the Functionality of the Autophagy Process.* Int J Mol Sci, 2018. **19**(2).
309. Klionsky, D.J., et al., *Guidelines for the use and interpretation of assays for monitoring autophagy (4th edition)(1).* Autophagy, 2021. **17**(1): p. 1-382.
310. Jung, S., H. Jeong, and S.W. Yu, *Autophagy as a decisive process for cell death.* Exp Mol Med, 2020. **52**(6): p. 921-930.
311. Capozzi, A., et al., *Modulatory Effect of Gliadin Peptide 10-mer on Epithelial Intestinal CACO-2 Cell Inflammatory Response.* PLoS One, 2013. **8**(6): p. e66561.
312. Frossi, B., et al., *Mast cells are associated with the onset and progression of celiac disease.* J Allergy Clin Immunol, 2017. **139**(4): p. 1266-1274 e1.
313. Vincentini, O., et al., *Gliadin-dependent cytokine production in a bidimensional cellular model of celiac intestinal mucosa.* Clin Exp Med, 2015. **15**(4): p. 447-54.
314. Kuo, L.J. and L.X. Yang, *Gamma-H2AX - a novel biomarker for DNA double-strand breaks.* In Vivo, 2008. **22**(3): p. 305-9.
315. Linan-Rico, A., et al., *Mini-review: Enteric glial cell reactions to inflammation and potential therapeutic implications for GI diseases, motility disorders, and abdominal pain.* Neurosci Lett, 2023. **812**: p. 137395.
316. Nogueira, L.T., et al., *The involvement of mast cells in the irinotecan-induced enteric neurons loss and reactive gliosis.* J Neuroinflammation, 2017. **14**(1): p. 79.
317. Wang, C., et al., *Antioxidant activity and protective effect of wheat germ peptides in an in vitro celiac disease model via Keap1/Nrf2 signaling pathway.* Food Res Int, 2022. **161**: p. 111864.
318. Khan, N.M., I. Ahmad, and T.M. Haqqi, *Nrf2/ARE pathway attenuates oxidative and apoptotic response in human osteoarthritis chondrocytes by activating ERK1/2/ELK1-P70S6K-P90RSK signaling axis.* Free Radic Biol Med, 2018. **116**: p. 159-171.
319. Keum, Y.S., et al., *Involvement of Nrf2 and JNK1 in the activation of antioxidant responsive element (ARE) by chemopreventive agent phenethyl isothiocyanate (PEITC).* Pharm Res, 2003. **20**(9): p. 1351-6.
320. Sun, Z., Z. Huang, and D.D. Zhang, *Phosphorylation of Nrf2 at multiple sites by MAP kinases has a limited contribution in modulating the Nrf2-dependent antioxidant response.* PLoS One, 2009. **4**(8): p. e6588.
321. Palova-Jelinkova, L., et al., *Gliadin fragments induce phenotypic and functional maturation of human dendritic cells.* J Immunol, 2005. **175**(10): p. 7038-45.
322. Kobayashi, A., et al., *Oxidative stress sensor Keap1 functions as an adaptor for Cul3-based E3 ligase to regulate proteasomal degradation of Nrf2.* Mol Cell Biol, 2004. **24**(16): p. 7130-9.
323. Yamamoto, T., et al., *Physiological significance of reactive cysteine residues of Keap1 in determining Nrf2 activity.* Mol Cell Biol, 2008. **28**(8): p. 2758-70.

324. Loboda, A., et al., *Role of Nrf2/HO-1 system in development, oxidative stress response and diseases: an evolutionarily conserved mechanism.* Cell Mol Life Sci, 2016. **73**(17): p. 3221-47.
325. Jiang, T., et al., *p62 links autophagy and Nrf2 signaling.* Free Radic Biol Med, 2015. **88**(Pt B): p. 199-204.
326. Rajaguru, P., et al., *Increased accumulation of dendritic cells in celiac disease associates with increased expression of autophagy protein LC3.* Indian J Pathol Microbiol, 2013. **56**(4): p. 342-8.
327. Comincini, S., et al., *Identification of Autophagy-Related Genes and Their Regulatory miRNAs Associated with Celiac Disease in Children.* Int J Mol Sci, 2017. **18**(2).
328. Manai, F., et al., *Trehalose Modulates Autophagy Process to Counteract Gliadin Cytotoxicity in an In Vitro Celiac Disease Model.* Cells, 2019. **8**(4).
329. Conte, M., et al., *Gliadin Peptide P31-43 Induces mTOR/NFkbeta Activation and Reduces Autophagy: The Role of Lactobacillus paracasei CBA L74 Postbiotc.* Int J Mol Sci, 2022. **23**(7).
330. Jessen, K.R. and R. Mirsky, *Astrocyte-like glia in the peripheral nervous system: an immunohistochemical study of enteric glia.* J Neurosci, 1983. **3**(11): p. 2206-18.
331. Zanoletti, L., et al., *Cytological, molecular, cytogenetic, and physiological characterization of a novel immortalized human enteric glial cell line.* Front Cell Neurosci, 2023. **17**: p. 1170309.
332. Hoff, S., et al., *Quantitative assessment of glial cells in the human and guinea pig enteric nervous system with an anti-Sox8/9/10 antibody.* J Comp Neurol, 2008. **509**(4): p. 356-71.
333. De Giorgio, R., et al., *Enteric glia and neuroprotection: basic and clinical aspects.* Am J Physiol Gastrointest Liver Physiol, 2012. **303**(8): p. G887-93.
334. von Boyen, G.B., et al., *Proinflammatory cytokines increase glial fibrillary acidic protein expression in enteric glia.* Gut, 2004. **53**(2): p. 222-8.
335. da Cunha Franceschi, R., et al., *Enteric glial reactivity to systemic LPS administration: Changes in GFAP and S100B protein.* Neurosci Res, 2017. **119**: p. 15-23.
336. Progatzky, F. and V. Pachnis, *The role of enteric glia in intestinal immunity.* Curr Opin Immunol, 2022. **77**: p. 102183.
337. Koretz, K., et al., *Sequential induction of MHC antigens on autochthonous cells of ileum affected by Crohn's disease.* Am J Pathol, 1987. **129**(3): p. 493-502.
338. Denzer, K., et al., *Exosome: from internal vesicle of the multivesicular body to intercellular signaling device.* J Cell Sci, 2000. **113 Pt 19**: p. 3365-74.
339. Gulbransen, B.D. and K.A. Sharkey, *Novel functional roles for enteric glia in the gastrointestinal tract.* Nat Rev Gastroenterol Hepatol, 2012. **9**(11): p. 625-32.
340. Gulbransen, B.D., J.S. Bains, and K.A. Sharkey, *Enteric glia are targets of the sympathetic innervation of the myenteric plexus in the guinea pig distal colon.* J Neurosci, 2010. **30**(19): p. 6801-9.
341. Grubisic, V. and B.D. Gulbransen, *Enteric glial activity regulates secretomotor function in the mouse colon but does not acutely affect gut permeability.* J Physiol, 2017. **595**(11): p. 3409-3424.
342. Sarosi, G.A., et al., *Capacitative Ca2+ entry in enteric glia induced by thapsigargin and extracellular ATP.* Am J Physiol, 1998. **275**(3): p. G550-5.
343. James, L.R., et al., *High-throughput analysis of calcium signalling kinetics in astrocytes stimulated with different neurotransmitters.* PLoS One, 2011. **6**(10): p. e26889.
344. Tang, W., et al., *Stimulation-evoked Ca2+ signals in astrocytic processes at hippocampal CA3-CA1 synapses of adult mice are modulated by glutamate and ATP.* J Neurosci, 2015. **35**(7): p. 3016-21.
345. Taheri, M., et al., *Diversity of Evoked Astrocyte Ca(2+) Dynamics Quantified through Experimental Measurements and Mathematical Modeling.* Front Syst Neurosci, 2017. **11**: p. 79.

346. Astesana, V., et al., *Correction to: [Pt(O,O'-acac)(gamma-acac)(DMS)]: Alternative Strategies to Overcome Cisplatin-Induced Side Effects and Resistance in T98G Glioma Cells.* Cell Mol Neurobiol, 2021. **41**(3): p. 589.
347. Bird, G.S., et al., *Methods for studying store-operated calcium entry.* Methods, 2008. **46**(3): p. 204-12.
348. Negri, S., et al., *Group 1 metabotropic glutamate receptors trigger glutamate-induced intracellular Ca(2+) signals and nitric oxide release in human brain microvascular endothelial cells.* Cell Mol Life Sci, 2020. **77**(11): p. 2235-2253.
349. Zhang, W., et al., *Endothelin-activated calcium signaling in enteric glia derived from neonatal guinea pig.* Am J Physiol, 1997. **272**(5 Pt 1): p. G1175-85.
350. Circu, M.L., et al., *Contribution of glutathione status to oxidant-induced mitochondrial DNA damage in colonic epithelial cells.* Free Radic Biol Med, 2009. **47**(8): p. 1190-8.
351. Circu, M.L. and T.Y. Aw, *Reactive oxygen species, cellular redox systems, and apoptosis.* Free Radic Biol Med, 2010. **48**(6): p. 749-62.
352. Ricci, C., et al., *Mitochondrial DNA damage triggers mitochondrial-superoxide generation and apoptosis.* Am J Physiol Cell Physiol, 2008. **294**(2): p. C413-22.
353. Saelens, X., et al., *Toxic proteins released from mitochondria in cell death.* Oncogene, 2004. **23**(16): p. 2861-74.
354. Elmore, S., *Apoptosis: a review of programmed cell death.* Toxicol Pathol, 2007. **35**(4): p. 495-516.
355. Orrenius, S., V. Gogvadze, and B. Zhivotovsky, *Mitochondrial oxidative stress: implications for cell death.* Annu Rev Pharmacol Toxicol, 2007. **47**: p. 143-83.
356. Ott, M., et al., *Cytochrome c release from mitochondria proceeds by a two-step process.* Proc Natl Acad Sci U S A, 2002. **99**(3): p. 1259-63.
357. Chirdo, F.G., et al., *The gliadin p31-43 peptide: Inducer of multiple proinflammatory effects.* Int Rev Cell Mol Biol, 2021. **358**: p. 165-205.
358. Duarte Azevedo, M., S. Sander, and L. Tenenbaum, *GDNF, A Neuron-Derived Factor Upregulated in Glial Cells during Disease.* J Clin Med, 2020. **9**(2).
359. Marietta, E.V., C.S. David, and J.A. Murray, *Important lessons derived from animal models of celiac disease.* Int Rev Immunol, 2011. **30**(4): p. 197-206.
360. Mohammed, A.D., et al., *Gut Antibody Deficiency in a Mouse Model of CVID Results in Spontaneous Development of a Gluten-Sensitive Enteropathy.* Front Immunol, 2019. **10**: p. 2484.
361. Abadie, V., C. Khosla, and B. Jabri, *A Mouse Model of Celiac Disease.* Curr Protoc, 2022. **2**(8): p. e515.
362. Manai, F., et al., *Dimethyl Fumarate and Intestine: From Main Suspect to Potential Ally against Gut Disorders.* Int J Mol Sci, 2023. **24**(12).
363. Fabrini, R., et al., *Nuclear shield: a multi-enzyme task-force for nucleus protection.* PLoS One, 2010. **5**(12): p. e14125.
364. Kotera, J., K. Fujishige, and K. Omori, *Immunohistochemical localization of cGMP-binding cGMP-specific phosphodiesterase (PDE5) in rat tissues.* J Histochem Cytochem, 2000. **48**(5): p. 685-93.
365. Ott, C., et al., *Detailed analysis of the human mitochondrial contact site complex indicate a hierarchy of subunits.* PLoS One, 2015. **10**(3): p. e0120213.
366. Muhlenbein, N., et al., *Organization and function of the small Tim complexes acting along the import pathway of metabolite carriers into mammalian mitochondria.* J Biol Chem, 2004. **279**(14): p. 13540-6.
367. Anandatheerthavarada, H.K., N.B.V. Sepuri, and N.G. Avadhani, *Mitochondrial targeting of cytochrome P450 proteins containing NH2-terminal chimeric signals involves an unusual TOM20/TOM22 bypass mechanism.* J Biol Chem, 2009. **284**(25): p. 17352-17363.
368. Tamai, S., et al., *Characterization of the mitochondrial protein LETM1, which maintains the mitochondrial tubular shapes and interacts with the AAA-ATPase BCS1L.* J Cell Sci, 2008. **121**(Pt 15): p. 2588-600.

369. Li, Y., et al., *LETM1 is required for mitochondrial homeostasis and cellular viability (Review).* Mol Med Rep, 2019. **19**(5): p. 3367-3375.

Supplementary material

9.1. Supplementary Tables

Supplementary table T1

3' Reverse primers		
Gene	Sequence	Expected band size (bp)
ID2	GCAGGCTGACAATAGTGGGA	462
Fos	GGATGATGCTGGGAACAGGA	1054
NS1	ATGTCCTGGAAGAGAAGGCA	678
JUN	TTCCTCATGCGCTTCCTCTC	912
E2F1	CAGGGTCTGCAATGCTACGA	944
ßCAT	TTATGCAAGGTCCCAGCGGT	806
TAg	CACCTGGCAAACTTTCCTCA	1214
MYB	CTTCTGGAAGCTTGTGGCCA	780
ID3	ATGACAAGTTCCGGAGCGAG	453
E7	GCCCATTAACAGGTCTTCCA	404
E6	ATTCGCCCTTTTACAGCTGG	636
BCL2	TCTGCGAAGTCACGACGGTA	440
HOXA9	GTTTAATGCCATAAGGCCGG	515
BMI1	GGGCCATTTCTTCTCCAGGT	782
PymT	CATCTCGGGTTGGTGTTCCA	606
Core	ACTTTACCCACGTTGCGCGA	487
OCT3	GCAAAGCAGAAACCCTCGTG	846
KLF4	AAGATCAAGCAGGAGGCGGT	1084
ID1	AGAAGCACCAAACGTGACCA	980
MYC	AGTGGGCTGTGAGGAGGTTT	1001
Lmo2	TTTCCGTCCCAGCTTGTAGT	822
NFE2L2	GCTGCTGAAGGAATCCTCAA	1008
YAP1	GCCAGGATGTGGTCTTGTTC	950
Nanog	TATGGAGCGGAGCAGCATTC	935
SOX2	CTCGCAGACCTACATGAACG	846
RHOA	AAGCATTTCTGTCCCAACGT	562
EZH2	ACTTCGAGCTCCTCTGAAGC	1481
GLI1	CACCACATCAACAGCGAGCA	1144
v-MYC	GACACCCTGAGCGATTCAGA	1052
SUZ12	TACCCTGGAAGTCCTGCTTG	769
ZFP217	CAAGAAGGGAGCACCGACAA	1188
ID4	CAGCAAAGTGGAGATCCTGC	652
REX	GCGAGCTCATTACTTGCAGG	920

Table T1. *List of the 3' reverse primers used to identify the integrated genes. The primer sequence is reported together with the expected band size as base pairs (bp).*

Supplementary Table T2

GFAP	Forward primer: 5′-CTGCTCAATGTCAAGCTG
	Reverse primer: 3′-GCTGGTTTCTCGAATCTG
SOX10	Forward primer: 5′-AAGACACTAGAATCCTGACC
	Reverse primer: 3′-CTGCAGAACAGGAAAATAGG
S100β	Forward primer: 5′-ACCAATATTCTGGAAGGGAG
	Reverse primer: 3′-CCTCTAAGAAATGGGAAAGC
PLP1	Forward primer: 5′-AGCTGAGTTCCAAATGACCT
	Reverse primer: 3′-AACGACGGTGAATGTTGAAAC
CCL2	Forward primer: 5′-CAGCCAGATGCAATCAATGCC
	Reverse primer: 3′-TGGAATCCTGAACCCACTTCT
GAPDH	Forward primer: 5′-TCGGAGTCAACGGATTTG
	Reverse primer: 3′-CAACAATATCCACTTTACCAGAG
CCL2	Forward primer: 5′- GCTCTGAGCCTCCTTATC
	Reverse primer: 3′- GCAAGAACAGGATAGCTG
IL-6	Forward primer: 5′- GCAGAAAAAGGCAAAGAATC
	Reverse primer: 3′- CTACATTTGCCGAAGAGC
GDNF	Forward primer: 5′- CAGTGACTCAAATATGCCAG
	Reverse primer: 3′- TGCCATTTGTTTATCTGGTG
RPLP0	Forward primer: 5′- ATGCCCAGGGAAGACACCCC
	Reverse primer: 3′- CGAAGGGACATGCGGATCTCCTGC

Table T2. *List of the 5' forward and 3' reverse primers used to amplify the enteric glial marker genes.*

Supplementary Table T3

Days	wt	ClK
0	0	0
4	1	1
8	1	3.3
11	1	5.6
13	2.6	8.9
15	3.6	12.2
19	5.2	15.5
22	5.2	18.8
25	6.2	22.1
29	6.2	25.4
32		28.7
35		32
36		32
39		35.3
41		38.6
43		41.9

Table T3. *Cumulative population doublings (expressed in days) of primary hEGCs and hEGC-ClK cells. The clone was cultivated for more than 40 days. Primary cells stopped their growth after 29 days. Mock-infected control cells died 10 days after infection (data not shown).*

Supplementary Table T4

N° of chromosomes	N° of metaphases
42	1
43	11
44	31
45	9
46	7
47	2
48	1
49	1
63	1
66	1
68	1
71	1
72	1
73	1
75	1
78	1
79	4
82	1
83	2
84	3
85	4
86	9
87	3
88	1
89	1
90	1
Tot.	100

Table T4. *Numerical data regarding the distribution of chromosome numbers. The two modal values, 44 and 86 respectively, are highlighted in dark grey.*

Supplementary Table T5

HLA-A*	HLA-B*	HLA-C*	HLA-DRB1*	HLA-DQA1*	HLA-DQB1*
01:01	07:02	07:01	13:01	01:02	06:02
30:01	08:01	12:03	15:01	01:03	06:03

Table T5. *HLA genotyping of hEGC-ClK clone. Results were collected through PRC-SSO and subsequent validation with PCR-SSP*.

9.2. Supplementary Figures

Supplementary Figure S1

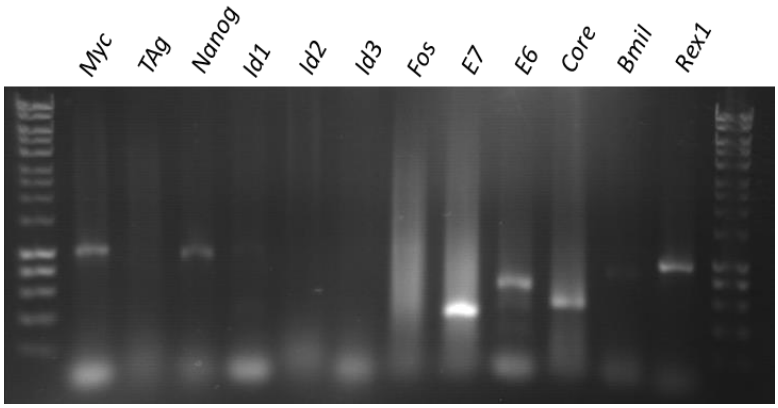

Figure S1. *Electrophoresis analysis of the integrated genes. The ladder (1 kb) is reported on both sides.*

Supplementary Figure S2

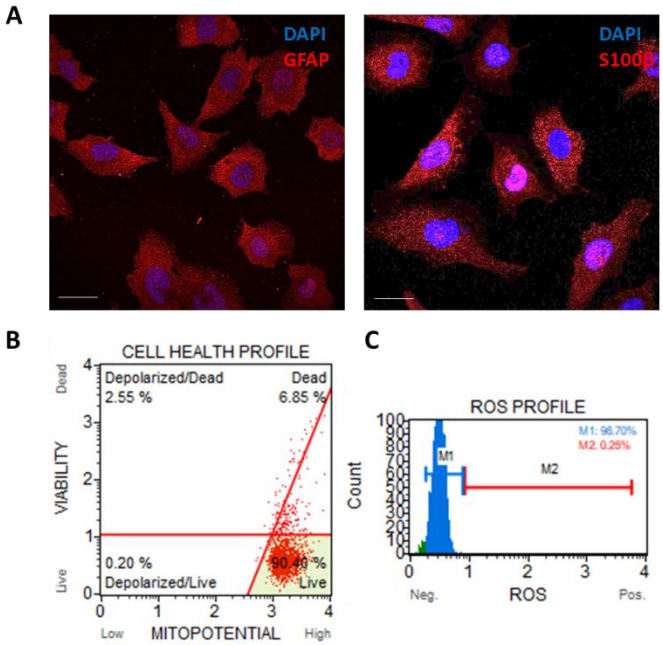

Figure S2. *Preliminary characterization of hEGC-ClK cells at passage p35 through* ***(A)*** *immunofluorescence assay for the glial markers GFAP and S100β,* ***(B)*** *flow cytometry analysis of mitochondrial depolarization (events collected: 2000), and* ***(C)*** *intracellular ROS levels analysis (M1 gate: ROS-; M2 gate: ROS+).*

Supplementary Figure S3

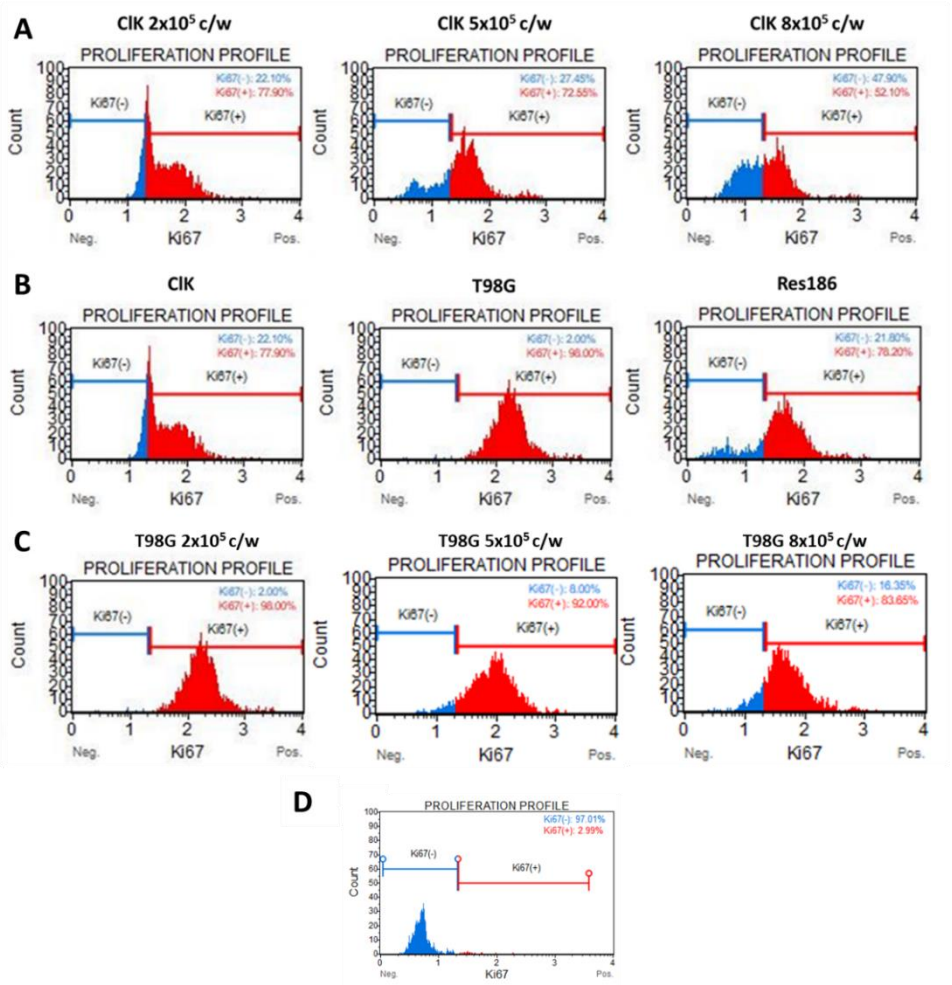

Figure S3. *Cytofluorimetric analysis of Ki-67 levels in hEGC-ClK cells.* ***(A)*** *Analysis of Ki-67 expression levels in hEGC-ClK at increasing confluences. Ki-67 positive cells are reported in red whereas Ki-67 negative cells in blue. Events collected: 2000. Experiments were performed in triplicate.* ***(B)*** *Analysis of Ki-67 expression levels in hEGC-ClK, T98G, and Res186 cells. Ki-67 positive cells are reported in red whereas Ki-67 negative cells in blue. Events collected: 2000. Experiments were performed in duplicate.* ***(C)*** *Analysis of Ki-67 expression levels in T87G at increasing confluences. Ki-67 positive cells are reported in red whereas Ki-67 negative cells in blue. Events collected: 2000.* ***(D)*** *Isotypic IgG control.*

Supplementary Figure S4

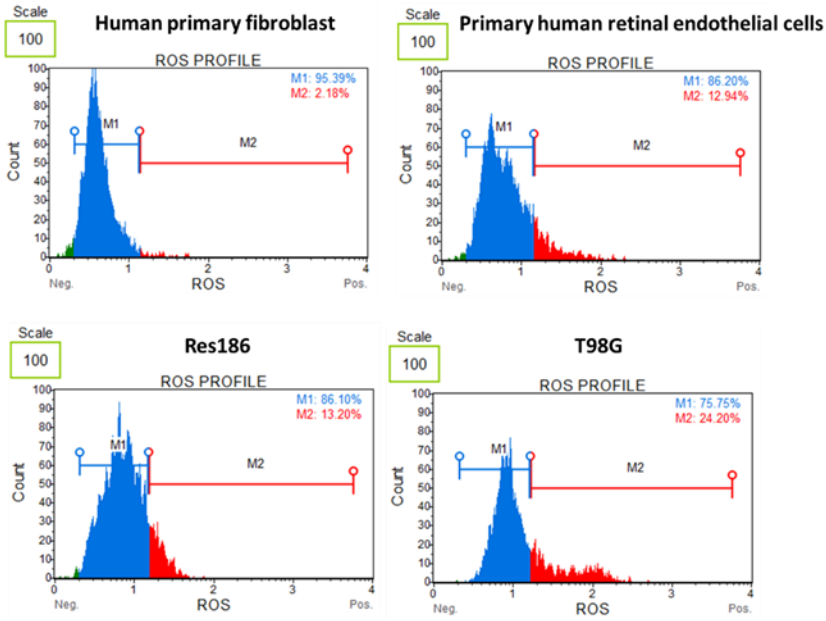

Figure S4. *Cytofluorimetric analysis of intracellular ROS levels in human primary fibroblasts and retinal endothelial cells (normal cells) as well as in two glioma cell lines, i.e., Res186 (Grade I) and T98G (Grade IV). M1 gate: ROS-; M2 gate: ROS+. Events collected: 2000 cells.*

Supplementary Figure S5

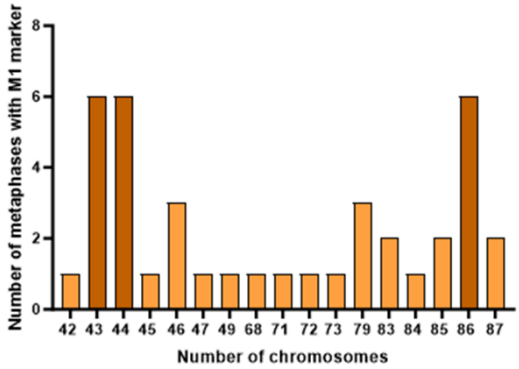

Figure S5. *Distribution of the marker M1 in hEGC-ClK metaphases. On the X-axis is reported the number of chromosomes whereas on the y-axis, the number of metaphases showing the M1 marker. Three significant peaks were observed in metaphases with 43, 44, and 86 chromosomes*.

Supplementary Figure S6

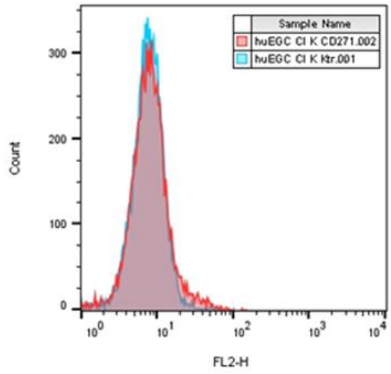

Figure S6. *Analysis of CD271 expression levels in the hEGC-ClK clone by flow cytometry. Light blue curve indicated unstained cells whereas red fluorescence signals were detected from cells stained with PE-labelled CD271 antibody.*

Supplementary Figure S7

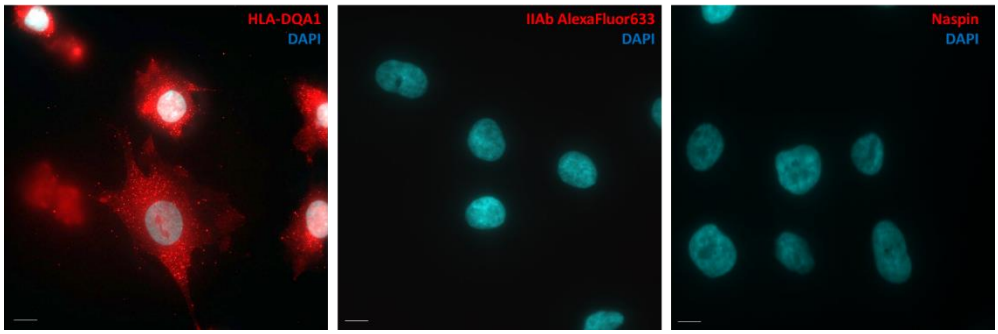

Figure S7. *Immunofluorescence of the HLA-DQA1 molecule. The analysis was performed using specific anti-HLA-DQA1 IgG antibody conjugated with AlexaFluor633. Nuclei were stained with DAPI. Scale bars (= 10 μm) are reported. Negative controls were performed using the secondary antibody alone and anti-naspin IgG antibody.*

Supplementary Figure S8

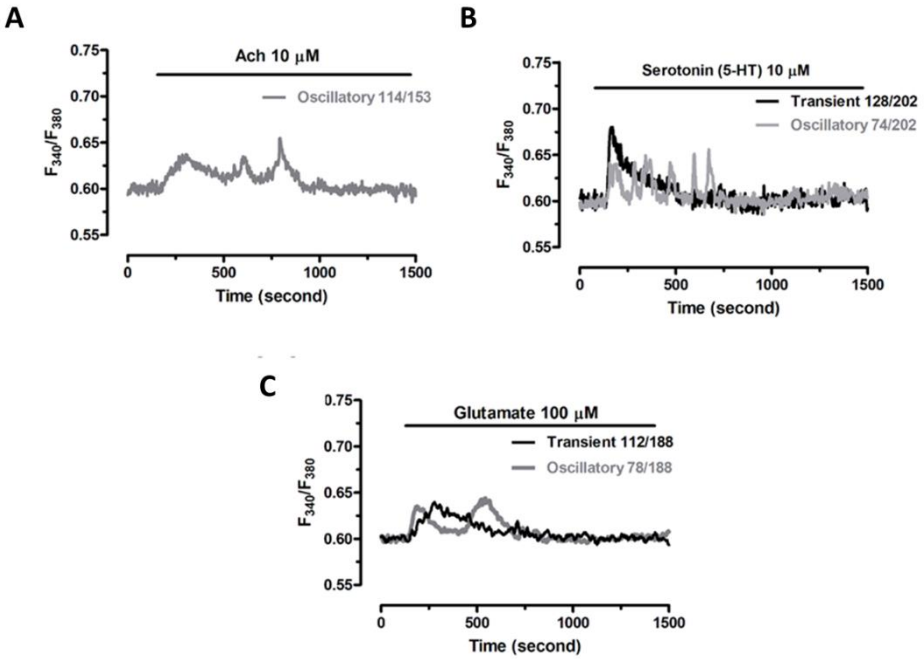

Figure S8. *Acetylcholine (Ach), serotonin (5-HT), and glutamate induce an increase in $[Ca^{2+}]_i$ in hEGC-ClK clone.* ***(A)*** *Ach (10 μM) triggered oscillatory Ca^{2+} signals in hEGC-ClK cells.* ***(B)*** *The Ca^{2+} response to 5-HT (10 μM) was characterized by both transient (black line) and oscillatory (grey line) patterns.* ***(C)*** *Glutamate (100 μM) induces both transient (black line) or oscillatory (grey line) increase in $[Ca^{2+}]_i$.*

Supplementary Figure S9

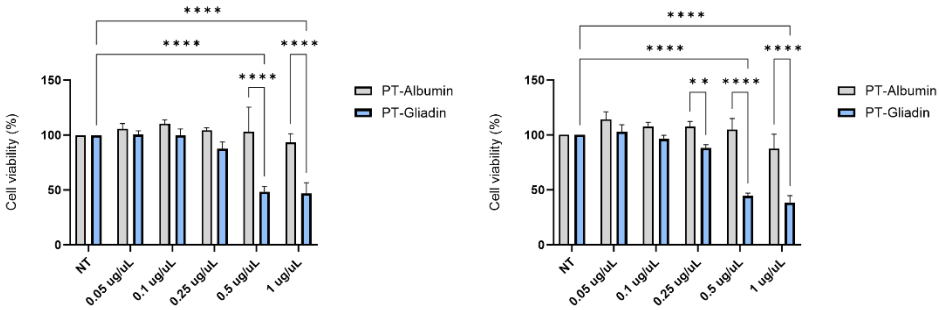

Figure S9*. MTS assay of ECGs treated with increasing concentration of digested gliadin. Analysis was performed at 12 hours p.t. The values on the Y-axis, reported as mean ± SD, indicate cell viability (%) normalized with that of control cells. The asterisks indicate p<0.05 (*), p<0.01 (**) or p<0.001 (***), p<0.0001(****) Two-Way ANOVA, compared with relative control cells. The experiments were performed in three independent biological replicas.*

Supplementary Figure S10

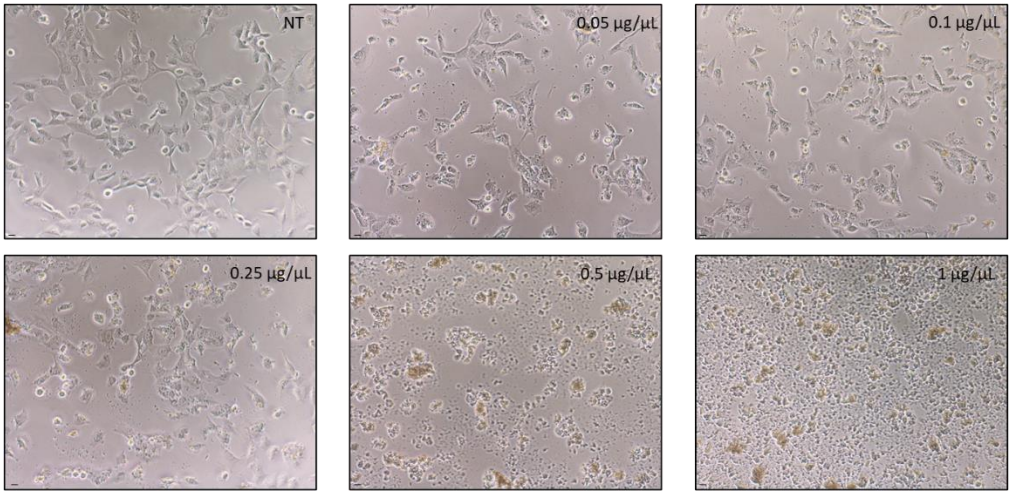

Figure S10. *Cytotoxic effect of digested gliadin on hEGCs. Bright microscopy analysis of hEGC-ClK cells treated with increasing concentration of PT-gliadin. Cells were seeded at "low confluence", i.e., 500.000 cells/well in a 6-well microplate and cultured per 24 hours. Images were visualized through the Nikon Eclipse TS-100 phase-contrast microscope. Cells were analyzed 24 hours p.t. Images were collected at 10X magnification. Size bars (= 10 µm) are reported*

Supplementary Figure S11

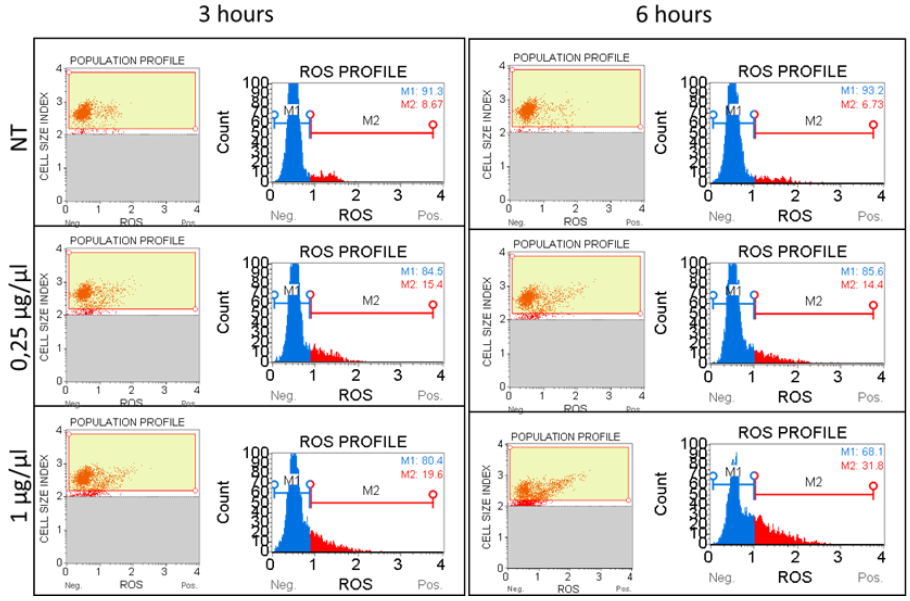

Figure S11. *Cytofluorimetric plots of intracellular ROS levels in EGCs treated with digested gliadin. Analysis was performed at 3 and 6 hours p.t. (gliadin concentration: 0.25 µg/µL, 1 µg/µL). Events collected: 2000. M1: ROS – population (blue); M2: ROS+ population (red).*

Supplementary Figure S12

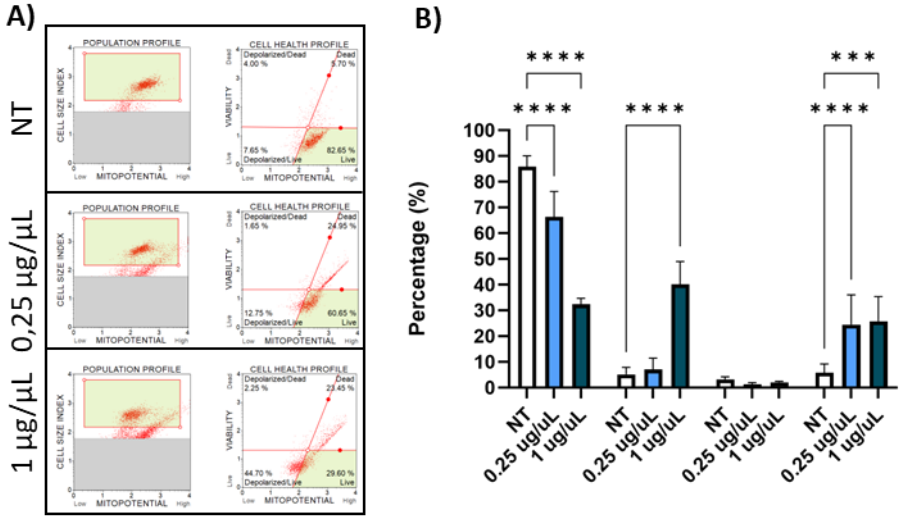

Figure S12. *Analysis of mitochondrial membrane potential (ΔΨm) in EGCs cells treated with Pt-gliadin. Analysis was performed at 6 hours post-treatment (gliadin concentration: 0.25 µg/µL, 1 µg/µL).* ***(A)*** *Cytofluorimetric plot reporting the mitochondrial depolarization levels of hEGCs. Events collected: 2000.* ***(B)*** *Histogram showing the depolarization status of EGCs mitochondria. Experiments were performed in triplicate. Data are reported as mean ± SD. The asterisks indicate p<0.05 (*), p<0.01 (**) or p<0.001 (***), p<0.0001(****) Two-Way ANOVA, compared with relative control cells. On the Y-axis is reported the number of cells expressed as percentages (%).*

Supplementary Figure S13

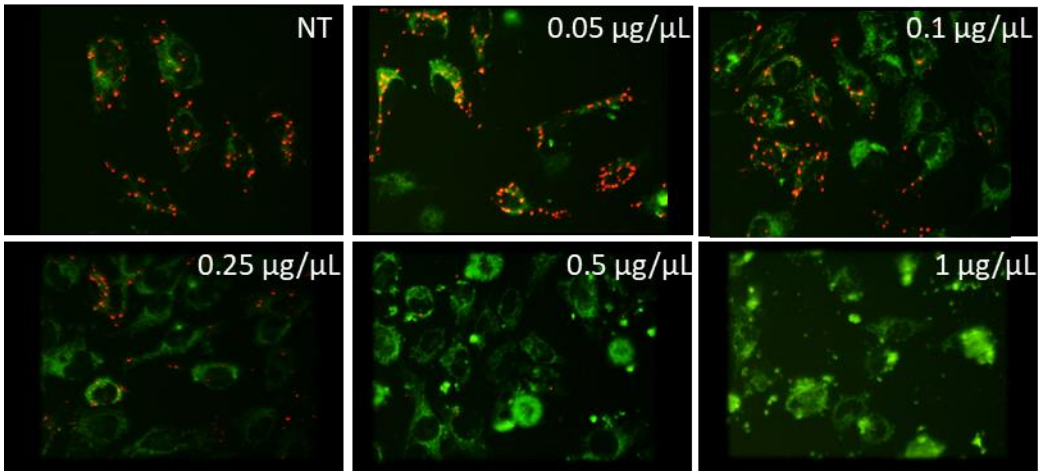

Figure S13. *Analysis of mitochondrial membrane potential (ΔΨm) in EGCs cells treated with Pt-gliadin (0.25 µg/µl and 1 µg/µl). Pictures were collected 3 hours after the treatment. Fluorescence microscope observation (40X) at 490 nm following JC-1 administration. Orange-red spots indicated healthy mitochondria. Size bars (= 10 µm) are reported.*

Supplementary Figure S14

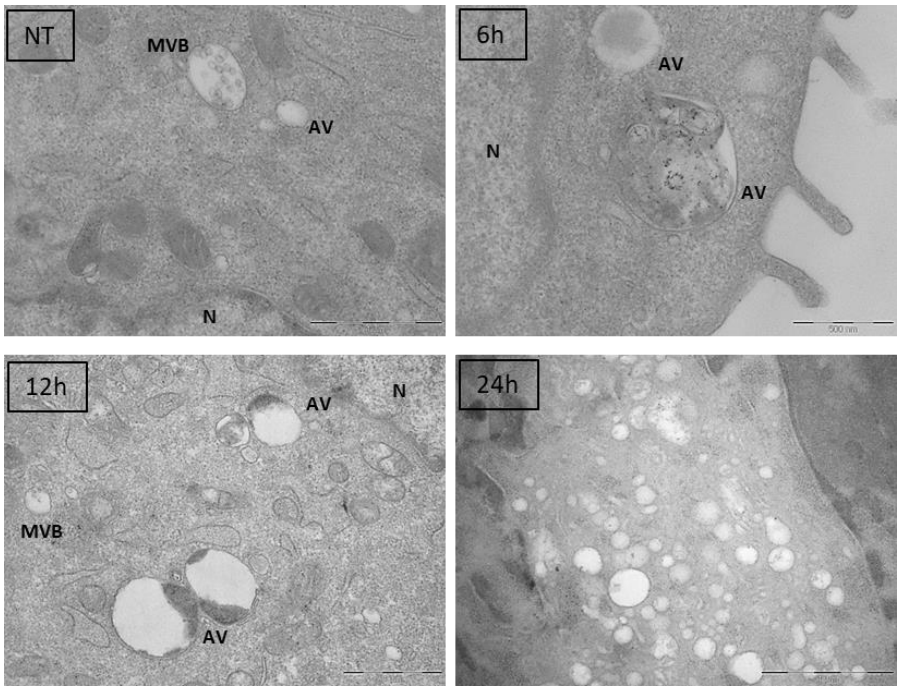

Figure S14. *Electron microscopy analysis of EGCs treated with digested gliadin (0.5 µg/µl). Pictures were collected 6, 12, and 24 hours p.t. MVB: multivesicular bodies, AV: autophagic vesicles; N: nucleus. Scale bars (500 µM) are reported.*

Supplementary Fig. S15

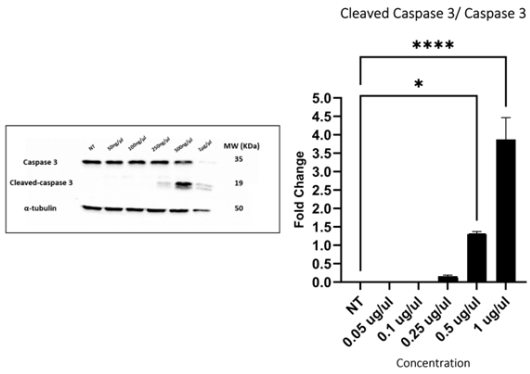

Figure S15. *Immunoblotting analysis of Caspase 3 and cleaved caspase 3 levels and relative densitometric analysis in EGCs at 6 hours p.t. after digested gliadin treatment (0.05 µg/µL, 0.1 µg/µL, 0.25 µg/µL, 0.5 µg/µL, 1 µg/µL). α-tubulin expression was used as housekeeping control. Experiments were performed in triplicate. Data are reported as mean ± SD. The asterisks indicate p<0.05 (*), p<0.01 (**) or p<0.001 (***), p<0.0001(****) One-Way ANOVA, compared with relative control cells.*

Supplementary Figure S16

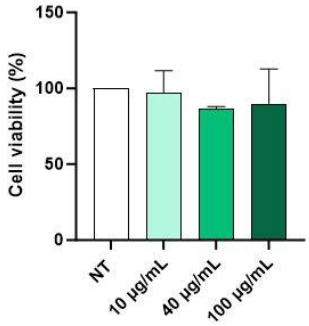

Figure S16. *MTS assay of murine astrocytes treated with increasing concentrations of p31-43 (10, 20, 40, 50, 100, 200, and 400 µg/mL). Analysis was performed 24 hours p.t. The values on the Y-axis, reported as mean ± SD, indicate cell viability (%) normalized with that of control cells. The asterisks indicate p<0.05 (*), p<0.01 (**) or p<0.001 (***), p<0.0001(****) One-Way ANOVA, compared with relative control cells. Experiments were performed in triplicate*

Supplementary Figure S17

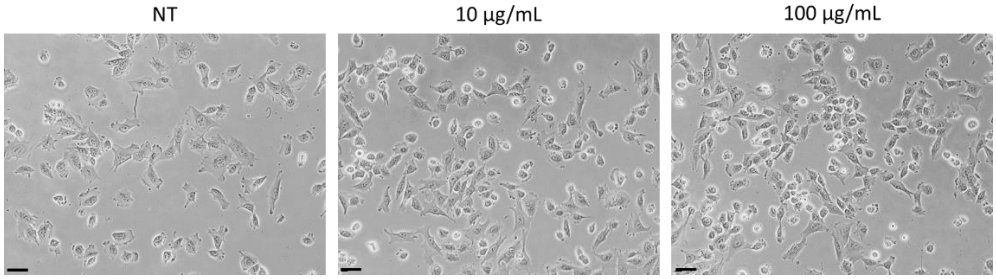

Figure S17. *Bright microscopy analysis of hEGC-ClK cells treated with 10 µg/ml and 100 µg/ml of p-3143. Images were visualized through the Nikon Eclipse TS-100 phase-contrast microscope. Cells were analyzed 24 hours p.t. Images were collected at 10X magnification. Size bars (= 10 µm) are reported.*

Supplementary Figure S18

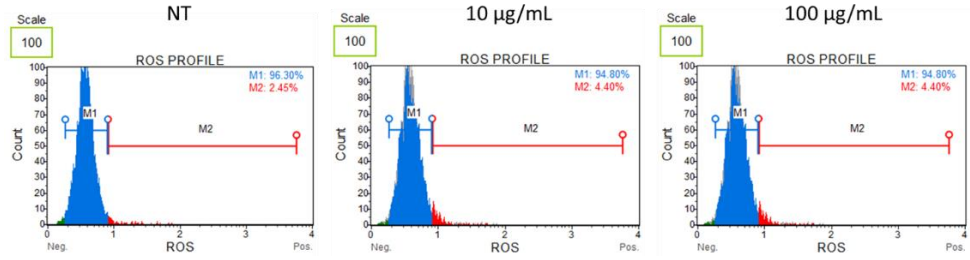

Figure S18. *Cytofluorimetric plots of intracellular ROS levels in EGCs treated with p31-43. Analysis was performed at 4 hours p.t. (10 µg/ml and 100 µg/ml). Events collected: 2000. M1: ROS – population (blue); M2: ROS+ population (red).*

Supplementary Figure S19

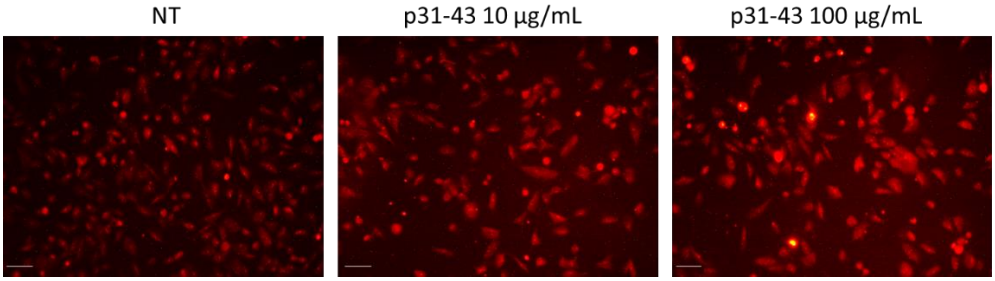

Figure S19. *Oxidative stress evaluation using the fluorescent dye DHE (1 µL/mL) by fluorescent microscope observations. Cells were treated with p31-43 at 10 µg/mL and 100 µg/mL. Scale bars (=10 µm) are reported. Pictures were collected at 4 hours p.t.*

Supplementary Figure S20

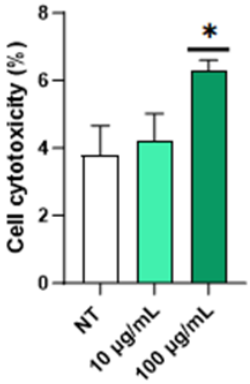

Figure S20. *LDH assay on hEGC-ClK cells treated with p31-43 (100 µg/mL) at 6 hours p.t. The values on the Y-axis, reported as mean ± SD, indicate cell cytotoxicity (%) normalized with that of control cells. The asterisks indicate p<0.05 (*), p<0.01 (**) or p<0.001 (***), p<0.0001(****) One-Way ANOVA, compared with relative control cells. Experiments were performed in triplicate.*

Supplementary Figure S21

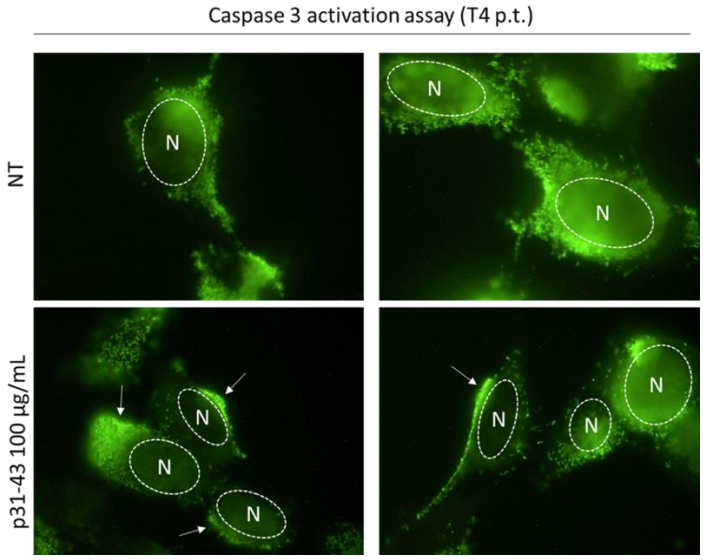

Figure S21. *Immunofluorescence analysis of caspase-3 activation. hEGC-ClK cells were treated with p31-43 (100 µg/mL) and a high-affinity DNA-binding dye linked to the DEVD peptide was added to the culture medium. Pictures were collected at 4 hours after treatment.*

Supplementary Figure S22

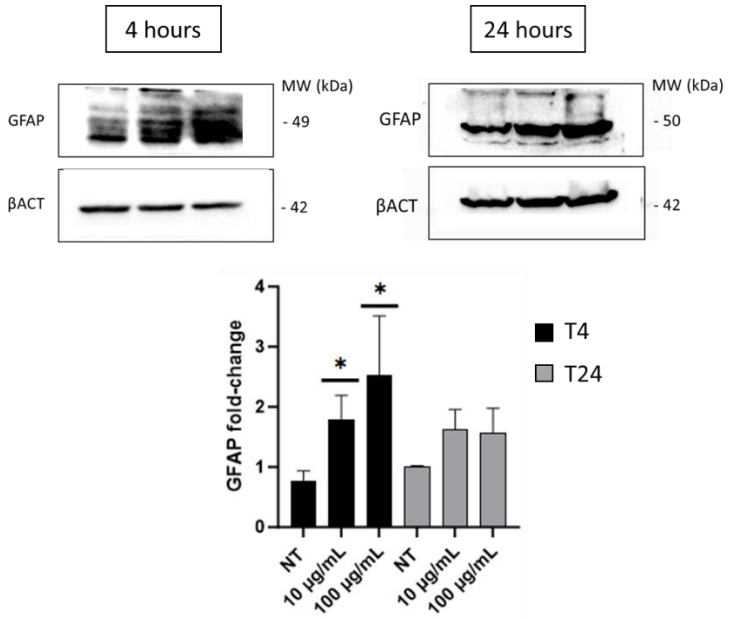

Figure S22. *Immunoblotting of GFAP levels and relative densitometric analysis in hEGCs at 4 and 24 p.t.(10 µg/mL and 100 µg/mL). β-actin expression was used as housekeeping control. Experiments were performed in triplicate. Data are reported as mean ± SD. The asterisks indicate p<0.05 (*), One-Way ANOVA, compared with relative control cells.*

Supplementary Figure S23

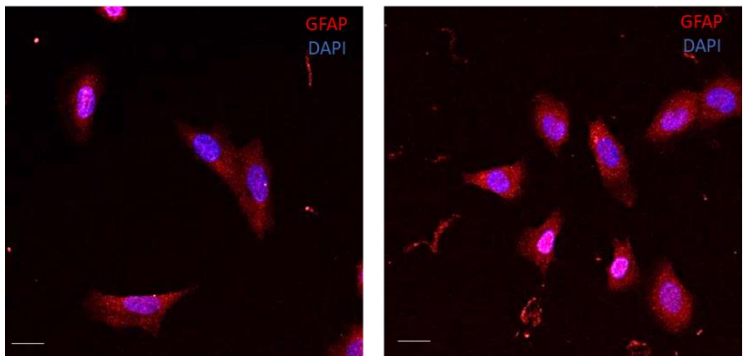

Figure S23. *Immunofluorescence of GFAP in hEGCs cells treated with p31-43 (100 µg/mL). The analysis was performed using a specific anti-GFAP antibody conjugated with AlexaFluor633. Nuclei were stained with DAPI. Scale bars (=10 µM) are reported. Pictures were collected at 24 hours p.t.*

Supplementary Figure S24

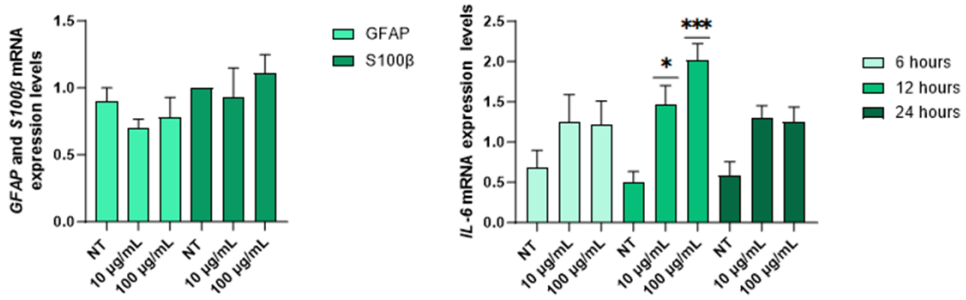

Figure S24. *GFAP, S100β, and IL-6 mRNA expression level analysis in mEGCs cells treated with p31-43 (10 and 100 µg/mL). The expression levels of the selected genes in treated cells were compared with those of non-treated (NT) cells. In the Y-axis, relative quantification values are reported. Data are reported as mean ± SE. (*) indicate $p \leq 0.05$, (***) indicate $p \leq 0.001$, ANOVA Kruskal-Wallis. Experiments were performed on three independent biological replicas.*

Supplementary Figure S25

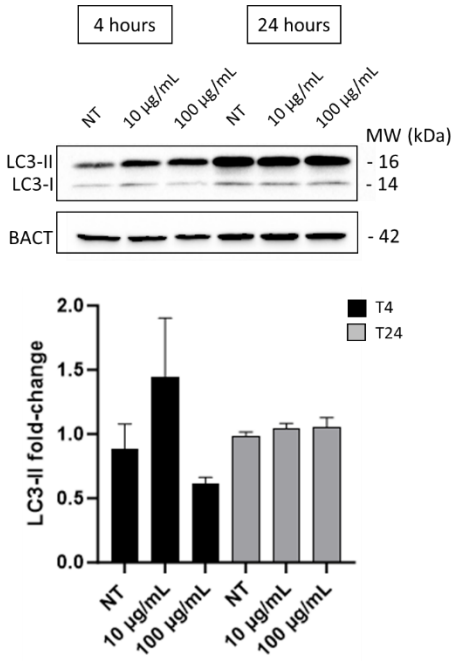

Figure S25. *Immunoblotting of LC3-II levels and relative densitometric analysis in hEGCs at 4 and 24 p.t.(10 µg/mL and 100 µg/mL). β-actin expression was used as housekeeping control. Experiments were performed in triplicate. Data are reported as mean ± SD.*

Acknowledgements

I would like to take this moment to express my deep appreciation and gratitude to the remarkable individuals who have been instrumental in the successful completion of my PhD thesis.

To Professor Sergio Comincini, my esteemed supervisor, your unwavering guidance, mentorship, and wisdom have been the cornerstones of this academic journey. Your expertise and commitment to the field have shaped my academic growth in immeasurable ways.

I also extend my sincere thanks to Dr. Federico Manai, my co-supervisor, for your insightful advice, encouragement, and the collaborative spirit you brought to this research. Your presence has been instrumental in shaping the direction of this work.

A special note of appreciation goes to Professor Gianluca Matteoli, my supervisor at KU Leuven. Your insights, support, and the international perspective you brought to my research have been truly transformative.

I would like to express my appreciation to Professor Anita Ferraretto, Professor Dmitry Lim, and Professor Bram Verstockt for finding the time to read this thesis and providing comments. Your feedback and evaluation have been instrumental in refining the quality and rigor of this work.

I would also like to thank my lab collegues, both in Pavia and Leuven. I am profoundly thankful for the countless hours we have spent together in the lab, for the laughter we have shared, and for the lessons I have learned from you all.

To all those who have played a part, big or small, in this academic endeavor, your contributions are greatly appreciated. Thank you for your dedication and support in helping me reach this milestone. This thesis would not have been possible without the support of these remarkable individuals, and I am deeply thankful for their guidance and encouragement throughout this journey.

frontiers | Frontiers in Cellular Neuroscience

TYPE Original Research
PUBLISHED 20 April 2023
DOI 10.3389/fncel.2023.1170309

OPEN ACCESS

EDITED BY
Valerio Magnaghi,
University of Milan, Italy

REVIEWED BY
Dmitry Lim,
University of Eastern Piedmont, Italy
Giuseppina D'Alessandro,
Sapienza University of Rome, Italy

*CORRESPONDENCE
Federico Manai
federico.manai01@universitadipavia.it

†These authors have contributed equally to this work and share first authorship

SPECIALTY SECTION
This article was submitted to Cellular Neurophysiology, a section of the journal Frontiers in Cellular Neuroscience

RECEIVED 21 February 2023
ACCEPTED 22 March 2023
PUBLISHED 20 April 2023

CITATION
Zanoletti L, Valdata A, Nehlsen K, Faris P, Casali C, Cacciatore R, Sbarsi I, Carriero F, Arfini D, van Baarle L, De Simone V, Barbieri G, Raimondi E, May T, Moccia F, Bozzola M, Matteoli G, Comincini S and Manai F (2023) Cytological, molecular, cytogenetic, and physiological characterization of a novel immortalized human enteric glial cell line. *Front. Cell. Neurosci.* 17:1170309. doi: 10.3389/fncel.2023.1170309

Cytological, molecular, cytogenetic, and physiological characterization of a novel immortalized human enteric glial cell line

Lisa Zanoletti[1,2†], Aurora Valdata[1†], Kristina Nehlsen[3], Pawan Faris[1,4], Claudio Casali[1], Rosalia Cacciatore[5], Ilaria Sbarsi[5], Francesca Carriero[1], Davide Arfini[1], Lies van Baarle[2], Veronica De Simone[2], Giulia Barbieri[1], Elena Raimondi[1], Tobias May[3], Francesco Moccia[1], Mauro Bozzola[6], Gianluca Matteoli[2], Sergio Comincini[1] and Federico Manai[1*]

[1]Department of Biology and Biotechnology "L. Spallanzani", University of Pavia, Pavia, Italy, [2]Department of Chronic Diseases and Metabolism (CHROMETA), KU Leuven, Leuven, Belgium, [3]InSCREENeX GmbH, Braunschweig, Germany, [4]Department of Biology, College of Science, Salahaddin University-Erbil, Erbil, Iraq, [5]Immunohematology and Transfusion Service, I.R.C.C.S. Policlinico San Matteo, Pavia, Italy, [6]University of Pavia, Pavia, Italy

Enteric glial cells (EGCs), the major components of the enteric nervous system (ENS), are implicated in the maintenance of gut homeostasis, thereby leading to severe pathological conditions when impaired. However, due to technical difficulties associated with EGCs isolation and cell culture maintenance that results in a lack of valuable *in vitro* models, their roles in physiological and pathological contexts have been poorly investigated so far. To this aim, we developed for the first time, a human immortalized EGC line (referred as ClK clone) through a validated lentiviral transgene protocol. As a result, ClK phenotypic glial features were confirmed by morphological and molecular evaluations, also providing the consensus karyotype and finely mapping the chromosomal rearrangements as well as HLA-related genotypes. Lastly, we investigated the ATP- and acetylcholine, serotonin and glutamate neurotransmitters mediated intracellular Ca^{2+} signaling activation and the response of EGCs markers (*GFAP*, *SOX10*, *S100β*, *PLP1*, and *CCL2*) upon inflammatory stimuli, further confirming the glial nature of the analyzed cells. Overall, this contribution provided a novel potential *in vitro* tool to finely characterize the EGCs behavior under physiological and pathological conditions in humans.

KEYWORDS

enteric glial cells, enteric nervous system, transgene immortalization, viral transduction, immortalized human cell line

1. Introduction

The Enteric Nervous System (ENS), known as "the second brain" in the gut, regulates gastrointestinal (GI) physiology, by controlling intestinal motility, secretion, blood circulation, and inflammatory response (Rühl et al., 2004; Bassotti et al., 2007). Although for many years enteric glial cells (EGCs), the largest component of the ENS, have been ascribed the unique role

as supportive to neuronal functions by supplying nutrients to the enteric neurons, in the last decades, they have been known to be involved in several biological processes such as the regulation of intestinal homeostasis, maintenance of the epithelial barrier integrity, and gut defense (Seguella and Gulbransen, 2021). EGCs were originally identified in the last years of the XIX century, while detailed morphological analyses and identification of specific markers were performed secondly (Gabella, 1972; Jessen and Mirsky, 1980; Gabella, 1981). These astrocyte-like cells are primarily present in the submucosal and myenteric plexuses with ratios of 1.3 and 5.9 compared to neurons, respectively (Hoff et al., 2008). Based on their location in the gut, four types of EGCs can be distinguished. Myenteric glia and submucosal glia (Type I) are associated with neuronal cell bodies in the myenteric and submucosal plexus, while type II EGCs are located within the nerve fiber bundles connecting myenteric glia. Type III cells are in the mucosa and elongated type IV cells in the longitudinal muscle layer (Hanani and Reichenbach, 1994; Gulbransen and Christofi, 2018; Seguella and Gulbransen, 2021). The main markers for EGCs identification are GFAP, S100β, and SOXE (Sox8/9/10). GFAP is the primary protein involved in the formation of intermediate filaments (IF) in astrocytes. This protein is expressed both in Central (CNS) and Peripheral Nervous Systems (PNS) in different isoforms and splice variants, thus contributing to different biological processes, such as injury healing, gliosis, and inflammation (Middeldorp and Hol, 2011; Yang and Wang, 2015). S100β is a cytoplasmic EF-hand type Ca^{2+}-Zn^{2+} binding protein of the S100 family, which plays a key role in maintaining microenvironmental homeostasis as well as in inflammatory responses in a concentration-dependent manner. Particularly, over-expression and secretion of S100β lead to the NF-kB-mediated production of iNOS and nitric oxide (NO) by binding to Receptor for Advanced Glycation Endproducts (RAGE), with the consequent activation of MyD88 (Rühl, 2005; Cirillo et al., 2011a). Finally, SOXE is a transcription factor group expressed in the mature EGCs, mainly adopted for quantitative analyses (Hoff et al., 2008; De Giorgio et al., 2012).

Recent studies demonstrated the involvement of enteric glia in inflammation and immune response by regulating neuroendocrine signaling and antigen-presenting mechanisms (Gulbransen and Christofi, 2018). Moreover, EGCs seem to be involved in the pathogenesis of different intestinal disorders, such as inflammatory bowels diseases (IBDs) and celiac disease, and recently they have been identified as part of the tumor microenvironment in colorectal cancer, pointing to these cells as new potential therapeutic targets (Savidge et al., 2007; Cirillo et al., 2009; von Boyen et al., 2011; Li et al., 2018; Pochard et al., 2018; Valès et al., 2019). However, due to technical difficulties, *in vitro*, *ex vivo,* and *in vivo* enteric glia studies are limited (Rühl et al., 2001a; Middlemiss et al., 2002; Grundmann et al., 2015; Rosenbaum et al., 2016; Le Berre-Scoul et al., 2017; D'Errico et al., 2018; Wang et al., 2018; Cerantola et al., 2020). Indeed, as reported by Soret et al. (2013), although for *in vitro* experiments EGCs can be isolated with different methods from guinea pig-, mouse-, rat-, and human- specimens, these methodologies require several passages that can affect the overall quality. Hence, possible cross-contamination with other cell types and EGCs de-differentiation represent a critical point in the study of their role in health and disease, thereby leading to the development of new standardized EGC models.

In this work, by making use of an established lentiviral transduction protocol (Lipps et al., 2018), we generated a novel immortalized human EGC line derived from the myenteric plexus (MP) which may represent a valuable tool to bridge the gap in *in vitro* EGCs knowledge.

2. Materials and methods

2.1. Human and murine EGCs isolation and established human cell lines culture conditions

Primary human EGCs (hEGCs) were isolated from the colon of a 75-year-old female donor. The tissue was obtained from Tissue Solutions (Glasgow, Scotland, United Kingdom) under ethics approval and donor consent (Declaration of Helsinki 1964 and its later amendments). Tissue (roughly 2 cm^3) was collected and stored in HypoThermosol medium (BioLife Solutions, Bothell, WA, United States). The myenteric plexus (MP) was then isolated as described (Soret et al., 2013), cut into 1–2 mm fragments, and incubated for 20 min at 37°C. The fragments were homogenized with repeated pipetting in pre-warmed Digest Medium (6 mL/g of bioptic material) composed of Liver Digest Medium (Thermo Fisher Scientific, Waltham, MA, United States) supplemented with 2000 U of DNAse I, 10 mg of Liberase (Sigma-Aldrich, Burlington, MA, United States), 1 mL of trypsin 2.5% and 30 µL (stock solution 100 U/mL) of collagenase type I (Thermo Fisher Scientific). After incubation, the cell/tissue suspension was passed through a nylon mesh (100 µm) and centrifuged twice for 5 minutes at 200 x g. Cells were then cultivated with appropriate hECGs medium in plates pre-coated with hAEC Coating solution (InSCREENeX, Braunschweig, Germany) at 37°C and 5% CO_2.

Murine primary EGCs (mEGCs) were isolated as described (Ibiza et al., 2016). Briefly, the muscularis layer and the submucosa were separated using a dissection microscope. The lamina propria was then scraped mechanically from the underlying mucosa using a coverslip. The isolated tissue was subsequently digested with Liberase and DNase I (Sigma-Aldrich) in RPMI (Euroclone, Milan, Italy) supplemented with 1% HEPES, 1% sodium pyruvate, 1% L-glutamine, 0.1 mg/mL streptomycin, 100 units/mL penicillin, and 0.1% of β-mercaptoethanol (Sigma-Aldrich) for 40 min at 37°C. The cell suspension was then passed using a 100 µm filter.

Human established low-grade astrocytoma Res186 (Bobola et al., 2005), high-grade astrocytoma T98G cells, and BJ hTERT human fibroblasts (ATCC, Guernsey, Ireland), used as controls, were cultivated in D-MEM medium supplemented with 10% FBS, 100 units/mL penicillin, 0.1 mg/mL streptomycin and 1% L-glutamine (Euroclone), at 37°C and 5% CO_2 atmosphere.

2.2. hECGs lentiviral transduction and identification of integrated genes

hEGCs were immortalized as described (Lipps et al., 2018). In detail, hEGCs were transduced with self-inactivating lentiviral vectors after they reached 80% of confluence through different rounds of lentiviral infection with a MOI between 1 and 5. The lentiviral transduced genes used are listed in Supplementary Table S1. Cells were incubated overnight with lentiviral vectors at 37°C/5%

CO_2 in culture medium supplemented with Polybrene (8 µg/mL). After medium removal, 30 independent clones were selected for growing features. Among these, a relevant clone, hereafter referred to as ClK, was selected for further characterization and the cumulative population doubling level (cPDL) was calculated, according to ATCC's recommendations. The integrated lentiviral genes were then confirmed through a PCR scheme, using a consensus forward primer (GGAGGCCTAGGCTTTTGCAA) located within the SV40 promoter sequence coupled with genes-specific reverse primers (Supplementary Table S1). Genomic DNA of the transduced cells was extracted with DNAzol reagent (Gibco Fisher Scientific, Dublin, Ireland), according to the manufacturer's instructions. PCR was performed on 0.5 µg of template using the Mango-Taq Polymerase Kit (PJK-Biotech, Kleinblittersdorf, Germany). The adopted amplification protocol consisted of 40 cycles: 94°C (30 s)/55°C (45 s)/72°C (45 s). The presence/absence of the investigated genes was evaluated by agarose gel (2% *w/v*) electrophoresis.

2.3. Molecular characterization of ClK clone

Cumulative population doubling level (cPDL) was calculated following the ATCC guidelines, specifically $n = 3.32$ (logUCY-logl) + X, with n indicating the final PDL number at a given subculture, UCY representing the cell yield at that point, l indicating the cell number used as inoculum to start the subculture, and X representing the doubling level of the inoculum used to initiate the subculture. The expression of the enteric glial-specific markers (i.e., GFAP, SOX10, and S100β) and HLA class II molecules was analyzed using immunofluorescence. To this purpose, ClK cells (2×10^4) were seeded on coverslips pre-coated for 2 h at 37°C/5% CO_2 with huAEC Coating Solution (InSCREENeX) and cultured for 24 h. The fixation step was performed after a wash with PBS using 4% paraformaldehyde (PFA) for 15 min at room temperature (RT). Again, the coverslips were washed three times with PBS and incubated with 0.1% saponin (*v/v*) in PBS for 15 min (RT). Cells were then incubated for 1 h at RT with primary antibodies anti-GFAP, anti-SOX10, anti-S100β (Immunological Sciences, Rome, Italy), and anti-HLA-DQA1 (Abcam, Cambridge, United Kingdom) diluted 1:30 in 5% non-fat milk in PBS (*w/v*). After three washes with PBS, species-specific AlexaFluor633- and AlexaFluor488-labeled secondary antibodies (Thermo Fisher Scientific) were used at final dilution of 1:30 for 1 h (RT). Finally, after three washes with PBS, slides were stained with DAPI (0.4 µg/mL) (Sigma-Aldrich) for 8 min (RT). After a wash with distilled water, slides were mounted adding a drop of Dako Fluorescence Mounting Medium (DAKO, Jena, Germany) and sealed. Fluorescence signals were visualized using LEICA TCS SP8 STED 3X confocal microscope (Leica, Wetzlar, Germany). Specificity of the signal was assessed through negative controls, e.g., anti-Naspin antibody (Immunological Sciences).

The expression of CD31, CD45, CD271, and CD326 proteins was analyzed by flow cytometry. ClK cells (5×10^4) were seeded in a pre-coated 6-multiwell plate until they reached 100% of confluence (48 h post-seeding). Then, cells were detached and centrifuged at 500 x g for 3 min at 4°C. After the removal of the supernatant, cells were stained with L/D efluor (Thermo Fisher Scientific) diluted 1:400 in PBS for 30 min at 4°C in the dark. Cells were then centrifuged as described and Fc block (1:100 in FACS buffer) was performed for 15 min at 4°C. After this step, cells were centrifuged at 500 x g for 3 min and incubated with extracellular staining mix containing specific anti-CD31-PE (Diluition: 1:300), CD45-PE-Cy5 (Diluition: 1:300), CD271-PE and CD326-PE-Cy7 (Diluition: 1:100) primary antibodies (BioLegend, San Diego, CA, United States) for 20 min at 4°C in the dark. Finally, cells were centrifuged as described, washed in appropriate buffer, and then resuspended into 200 µL of FACS buffer. The analysis was performed by BD FACSymphony A5 flow cytometer (BD, Franklin Lakes, NJ, United States) setting Forward Scatter (FSC) > 200 to exclude cellular debris.

2.4. Real-time PCR expression analysis

Total RNA was extracted from ClK cells with RNeasy Plus Micro Kit (QIAGEN, Hilden, Germany) according to manufacturer's instructions and RNA quantification was performed using Nanodrop 1,000 (Thermo Fisher Scientific, Waltham, MA, United States). *GFAP*, *SOX10*, *S100β*, *PLP1*, and *GAPDH* cDNAs were obtained using random hexamers primers (Applied Biosystems, Forster City, CA, United States) as reported (Comincini et al., 2013). The genes, whose forward and reverse primers are reported in Supplementary Table S2, were amplified with LightCycler 480 SYBR Green I Master (Roche, Basel, Switzerland). Real-time PCR was performed using 2 µg of each cDNA amplified by means of Step-One PCR instrument (Applied Biosystems), with the following thermal profile: incubation of 95°C for 300 s, followed by 45 cycles of denaturation at 95°C for 10 s, annealing at 60°C for 15 s and elongation at 72°C for 15 s with fluorescence collection. After incubation at 95°C for 5 s, melting curve analysis was performed from 60 to 95°C, collecting data every centigrade degree (5 readings/°C). Samples were analyzed in duplicate, data were normalized to *GAPDH* and relative quantification (Schmittgen and Livak, 2008) was employed to calculate relative changes in gene expression.

2.5. HLA genotyping

Genomic DNA was isolated from ClK cells (1×10^6) using Maxwell CSC Blood DNA automated Purification System (Promega, Madison, WI, United States) following the manufacturer's instructions. HLA class I and II genotyping were performed with sequence-specific oligonucleotide-primed polymerase chain reaction (PCR-SSO) using the LABScan3D system (One Lambda Inc., Canoga Park, CA, https://www.graphpad.com/scientific-software/prism/) based on the Luminex xMAP technology (Luminex, Austin, Texas, United States). This technology was applied with LABType commercial kits (One Lambda Inc.) for class I HLA-A, B, C, and class II HLA-DRB1, DQA1, DQB1 genotyping, CWD (Common and Well-Documented alleles) and XR (High Resolution). The adopted amplification protocol occurred in 5 cycles (96°C x 20 s/70°C x 20 s/62°C x 20 s) with additional 30 cycles (96°C x 10 s/70°C x 15 s/62°C x 20 s). Amplifications were then evaluated by 2% agarose pre-casting electrophoresis.

2.6. Metaphase spread preparation

ClK cells (6×10^5 at passage 21, p21) were seeded in 10 cm diameter Petri dishes. After 24 h, to accumulate metaphase-blocked cells, nocodazole (Sigma-Aldrich) was added to the cultures at a final concentration of 1.34 µM for 2 h at 37°C and 5% CO_2. Subsequently, cells were detached using 0.5 ml of trypsin–EDTA (Thermo FisherScientific) and resuspended in PBS. Samples were centrifuged at 2200 x g for 10 min and resuspended in 10 ml of pre-warmed hypotonic solution (75 mM KCl) for 15 min at 37°C. Then, after another centrifugation at 2200 x g for 10 min, the pellet was resuspended in 10 ml of fixative solution (methanol and acetic acid, 3:1) for 45 min at −20°C. This passage was repeated once using fresh fixative solution. Cells were then centrifuged as before and resuspended in an appropriate volume of fresh fixative solution, according to the pellet size. Finally, the cell suspension was dropped on microscope slides pre-treated with fixative solution, and air-dried. Slides were then stained with DAPI (0.4 µg/mL) (Sigma-Aldrich, Burlington, MA, United States) for 8 min (RT). After a wash with distilled water, slides were mounted adding a drop of Dako Fluorescence Mounting Medium (DAKO) and sealed. Visualization was performed using a fluorescence microscope Axioplan (Zeiss, Oberkochen, Germany) provided with a Charged-Couple Device (CCD) camera (Photometrics). A sample of 100 images was collected and analyzed.

2.7. BAC extraction

Specific human BAC probes, with pBACe3.6 backbone, were purchased from BACPAC Human Resources (Emeryville, CA, United States). The probes used for Fluorescence *in Situ* Hybridization (FISH) experiments were RP11-160F8 (5q11.2, coordinates: 54.033.661–54.188.673) and RP11-69A18 (5q35.1, coordinates: 171.790.208–171.957.002). The purified *E. coli* LB stabs were propagated on LB agar with chloramphenicol (12.5 µg/mL) and single colonies were then isolated and expanded overnight in LB with antibiotic at 37°C in agitation. The obtained cultures were collected and centrifuged at 9600 x g for 30 min. After supernatant removal, the pellet was resuspended in 5 mL of P1 buffer (Tris–HCl 50 mM, pH 8; EDTA 10 mM; RNasi A 100 µg/mL) before the addition of 10 mL of P2 buffer (NaOH 200 mM; SDS 1%). The tubes were incubated for 5 min after gentle mixing. Later, 10 mL of P3 buffer (K-acetate 3 M) were added and the subsequent incubation was performed for 15 min at 4°C. The tubes were centrifuged at 9600 x g for 1 h and the supernatant was collected and centrifuged again for 45 min at 9600 x g. The obtained sample was loaded and purified using a QIAGEN-tip 100 column from the Qiagen Plasmid Mini Kit (QIAGEN, Hilden, Germany), according to manufacturer's instructions. The final elution was centrifuged at 9600 x g for 45 min after the addition of 3.5 mL of isopropanol. The pellet was then resuspended in 70% ethanol and centrifuged again at 9600 x g for 20 min. After air-drying, the pellet was finally resuspended in a proper volume of sterile water. The purified BACs were digested using *EcoRI* enzyme and loaded onto 1% agarose gel to verify the presence of the inserts. BAC DNA quantification was performed using NanoDrop 1,000 spectrophotometer (Thermo Fisher Scientific).

2.8. Fluorescence *in situ* hybridization

For probes labeling, i 4 µL of Biotin/Digoxigenin-Nick Translation Mix (Roche), 1 µg of BAC probes, and sterile water were added to reach the final volume of 20 µL. The microtubes were then incubated at 15°C for 3 h. The reaction of nick translation was blocked using 1 µL of EDTA (25 mM, pH 8) before the addition of 10 µL of salmon sperm DNA (1 µg/µL), 2 µL of dextran blue (stock solution 1.8%, filtered), 10 µL of Roche human COT DNA (1 µg/µL), 17.2 µL of ammonium acetate (2.14 M, pH 8) and 151 µL of pre-refrigerated 100% ethanol. The samples were incubated for 2 h at −20°C and then centrifuged at 1100 x g for 20 min (RT). After supernatant removal, the pellets were dried, resuspended in 35 µL of hybridization solution (25% formamide, 10% dextran sulfate, 1% tween-20, 2X SSC), and stored at −20°C. Next, slides were incubated overnight at 37°C and then denatured for 2.5 min at 78°C after the addition of 150 µL of 70% formammide (Sigma-Aldrich), 2X saline sodium citrate (SSC, Sigma-Aldrich), and sterile water. After the denaturation step, slides were treated with 2X SSC (4°C) for 2.5 min and then dehydrated through the ethanol series (75–95-100%), 3 min each. Probes were denatured at 80°C for 8 min and then stored in ice to block the reaction.

For *in situ* hybridization and probe detection, on each slide, 15 µL of the labeled probe were added. The slides were then stored overnight at 37°C in a moisture chamber. Post-hybridization washes (3 washes of 5 min each) were performed using formamide 50% 2X SSC at 45°C, followed by 3 washes of 5 min with 2X SSC at 45°C. Slides were immediately permeabilized at 37°C for 30 min by adding 60 µL of 3% BSA in 0.1% Tween-20 4X SSC. Probes were incubated at 37°C for 30 min with anti-DIG and anti-BIO antibodies (Abcam), respectively conjugated to rhodamine and FITC fluorophores and diluted in 1% BSA, 0.1% Tween20 and 4X SSC. Three washes of 5 min each in 4X SSC and 0.1% Tween20 were then performed at 42°C. Slides were then treated with 60 µL of species-specific secondary antibodies labeled with rhodamine and FITC (1%BSA, 0.1% Tween20, 4X SSC) and further incubated at 37°C for 30 min. Two washes were performed as previously described, followed by a third one in 4X SSC (RT). Slides were covered with DAPI (0.4 µg/mL) (Sigma-Aldrich) and incubated for 8 min (RT). After a wash with distilled water, slides were further mounted by adding a drop of Dako Fluorescence Mounting Medium (DAKO) and sealed. Finally, probe detection was performed using an Axioplan fluorescent microscope (Carl Zeiss) provided with a Charged-Couple Device (CCD) camera (Photometrics).

2.9. Electron microscopy analysis

ClK ultrastructure analysis was performed by transmission electron microscopy (TEM). Cells (1×10^6, p21) were centrifuged at 800 x g for 5 min and fixed with 2.5% glutaraldehyde in PBS for 2 h (RT). Cells were then washed and rinsed in PBS (pH 7.2) overnight and post-fixed in 1% aqueous OsO_4 (Sigma-Aldrich) for 1 h (RT).

Cells were pre-embedded in 2% agarose in water, dehydrated in acetone, and finally embedded in epoxy resin (Electron Microscopy Sciences, EM-bed812). Ultrathin sections (60–80 nm) were collected on nickel grids and stained with uranyl acetate and lead citrate. The specimens were observed with a JEM 1200 EX II (JEOL, Peabody, MA, United States) electron microscope, equipped with the MegaView G2 CCD camera (Olympus OSIS, Tokyo, Japan) and operating at 120 kV. The morphology of organelles (at least 20 for each type) was then analysed by two independent evaluators.

2.10. Flow cytometry analysis

For ClK cells (p21), mitochondrial membrane potentials, intracellular reactive oxygen species (ROS), and cell proliferation indexes were determined through flow cytometry analyses using Muse Cell Analyzer and dedicated kits (MitoPotential, Oxidative Stress and Ki-67 Assays Luminex), as described (Carriero et al., 2021; Slivinschi et al., 2022).

For MitoPotential aanalysis, after trypsinization and collection, cells were washed in Assay Buffer 1X, and resuspended in 100 µL of the same solution. Then, 95 µL of pre-diluted MitoPotential Reagent (1:1000) were added and cells were subsequently incubated for 25 min at 37°C. Finally, 5 µL of 7-AAD were added and the samples were analyzed after an incubation of 5 min in the dark (RT).

For oxidative stress analysis, after trypsinization and collection, cells were washed in Assay Buffer 1X and the pellet was resuspended in 10 µL of Assay Buffer 1X. Then, 190 µL of pre-diluted Oxidative Stress Reagent (1:800) were added and cells were subsequently incubated for 30 min at 37°C before the analysis. For Ki-67 proliferation analysis, after trypsinization and collection, cells were washed with PBS and resuspended in 1X Fixation solution for 15 min (RT). Then, cells were treated with Permeabilization solution for 15 min (RT) and subsequently incubated with Assay Buffer 1X for the same time interval. Subsequently, Muse Hu IgG1-PE (isotypic control) or Hu Ki67-PE antibodies were added, mixed, and incubated for 30 min (RT) before the analysis.

2.11. Ca^{2+} signals measurements

Ca^{2+} imaging was carried out by bathing EGCs in Physiological Salt Solution (PSS, 150 mM NaCl, 6 mM KCl, 1.5 mM CaCl2, 1 mM $MgCl_2$, 10 mM glucose, 10 mM HEPES). In Ca^{2+}-free solutions, Ca^{2+} was replaced with 2 mM NaCl with the addition of 0.5 mM EGTA. Solutions were titrated to pH 7.4 with NaOH. The osmolarity of PSS was measured with an osmometer (WESCOR 5500, Logan, UT, United States) and was equal to 338 mmol/Kg.

Ca^{2+} imaging was performed as described (Faris et al., 2020; Astesana et al., 2021). Briefly, cells (2×10^4) were plated on round glass (8 mm) coverslips coated with huAEC Coating Solution (In-SCREENeX). The next day cells were loaded with fura-2 acetoxymethyl ester at the final concentration of 4 µM (Fura-2/AM, 1 mM stock in DMSO) in PSS for 30 min at 37°C and 5% CO2. After de-esterification in PSS for 15 min, the coverslip was mounted in a small size Petri dish, and cells were observed under an upright epifluorescence Axiolab microscope (Carl Zeiss) equipped with a Zeiss 40X Achroplan objective (water-immersion, 2.0 mm working distance, 0.9 numerical aperture). Cells were alternatively excited at 340 and 380 nm by using a filter wheel (Lambda 10, Sutter Instrument, Novato, CA, United States). Fluorescent emission was detected at 510 nm using an Extended-ISIS CCD camera (Photonic Science, Millham, United Kingdom). The fluorescent signals were measured and plotted on-line from 10 up to 40 selected regions of interest (ROIs), each corresponding to a well-defined single cell. The intracellular Ca^{2+} concentration was monitored by measuring for each ROI the ratio of the mean fluorescence emitted at 510 nm when exciting alternatively at 340 and 380 nm (Ratio F340/F380). An increase in $[Ca^{2+}]i$ causes an increase in the ratio (Faris et al., 2020; Astesana et al., 2021). Ratio measurements were performed and plotted on-line every 3 s. All experiments were conducted at RT (22–24°C).

2.12. Statistical analysis

The data were analyzed using the statistical software GraphPad Prism 9.1.2.[1] Data obtained from flow cytometry experiments are presented as mean ± SE. Differences were considered statistically significant when $p \leq 0.05$. The statistical tests used for each experiment are reported in figure legends. All the Ca^{2+} signaling data were obtained from at least three different batches of ClK cells. Each trace shown is the average of the Ca^{2+} tracings recorded from multiple cells displaying a similar Ca^{2+} activity within the same field of view. The peak amplitude of ATP-induced intracellular Ca^{2+} release and entry were measured by evaluating the difference between the F340/F380 ratio at the peak of the Ca^{2+} response and the mean F340/F380 ratio of 1 min baseline recording before agonist addition. Pooled data are presented as mean ± SE, and statistical significance ($p \leq 0.05$) was evaluated by One-Way ANOVA analysis. The number of cells measured for each experimental condition is indicated in, or above, the corresponding bar histogram.

3. Results

3.1. Generation of immortalized EGCs

Primary hEGCs were isolated from a human intestinal biopsy and then transduced with lentiviral vectors carrying 33 different genes (Supplementary Table S1), as previously described (Lipps et al., 2018). A total of 30 clones were selected according to their proliferative rate and expanded for two months. Among these, one relevant clone (hereafter referred to as ClK) was selected for further investigations according to its morphological characteristics and growth rate. PCR analysis on ClK cells identified 8 integrated transgenes, i.e., *Core*, *BMI1*, *E6*, *E7*, *ID1*, *MYC*, *Nanog*, and *REX* (Supplementary Figure S1). As highlighted in Figure 1A, ClK cells showed a similar morphology to primary mouse (mEGCs) and human (hEGCs) ones. Subsequently, the cumulative population doubling/days (cPDL) was calculated for ClK cells and compared with that of primary hEGCs. As shown in Figure 1B, the selected clone showed increasing cPDL compared to

1 https://www.graphpad.com/scientific-software/prism/

10.3389/fncel.2023.1170309

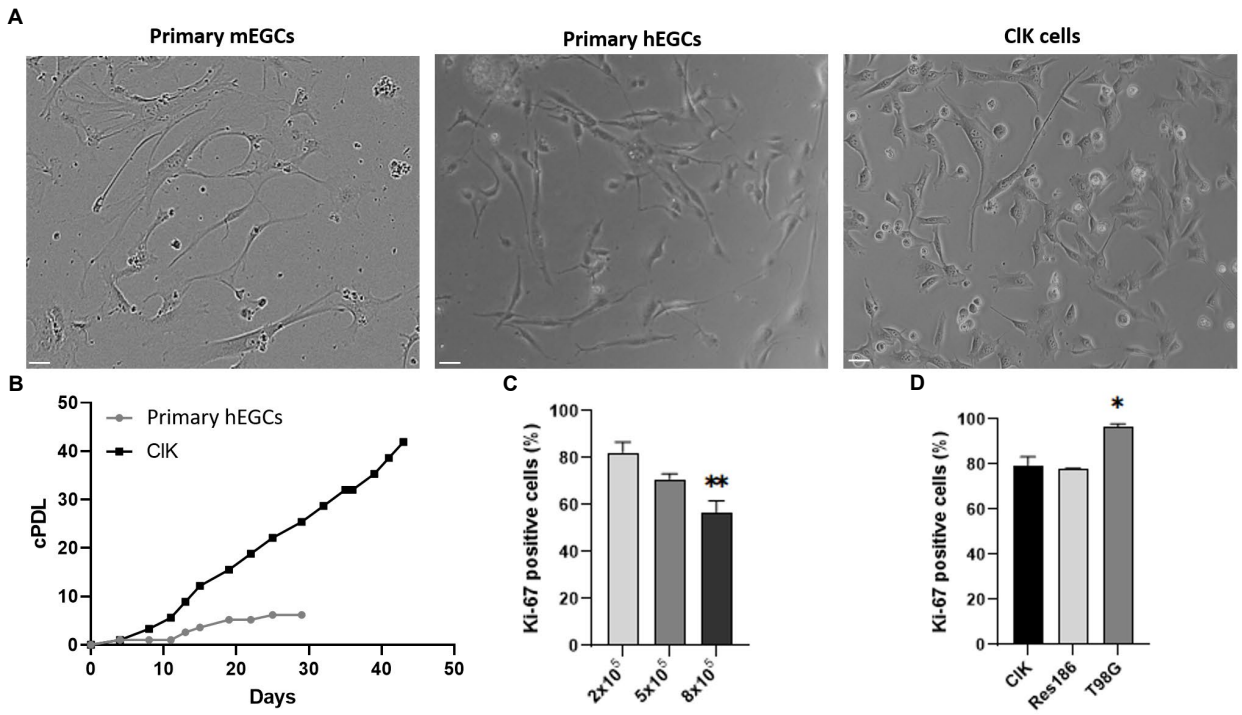

FIGURE 1
Comparative analysis of ClK morphology and proliferation. **(A)** Optical microscope analysis (brightfield) of primary hEGCs (2days post-isolation), primary mEGCs (2days post-isolation), and ClK cells (p21). Size bars (= 10μm) are reported. **(B)** Cumulative population doublings (cPDL) of primary hEGCs and ClK cells following a time-kinetics. Mock-infected control cells died 10days after infection (data not shown). cPDL values are reported in Supplementary Table S3. **(C)** Percentage of Ki-67 positive ClK cells at different cells concentrations (i.e., 2–5-8×10^5). On X-axis is reported the number of cells whereas on Y-axis the percentage of cells positive to Ki-67. (**) indicates $p<0.01$, ANOVA One-Way compared with the lower concentration. **(D)** Comparison of the percentages of Ki-67 ClK positive cells with human low- (Res186) and high-grade astrocytoma (T98G) established cell lines, all at 2×10^5. (*) indicates $p<0.05$, ANOVA One-Way, compared with ClK cells. Experiments were performed on three independent biological replicas. Corresponding cytofluorimetric plots are reported in Supplementary Figure S2.

primary hEGCs, which reached a plateau after 19 days. Furthermore, primary hEGC growth stopped after 29 days and became senescent, thus leading to the primary cell culture death after subculturing. ClK cells have been already expanded until passage 35, and preliminary analyses confirmed they maintain their morphology as well as the expression of the glial markers GFAP and S100β. Moreover, flow cytometry assays showed that also at this passage ClK cells have low amount of intracellular ROS levels as well as no event of mitochondrial depolarization (Supplementary Figure S2).

Basing on the assayed proliferation rates and accordingly to technical recommendations (Lipps et al., 2018), ClK cells at an early culture passage (p21) were then used for subsequent morphological, cytogenetic, molecular, and physiological analyses. Proliferation levels of ClK clone was then studied through flow cytometry analysis of the Ki-67 expression. Specifically, ClK cells were seeded at different concentrations for 24 h (2–5-8 × 10^5 in a multiwell-6) and then compared with the same concentrations of two established glioma cell lines at different malignancy grades, respectively Res186 (WHO grade I) and T98G (IV). As reported (Figure 1C), the percentage of Ki-67 positive cells significantly decreased in a concentration-dependent manner. Moreover, the amount of ClK-positive cells was comparable with those detected in Res186 cells, while they were significantly lower compared with those scored in T98G cells (Figure 1D). Furthermore, the percentage of Ki-67-positive cells in the T98G cell line did not show variations due to the cell confluence (Supplementary Figure S3).

3.2. Ultrastructural analysis and mitochondrial membrane potential (ΔΨm) measurement

Cellular and organelles morphology was investigated through ultrastructural analysis by TEM. Particularly, as reported in Figure 2A, integrity of mitochondrial shape and internal membrane crests was verified. Moreover, no significant alterations were detected in the other cellular organelles, such as Golgi apparatus and endoplasmic reticulum. Then, the mitochondrial membrane potential (ΔΨm) was studied since alterations in mitochondria functionality can affect the ΔΨm and, as a consequence, cell viability (Kroemer and Reed, 2000). Specifically, mitochondrial depolarization was assessed through flow cytometry (Figure 2B). As reported, a statistically significant low percentage of cells characterized by depolarized events were detected (i.e., depolarized live cells = 2.90%; depolarized dead cells = 1.90%) in the overall cell population. Lastly, basal intracellular reactive oxygen species (ROS) levels were investigated using flow cytometry analysis. Increased ROS levels are indeed typical of transformed or pathological cells, produced by a large variety of internal and environmental factors (Yang et al., 2018). As shown (Figure 2C), ClK cells were characterized by relatively low intracellular levels of ROS (i.e., 5.57%). Moreover, as reported in Supplementary Figure S4, ClK cells showed intracellular ROS levels similar to human primary fibroblasts, while human primary retinal endothelial cells as well as glioma cell lines (i.e.,

10.3389/fncel.2023.1170309

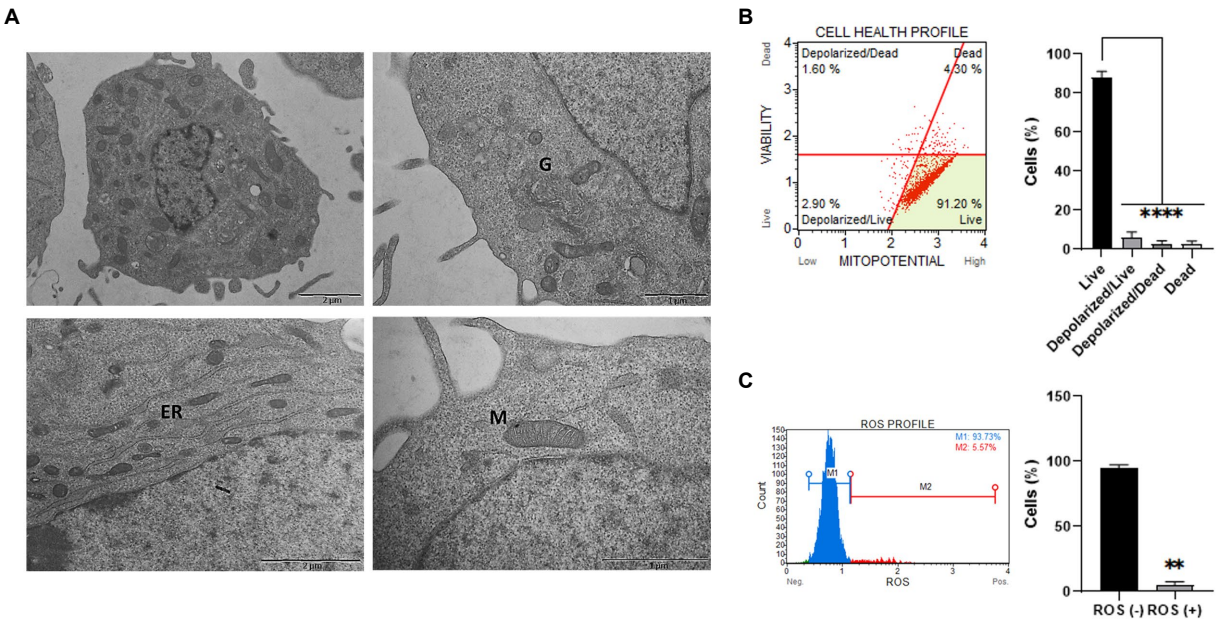

FIGURE 2
Ultrastructural and functional characterization of ClK cells. **(A)** TEM analysis of EG ClK cells (p21). M: mitochondria; G: Golgi apparatus; ER: endoplasmic reticulum. Scale bars (1–2μm) are reported. **(B)** Cytofluorimetric plot and relative histogram reporting the mitochondrial depolarization percentages of ClK cells. Events collected: 2000 cells. Experiments were performed on three independent biological replicates. Data are reported as mean±SE. On Y-axis is reported the number of cells expressed as percentages (%). (****) indicate $p \leq 0.0001$, ANOVA One-Way. **(C)** Cytofluorimetric ROS profile plot (M1 gate: ROS-; M2 gate: ROS+) and relative histograms are reported. Events collected: 2,000 cells. Experiments were performed on three independent biological replicates. Histograms data are represented as mean±SE. On Y-axis is reported the number of cells expressed as percentages (%). (**) indicates $p \leq 0.01$, *t*-test.

Res186 and T98G) showed higher basal ROS levels compared with ClK cells.

3.3. Cytogenetic analysis

Considering the transgenes integration events, ClK cells were selected for the cytogenetic analysis to verify the genome integrity and the presence of chromosomal rearrangements. The chromosome number was counted in a sample of 100 metaphase spreads. As reported in Figure 3A, heteroploidy was observed in the analyzed cell population. Notably, two main cell populations were observed: one near-diploid (31% of the cells, chromosome number $2n = 44$) and one near-tetraploid (9% of the cells, chromosome number $2n = 86$). Karyotype reconstruction was carried out in a sample of 20 metaphase spreads belonging to the most represented cell population ($2n = 44$), using reverse DAPI banding (Figure 3B). The analysis of the reconstructed karyotypes showed a monosomy of chromosomes 5, 13, and 15 as well as the presence of a big metacentric derivative chromosome comparable in size to chromosome 1. A small chromosome fragment (marker M1) was also identified in single copy in 39% of the analyzed metaphase spreads. In particular, the M1 marker was present in 19% of the cells with a total chromosome number of 44 as well as in 19% of the metaphases presenting 86 chromosomes (Supplementary Figure S5). A direct comparison between the large metacentric derivative chromosome and the long arm of chromosome 5 highlighted a striking similarity in their banding pattern. Therefore, it was first hypothesized that the rearranged chromosome originated from a translocation event involving the 5q arm and an unidentified chromosome fragment, leading to a partial monosomy of chromosome 5. The resulting large metacentric chromosome was indeed designated as der5.

The involvement of the long arm of chromosome 5 in the formation of the large derivative chromosome was verified through two-color FISH experiments using DNA probes specific for the sub-centromeric (RP11-160F8, band: q11.2, red) and sub-telomeric (RP11-69A18, band: q35.1, green) regions of chromosome 5. The chromosomal localization of the two probes was first verified by FISH on control human metaphase spreads (data not shown). Subsequently, the probes were contrastingly labelled and co-hybridized to ClK metaphases at p21. Clear fluorescence signals were detected on both normal chromosomes 5 (Figure 4A) and on the derivative marker chromosome (Figure 4B), thus confirming that the region comprised between bands 5q11.2 and 5q35.1 is involved in der5 translocation. FISH signals also provided accurate insights into the orientation of the translocated 5q fragment, which has been shown to precisely mirror the canonical arrangement reported on the original chromosome 5 (Figure 4B).

3.4. Assessment of the glial phenotype of ClK cells through the analysis of specific enteric glial markers

Flow cytometry analysis was performed to assess the homogeneity in the cell-of-origin composition of ClK clone as well as to exclude the

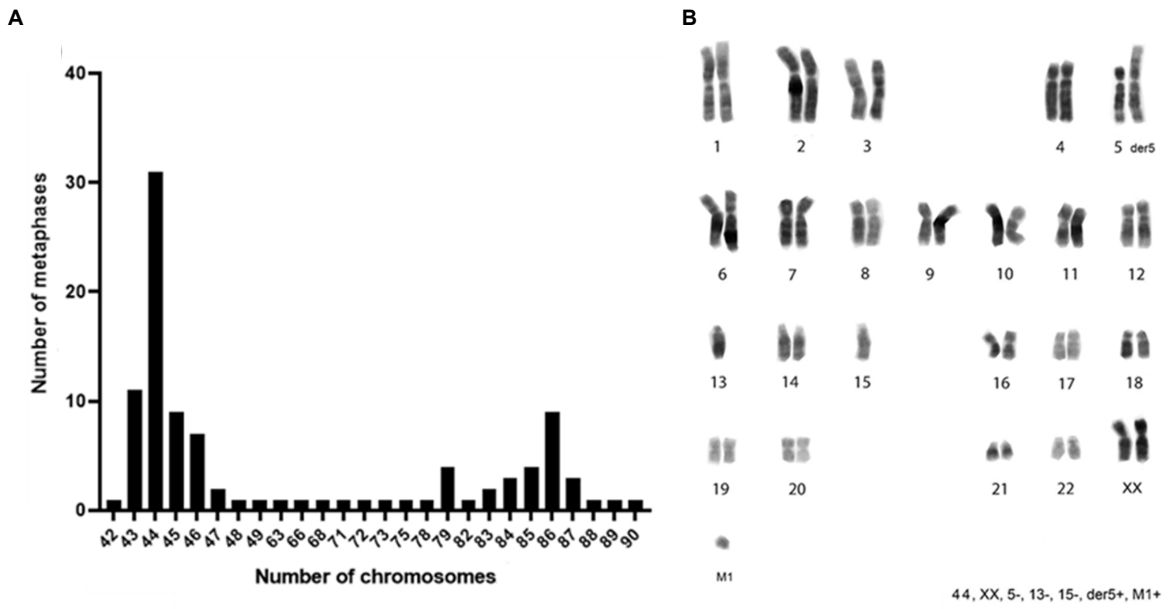

FIGURE 3
Chromosomes distribution and karyotype reconstruction of ClK clone. **(A)** Distribution of the number of chromosomes counted in 100 metaphases and **(B)** consensus karyotype of the ClK clone. The related values are reported in Supplementary Table S4.

presence of markers specific for other cell lines, such as CD31 for endothelial (Woodfin et al., 2007), CD45 for hematopoietic (Al Barashdi et al., 2021), and CD326 for epithelial cells (Keller et al., 2019). As shown in Figure 5A, no highly expressing sub-populations for the analyzed markers were observed in ClK cells. Furthermore, no positivity for CD271, a marker of mesenchymal stem cells (Álvarez-Viejo et al., 2015), was detected in the analyzed cells, since the signal was nearly overlapping the mock unstained control (Supplementary Figure S6). Finally, the expression of the enteric glial-specific makers GFAP, SOX10, and S100β (Ochoa-Cortes et al., 2016), were investigated through immunofluorescence analysis. As reported (Figure 5B), ClK cells expressed the three enteric glial markers. Furthermore, immunofluorescence analysis for the nucleoplasmatic shuttle protein SOX10 demonstrated its nuclear localization. Since EGCs express both class I and II HLA molecules on their plasma membrane (Geboes et al., 1992; da Silveira et al., 2011), basal expression of HLA molecules was studied in untreated ClK cells through immunofluorescence using a specific anti-HLA antibody. Specifically, expression levels of HLA-DQA1 were investigated in first instance due to the association with intestinal disorders (e.g., celiac disease) and drug response (Murray et al., 2007; Sazonovs et al., 2020). As reported in Supplementary Figure S7, the expression of HLA-DQA1 was confirmed by the detection of specific fluorescence signals in ClK cells although with intensity differences among cells. Specificity of all the fluorescence signals was confirmed through negative control staining. Then, HLA genotyping was performed on ClK cells. As reported in Supplementary Table S5, PCR-SSO results showed the HLA molecules expressed in the ClK clone.

Then, mRNA expression levels of *GFAP*, *SOX10*, *S100β*, *CCL2*, and *PLP1* genes were investigated through Real-Time PCR analysis after lipopolysaccharide (LPS) and/or IFN-γ treatment. Inflammatory stimuli can activate enteric glia both *in vitro* and *in vivo*, thus leading EGCs activation and consequent increase of the glial cells' markers (von Boyen et al., 2004; Liñán-Rico et al., 2016; Rosenbaum et al., 2016; da Cunha Franceschi et al., 2017; Progatzky and Pachnis, 2022). Considering these premises, ClK cells were treated with different concentrations of LPS (i.e., 100 ng/mL and 1 μg/mL), IFN-γ (i.e., 5 ng/mL), or a combination of both (i.e., LPS 100 ng/mL + IFN-γ 5 ng/mL). As reported in Figure 6, at 24 h post-treatment *GFAP* mRNA levels showed an increasing trend in all treatments but only in presence of IFN-γ or in correspondence of LPS + IFN-γ statistically significant increases were scored compared with non-treated (NT) cells. *SOX10* did not show significant variations; conversely, a statistically significant increase in *S100β* mRNA levels was observed in the samples treated with LPS 1 μg/mL and IFN-γ. An increasing trend in *PLP1* mRNA expression was also detected in the analyzed samples, with however a statistically significant variation in correspondence of LPS + IFN-γ sample. Finally, expression levels of *CCL2* showed a statistically significant increase in all treatments except for IFN-γ.

3.5. ATP trigger intracellular Ca^{2+} signaling in ClK cells

An increase in intracellular Ca^{2+} concentration ($[Ca^{2+}]i$) is the most common mechanism whereby EGCs respond to extracellular stimulation (Boesmans et al., 2013, 2019; Seguella and Gulbransen, 2021). It has long been known that neuron-to-glia communication requires neuronal release of ATP, which in turn binds to postsynaptic Gq/11 coupled P2Y1 receptors to induce an increase in $[Ca^{2}+]i$ (Gomes et al., 2009; Brown et al., 2016; Boesmans et al., 2019; Seguella and Gulbransen, 2021). Therefore, assessing ATP-induced intracellular Ca^{2+} signaling represents a widespread strategy to confirm the functionality of the ClK clone (Boesmans et al., 2013; Soret et al., 2013). According to our results, ATP (100 μM) induced intracellular Ca^{2+} signals in the majority of cells (97.3%, $n = 147$), which displayed either a transient $[Ca^{2+}]i$ spike (69.2%,

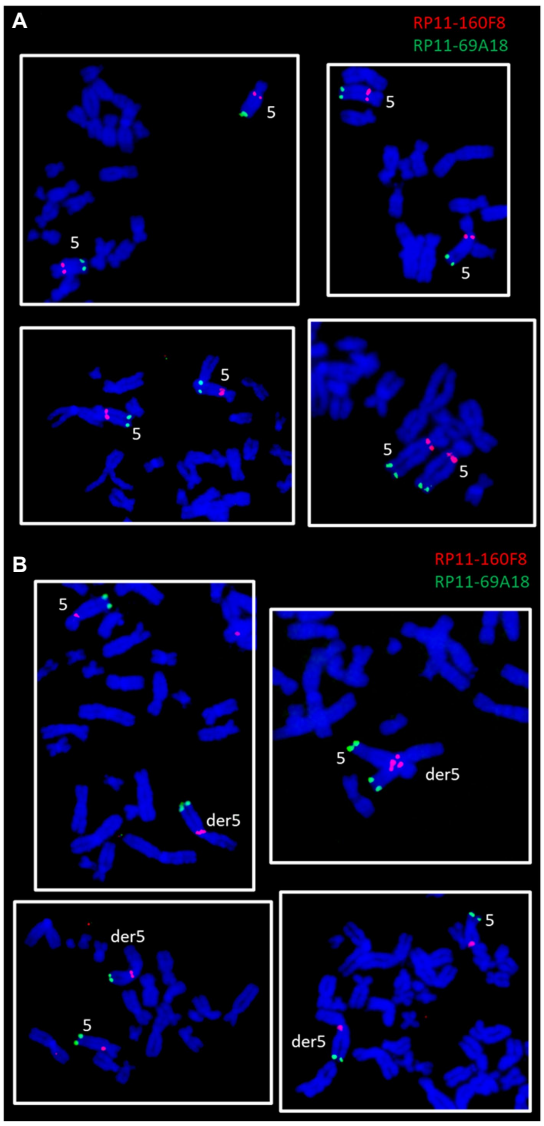

FIGURE 4
FISH experiments on ClK clone (p21) metaphases lacking **(A)** or presenting **(B)** the der5 chromosome. The panel reports two-color FISH experiments performed using a sub-centromeric (RP11-160F8, red) and a sub-telomeric (RP11-69A18, green) DNA probe specific for the long arm of chromosome 5.

$n=99$) or a biphasic increase in $[Ca^{2+}]$i (30.8%, $n=44$) that comprised an initial Ca^{2+} peak followed by a prolonged plateau above the resting Ca^{2+} levels (Figure 7A). The Ca^{2+} response to ATP was abolished by suramin (Figure 7B), a non-selective P2Y receptor antagonist (Boesmans et al., 2013, 2019), and by MRS-2179 (10 μM) (Figure 7C), a selective P2Y1 receptor blocker (Boesmans et al., 2013; Mishra et al., 2016). Of note, the Ca^{2+} response to ATP resumed upon washout of MRS-2179 (Figure 7C), but not suramin (not shown). Statistical analysis of these data is reported in Figure 7D. These results showed that ATP was able to reliably evoke intracellular Ca^{2+} signals in ClK cells.

Based upon the evidence obtained from EGCs isolated from different animal species, the Ca^{2+} response to ATP in ClK cells was likely to be triggered by inositol-1,4,5-trisphosphate (InsP3)-dependent Ca^{2+} release from the endoplasmic reticulum (ER) (Verkhratsky and Parpura, 2014). Accordingly, in the absence of extracellular Ca^{2+} (0 Ca^{2+}), ATP (100 μM) evoked a transient increase in $[Ca^{2+}]$i, which was consistent with the depletion of endogenous Ca^{2+} stores (Figure 8A). The magnitude of the increase in $[Ca^{2+}]$i peak was significantly lower ($p<0.001$) compared to the Ca^{2+} response induced by ATP in the presence of extracellular Ca^{2+} (0.078 ± 0.004, $n=220$, vs. 0.093 ± 0.004, $n=179$). Interestingly, the subsequent re-addition of extracellular Ca^{2+} to the perfusate induced a second, discernible peak in $[Ca^{2+}]$i that was due to extracellular Ca^{2+} entry in 167 out of 227 cells (Figure 8A). The agonist, i.e., ATP, was removed 100 s before restitution of external Ca^{2+} (Figure 8A). Therefore, ATP-induced extracellular Ca^{2+} entry did not occur either through ionotropic P2X receptors or second messengers operated channels (SMOCs) and was likely to be mediated by store-operated Ca^{2+} entry (SOCE), a ubiquitous Ca^{2+} entry route that only requires the previous depletion of the ER Ca^{2+} pool (Bird et al., 2008; Negri et al., 2020) and sustains the Ca^{2+} response to ATP in enteric glia (Sarosi et al., 1998). To further support this evidence, we adopted an established pharmacological approach to inhibit InsP3-induced ER Ca^{2+} release and SOCE. Blocking phospholipase Cβ (PLCβ) with U73122 (10 μM, 20 min) (Figures 8B,D; Zhang et al., 2003), and inhibiting InsP3 receptors (InsP3Rs) with 2-Aminoethyl diphenylborinate (2-APB; 50 μM, 20 min) (Figures 8B,D) suppressed ATP-induced ER Ca^{2+} mobilization (Muller and Taylor, 2017; Astesana et al., 2021). In addition, the intracellular Ca^{2+} response to ATP was abolished by interfering with the activity of Sarco-Endoplasmic Ca^{2+}-ATPase activity (SERCA) with cyclopiazonic acid (CPA) (Dragoni et al., 2014; Figures 8C,D). SERCA represents the Ca^{2+} pump that sequesters cytosolic Ca^{2+} into ER lumen and is, therefore, responsible for maintaining ER Ca^{2+} concentration ($[Ca^{2+}]$ER) (Verkhratsky and Parpura, 2014). CPA blocks SERCA activity, thereby causing a transient increase in $[Ca^{2+}]$i that results from passive leakage of Ca^{2+} from the followed by the recovery of to the baseline due to the concerted activity of Na^+/Ca^{2+} exchanger, plasma membrane Ca^{2+}-ATPase and mitochondria (Bird et al., 2008; Negri et al., 2020). As shown in Figure 8C, CPA (30 μM) caused a transient rise in $[Ca^{2+}]$i under 0 Ca^{2+} conditions, which reflected ER Ca^{2+} depletion. Indeed, after 20 min in the presence of CPA, ATP failed to elevate $[Ca^{2+}]$i, thereby confirming that InsP3-induced ER Ca^{2+} release was the mechanism responsible for the initial Ca^{2+} peak. SOCE is the Ca^{2+} entry pathway activated upon InsP3-induced reduction in $[Ca^{2+}]$ER to refill the endogenous Ca^{2+} reservoir and prolong the Ca^{2+} response to extracellular stimuli in non-excitable cells (Prakriya and Lewis, 2015), including glial cells (Verkhratsky and Parpura, 2014). The role of SOCE in ATP-induced extracellular Ca^{2+} entry in ClK cells was examined by exploiting the "Ca^{2+} add-back" protocol described in Figure 8A in the absence and in the presence of two established blockers of Orai1 (Zhang et al., 2003), which provides the pore-forming subunit of store-operated Ca^{2+} channels (SOCs) in glial cells (Toth et al., 2019). ATP-induced extracellular Ca^{2+} entry in ClK cells was significantly reduced ($p<0.005$) by pretreating the cells with BTP-2 (20 μM, 20 min) or Pyr6 (10 μM, 20 min) (Figures 8E,F), while ER Ca^{2+} release was not impaired (Figures 8E,F), thereby confirming the selectivity of each drug towards SOCE. These findings, therefore, confirm that ATP, the main mediator of the neuron-to-glia communication in the ENS, is able to activate the ClK clone through an increase in $[Ca^{2+}]$i, which arises downstream of P2Y1 receptors and requires InsP3-dependent ER Ca^{2+} release and SOCE.

Finally, we assess whether other neurotransmitters were able to activate ClK cells by increasing $[Ca^{2+}]$i. Supplementary Figure S8

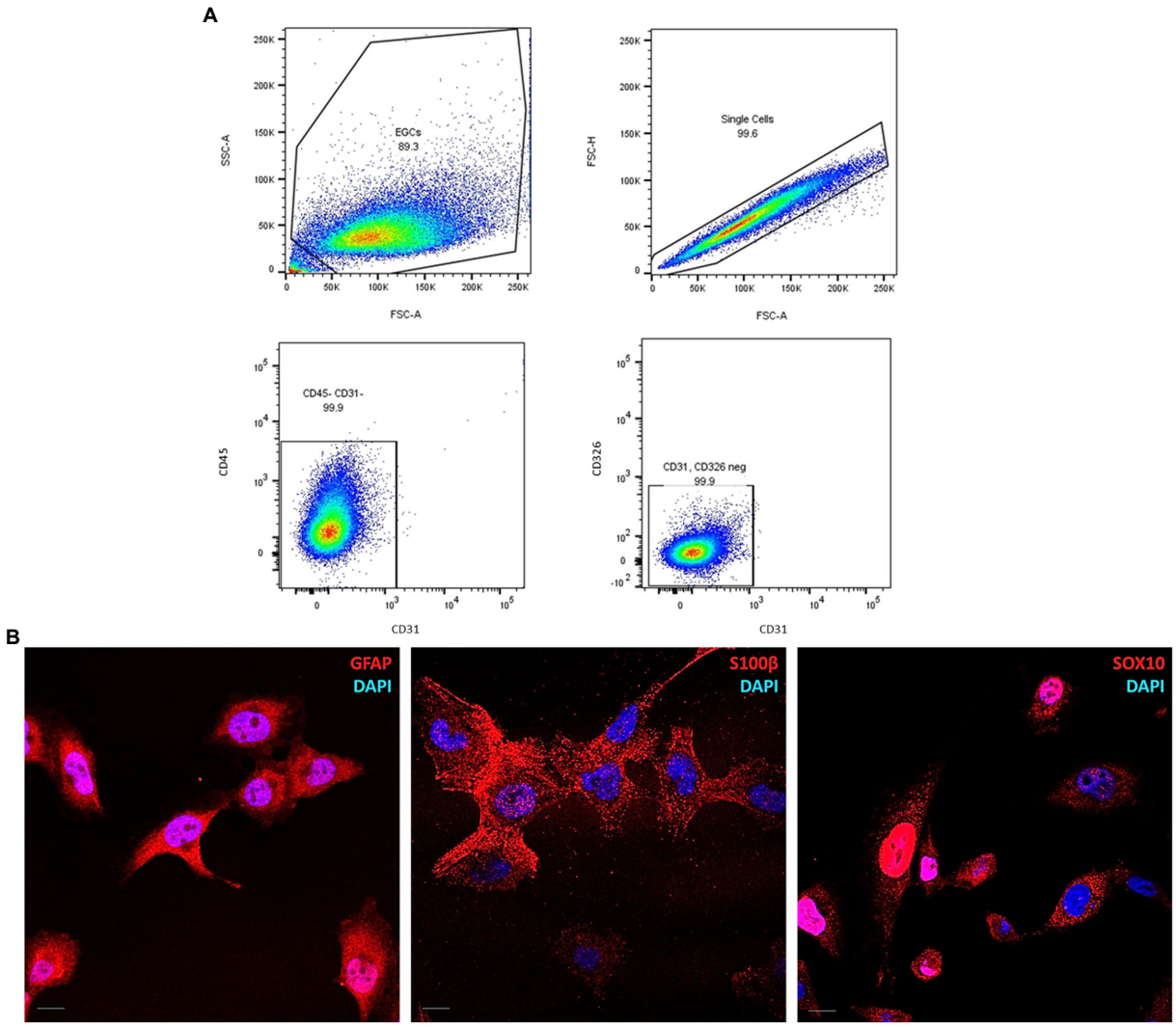

FIGURE 5
Molecular characterization of ClK cells. **(A)** Pseudocolor plots of CD31, CD45, and CD326 expression in ClK cells. Event collected: 10,000 cells. **(B)** Immunofluorescence of the enteric glial markers GFAP, SOX10, and S100β. The analysis was performed using specific anti-GFAP, anti-SOX10, and anti-S100β IgG antibodies conjugated with AlexaFluor633. Nuclei were stained with DAPI. Scale bars (=10μm) are reported.

shows that acetylcholine (Ach, 10 μM) (**Panel A**), serotonin (5-hydroxytryptamine or 5-HT, 10 μM) (**Panel B**), and glutamate (100 μM) (**Panel C**) elicited intracellular Ca^{2+} signals that could adopt either a transient or an oscillator pattern. Therefore, as commonly reported for EGCs (Boesmans et al., 2013, 2019; Seguella and Gulbransen, 2021), intracellular Ca^{2+} signalling is also crucial to the activation of ClK cells by enteric neurotransmitters.

4. Discussion

Interest in EGCs biology has increased in recent years due to the discovery of their key roles in intestinal homeostasis. However, the lack of proper methods to isolate and manipulate these cells has hampered their characterization from both phenotypical and functional points of view (Wang et al., 2018). Biological studies of EGCs are also challenging since these cells *in vivo* constitute a heterogeneous population according to their intestinal topology. Furthermore, the lack of a suitable human model still represents an important limitation in functional studies of EGCs. Nowadays, EGCs can be isolated from different organisms (e.g., guinea pig, mouse, rat and human) although with several technical difficulties (Soret et al., 2013). Another problem is represented by the tendency of these cells to de-differentiate *in vitro* in both neurons and non-myelinating Schwann cells (Jessen and Mirsky, 1983). De-differentiation of EGCs is also enhanced by the time-requiring steps necessary for the purification and establishment of these cells from the intestine (Soret et al., 2013).

In this work, a validated transduction approach was used to generate immortalized human EGC clones. This method generates immortalized cell lines that closely resemble their original precursors in a rapid and reliable way (Lipps et al., 2018). Compared to other currently available techniques (e.g., iPS differentiation or trans-differentiation), this protocol avoids the risk of obtaining heterogeneous cell lines or cells with low proliferation rates. Moreover, contrary to other techniques such as the reactivation of human telomerase reverse transcriptase (hTert), this transduction method can be used virtually with every cell type (Lipps et al., 2018).

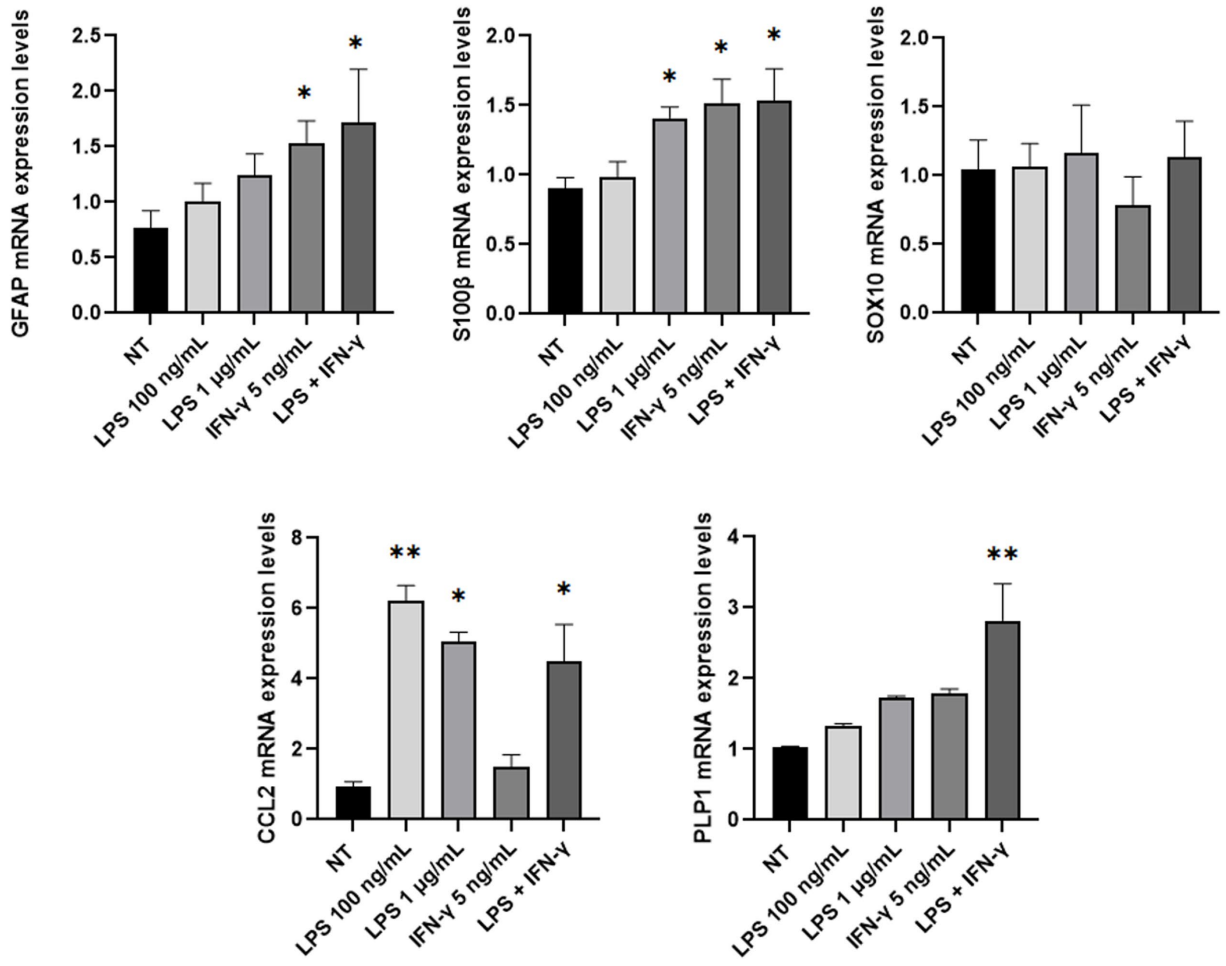

FIGURE 6
GFAP, SOX10, S100β, PLP1, and *CCL2* mRNA expression level analysis in ClK cells treated with different inflammatory stimuli for 24h. The expression levels of the selected genes in treated cells were compared with those of non-treated (NT) cells. In the Y-axis, relative quantification values are reported. Data are reported as mean±SE. (*) indicate $p \leq 0.05$, (**) indicate $p \leq 0.01$, ANOVA Kruskal-Wallis. Experiments were performed on three independent biological replicas.

As reported in this contribution, an immortalized EGC line (referred to as ClK clone) was obtained starting from a human surgery of the myenteric plexus of a histologically normal intestinal tissue with no aberrations. Compared to primary cells that reached growth plateau and arrest (respectively, 19- and 29-days post-isolation), increasing cPDL revealed that ClK cells acquired an actively proliferating phenotype. Notably, flow cytometry analysis of Ki-67, a well-known marker of cell proliferation (Sun and Kaufman, 2018), showed a significant reduction in the Ki-67 positive sub-population in ClK cells compared with the high-grade astrocytoma T98G cell line as well as a decreasing trend according to cell confluence. These data suggested a possible contact inhibition of proliferation for ECGs, a characteristic typical of noncancerous cells that is generally lost in transformed cells (Pavel et al., 2018). This hypothesis was also supported by the evidence collected on other developed immortalized cell lines derived with the same transduction protocol that did not show the ability to develop tumors *in vivo* (Lipps et al., 2018). Furthermore, TEM and flow cytometry analyses showed no evident structural/morphological variations both in the topology and in the intracellular compartments of ClK cells, as well as perturbations of mitochondrial membrane potential. Moreover, ROS intracellular levels were detected in less than 6% of the analyzed cells. As demonstrated by subsequent flow cytometry and immunofluorescence analyses, ClK cells express the EGCs-specific markers (i.e., GFAP, SOX10, and S100β) (Hoff et al., 2008; De Giorgio et al., 2012), that are associated with mature EGCs and are implicated in several biological pathways (Bush et al., 1998; Rühl et al., 2001b; von Boyen et al., 2004; Cirillo et al., 2011b; da Cunha Franceschi et al., 2017), but no expression was observed for endothelial, hematopoietic, and epithelial specific markers (Woodfin et al., 2007; Álvarez-Viejo et al., 2015; Keller et al., 2019; Al Barashdi et al., 2021), underlining the lack of contamination by other cell types in the isolated EGCs. Notably, the analysis of the mRNA expression levels of *GFAP*, *SOX10*, *S100β*, *PLP1*, and *CCL2* EGC markers (von Boyen et al., 2004; Liñán-Rico et al., 2016; Rosenbaum et al., 2016; da Cunha Franceschi et al., 2017; Progatzky and Pachnis, 2022) demonstrated the capability of ClK cells to react against inflammatory stimuli, as expected for EGCs. Considering emerging evidence regarding HLA expression by EGCs (Koretz et al., 1987; Geboes et al., 1992; Denzer et al., 2000; da Silveira et al., 2011) immunofluorescence as well as HLA genotyping through reverse PCR-SSO were performed. The analyzes revealed that ClK cells expressed HLA-DQA1 molecule and

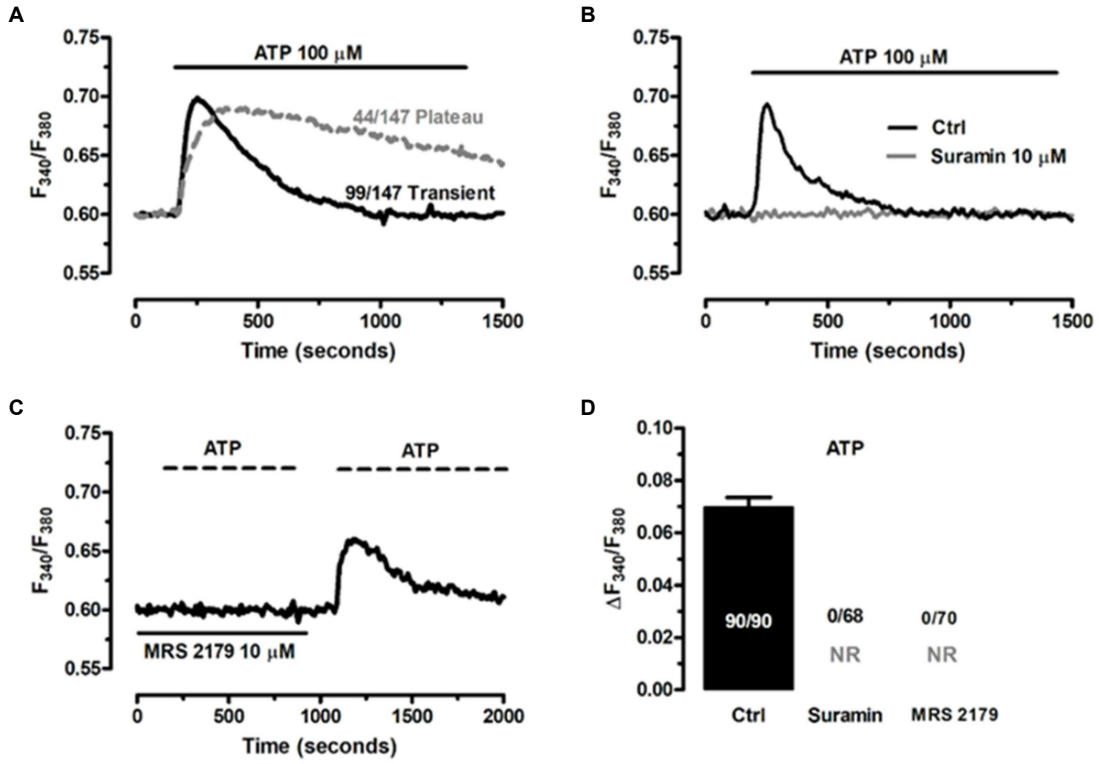

FIGURE 7
ATP induces P2Y1 receptor-mediated increase in $[Ca^{2+}]'$ in ClK cells. **(A)** ATP (100μM) triggered heterogeneous Ca^{2+} signals in ClK cells. **(B)** The Ca^{2+} response to ATP (100μM) was abrogated upon preincubation with suramin (10μM, 30min), a non-specific P2Y receptor inhibitor. **(C)** Pretreating the ClK cells with MRS-2179 (10μM, 30min), a competitive antagonist of P2Y1 receptor abolished the $Ca2^{+}$ response to ATP (100μM), whereas the signals resumed upon washout of inhibitor. **(D)** Mean±SE the amplitude of the Ca^{2+} response to ATP in the absence (Ctrl) and presence of P2Y receptor blockers. In panel (D); NR: no response.

identified a narcolepsy-cataplexy associated allele (namely, HLA-DQB1*0602) (Lin et al., 2001), whereas no alleles associated with intestinal diseases (e.g., celiac disease, inflammatory bowel diseases) or co-morbidities were found (e.g., diabetes).

An accurate cytogenetic analysis of ClK clone was carried out to investigate the presence of structural and numerical chromosome changes, which have been shown to frequently occur *in vitro* upon immortalization processes (Goymer, 2008). Firstly, the distribution of the chromosome number per metaphase was assessed. As reported, ClK cells showed a modal karyotype of 44 chromosomes ($2n = 44$) together with one recurrent chromosomal rearrangement, as already described for other cell lines obtained with this technology (Lipps et al., 2018). Notably, the distribution of the chromosome number showed a tendency to acquire a near-tetraploid arrangement (4n), as suggested by the second modal value detected ($2n = 86$). In the majority of the analyzed metaphases, a big metacentric derivative chromosome (der5), as well as a small chromosome fragment (M1), were also detected. As M1 occurs in a single copy in a considerable number of metaphases (38%), it may be hypothesized that it contains a functional centromere. Nevertheless, immunofluorescence experiments targeting the centromere-specific histone variant CENP-A are further required to validate this assumption (Quénet and Dalal, 2012). The origin of the large metacentric rearranged chromosome has been also objecting of deepen the analysis. According to the preliminary results obtained from the reverse DAPI banding, it was first hypothesized that this chromosome contained the entire 5q arm. This assumption was later confirmed by two-color FISH experiments using DNA BAC probes specific for the sub-centromeric and sub-telomeric regions of the long arm of chromosome 5. The results obtained clearly confirmed the involvement of the 5q arm in the formation of the der5 chromosome. In light of these data, the consensus karyotype of the ClK cell line at p21 was designated as 44, XX, 5-, 13-, 15-, der5+, M1+/−. At present, the origin of the other translocated arm remains unidentified. Additional FISH experiments might be required to fully dissect der5 composition. Given the complete monosomy of chromosomes 13 and 15 detected in the modal karyotype, a likely hypothesis is that the long arm of their missing homolog may be involved in this rearrangement. Future perspectives might include the analysis of ClK karyotype at higher culture passages to provide clear hints into its evolution over time. However, as already reported, cell lines obtained with this transduction approach showed few ploidy changes after extended cultivation, suggesting a relative stability of the karyotype (Lipps et al., 2018).

ATP represents one of the most ubiquitous mediators of intercellular communication between enteric neurons and EGCs (Seguella and Gulbransen, 2021). Accordingly, ATP can be released either by direct stimulation of intrinsic nerves (Gulbransen and Sharkey, 2009; Gulbransen and Sharkey, 2012) or extrinsic cholinergic nerve fibers, which may co-release acetylcholine and ATP (Gulbransen et al., 2010; Gulbransen and Sharkey, 2012). ATP-evoked intracellular Ca^{2+} signals in EGCs integrate neuronal activity in the myenteric plexus and are instrumental to coordinate patterns of contractive activity in the GI (Gulbransen and Sharkey, 2009; Seguella and Gulbransen, 2021). The Ca^{2+} response to ATP in cultured EGCs from multiple sources (e.g.,

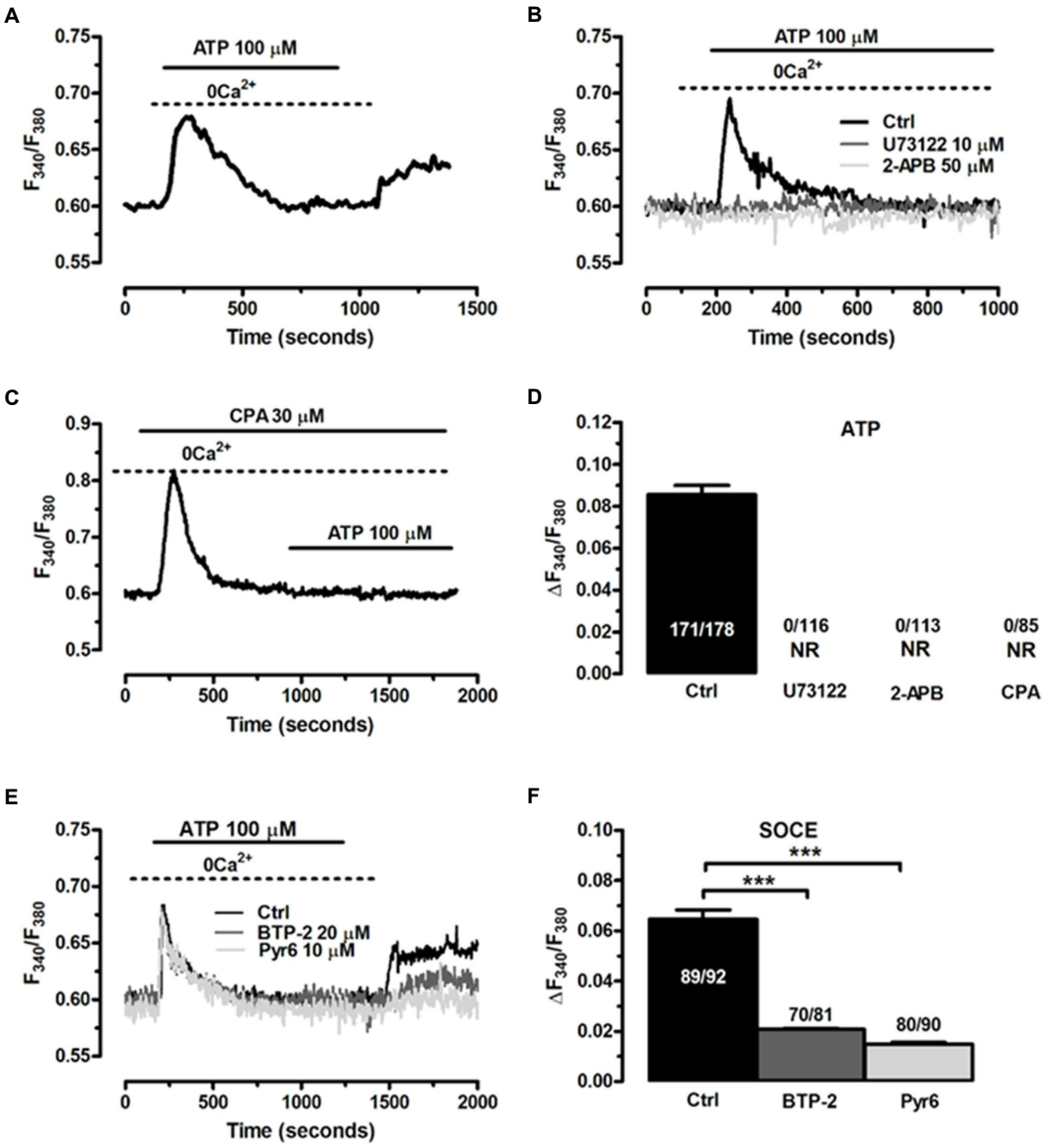

FIGURE 8
The Ca^{2+} response to ATP requires $InsP_3$-induced ER Ca^{2+} release and SOCE activation in ClK cells. **(A)** Cells perfused with ATP (100μM) in the absence of extracellular Ca^{2+} responded with a transient increase in $[Ca^{2+}]i$, whereas restoration of extracellular Ca^{2+} caused a second elevation in $[Ca^{2+}]i$. ATP was removed 100s before re-addition of extracellular Ca^{2+}. **(B)** ATP-induced transient Ca^{2+} release was blocked upon preincubation of the ClK cells with U73122 (10μM, 30min), a selective PLC inhibitor, and 2-APB (50μM, 30min), which blocks $InsP_3Rs$ under 0 Ca^{2+} conditions. ATP was administered at 100μM. **(C)** Pharmacological depletion of the ER Ca^{2+} pool with CPA (30μM) in the absence of extracellular Ca^{2+} (0 Ca^{2+}) inhibits the Ca^{2+} release evoked by ATP (100μM). Note the intracellular Ca^{2+} transient evoked by CPA due to the passive leakage of ER Ca^{2+} in the cytosol, as more widely described in the text. **(D)** Mean±SE of the amplitude of ATP-induced intracellular Ca^{2+} release under the designated treatments. **(E)** ATP-induced extracellular Ca^{2+} entry was dramatically reduced by selectively blocking SOCE with BTP-2 (20μM, 20min) or Pyr6 (10μM, 10min). **(F)** mean±SE of the amplitude of the peak Ca^{2+} entry by ATP under the designated treatments. In panel d; NR: no response. One-way ANOVA analysis was used for Statistical comparison. In Panel F: (***) $p \leq 0.005$.

human, mouse, rat, guinea pig) is operated by the Gq/11 coupled P2Y1 receptors (Gomes et al., 2009; Brown et al., 2016; Boesmans et al., 2019; Seguella and Gulbransen, 2021), triggered by InsP3-induced ER Ca^{2+} mobilization (Grubišić and Gulbransen, 2017) and prolonged by SOCE (Sarosi et al., 1998). We found that ATP could evoke two different patterns of intracellular Ca^{2+} signals in ClK cells: a transient increase in $[Ca^{2+}]i$ that returned to the baseline despite the continuous exposure to the agonist, and a biphasic Ca^{2+} signal that persisted as long as ATP was present in the perfusate. Prolonged stimulation with ATP has previously been shown to induce a biphasic increase in $[Ca^{2+}]i$ in guinea pig EGCs (Kimball and Mulholland, 1996; Gulbransen and Sharkey, 2009), whereas variable waveforms (transient vs. sustained) were evoked by ATP in mouse (Boesmans et al., 2019) and human (Boesmans et al., 2013) EGCs. For instance, besides inducing a transient Ca^{2+} spike, ATP could evoke a biphasic increase in mouse EGCs (Boesmans et al., 2019) and multiple Ca^{2+} spikes in human ones (Brown et al., 2016). Likewise, ATP evokes intracellular Ca^{2+} signals of different kinetics also in mouse brain astrocytes (James et al., 2011; Tang et al., 2015; Taheri et al., 2017) and this heterogeneity in ATP-induced Ca^{2+} waveforms may be due to the different extent of either ATP degradation by ectonucleotidases (Berra-Romani et al., 2004) or SOCE activation (Taheri et al., 2017). Thus, the diversity of ATP-induced intracellular Ca^{2+} signals in ClK cells

reflected the variability previously reported in both enteric and brain glial cells. The following evidence indicated that the Ca^{2+} response to ATP in the ClK clone is operated by P2Y1 receptors, triggered by InsP3-induced ER Ca^{2+} release, and sustained by SOCE. Firstly, the onset of the Ca^{2+} signal was abrogated by blocking P2Y1 receptors with either suramin or MRS-2179 (Boesmans et al., 2013, 2019; Mishra et al., 2016). Secondly, the Ca^{2+} response to ATP arose in the absence of extracellular Ca^{2+}, although the plateau phase was abolished and the duration of the Ca^{2+} signal was significantly shorter as compared to ClK cells displaying a transient $[Ca^{2+}]$i rise also in PSS. Thus, mobilization of the endogenous Ca^{2+} store is required to trigger ATP-induced intracellular Ca^{2+} signals in these cells. Thirdly, ATP-induced intracellular Ca^{2+} release was abrogated by preventing InsP3 production with U73122 and by directly blocking InsP3Rs with 2-APB (Zhang et al., 2003; Astesana et al., 2021). Moreover, ATP failed to induce a detectable increase in $[Ca^{2+}]$i upon depletion of the ER Ca^{2+} store with the SERCA inhibitor, CPA, which provides a common pharmacological tool to cause a drop in $[Ca^{2+}]_{ER}$ in EGCs (Kimball and Mulholland, 1996; Zhang et al., 2003). Fourthly, extracellular Ca^{2+} entry was required to achieve the full Ca^{2+} peak and to sustain the plateau in ClK cells displaying a long-lasting Ca^{2+} response. The "Ca^{2+} add-back" protocol revealed that, after the initial depletion of the InsP3-sensitive ER Ca^{2+} pool, ATP induced the influx of extracellular Ca^{2+}. As widely discussed elsewhere (Bird et al., 2008; Negri et al., 2020), Ca^{2+} entry did not require the presence of the agonist in the perfusate, which is the hallmark of SOCE activation. In agreement with this hypothesis, ATP-evoked extracellular Ca^{2+} was strongly reduced by BTP-2 and Pyr6, two pyrazole-derivatives that selectively block Orai1, the pore-forming subunits of SOCs in glial cells (Toth et al., 2019). Previous contributions have shown that SOCE prolonged the Ca^{2+} response evoked in guinea pig EGCs by ATP (Sarosi et al., 1998) and endothelin-1 (Zhang et al., 1997), whereas this is the first time that SOCE activation is reported in a human-derived EGCs. Whereas the full characterization of the Ca^{2+} handling machinery awaits future investigation, this preliminary evidence demonstrates that the ClK cells are able to generate a functional Ca^{2+} signal in response to ATP, one of the main mediators of neuron-to-glia communication in the ENS. Furthermore, ClK cells displays intracellular $[Ca^{2+}]$ signals also in response to other enteric neurotransmitters, such as Ach, 5-HT, and glutamate, which are known to activate EGCs through an increase in $[Ca^{2+}]$i (Boesmans et al., 2013, 2019; Seguella and Gulbransen, 2021).

In conclusion, the isolation and characterization of the described human immortalized EGCs might represent a potential *in vitro* valuable tool for many applications including drug discovery as well as for disease understanding and personalized medicine approaches.

Data availability statement

The raw data supporting the conclusions of this article will be made available by the authors, without undue reservation.

Ethics statement

The studies involving human participants were reviewed and approved by Tissue Solutions (Glasgow, Scotland, United Kingdom). The patients/participants provided their written informed consent to participate in this study.

Author contributions

GB, FrM, FeM, ER, TM, and SC: conceptualization. LZ, AV, KN, PF, CC, RC, IS, FC, DA, and FeM: investigation. FeM, PF, and KN: data analysis. FeM: writing-original draft preparation. RC, VDS, LvB, GB, FrM, ER, PF, and SC: writing-review and editing. FrM, FeM, ER, TM, GM, and SC: supervision. FeM and SC: project administration. MB, FeM, and SC: funding acquisition. All authors contributed to the article and approved the submitted version.

Acknowledgments

This research was supported by the Italian Ministry of Education, University and Research (MIUR): Dipartimenti di Eccellenza Program (2018–2022), Dept. of Biology and Biotechnology "L. Spallanzani," University of Pavia. This work was also supported by Associazione Italiana Celiachia - APS (A.I.C. - APS) grant no 001_FC_2018 and "Il Bambino e il suo pediatra" Onlus. VDS was supported by a postdoctoral fellowship in Fundamental Research by the Stichting tegen Kanker. GM's lab was supported by FWO grants G0A7919N and G088816N. The authors give thanks to Patrizia Vaghi and Amanda Oldani (PASS-Bio Med, Centro Grandi Strumenti, University of Pavia, Pavia, 27100, Italy) for the microscope acquisitions.

Conflict of interest

TM holds a patent for the immortalization technology described in this manuscript and is a shareholder of InSCREENeX GmbH, which commercializes cell lines immortalized by the described technology. TM and KN are employees of InSCREENeX GmbH.

The remaining authors declare that the research was conducted in the absence of any commercial or financial relationships that could be construed as a potential conflict of interest.

Publisher's note

Supplementary material

The Supplementary material for this article can be found online at: https://www.frontiersin.org/articles/10.3389/fncel.2023.1170309/full#supplementary-material

References

Al Barashdi, M. A., Ali, A., McMullin, M. F., and Mills, K. (2021). Protein tyrosine phosphatase receptor type C (PTPRC or CD45). *J. Clin. Pathol.* 74, 548–552. doi: 10.1136/jclinpath-2020-206927

Álvarez-Viejo, M., Menéndez-Menéndez, Y., and Otero-Hernández, J. (2015). CD271 as a marker to identify mesenchymal stem cells from diverse sources before culture. *World J. Stem Cells* 7, 470–476. doi: 10.4252/wjsc.v7.i2.470

Astesana, V., Faris, P., Ferrari, B., Siciliani, S., Lim, D., Biggiogera, M., et al. (2021). Correction to: [Pt(O,O'-acac)(γ-acac)(DMS)]: alternative strategies to overcome cisplatin-induced side effects and resistance in T98G glioma cells. *Cell. Mol. Neurobiol.* 41:589. doi: 10.1007/s10571-020-00896-1

Bassotti, G., Villanacci, V., Antonelli, E., Morelli, A., and Salerni, B. (2007). Enteric glial cells: new players in gastrointestinal motility? *Lab. Investig.* 87, 628–632. doi: 10.1038/labinvest.3700564

Berra-Romani, R., Rinaldi, C., Raqeeb, A., Castelli, L., Magistretti, J., Taglietti, V., et al. (2004). The duration and amplitude of the plateau phase of ATP- and ADP-evoked ca(2+) signals are modulated by ectonucleotidases in *in situ* endothelial cells of rat aorta. *J. Vasc. Res.* 41, 166–173. doi: 10.1159/000077146

Bird, G. S., DeHaven, W. I., Smyth, J. T., and Putney, J. W. Jr. (2008). Methods for studying store-operated calcium entry. *Methods* 46, 204–212. doi: 10.1016/j.ymeth.2008.09.009

Bobola, M. S., Silber, J. R., Ellenbogen, R. G., Geyer, J. R., Blank, A., and Goff, R. D. (2005). O6-methylguanine-DNA methyltransferase, O6-benzylguanine, and resistance to clinical alkylators in pediatric primary brain tumor cell lines. *Clin. Cancer Res.* 11, 2747–2755. doi: 10.1158/1078-0432.CCR-04-2045

Boesmans, W., Cirillo, C., Van den Abbeel, V., Van den Haute, C., Depoortere, I., Tack, J., et al. (2013). Neurotransmitters involved in fast excitatory neurotransmission directly activate enteric glial cells. *Neurogastroenterol. Motil.* 25, e151–e160. doi: 10.1111/nmo.12065

Boesmans, W., Hao, M. M., Fung, C., Li, Z., Van den Haute, C., Tack, J., et al. (2019). Structurally defined signaling in neuro-glia units in the enteric nervous system. *Glia* 67, 1167–1178. doi: 10.1002/glia.23596

Brown, I. A., McClain, J. L., Watson, R. E., Patel, B. A., and Gulbransen, B. D. (2016). Enteric glia mediate neuron death in colitis through purinergic pathways that require connexin-43 and nitric oxide. *Cell. Mol. Gastroenterol. Hepatol.* 2, 77–91. doi: 10.1016/j.jcmgh.2015.08.007

Bush, T. G., Savidge, T. C., Freeman, T. C., Cox, H. J., Campbell, E. A., Mucke, L., et al. (1998). Fulminant jejuno-ileitis following ablation of enteric glia in adult transgenic mice. *Cells* 93, 189–201. doi: 10.1016/s0092-8674(00)81571-8

Carriero, F., Martinelli, C., Gabriele, F., Barbieri, G., Zanoletti, L., Milanesi, G., et al. (2021). Berberine photo-activation potentiates cytotoxicity in human astrocytoma cells through apoptosis induction. *J. Pers. Med.* 11:942. doi: 10.3390/jpm11100942

Cerantola, S., Caputi, V., Marsilio, I., Ridolfi, M., Faggin, S., Bistoletti, M., et al. (2020). Involvement of enteric glia in small intestine neuromuscular dysfunction of toll-like receptor 4-deficient mice. *Cells* 9:838. doi: 10.3390/cells9040838

Cirillo, C., Sarnelli, G., Esposito, G., Grosso, M., Petruzzelli, R., Izzo, P., et al. (2009). Increased mucosal nitric oxide production in ulcerative colitis is mediated in part by the enteroglial-derived S100B protein. *Neurogastroenterol. Motil.* 21, 1209–e112. doi: 10.1111/j.1365-2982.2009.01346

Cirillo, C., Sarnelli, G., Esposito, G., Turco, F., Steardo, L., and Cuomo, R. (2011b). S100B protein in the gut: the evidence for enteroglial-sustained intestinal inflammation. *World J. Gastroenterol.* 17, 1261–1266. doi: 10.3748/wjg.v17.i10.1261

Cirillo, C., Sarnelli, G., Turco, F., Mango, A., Grosso, M., Aprea, G., et al. (2011a). Proinflammatory stimuli activates human-derived enteroglial cells and induces autocrine nitric oxide production. *Neurogastroenterol. Motil.* 23, e372–e382. doi: 10.1111/j.1365-2982.2011.01748

Comincini, S., Allavena, G., Palumbo, S., Morini, M., Durando, F., Angeletti, F., et al. (2013). microRNA-17 regulates the expression of ATG7 and modulates the autophagy process, improving the sensitivity to temozolomide and low-dose ionizing radiation treatments in human glioblastoma cells. *Cancer Biol. Ther.* 14, 574–586. doi: 10.4161/cbt.24597

da Cunha Franceschi, R., Nardin, P., Machado, C. V., Tortorelli, L. S., Martinez-Pereira, M. A., Zanotto, C., et al. (2017). Enteric glial reactivity to systemic LPS administration: changes in GFAP and S100B protein. *Neurosci. Res.* 119, 15–23. doi: 10.1016/j.neures.2016.12.005

da Silveira, A. B., de Oliveira, E. C., Neto, S. G., Luquetti, A. O., Fujiwara, R. T., Oliveira, R. C., et al. (2011). Enteroglial cells act as antigen-presenting cells in chagasic megacolon. *Hum. Pathol.* 42, 522–532. doi: 10.1016/j.humpath.2010.06.016

De Giorgio, R., Giancola, F., Boschetti, E., Abdo, H., Lardeux, B., and Neunlist, M. (2012). Enteric glia and neuroprotection: basic and clinical aspects. *Am. J. Physiol. Gastrointest. Liver Physiol.* 303, G887–G893. doi: 10.1152/ajpgi.00096.2012

Denzer, K., Kleijmeer, M. J., Heijnen, H. F., Stoorvogel, W., and Geuze, H. J. (2000). Exosome: from internal vesicle of the multivesicular body to intercellular signaling device. *J. Cell Sci.* 113, 3365–3374. doi: 10.1242/jcs.113.19.3365

D'Errico, F., Goverse, G., Dai, Y., Wu, W., Stakenborg, M., Labeeuw, E., et al. (2018). Estrogen receptor β controls proliferation of enteric glia and differentiation of neurons in the myenteric plexus after damage. *Proc. Natl. Acad. Sci. U. S. A.* 115, 5798–5803. doi: 10.1073/pnas.1720267115

Dragoni, S., Laforenza, U., Bonetti, E., Reforgiato, M., Poletto, V., Lodola, F., et al. (2014). Enhanced expression of stim, Orai, and TRPC transcripts and proteins in endothelial progenitor cells isolated from patients with primary myelofibrosis. *PLoS One* 9:e91099. doi: 10.1371/journal.pone.0091099

Faris, P., Ferulli, F., Vismara, M., Tanzi, M., Negri, S., Rumolo, A., et al. (2020). Hydrogen sulfide-evoked intracellular Ca^{2+} signals in primary cultures of metastatic colorectal cancer cells. *Cancers* 12:3338. doi: 10.3390/cancers12113338

Gabella, G. (1972). Fine structure of the myenteric plexus in the Guinea-pig ileum. *J. Anat.* 111, 69–97.

Gabella, G. (1981). Ultrastructure of the nerve plexuses of the mammalian intestine: the enteric glial cells. *Neuroscience* 6, 425–436. doi: 10.1016/0306-4522(81)90135-4

Geboes, K., Rutgeerts, P., Ectors, N., Mebis, J., Penninckx, F., Vantrappen, G., et al. (1992). Major histocompatibility class II expression on the small intestinal nervous system in Crohn's disease. *Gastroenterology* 103, 439–447. doi: 10.1016/0016-5085(92)90832-j

Gomes, P., Chevalier, J., Boesmans, W., Roosen, L., van den Abbeel, V., Neunlist, M., et al. (2009). ATP-dependent paracrine communication between enteric neurons and glia in a primary cell culture derived from embryonic mice. *Neurogastroenterol. Motil.* 21, 870–e62. doi: 10.1111/j.1365-2982.2009.01302.x

Goymer, P. (2008). Natural selection: the evolution of cancer. *Nature* 454, 1046–1048. doi: 10.1038/4541046a

Grubišić, V., and Gulbransen, B. D. (2017). Enteric glial activity regulates secretomotor function in the mouse colon but does not acutely affect gut permeability. *J. Physiol.* 595, 3409–3424. doi: 10.1113/JP273492

Grundmann, D., Klotz, M., Rabe, H., Glanemann, M., and Schäfer, K. H. (2015). Isolation of high-purity myenteric plexus from adult human and mouse gastrointestinal tract. *Sci. Rep.* 5:9226. doi: 10.1038/srep09226

Gulbransen, B. D., Bains, J. S., and Sharkey, K. A. (2010). Enteric glia are targets of the sympathetic innervation of the myenteric plexus in the Guinea pig distal colon. *J. Neurosci.* 30, 6801–6809. doi: 10.1523/JNEUROSCI.0603-10.2010

Gulbransen, B. D., and Christofi, F. L. (2018). Are we close to targeting enteric glia in gastrointestinal diseases and motility disorders? *Gastroenterology* 155, 245–251. doi: 10.1053/j.gastro.2018.06.050

Gulbransen, B. D., and Sharkey, K. A. (2009). Purinergic neuron-to-glia signaling in the enteric nervous system. *Gastroenterology* 136, 1349–1358. doi: 10.1053/j.gastro.2008.12.058

Gulbransen, B. D., and Sharkey, K. A. (2012). Novel functional roles for enteric glia in the gastrointestinal tract. *Nat. Rev. Gastroenterol. Hepatol.* 9, 625–632. doi: 10.1038/nrgastro.2012.138

Hanani, M., and Reichenbach, A. (1994). Morphology of horseradish peroxidase (HRP)-injected glial cells in the myenteric plexus of the Guinea-pig. *Cell Tissue Res.* 278, 153–160. doi: 10.1007/BF00305787

Hoff, S., Zeller, F., von Weyhern, C. W., Wegner, M., Schemann, M., Michel, K., et al. (2008). Quantitative assessment of glial cells in the human and Guinea pig enteric nervous system with an anti-Sox8/9/10 antibody. *J. Comp. Neurol.* 509, 356–371. doi: 10.1002/cne.21769

Ibiza, S., García-Cassani, B., Ribeiro, H., Carvalho, T., Almeida, L., Marques, R., et al. (2016). Glial-cell-derived neuroregulators control type 3 innate lymphoid cells and gut defence. *Nature* 535, 440–443. doi: 10.1038/nature18644

James, L. R., Andrews, S., Walker, S., de Sousa, P. R., Ray, A., Russell, N. A., et al. (2011). High-throughput analysis of calcium signalling kinetics in astrocytes stimulated with different neurotransmitters. *PLoS One* 6:e26889. doi: 10.1371/journal.pone.0026889

Jessen, K. R., and Mirsky, R. (1980). Glial cells in the enteric nervous system contain glial fibrillary acidic protein. *Nature* 286, 736–737. doi: 10.1038/286736a0

Jessen, K. R., and Mirsky, R. (1983). Astrocyte-like glia in the peripheral nervous system: an immunohistochemical study of enteric glia. *The Journal of neuroscience: the official journal of the Society for Neuroscience* 3, 2206–2218. doi: 10.1523/JNEUROSCI.03-11-02206.1983

Keller, L., Werner, S., and Pantel, K. (2019). Biology and clinical relevance of EpCAM. *Cell Stress* 3, 165–180. doi: 10.15698/cst2019.06.188

Kimball, B. C., and Mulholland, M. W. (1996). Enteric glia exhibit P2U receptors that increase cytosolic calcium by a phospholipase C-dependent mechanism. *J. Neurochem.* 66, 604–612. doi: 10.1046/j.1471-4159.1996.66020604.x

Koretz, K., Momburg, F., Otto, H. F., and Möller, P. (1987). Sequential induction of MHC antigens on autochthonous cells of ileum affected by Crohn's disease. *Am. J. Pathol.* 129, 493–502.

Kroemer, G., and Reed, J. C. (2000). Mitochondrial control of cell death. *Nat. Med.* 6, 513–519. doi: 10.1038/74994

Le Berre-Scoul, C., Chevalier, J., Oleynikova, E., Cossais, F., Talon, S., Neunlist, M., et al. (2017). A novel enteric neuron-glia coculture system reveals the role of glia in neuronal development. *J. Physiol.* 595, 583–598. doi: 10.1113/JP271989

Li, Y., Ge, Y., Zhu, W., Gong, J., Cao, L., Guo, Z., et al. (2018). Increased enteric glial cells in proximal margin of resection is associated with postoperative recurrence of Crohn's disease. *J. Gastroenterol. Hepatol.* 33, 638–644. doi: 10.1111/jgh.13973

Lin, L., Hungs, M., and Mignot, E. (2001). Narcolepsy and the HLA region. *J. Neuroimmunol.* 117, 9–20. doi: 10.1016/s0165-5728(01)00333-2

Liñán-Rico, A., Turco, F., Ochoa-Cortes, F., Harzman, A., Needleman, B. J., Arsenescu, R., et al. (2016). Molecular signaling and dysfunction of the human reactive enteric glial cell phenotype: implications for GI infection, IBD, POI, neurological, motility, and GI disorders. *Inflamm. Bowel Dis.* 22, 1812–1834. doi: 10.1097/MIB.0000000000000854

Lipps, C., Klein, F., Wahlicht, T., Seiffert, V., Butueva, M., Zauers, J., et al. (2018). Expansion of functional personalized cells with specific transgene combinations. *Nat. Commun.* 9:994. doi: 10.1038/s41467-018-03408-4

Middeldorp, J., and Hol, E. M. (2011). GFAP in health and disease. *Prog. Neurobiol.* 93, 421–443. doi: 10.1016/j.pneurobio.2011.01.005

Middlemiss, P. J., Jiang, S., Wang, J., and Rathbone, M. P. (2002). A method for purifying enteric glia from rat myenteric plexus. *In Vitro Cell. Dev. Biol. Anim.* 38, 188–190. doi: 10.1290/1071-2690(2002)038<0188:AMFPEG>2.0.CO;2

Mishra, A., Reynolds, J. P., Chen, Y., Gourine, A. V., Rusakov, D. A., and Attwell, D. (2016). Astrocytes mediate neurovascular signaling to capillary pericytes but not to arterioles. *Nat. Neurosci.* 19, 1619–1627. doi: 10.1038/nn.4428

Muller, M. S., and Taylor, C. W. (2017). ATP evokes Ca^{2+} signals in cultured foetal human cortical astrocytes entirely through G protein-coupled P2Y receptors. *J. Neurochem.* 142, 876–885. doi: 10.1111/jnc.14119

Murray, J. A., Moore, S. B., Van Dyke, C. T., Lahr, B. D., Dierkhising, R. A., Zinsmeister, A. R., et al. (2007). HLA DQ gene dosage and risk and severity of celiac disease. *Clin. Gastroenterol. Hepatol.* 5, 1406–1412. doi: 10.1016/j.cgh.2007.08.013

Negri, S., Faris, P., Pellavio, G., Botta, L., Orgiu, M., Forcaia, G., et al. (2020). Group 1 metabotropic glutamate receptors trigger glutamate-induced intracellular Ca^{2+} signals and nitric oxide release in human brain microvascular endothelial cells. *Cell. Mol. Life Sci.* 77, 2235–2253. doi: 10.1007/s00018-019-03284-1

Ochoa-Cortes, F., Turco, F., Linan-Rico, A., Soghomonyan, S., Whitaker, E., Wehner, S., et al. (2016). Enteric glial cells: a new frontier in Neurogastroenterology and clinical target for inflammatory bowel diseases. *Inflamm. Bowel Dis.* 22, 433–449. doi: 10.1097/MIB.0000000000000667

Pavel, M., Renna, M., Park, S. J., Menzies, F. M., Ricketts, T., Füllgrabe, J., et al. (2018). Contact inhibition controls cell survival and proliferation via YAP/TAZ-autophagy axis. *Nat. Commun.* 9:2961. doi: 10.1038/s41467-018-05388-x

Pochard, C., Coquenlorge, S., Freyssinet, M., Naveilhan, P., Bourreille, A., Neunlist, M., et al. (2018). The multiple faces of inflammatory enteric glial cells: is Crohn's disease a gliopathy? *Am. J. Physiol. Gastrointest. Liver Physiol.* 315, G1–G11. doi: 10.1152/ajpgi.00016.2018

Prakriya, M., and Lewis, R. S. (2015). Store-operated calcium channels. *Physiol. Rev.* 95, 1383–1436. doi: 10.1152/physrev.00020.2014

Progatzky, F., and Pachnis, V. (2022). The role of enteric glia in intestinal immunity. *Curr. Opin. Immunol.* 77:102183. doi: 10.1016/j.coi.2022.102183

Quénet, D., and Dalal, Y. (2012). The CENP-A nucleosome: a dynamic structure and role at the centromere. *Chromosom. Res.* 20, 465–479. doi: 10.1007/s10577-012-9301-4

Rosenbaum, C., Schick, M. A., Wollborn, J., Heider, A., Scholz, C. J., Cecil, A., et al. (2016). Activation of myenteric glia during acute inflammation in vitro and in vivo. *PLoS One* 11:e0151335. doi: 10.1371/journal.pone.0151335

Rühl, A. (2005). Glial cells in the gut. *Neurogastroenterol. Motil.* 17, 777–790. doi: 10.1111/j.1365-2982.2005.00687

Rühl, A., Franzke, S., and Stremmel, W. (2001a). IL-1beta and IL-10 have dual effects on enteric glial cell proliferation. *Neurogastroenterol. Motil.* 13, 89–94. doi: 10.1046/j.1365-2982.2001.00245.x

Rühl, A., Nasser, Y., and Sharkey, K. A. (2004). Enteric glia. *Neurogastroenterol. Motil.* 16, 44–49. doi: 10.1111/j.1743-3150.2004.00474.x

Rühl, A., Trotter, J., and Stremmel, W. (2001b). Isolation of enteric glia and establishment of transformed enteroglial cell lines from the myenteric plexus of adult rat. *Neurogastroenterol. Motil.* 13, 95–106. doi: 10.1046/j.1365-2982.2001.00246.x

Sarosi, G. A., Barnhart, D. C., Turner, D. J., and Mulholland, M. W. (1998). Capacitative Ca^{2+} entry in enteric glia induced by thapsigargin and extracellular ATP. *Am. J. Phys.* 275, G550–G555. doi: 10.1152/ajpgi.1998.275.3.G550

Savidge, T. C., Newman, P., Pothoulakis, C., Ruhl, A., Neunlist, M., Bourreille, A., et al. (2007). Enteric glia regulate intestinal barrier function and inflammation via release of S-nitrosoglutathione. *Gastroenterology* 132, 1344–1358. doi: 10.1053/j.gastro.2007.01.051

Sazonovs, A., Kennedy, N. A., Moutsianas, L., Heap, G. A., Rice, D. L., Reppell, M., et al. (2020). HLA-DQA1*05 carriage associated with development of anti-drug antibodies to infliximab and adalimumab in patients with Crohn's disease. *Gastroenterology* 158, 189–199. doi: 10.1053/j.gastro.2019.09.041

Schmittgen, T. D., and Livak, K. J. (2008). Analyzing real-time PCR data by the comparative C(T) method. *Nat. Protoc.* 3, 1101–1108. doi: 10.1038/nprot.2008.73

Seguella, L., and Gulbransen, B. D. (2021). Enteric glial biology, intercellular signalling and roles in gastrointestinal disease. *Nat. Rev. Gastroenterol. Hepatol.* 18, 571–587. doi: 10.1038/s41575-021-00423-7

Slivinschi, B., Manai, F., Martinelli, C., Carriero, F., D'Amato, C., Massarotti, M., et al. (2022). Enhanced delivery of rose Bengal by amino acids starvation and exosomes inhibition in human astrocytoma cells to potentiate anticancer photodynamic therapy effects. *Cells* 11:2502. doi: 10.3390/cells11162502

Soret, R., Coquenlorge, S., Cossais, F., Meurette, G., Rolli-Derkinderen, M., and Neunlist, M. (2013). Characterization of human, mouse, and rat cultures of enteric glial cells and their effect on intestinal epithelial cells. *Neurogastroenterol. Motil.* 25, e755–e764. doi: 10.1111/nmo.12200

Sun, X., and Kaufman, P. D. (2018). Ki-67: more than a proliferation marker. *Chromosoma* 127, 175–186. doi: 10.1007/s00412-018-0659-8

Taheri, M., Handy, G., Borisyuk, A., and White, J. A. (2017). Diversity of evoked astrocyte Ca^{2+} dynamics quantified through experimental measurements and mathematical modeling. *Front. Syst. Neurosci.* 11:79. doi: 10.3389/fnsys.2017.00079

Tang, W., Szokol, K., Jensen, V., Enger, R., Trivedi, C. A., Hvalby, Ø., et al. (2015). Stimulation-evoked Ca2+ signals in astrocytic processes at hippocampal CA3-CA1 synapses of adult mice are modulated by glutamate and ATP. *J. Neurosci.* 35, 3016–3021. doi: 10.1523/JNEUROSCI.3319-14.2015

Toth, A. B., Hori, K., Novakovic, M. M., Bernstein, N. G., Lambot, L., and Prakriya, M. (2019). CRAC channels regulate astrocyte Ca^{2+} signaling and gliotransmitter release to modulate hippocampal GABAergic transmission. *Sci. Signal.* 12:eaaw5450. doi: 10.1126/scisignal.aaw5450

Valès, S., Bacola, G., Biraud, M., Touvron, M., Bessard, A., Geraldo, F., et al. (2019). Tumor cells hijack enteric glia to activate colon cancer stem cells and stimulate tumorigenesis. *EBioMedicine* 49, 172–188. doi: 10.1016/j.ebiom.2019.09.045

Verkhratsky, A., and Parpura, V. (2014). Store-operated calcium entry in neuroglia. *Neurosci. Bull.* 30, 125–133. doi: 10.1007/s12264-013-1343-x

von Boyen, G. B., Schulte, N., Pflüger, C., Spaniol, U., Hartmann, C., and Steinkamp, M. (2011). Distribution of enteric glia and GDNF during gut inflammation. *BMC Gastroenterol.* 11:3. doi: 10.1186/1471-230X-11-3

von Boyen, G. B., Steinkamp, M., Reinshagen, M., Schäfer, K. H., Adler, G., and Kirsch, J. (2004). Proinflammatory cytokines increase glial fibrillary acidic protein expression in enteric glia. *Gut* 53, 222–228. doi: 10.1136/gut.2003.012625

Wang, Z., Ocadiz-Ruiz, R., Sundaresan, S., Ding, L., Hayes, M., Sahoo, N., et al. (2018). Isolation of enteric glial cells from the submucosa and lamina Propria of the adult mouse. *J. Vis. Exp.* 138:57629. doi: 10.3791/57629

Woodfin, A., Voisin, M. B., and Nourshargh, S. (2007). PECAM-1: a multi-functional molecule in inflammation and vascular biology. *Arterioscler. Thromb. Vasc. Biol.* 27, 2514–2523. doi: 10.1161/ATVBAHA.107.151456

Yang, H., Villani, R. M., Wang, H., Simpson, M. J., Roberts, M. S., Tang, M., et al. (2018). The role of cellular reactive oxygen species in cancer chemotherapy. *J. Exp. Clin. Cancer Res.* 37:266. doi: 10.1186/s13046-018-0909-x

Yang, Z., and Wang, K. K. (2015). Glial fibrillary acidic protein: from intermediate filament assembly and gliosis to neurobiomarker. *Trends Neurosci.* 38, 364–374. doi: 10.1016/j.tins.2015.04.003

Zhang, W., Sarosi, G. Jr., Barnhart, D., Yule, D. I., and Mulholland, M. W. (1997). Endothelin-activated calcium signaling in enteric glia derived from neonatal Guinea pig. *Am. J. Phys.* 272, G1175–G1185. doi: 10.1152/ajpgi.1997.272.5.G1175

Zhang, W., Segura, B. J., Lin, T. R., Hu, Y., and Mulholland, M. W. (2003). Intercellular calcium waves in cultured enteric glia from neonatal Guinea pig. *Glia* 42, 252–262. doi: 10.1002/glia.10215

International Journal of
Molecular Sciences

MDPI

Article

Gluten Exorphins Promote Cell Proliferation through the Activation of Mitogenic and Pro-Survival Pathways

Federico Manai [1,*,†], Lisa Zanoletti [1,2,†], Giulia Morra [3,4], Samman Mansoor [3], Francesca Carriero [1], Elena Bozzola [5], Stella Muscianisi [6] and Sergio Comincini [1,*]

1 Department of Biology and Biotechnology "L.Spallanzani", University of Pavia, 27100 Pavia, Italy
2 Laboratory for Mucosal Immunology, TARGID, Department of Chronic Diseases, Metabolism and Ageing, KU Leuven, 3000 Leuven, Belgium
3 SCITEC, Consiglio Nazionale delle Ricerche, 20131 Milano, Italy
4 Department of Physiology and Biophysics, Weill Cornell Medicine, New York, NY 10065, USA
5 Pediatric Unit, I.R.C.C.S. Bambino Gesù Children Hospital, 00165 Roma, Italy
6 Cell Factory and Pediatric Hematology/Oncology, Fondazione IRCCS Policlinico San Matteo, 27100 Pavia, Italy
* Correspondence: federico.manai01@universitadipavia.it (F.M.); sergio.comincini@unipv.it (S.C.)
† These authors contributed equally to this work.

Abstract: Celiac disease (CD) is a chronic and systemic autoimmune disorder that affects preferentially the small intestine of individuals with a genetic predisposition. CD is promoted by the ingestion of gluten, a storage protein contained in the endosperm of the seeds of wheat, barley, rye, and related cereals. Once in the gastrointestinal (GI) tract, gluten is enzymatically digested with the consequent release of immunomodulatory and cytotoxic peptides, i.e., 33mer and p31-43. In the late 1970s a new group of biologically active peptides, called gluten exorphins (GEs), was discovered and characterized. In particular, these short peptides showed a morphine-like activity and high affinity for the δ-opioid receptor (DOR). The relevance of GEs in the pathogenesis of CD is still unknown. Recently, it has been proposed that GEs could contribute to asymptomatic CD, which is characterized by the absence of symptoms that are typical of this disorder. In the present work, GEs cellular and molecular effects were in vitro investigated in SUP-T1 and Caco-2 cells, also comparing viability effects with human normal primary lymphocytes. As a result, GEs treatments increased tumor cell proliferation by cell cycle and Cyclins activation as well as by induction of mitogenic and pro-survival pathways. Finally, a computational model of GEs interaction with DOR is provided. Altogether, the results might suggest a possible role of GEs in CD pathogenesis and on its associated cancer comorbidities.

Keywords: celiac disease; gluten; gluten exorphins; opioid receptors; δ-opioid receptor

Citation: Manai, F.; Zanoletti, L.; Morra, G.; Mansoor, S.; Carriero, F.; Bozzola, E.; Muscianisi, S.; Comincini, S. Gluten Exorphins Promote Cell Proliferation through the Activation of Mitogenic and Pro-Survival Pathways. *Int. J. Mol. Sci.* **2023**, *24*, 3912. https://doi.org/10.3390/ijms24043912

Academic Editors: Sandra Marmiroli and Roberta Di Pietro

Received: 4 January 2023
Revised: 10 February 2023
Accepted: 13 February 2023
Published: 15 February 2023

1. Introduction

Celiac disease (CD), also referred as celiac sprue and gluten-sensitive enteropathy, is a chronic immune-mediated enteropathy affecting the small intestine of individuals with a genetic predisposition which is also characterized by extra-intestinal symptoms. This disorder is triggered by the ingestion of gluten, a mixture of storage proteins in the seeds of mature grains of wheat, barley, and rye. Particularly, the inflammatory and immune-mediated response is caused by the biological activity exerted by immunogenic and cytotoxic peptides released after the enzymatic digestion of gluten in the gastrointestinal (GI) tract [1,2]. According to the Oslo definition and subsequent clarifications [3,4], CD can be subdivided into symptomatic CD, in which it is possible to recognize different subtypes (i.e., classic CD, subclinical CD, and refractory CD) [1,5].

Gluten exorphins (GEs) are a family of small peptides (four/five amino acids) derived from the enzymatic digestion of gluten in the GI tract exerted by pancreatic elastase [6].

These peptides, described as agonist of opioid receptors (ORs), were originally identified in 1979 by Zioudrou and colleagues [7]. The role of GEs in CD pathogenesis is still unknown. Recently, it has been proposed that GEs could play a key role in the onset of the asymptomatic form of CD, by masking the deleterious effects of gluten protein on gastrointestinal lining and function [8]. GEs (classified as A4, A5, B4, B5, C5) showed affinity for ORs with different selectivity (EC_{50}) for δ-opioid receptor (DOR), κ-opioid receptor (KOR) and μ-opioid receptor (MOR). Particularly, B5 is the most potent among GEs and exerts its biological activity mainly through the binding with DOR [9–12]. DOR is a seven transmembrane domain receptor coupled with G protein (GCPR) coded by the *ORPD* gene. The agonists of this receptor have demonstrated potent analgesic properties as well as the ability to activate several intracellular pathways, such as AC, different phospholipases, Erk1/2, Akt, c-Jun as well as Ca^{2+} signaling [13]. Recent in vitro studies showed that GEs can cross the intestinal epithelium without cytotoxic effects and increasing cell viability, suggesting a possible role in metabolic and proliferative processes of enterocytes [14,15]. It has been demonstrated that DOR receptor is over-expressed on the plasma membrane during inflammatory processes [15–19] as well as in cancer [20–25]. This characteristic may play an important role in the onset of CD comorbidities, specifically enteropathy-associated T-cell lymphoma (EATL) and small bowel carcinoma (SBC), which are associated with undiagnosed CD or not strictly adherent gluten-free diet (GFD) [26,27].

The aim of this work was to investigate the molecular and cellular effect of GEs in established SUP-T1 and Caco-2 cells, respectively, as in vitro models of lymphoblastic T-cells and intestinal epithelial barrier, in order to suggest possible functional interplays of GEs in the context of CD and on its associated cancer comorbidities.

2. Results

2.1. SUP-T1 and Caco-2 Cells Differentially Express DOR

A preliminary analysis was performed to study the levels of DOR expression in SUP-T1 and Caco-2 cells. DOR protein expression was assessed through immunofluorescence and immunoblotting analyses. As reported in Figure 1, DOR was expressed in the investigated cell lines. Particularly, immunoblotting analysis showed that SUP-T1 expressed significantly higher levels of DOR compared with Caco-2 cells. Immunoblotting analysis was also performed to investigate DOR expression levels on normal human primary fibroblasts, which showed significantly lower levels compared with SUP-T1 cells.

2.2. GEs Treatment Promoted SUP-T1 Cells Proliferation

Based on the higher DOR expression profile, GEs effects were primary investigated in SUP-T1 cells. To this purpose, cell proliferation was initially evaluated adding GEs at the concentrations reported in BIOPEP, a database in which all the biologically active peptides and their EC_{50} are described. Cell proliferation was investigated by means of cytofluorimetric analysis at 24 h post-treatment (p.t.) after GEs administration to the culture media. As showed in Figure 2A, an increasing trend in SUP-T1 cell proliferation was observed after the addition of GEs compared with non-treated (NT) cells. Particularly, SUP-T1 proliferation was significantly higher following A5, B4, B5 and C5 treatments. Moreover, based on their reduced employed concentrations, 3.4 and 0.02 μM, respectively, B4 and B5 exerted the major effects compared with the other ones (i.e., A4, A5 and C5). The same analysis was also performed on normal human primary fibroblasts to understand whether GEs were able to induce proliferation in normal cells. As reported (Figure 2B), a slight and not statistically significant increase in cell proliferation was scored.

T1 and Caco-2 cells. DOR protein expression was assessed through immunofluorescence and immunoblotting analyses. As reported in Figure 1, DOR was expressed in the investigated cell lines. Particularly, immunoblotting analysis showed that SUP-T1 expressed significantly higher levels of DOR compared with Caco-2 cells. Immunoblotting analysis was also performed to investigate DOR expression levels on normal human primary fibroblasts, which showed significantly lower levels compared with SUP-T1 cells.

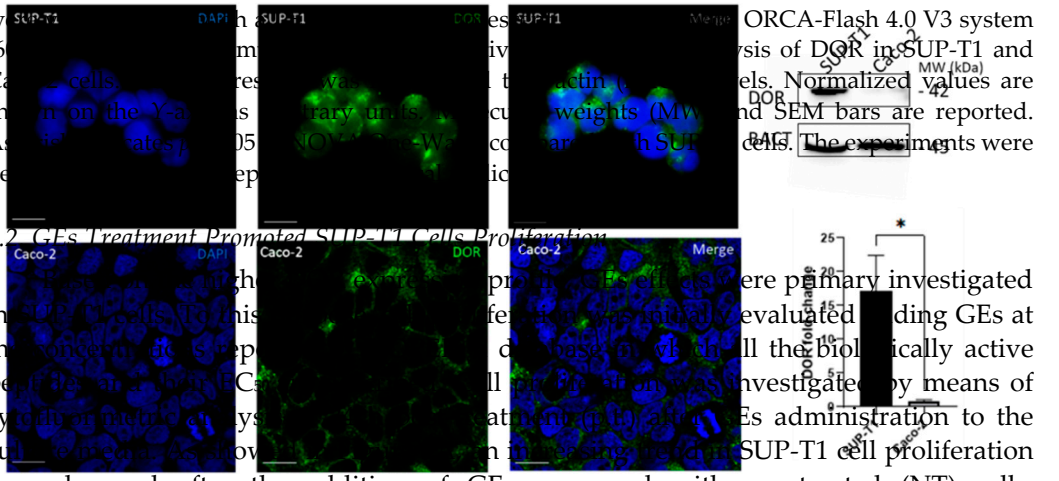

Figure 1. Analysis of DOR expression levels. On the left, immunofluorescence of DOR (green) in SUP-T1 and Caco-2 cell lines. Nuclei were stained in DAPI. Scale bars (10 µm) are reported. Images were visualized through a LEICA DM6 B fluorescent microscope with ORCA-Flash 4.0 V3 system (60X). On the right, immunoblotting and relative densitometric analysis of DOR in SUP-T1 and Caco-2 cells. DOR expression was normalized to β-actin (BACT) levels. Normalized values are shown on the Y-axis as arbitrary units. Molecular weights (MW) and SEM bars are reported. Asterisk indicates $p < 0.05$ (ANOVA One-Way), compared with SUP-T1 cells. The experiments were performed on three independent biological replicas.

2.2. GEs Treatment Promoted SUP-T1 Cells Proliferation

Eight GEs (A4, A5, B4, B5, C5, A6, B6 and C6) were primary investigated in order to evaluate their effects on cell proliferation. Initially, we evaluated the binding GEs at the concentrations reported in the BIOPEP database [27] on all the biologically active peptides. Cell proliferation was investigated by means of cytofluorimetric analysis after GEs administration to the culture media. As shown in Figure 2A, SUP-T1 cell proliferation was observed after the addition of GEs compared with non-treated (NT) cells. Particularly, SUP-T1 proliferation was significantly higher following A5, B4, B5 and C5 treatments. Moreover, based on their reduced employed concentrations, 3.4 and 0.02 µM, respectively, B4 and B5 exerted the major effects compared with the other ones (i.e., A4, A5 and C5). The same analysis was also performed on normal human primary fibroblasts to understand whether GEs were able to induce proliferation in normal cells. As reported (Figure 2B), a slight and not statistically significant increase in cell proliferation was scored.

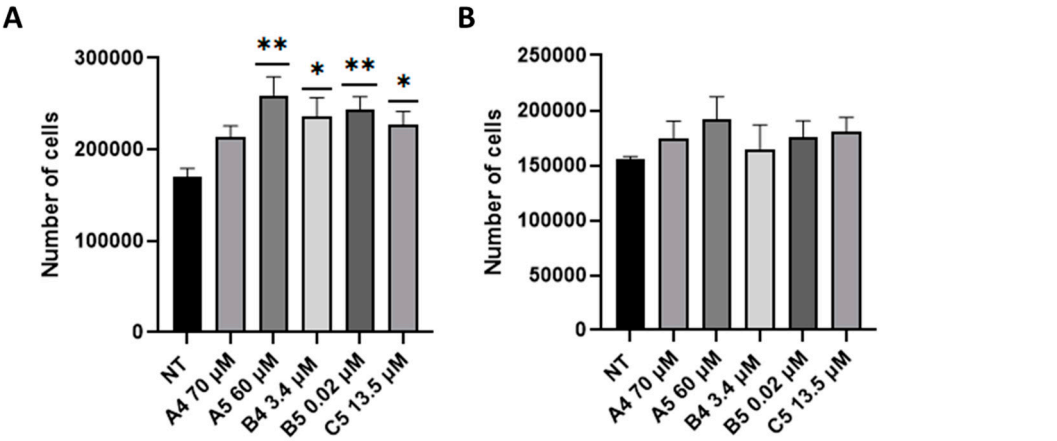

Figure 2. Analysis of cell proliferation following GEs administration. (**A**) SUP-T1 and (**B**) normal human primary fibroblasts cell proliferation after GEs administration at 24 h p.t. GEs were used according to the concentration reported in the BIOPEP database. Cytofluorimetric analysis was performed through Muse Cell Analyzer. Asterisks indicated $p < 0.05$ (*) or $p < 0.01$ (**), compared with non-treated (NT) cells. ANOVA One-Way test. Analysis was performed on four independent biological replicas with 1,000 events collected each. SEM bars are reported.

Considering the observed increase in cell proliferation, cell cycle progression in synchronized SUP-T1 cells was investigated by means of cytofluorimetric analysis after GEs treatments. Specifically, SUP-T1 cells were synchronized using colcemid, a derivative of colchicine capable of depolymerizing microtubules and arresting cells in metaphase [28]. After the removal of the cell cycle block, GEs were added to the culture media for 24 h. Cells in which the cell cycle was restored after colcemid administration (i.e., sample R) were used as the control. As shown in Figure S1, after GEs treatments a statistically significant decrease in the number of cells in G2/M was detected as well as a relative significant increase in G0/G1 phases compared with sample R. Again, based on their reduced employed concentrations, B4 and B5 exerted the major effects compared with the other assayed GEs. These GEs, in addition to their ability to induce cell proliferation, also stimulated

Int. J. Mol. Sci. **2023**, *24*, 3912 4 of 16

according to the concentrations reported in BIOPEP database, were further confirmed by a cytofluorimetric evaluation of Cyclins E2 and A expression in SUP-T1 cells, as documented in Figure S2. In particular, compared to untreated cells, GEs induced a general increase in Cyclins expression.

the concentrations reported in BIOPEP database, were further confirmed by a cytofluorimetric evaluation of Cyclins E2 and A expression in SUP-T1 cells, as documented in Figure S2. In particular, compared to untreated cells, GEs induced a general increase in Cyclins expression.

Alterations in cell viability/metabolism were then investigated starting from 1 to 4 h p.t. to reveal the cellular kinetic effects of GEs. As reported in Figure 3, an increase in cell viability/metabolism was observed following all GEs treatments although no significant differences were detected.

Alterations in cell viability/metabolism were then investigated starting from 1 to 4 h p.t. to reveal the cellular kinetic effects of GEs. As reported in Figure 3, an increase in cell viability/metabolism was observed following all GEs treatments although no significant differences were detected.

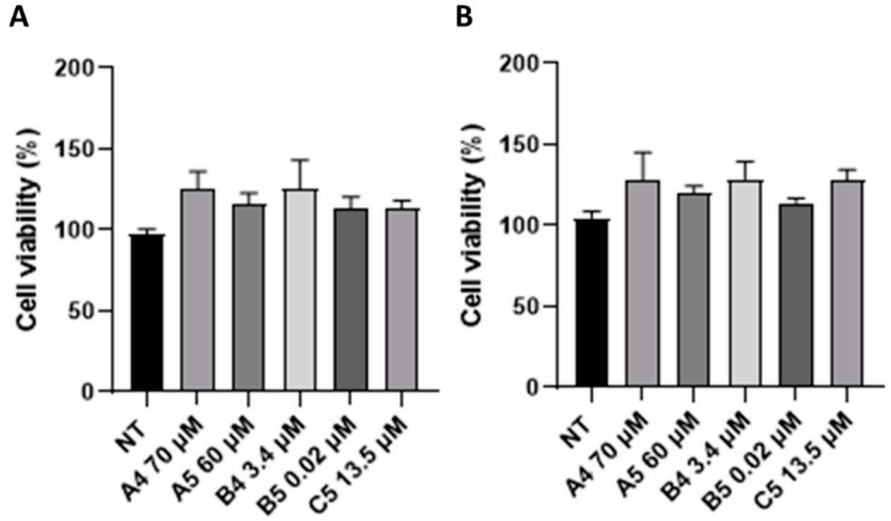

Figure 3. MTS analysis of SUP-T1 cell viability/metabolism at (**A**) 1 and (**B**) 4 h p.t. GEs were used according to the concentration reported in the BIOPEP database. Analysis was performed on three independent biological replicas. SEM bars are reported.

Figure 3. MTS analysis of SUP-T1 cell viability/metabolism at (**A**) 1 and (**B**) 4 h p.t. GEs were used according to the concentration reported in the BIOPEP database. Analysis was performed on three independent biological replicas. SEM bars are reported.

Considering the absence of significance in cell metabolic activity as well as the temporal bias that characterized the activity of GCPRs [29], increasing concentrations of these peptides (specifically, 5- to 10-fold compared to those reported in the BIOPEP database) were tested and cell viability was investigated at the same time intervals (i.e., 1 and 4 h p.t.) through MTS assay. As shown in Figure 4A, no cytotoxicity was detected. Conversely, a statistically significant concentration-dependent increase in cell metabolism was observed in SUP-T1 cells treated with exorphins A4 and A5 at all the tested concentrations at 4 h p.t. Since no significance was obtained for B4, B5, and C5 increasing their concentration 5- and 10-fold times, other concentrations were tested using the same experimental scheme. As shown in Figure 4B, MTS assay led to the identification of the effective concentrations for all the three tested GEs (i.e., B4 = 50 µM, B5 = 20 µM, and C5 = 250 µM).

Considering the absence of significance in cell metabolic activity as well as the temporal bias that characterized the activity of GCPRs [29], increasing concentrations of these peptides (specifically, 5- to 10-fold compared to those reported in the BIOPEP database) were tested and cell viability was investigated at the same time intervals (i.e., 1 and 4 h p.t.) through MTS assay. As shown in Figure 4A, no cytotoxicity was detected. Conversely, a statistically significant concentration-dependent increase in cell metabolism was observed in SUP-T1 cells treated with exorphins A4 and A5 at all the tested concentrations at 4 h p.t. Since no significance was obtained for B4, B5, and C5 increasing their concentration 5- and 10-fold times, other concentrations were tested using the same experimental scheme. As shown in Figure 4B, MTS assay led to the identification of the effective concentrations for all the three tested GEs (i.e., B4 = 50 µM, B5 = 20 µM, and C5 = 250 µM).

The minimum concentrations that were able to increase the cell metabolic activity (Figure 4A,B) were then tested though immunoblotting to study the induction of mitogenic and pro-survival pathways, specifically phosphorylation levels of Akt and Erk1/2 kinases. As reported in Figure 5, a significant increase in Akt phosphorylation ratio was observed following GEs administration. Erk1/2 phosphorylation levels were generally increased following GEs treatments, with however statistical significance only in A4, A5 and B4 samples.

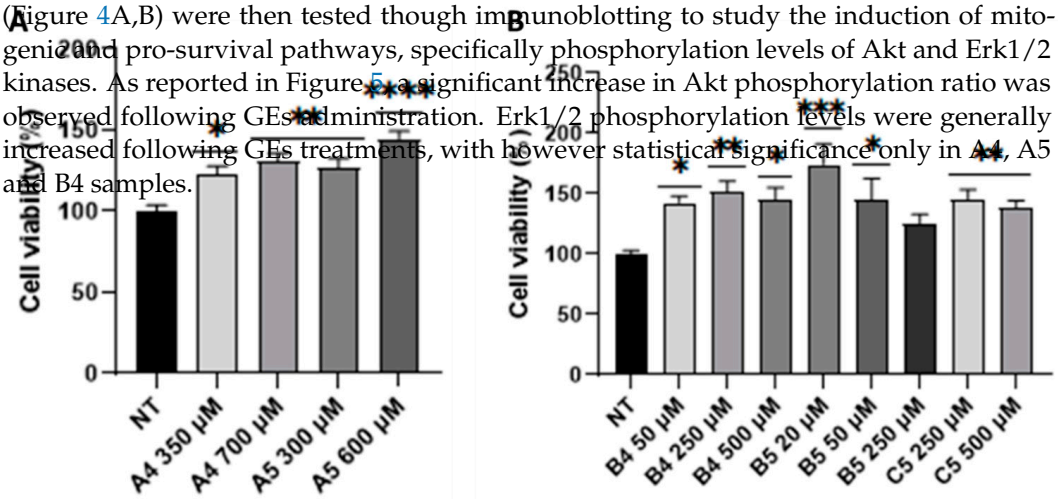

versely, a statistically significant concentration-dependent increase in cell metabolism was observed in SUP-T1 cells treated with exorphins A4 and A5 at all the tested concentrations at 4 h p.t. Since no significance was obtained for B4, B5, and C5 increasing their concentration 5- and 10-fold times, other concentrations were tested using the same experimental scheme. As shown in Figure 4B, MTS assay led to the identification of the effective concentrations for all the three tested GEs (i.e., B4 = 50 µM, B5 = 20 µM, and C5 = 250 µM).

Int. J. Mol. Sci. 2023, 24, x FOR PEER REVIEW 5 of 16

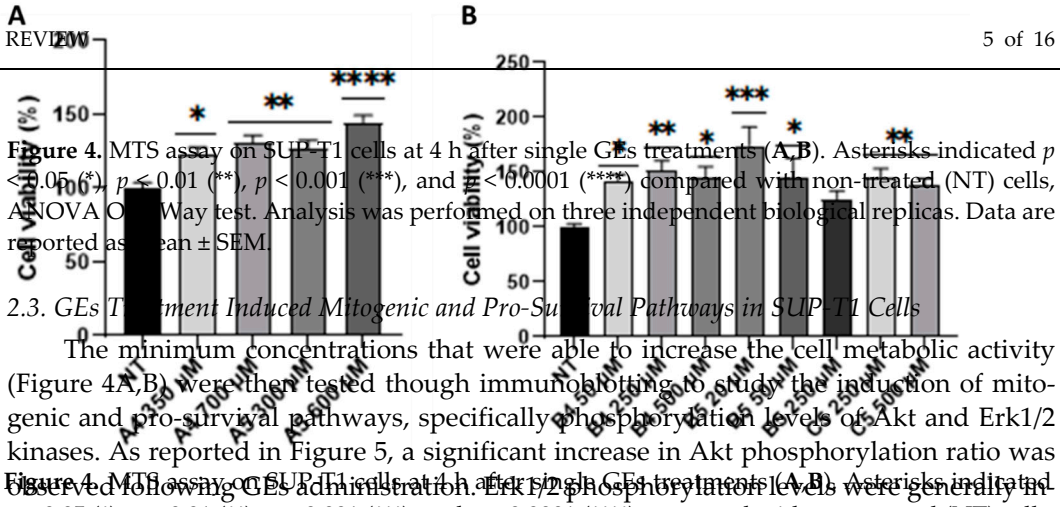

Figure 4. MTS assay on SUP-T1 cells at 4 h after single GEs treatments (A,B). Asterisks indicated $p < 0.05$ (*), $p < 0.01$ (**), $p < 0.001$ (***), and < 0.0001 (****) compared with non-treated (NT) cells, ANOVA One-Way test. Analysis was performed on three independent biological replicas. Data are reported as mean ± SEM.

2.3. GEs Treatment Induced Mitogenic and Pro-Survival Pathways in SUP-T1 Cells

The minimum concentrations that were able to increase the cell metabolic activity (Figure 4A,B) were then tested though immunoblotting to study the induction of mitogenic and pro-survival pathways, specifically phosphorylation levels of Akt and Erk1/2 kinases. As reported in Figure 5, a significant increase in Akt phosphorylation ratio was observed following GEs administration. Erk1/2 phosphorylation levels were generally increased following GEs treatments, with however statistical significance only in A4, A5 and B4 samples.

Figure 4. MTS assay on SUP-T1 cells at 4 h after single GEs treatments (A,B). Asterisks indicated $p < 0.05$ (*), $p < 0.01$ (**), $p < 0.001$ (***), and < 0.0001 (****) compared with non-treated (NT) cells, ANOVA One-Way test. Analysis was performed on three independent biological replicas. Data are reported as mean ± SEM.

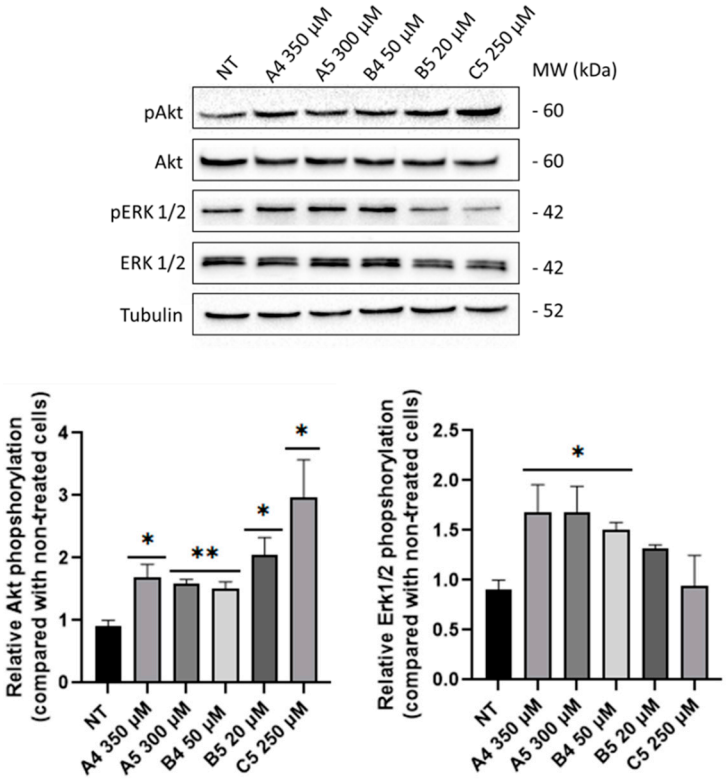

Figure 5. Akt and Erk1/2 phosphorylation levels in SUP-T1 cells at 4 h p.t. after GEs administration at the following concentrations: A4 = 350 µM, A5 = 300 µM, B4 = 50 µM, B5 = 20 µM and C5 = 250 µM. Akt and Erk1/2 were analyzed through immunoblotting and relative densitometric analyses (lower panels). Phosphorylated proteins were normalized to the total proteins and housekeeping levels. Normalized values are reported on *Y*-axis as arbitrary units. Molecular weights (MW) in kDa and SEM bars are shown. Asterisks indicate $p < 0.05$ (*) or $p < 0.01$ (**), compared with non-treated (NT) control cells (ANOVA One-Way). The experiments were performed on four independent biological replicas.

Figure 5. Akt and Erk1/2 phosphorylation levels in SUP-T1 cells at 4 h p.t. after GEs administration at the following concentrations: A4 = 350 µM, A5 = 300 µM, B4 = 50 µM, B5 = 20 µM and C5 = 250 µM. Akt and Erk1/2 were analyzed through immunoblotting and relative densitometric analyses (lower panels). Phosphorylated proteins were normalized to the total proteins and housekeeping levels. Normalized values are reported on *Y*-axis as arbitrary units. Molecular weights (MW) in kDa and SEM bars are shown. Asterisks indicate $p < 0.05$ (*) or $p < 0.01$ (**), compared with non-treated (NT) control cells (ANOVA One-Way). The experiments were performed on four independent biological replicas.

Subsequently, GEs were tested to investigate the activation of pro-survival pathways through the analysis of specific markers, i.e., the anti-apoptotic protein Bcl-2 [30] and the autophagy marker LC3-II [31], after 4 h p.t. As represented in Figure 6, all GEs treatments induced a significant increase in Bcl-2 levels. LC3-II levels showed an increasing trend but significant only for the B5 and C5 treatments. Since GEs were described as agonists of ORs, immunoblotting analysis was performed to investigate alterations in DOR expression levels after GEs treatment but no differences were detected.

Subsequently, GEs were tested to investigate the activation of pro-survival pathways through the analysis of specific markers, i.e., the anti-apoptotic protein Bcl-2 [30] and the autophagy marker LC3-II [31], after 4 h p.t. As represented in Figure 6, all GEs treatments induced a significant increase in Bcl-2 levels. LC3-II levels showed an increasing trend but significant only for the B5 and C5 treatments. Since GEs were described as agonists of ORs, immunoblotting analysis was performed to investigate alterations in DOR expression levels after GEs treatment but no differences were detected.

Int. J. Mol. Sci. **2023**, *24*, x FOR PEER REVIEW 6 of 16

but significant only for the B5 and C5 treatments. Since GEs were described as agonists of ORs, immunoblotting analysis was performed to investigate alterations in DOR expression levels after GEs treatment but no differences were detected.

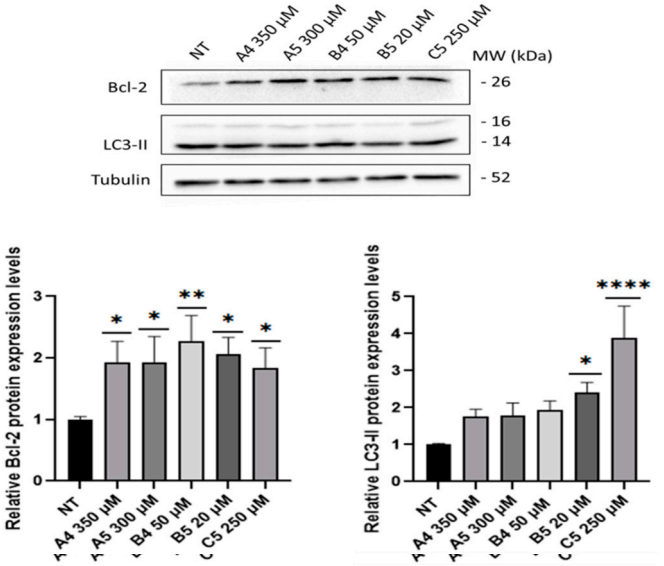

Figure 6. Bcl-2 and LC3-II levels in SUP-T1 cells at 4 h p.t. after GEs treatment: A4 = 350 µM, A5 = 300 µM, B4 = 50 µM, B5 = 20 µM and C5 = 250 µM. All the proteins were analyzed through immunoblotting and relative densitometric analyses. Bcl-2 and LC3-II were normalized to housekeeping levels. Bcl-2 proteins were normalized to housekeeping levels. Normalized values are reported on *y*-axis as arbitrary units. Molecular weights (MW) in kDa and SEM bars are shown. Asterisks indicated $p < 0.05$ (*), $p < 0.01$ (**), $p < 0.0001$ (****), compared with non-treated (NT) control cells (ANOVA One-Way). Bcl-2 and LC3-II levels were tested on four independent biological replicas.

Figure 6. Bcl-2 and LC3-II levels in SUP-T1 cells at 4 h p.t. after GEs treatment: A4 = 350 µM, A5 = 300 µM, B4 = 50 µM, B5 = 20 µM and C5 = 250 µM. All the proteins were analyzed through immunoblotting and relative densitometric analyses. Bcl-2 and LC3-II were normalized to housekeeping levels. Bcl-2 proteins were normalized to housekeeping levels. Normalized values are reported on *y*-axis as arbitrary units. Molecular weights (MW) in kDa and SEM bars are shown. Asterisks indicated $p < 0.05$ (*), $p < 0.01$ (**), $p < 0.0001$ (****), compared with non-treated (NT) control cells (ANOVA One-Way). Bcl-2 and LC3-II levels were tested on four independent biological replicas.

2.4. B5 Exorphin Induced Mitogenic and Pro-Survival Pathways in Caco-2 Cells

2.4. B5 Exorphin Induced Mitogenic and Pro-Survival Pathways in Caco-2 Cells

Considering that B5 was described as the most potent gluten exorphin [11], this peptide was tested through MTS assay in Caco-2 cells using the BIOPEP concentration of 0.02 µM. After 4 h p.t., no statistically significant increase was observed in cell metabolic activity. Again, MTS assay was performed at 4 h p.t. using the same concentrations tested in SUP-T1 cells. As represented in Figure 7, a concentration-dependent increase in cell viability was observed in Caco-2 cells, particularly for higher concentrations (>250 µM).

Considering that B5 was described as the most potent gluten exorphin [11], this peptide was tested through MTS assay in Caco-2 cells using the BIOPEP concentration of 0.02 µM. After 4 h p.t., no statistically significant increase was observed in cell metabolic activity. Again, MTS assay was performed at 4 h p.t. using the same concentrations tested in SUP-T1 cells. As represented in Figure 7, a concentration-dependent increase in cell viability was observed in Caco-2 cells, particularly for higher concentrations (>250 µM).

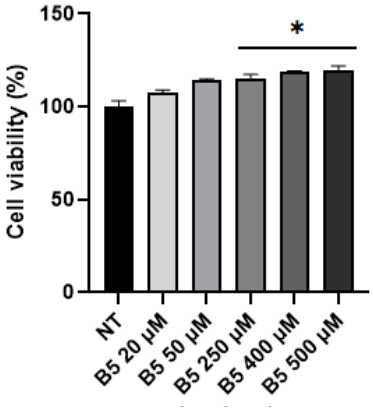

Figure 7. MTS assay on Caco-2 cells at 4 h p.t. Asterisk indicated $p \leq 0.05$ (*) compared with non-treated (NT) cells, ANOVA One-Way test. Analysis was performed on three independent biological replicas. Data are reported as mean ± SEM.

Figure 7. MTS assay on Caco-2 cells at 4 h p.t. Asterisk indicated $p \leq 0.05$ (*) compared with non-treated (NT) cells, ANOVA One-Way test. Analysis was performed on three independent biological replicas. Data are reported as mean ± SEM.

Similar to SUP-T1 cells, the expression of Akt, Erk1/2, and LC3-II proteins was investigated through immunoblotting in Caco-2 cells following different B5 micromolar administration. Furthermore, STAT3 phosphorylation was studied due to the role of this protein in intestinal epithelial cells (IECs) homeostasis [32]. An increasing trend in Akt phosphorylation was scored although not statistically significant (Figure S3). Conversely, as shown

Similar to SUP-T1 cells, the expression of Akt, Erk1/2, and LC3-II proteins was investigated through immunoblotting in Caco-2 cells following different B5 micromolar administration. Furthermore, STAT3 phosphorylation was studied due to the role of this protein in intestinal epithelial cells (IECs) homeostasis [32]. An increasing trend in Akt phosphorylation was scored although not statistically significant (Figure S3). Conversely, as shown

administration. Furthermore, STAT3 phosphorylation was studied due to the role of this protein in intestinal epithelial cells (IECs) homeostasis [32]. An increasing trend in Akt phosphorylation was scored although not statistically significant (Figure S3). Conversely as shown in Figure 8, an increasing trend in Erk1/2 phosphorylation was detected, although statistically significant starting from 250 µM of B5. Moreover, a decrease in LC3-II and STAT3 phosphorylation levels was observed using B5 concentrations at 400 and 500 µM.

in Figure 8, an increasing trend in Erk1/2 phosphorylation was detected, although statistically significant starting from 250 µM of B5. Moreover, a decrease in LC3-II and STAT3 phosphorylation levels was observed using B5 concentrations at 400 and 500 µM.

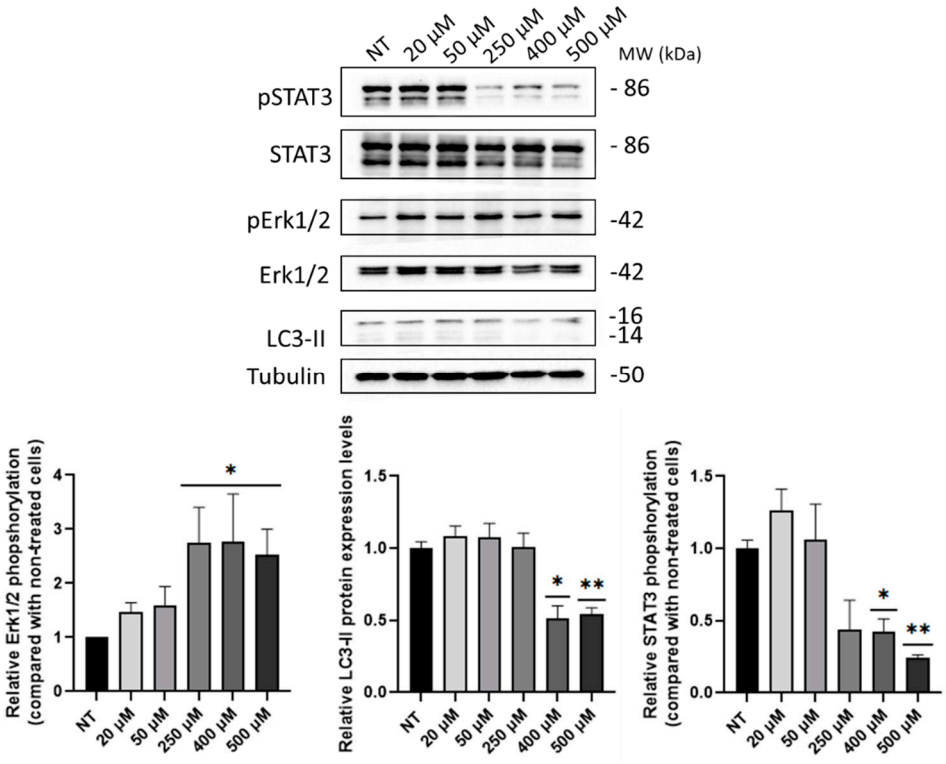

Figure 8. Phospho-Erk1/2, LC3-II, and phospho-STAT3 levels in Caco-2 cells at 4 h p.t. after B5 administration at increasing concentrations (i.e., 20, 50, 250, 400 and 500 µM). Phosphorylated proteins were normalized to the total proteins and housekeeping levels. Normalized values are reported on *Y*-axis as arbitrary units. Molecular weights (MW) in kDa and SEM bars are shown. Asterisks indicated $p \leq 0.05$ (*) or $p \leq 0.01$ (**), compared with non-treated (NT) control cells (ANOVA One-Way). The experiments were performed on three independent biological replicas.

Figure 8. Phospho-Erk1/2, LC3-II, and phospho-STAT3 levels in Caco-2 cells at 4 h p.t. after B5 administration at increasing concentrations (i.e., 20, 50, 250, 400 and 500 µM). Phosphorylated proteins were normalized to the total proteins and housekeeping levels. Normalized values are reported on *Y*-axis as arbitrary units. Molecular weights (MW) in kDa and SEM bars are shown. Asterisks indicated $p \leq 0.05$ (*) or $p \leq 0.01$ (**), compared with non-treated (NT) control cells (ANOVA One-Way). The experiments were performed on three independent biological replicas.

2.5. Gluten B Exorphins Did Not Induce Increase in Viability in Normal CD3+ and CD8+ T-Lymphocytes

The most effective B4 and B5 exorphins were selected and preliminary tested on primary T-cells isolated from 3 healthy subjects to determine their effects on viability at the same time intervals (i.e., 0 to 4 h p.t.) previously investigated in SUP-T1 cells. Specifically, B exorphins were investigated on PBMC-derived bulk CD3+ and on CD8+ cell subsets isolated by labeling with antigen-coated microbeads and magnetic capture. T-cells viability was evaluated in a time-kinetics interval by MTS assay, following BIOPEP database concentrations (i.e., 3.4 µM for B4 and 0.02 µM for B5) administration. As reported (Figure 9), in general, B4 and B5 exorphins induced a reduction on T-cells viability. In particular, B4 produced a slight but significant decrease in viability at 50 µM concentration at 30, 60 and 120 min in CD3+ and no significant reduction in CD8+ cells, respectively (Figure 9A,B). In B5 treatment at 20 µM, only CD3+ cells displayed a significant reduction in viability at 30, 60 and 120 min intervals, while CD8+ displayed a significant decrease at 60 and 120 min (Figure 9C,D).

The most effective B4 and B5 exorphins were selected and preliminary tested on primary T-cells isolated from 3 healthy subjects to determine their effects on viability at the same time intervals (i.e., 0 to 4 h p.t.) previously investigated in SUP-T1 cells. Specifically, B exorphins were investigated on PBMC-derived bulk CD3+ and on CD8+ cell subsets isolated by labeling with antigen-coated microbeads and magnetic capture. T-cells viability was evaluated in a time-kinetics interval by MTS assay, following BIOPEP database concentrations (i.e., 3.4 µM for B4 and 0.02 µM for B5) administration. As reported (Figure 9), in general, B4 and B5 exorphins induced a reduction on T-cells viability. In particular, B4 produced a slight but significant decrease in viability at 50 µM concentration at 30, 60 and 120 min in CD3+ and no significant reduction in CD8+ cells, respectively (Figure 9A,B). In B5 treatment at 20 µM, only CD3+ cells displayed a significant reduction in viability at 30, 60 and 120 min intervals, while CD8+ displayed a significant decrease at 60 and 120 min (Figure 9C,D).

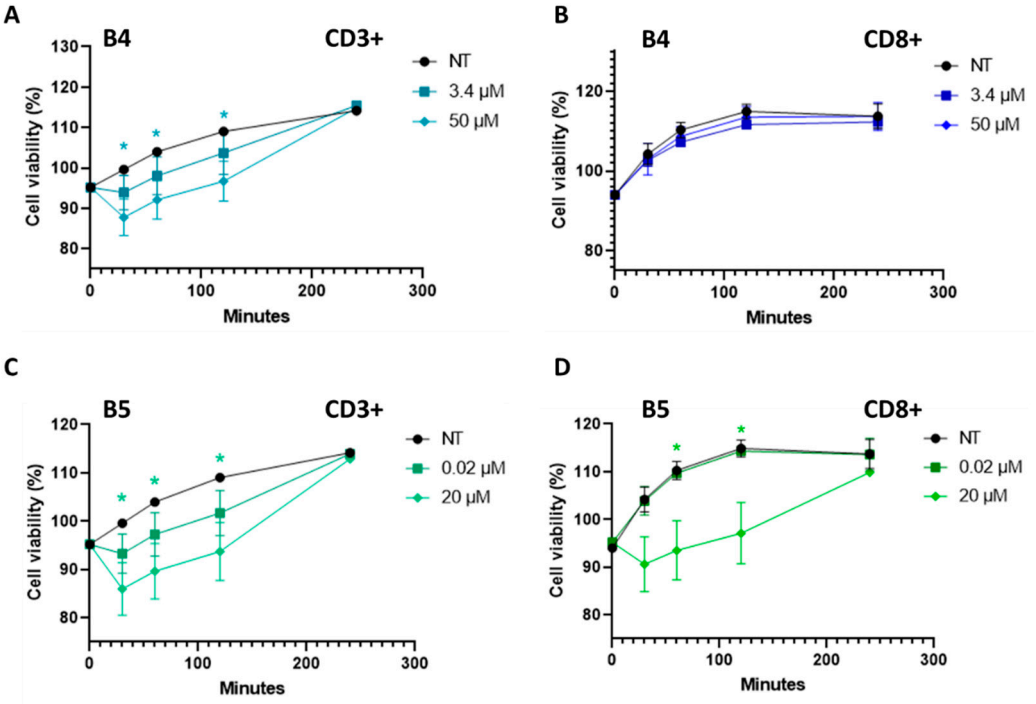

Figure 9. MTS time-kinetics viability assays of human normal primary CD3+ and CD8+ T-cells after B4 and B5 administration. (**A**) CD3+ T-cells viability after B4 treatment (3.4 and 50 µM). Cyan asterisks indicate $p < 0.05$, ANOVA One-Way, in 50 µM treated samples compared with non-treated (NT) cells at 30, 60 and 120 min. (**B**) CD8+ T-cells viability after B4 treatment (3.4 and 50 µM). (**C**) CD3+ T-cells viability after B5 treatment (0.02 and 20 µM). Green asterisks indicated $p < 0.05$, ANOVA One-Way, in B5 20 µM compared with non-treated (NT) cells at 30, 60 and 120 min. (**D**) CD8+ T-cells viability after B5 treatment (0.02 and 20 µM). Green asterisks indicated $p < 0.05$, ANOVA One-Way, in B5 20 µM compared with non-treated (NT) cells at 60 and 120 min. All the experiments were performed on three independent biological replicates, using human naïve T-cells isolated from 3 normal subjects. Data are reported as mean ± SEM.

2.6. B5 and A4 Showed a Differential DOR Dynamic Profile of Activation in Computational Models

The molecular determinants of the interaction between two selected GEs and DOR were investigated by means of Molecular Dynamics simulations. Multiple 1 µs trajectories were run for B5-DOR and A4-DOR complexes, using Leu-enkephalin-DOR as a control complex, after docking the three peptides into the binding site of the active DOR conformation (PDB code: 6PT2). The equilibrium poses of the three peptides, extracted as representative cluster centers after clustering each dataset according to the ligand position, are shown in Figure 10A. They all share the interaction between the peptide N-terminal domain and Asp128, its C-terminal domain interacting with Arg291, as well as the peptide Tyr1 pointing to His278. The most significant variability among the complexes is observed at extracellular loop EL3, with Trp284 strongly interacting with B5 Trp4 and less with Leu-enkephalin Phe4. A4 occasionally shows the least stable coordination with the binding site residues and the largest distance from Trp284 (Figure S4). Correspondingly, the structure of the intracellular side of the receptor bound to GEs is modulated with respect to control (Figure 10B). B5 is stabilized in a structure more like the Leu-enkephalin complex and the reference agonist-bound crystal structure 6PT2, albeit exploring also a wider TM6-TM3 distance (Figure 10B). In contrast, A4 drives the TM6-TM3 distance even further, thereby also occasionally affecting the known GPCR microswitches such as the toggle switch CWxP at Trp274 [48,74] and the NPxxY motif at Tyr318 [53,73]. These findings confirm that both GEs can sustain an active state of the receptor, but B5 shows a complex stability more closely resembling Leu-enkephalin, which might be connected to its stronger activity.

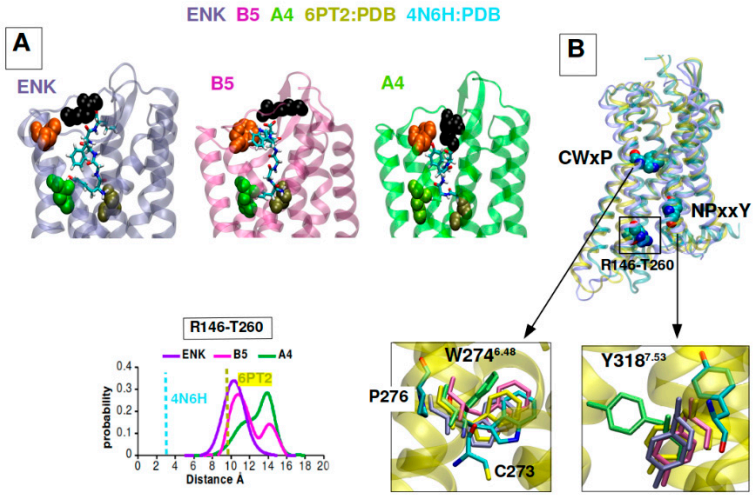

Figure 10. Computational models of GEs-DOR interactions. (**A**) Representative complexes of Leu-Enk-DOR, B5-DOR and A4-DOR extracted from simulations, showing the main contact points between peptide ligands and the receptor. (**B**) Superposition of agonist-bound crystal structure (6PT2), natrindole-bound crystal structure (4N6H) and representative structure of the Leu-enkephalin simulation, highlighting the micro-switches CWxP and NPxxY and residues 146 and 260 on TM3 and TM6 respectively. Bottom, left: distance histogram showing the distribution of distances between Cα atoms of R146 and T260. Right: Close-up superposition of W274 (toggle switch) and Y318 in the inactive natrindole structure (cyan) and in simulation representative snapshots.

Figure 10. Computational models of GEs-DOR interactions. (**A**) Representative complexes of Leu-Enk-DOR, B5-DOR and A4-DOR extracted from simulations, showing the main contact points between peptide ligands and the receptor. (**B**) Superposition of agonist-bound crystal structure (6PT2), natrindole-bound crystal structure (4N6H) and representative structure of the Leu-enkephalin simulation, highlighting the micro-switches CWxP and NPxxY and residues 146 and 260 on TM3 and TM6 respectively. Bottom, left: distance histogram showing the distribution of distances between Cα atoms of R146 and T260. Right: Close-up superposition of W274 (toggle switch) and Y318 in the inactive natrindole structure (cyan) and in simulation representative snapshots.

3. Discussion

To date, the effect of GEs released from the digestion of gluten was not deeply investigated. However, it has been demonstrated that GEs exert different effects in several physiological context, also depending on their ability to cross the intestinal epithelial barrier [14,15]. Specifically, it has been demonstrated that these peptides can bind ORs with different affinity, as reported by Zioudrou and colleagues [8]. As experimentally reported, exorphins A4 and A5 showed selectivity for the δ-opioid receptor (DOR) but not for κ (KOR); B4 and B5 showed affinity for δ- and µ-opioid receptor (MOR) but not for κ. Among these peptides, B5 was the most potent, with an EC_{50} of 0.05 µM for Guinea pig ileum (GPI) assay and 0.017 µM for MVD assay. On the opposite, B4 was less potent because of the lack of Leucine residue in position 5 [7,11,12].

Since gluten is the trigger of CD and different gluten derived peptides exert immunogenic and cytotoxic effects responsible for CD pathogenesis [1], GEs could be an interesting candidate to investigate in the context of this disorder. Specifically, the opioid activity of GEs could be implicated in the onset of the asymptomatic form of CD. As widely reported in the literature, DOR expression levels increase on the plasma membrane of intestinal cells during inflammatory processes; moreover, this over-expression is also mediated by DOR activation in a positive feedback loop [16–19]. These mechanisms could contribute to GEs activity in CD thus leading to the inhibition of abdominal pain that characterized the classical CD [6].

Considering these premises as well as that tumor comorbidities are associated with undiagnosed/untreated CD patients [1,26,27], the present work investigated the role of GEs in SUP-T1 and Caco-2 cells, after verifying the expression of DOR by immunofluorescence and immunoblotting. Considering that DOR agonists lead to the activation of proliferative pathways, such as PI3K/Akt and Erk1/2 [13,34–37], proliferation assays were performed on SUP-T1 cells using the concentration reported in the BIOPEP database. The obtained results demonstrated that GEs stimulate the proliferation of this cell line and, considering the concentration analyzed, confirmed the potent action of B and C compared with A gluten exorphins [11]. Furthermore, as highlighted by the significance levels, with five amino acids (i.e., A5 and B5) exerted a higher effect compared with their counter-

part of four amino acids (i.e., A4 and B4). These results were also corroborated by a cell cycle analysis on synchronized SUP-T1 cells. Conversely, no proliferative effects were observed in treated normal human primary fibroblasts although the expression of DOR was verified through immunoblotting. A possible hypothesis for this result could rely on the fact that DOR stimulation in fibroblast leads to the activation of p70(sK6), a protein implicated in cytoskeletal modifications as well as in cell migration, two processes involved in wound healing [38,39]. Subsequently, MTS assays using increasing concentration of GEs were performed starting from 1 to 4 h p.t. to study variation in cell metabolism. This temporal window was selected since mitogenic pathways are activated by ORs agonists in minutes/hours and the time-duration of the molecular response generated by GPCRs stimulation is influenced by different factors [29]. The collected results confirmed the increase in cell metabolism of SUP-T1 cells at 4 h p.t., thus leading to the identification of the minimum effective concentration. Considering the role of PI3K/Akt and Erk1/2 in cell proliferation as well as in DOR signaling pathway [13], phosphorylation of these two kinases was investigated by immunoblotting after 4 h p.t., accordingly to the MTS results. As showed, phosphorylation of Akt and Erk1/2 was observed in all GEs treatments. Furthermore, the levels of Bcl-2 were investigated to determine the effect of GEs treatments on apoptosis. Recent studies showed that IL-15 triggers anti-apoptotic pathways in intraepithelial lymphocytes (IELs) derived from RCDII patients through Bcl-2 and/or Bcl-XL [40]. As showed, all GEs led to an increase in Bcl-2 expression levels. Due to the crosstalk between autophagy and apoptosis [41] as well as in relation to the autophagy impairment caused by digested gliadin [42,43], the autophagy marker LC3-II was investigated. As reported, GEs treatments led to an increase in LC3-II levels of SUP-T1 cells, suggesting an increase in autophagy process induced by Erk1/2 activation [44] as well as by AMPK [45] due to the decreased levels of ATP generated by AC, a protein down-stream of DOR [6].

Considering the collected results as well as the evidence present in literature, B5 exorphin was selected and investigated in Caco-2 cells. Increasing concentrations of this peptide led to an increase in cell metabolism and to Erk1/2 activation. Moreover, a reduction in LC3-II levels was observed at the concentrations of 400 and 500 µM. This result could suggest a high autophagy flux and, as consequent, a massive degradation of LC3-II as well as an early blockage in the autophagy pathway. This second hypothesis is also suggested by the evidence collected in our laboratory that digested gliadin causes autophagy blockage in Caco-2 cells [42,43]. Lastly, STAT3 phosphorylation levels were assayed after B5 treatment due to its important role in IECs homeostasis. Particularly, STAT3 activation is implicated in wound healing, pathogen defense, and intestinal barrier integrity [46–49]. As reported, B5 treatment led to a reduction in STAT3 activation, thus leading to the hypothesis that GEs could contribute to the detrimental effects exerted by gliadin on IECs.

The results of the effects of GEs in reducing viability in human naïve CD3+ and CD8+ T cells agreed with those of DOR agonists that inhibited proliferation of murine T-cells [50]. Furthermore, Leu- and Met-enkephalins, that share sequence similarities with GEs, induced different effects on immune cells, according to their concentrations or to T-cell mitogenic status [51–53].

According to the data in the literature regarding the effects of enkephalins in immune cells, the behavior of GEs could be influenced by the metabolic status of the cells, as in the case of activated T-cells in inflammation [54,55], as well as by the DOR receptor levels on the plasma membrane, whose levels in T-cells are affected by different activating status [56–58].

Altogether, these results suggested a possible role of GEs in CD pathogenesis. Particularly, GEs could contribute to the induction of lymphocytes activation and infiltration as well as promoting IECs loss of homeostasis. Both these conditions could contribute to the maintenance of the CD inflammatory status and, possibly, to the onset of the asymptomatic form of CD. Future experiments might be aimed at evaluating GEs effects on human primary lymphocytes derived from CD patients as well as in organ cultures and to further dissect the molecular effects of GEs.

4. Materials and Methods

4.1. Cell Cultures and GEs Administration

SUP-T1 and Caco-2 cells were purchased from the American Type Culture Collection (ATCC). SUP-T1 were cultured in RPMI-1640 medium (Euroclone, Milano, Italy) supplemented with 10% FBS, 100 U/mL penicillin, 0.1 mg/mL streptomycin (Sigma, St. Louis, MO, USA), 1% Non-Essential Aminoacids (Euroclone) at 37 °C in a 5% CO_2 atmosphere. Caco-2 cells and normal human primary fibroblasts, isolated as reported [59], were cultured using DMEM medium (Euroclone). SUP-T1 and human primary fibroblasts were seeded at the final concentration of 1×10^5/mL whereas Caco-2 at the final concentration of 2×10^5/mL. Lyophilized GEs were purchased from ThermoFisher (Rockford, Illinois, USA), resuspended in anhydrous DMSO (BDH Chemicals, Radnor, PA, USA) and added to cell cultures 24 h after their seeding.

Peripheral blood mononuclear cells (PBMCs) were obtained from healthy donors after informed consent (Cell Factory, Policlinico S.Matteo, Pavia, Italy) by Ficoll-Lympholite (Cedarlane, Burlington, Ontario, Canada) density gradient separation. PBMCs were used in bulk (CD3+), or further separated into CD8+ cell subsets by labeling with antigen-coated microbeads and magnetic capture (Miltenyi Biotec, Bergisch Gladbach, Germany). After performing purity control by flow cytometry, cells were seeded in flat-bottomed 96 well plates at a concentration of 3×10^4 cells/mL in RPMI-1640 medium (Euroclone) supplemented with 10% FBS, 100 U/mL penicillin, 0.1 mg/mL streptomycin (Sigma) for 24 h before GEs administration.

GEs sequences, molecular weight and purity grades are reported in Supplementary Table S1. GEs stocks were kept at −80 °C. GEs treatments were initially performed according to the EC_{50} values reported in the BIOPEP database, in which are reported all the bioactive peptides and the relative EC_{50} [60]. Subsequently, other GEs concentrations were assayed through MTS assay.

4.2. Immunofluorescence Analysis

Immunofluorescence were performed as reported [61]. Specifically, SUP-T1 cells (2.5×10^5) were seeded in multiwell-6 plate in a final volume of 2.5 mL of RPMI. After 24 h they were collected, centrifuged at 300× *g* for 5 min and washed with PBS. Then, cells were fixed with ice-cold fixative solution (methanol and acetic acid, 3:1) for 20 min at −20 °C, added on a coverslip and dried at room temperature (RT). After this step, cells were incubated one hour at RT with a monoclonal anti-DOR primary antibody (Abcam, Cambridge, UK) diluted 1:60 in 5% non-fat milk (*w/v*) in T-TBS (138 mM NaCl, 20 mM Tris-HCl pH 7.6, 0.1% Tween-20). Subsequently, cells were washed three times with T-TBS and incubated with a species-specific polyclonal secondary antibody conjugated with AlexaFluor-488 at a 1:60 final dilution in 5% non-fat milk in T-TBS. Finally, the coverslip was washed three times with T-TBS and treated with ProLong Gold antifade reagent with DAPI (Invitrogen, Carlsbad, CA, USA) according to manufacturer's instructions. Caco-2 cells were treated in the same way using primary antibodies against DOR and α-tubulin. Fluorescent signal was observed using LEICA DM6 B fluorescent microscope with ORCA-Flash 4.0 V3 system (Leica, Wetzlar, Germania).

4.3. MTS Viability Assay

Cells viability was tested using the CellTiter 96 AQueous One Solution Cell Proliferation Assay kit (Promega, Madison, WI, USA) according to manufacturer's instructions. Cells (1×10^4) were seeded in multiwell-96 plate in 100 µL of growth medium. GEs were added after 24 h, and cells viability was tested after different time intervals by adding 20 µL of MTS reagent. Absorbance (490 nm) was detected using the microplate reader TECAN Sunrise (Männedorf, Switzerland). Each treatment was analyzed using at least 8 wells for each treatment.

4.4. Cytofluorimetric Analysis

Cells proliferation was assayed using the Muse Count & Viability Assay (Luminex), according to manufacturer's instructions. Cells (1×10^5) were seeded in a multiwell-24 plate in 1 mL of complete medium. GEs were added and cells collected 24 h p.t., washed with PBS and resuspended in 50 µL of PBS and 450 µL of Muse Count & Viability Reagent. After an incubation of 5 min at RT, cells were analyzed at the cytofluorometer.

Cell cycle analysis was performed as described [62]. Cells (2.5×10^5) were seeded in a multiwell-6 plate in 2.5 mL of complete medium. Colcemid (10 µg/mL) was added to synchronize cells in metaphase. After 24 h, colcemid was removed by substituting the culture medium and GEs were administered for additional 24 h. Cells were then collected, centrifuged at 300× *g* for 5 min and fixated overnight with 200 µL of 70% ethanol. Subsequently, cells were centrifuged and resuspended in propidium iodide (50 µg/mL) and RNAse A (0.1 mg/mL). The samples were analyzed after an overnight incubation at 4 °C by BD FACSLyrics (BD Bioscience, Franklin Lakes, NJ, USA).

Rabbit polyclonal Cyclin E2 (clone H-140) antibody form Santa Cruz Biotechnologies (Dallas, TX, USA) and a mouse monoclonal Cyclin A (clone CY-A1) antibody (Sigma) were used to analyze cell cycles as follows: 2 µg of each antibody were fluorescently conjugated using DyLight555 labelling kit (Biorad, Hercules, CA, USA) as described [63]. SUP-T1 cells (about 10^5 for each sample), treated for 24 h with the following micromolar amounts of GEs (i.e., A4 = 70; A5 = 60; B4 = 3.4; B5 = 0.02; C5 = 13.5, according to BIOPEP database) were then fixed and permeabilized using ice cold methanol for 15 min, washed twice with ice cold PBS and then blocked with PBS containing 1% Fetal Calf Serum (FCS) for 30 min at room temperature. After PBS washing, cells were incubated with 2 µL of each fluorescently labelled antibody in a PBS + FCS 1% volume of 50 µL for 2 h at room temperature. Finally, cells were washed twice with D-PBS and analyzed for fluorescence intensity using Guava Muse Cell Analyser (Luminex, Austin, TX, USA), analyzing 2000 events in two independent replicas.

4.5. Immunoblotting Analysis

Cells (2.5×10^5) were cultured in a multiwell-6 plate with 2.5 mL of complete medium. GEs were added and cells collected after 4 h p.t. Immunoblotting was performed as described [64]. Cells were collected and lysated in ice-cold Triton X-100 (50 mM Tris-HCl pH 7.4, 150 mM NaCl, 1% Triton X-100) supplemented with Complete Mini Protease Inhibitor cocktail 7X (Roche, Basel, Switzerland) and sodium orthovanadate 1 mM (Sigma). Proteins were quantified using the Quant-It Protein Assay Kit (Invitrogen, Carlsbad, CA, USA). Proteins (20–30 µg) were added to Laemmli sample buffer (2% SDS, 6% glycerol, 150 mM β-mercaptoethanol, 0.02% bromophenol blue and 0.5 M Tris-HCl pH 6.8), denaturated for 5 min at 95 °C and separated on 12% SDS-PAGE according to protein size. After electrophoresis, proteins were transferred onto nitrocellulose membrane using the Trans-Blot Turbo Transfer System (Biorad) according to the manufacturer's instructions. The membranes were then blocked 1 h at room temperature (RT) with 5% (*w/v*) non-fat milk in T-TBS (138 mM NaCl, 20 mM Tris-HCl pH 7.6, 0.1% Tween-20) and incubated overnight at 4 °C with monoclonal primary antibodies against DOR (Abcam, ab176324), Erk1/2 (#9102), phosphor-Erk1/2 (Tyr204/Tyr187, #5726), Akt (#9272), phopsho-Akt (Ser473, #9271), Bcl-2 (#9941), phospho-Bcl-2 (Ser70, #9941), STAT3 (#9139), phosphor-STAT3 (Tyr705, #9145), and LC3-II (#2775) (Cell Signaling, Danvers, MA, USA) diluted at 1:2000 in 5% non-fat milk in T-TBS, whereas monoclonal primary antibody against α-tubulin (Abcam, ab7291) or β-actin (Cell Signaling, #5125) were diluted at 1:4000. Species-specific peroxidase-labelled ECL secondary antibodies (Cell Signaling, 1:2000 dilution) were used in 5% non-fat milk in T-TBS. Proteins signals were detected using the ECL Prime Western Blotting Detection Kit (GE Healthcare) by means of Chemidoc MP (Biorad). Densitometric analysis was conducted with ImageJ software (http://rsbweb.nih.gov/ij (accessed on 1 October 2022)).

4.6. Molecular Dynamics Simulations

The peptide–receptor complexes were modelled starting from the active DOR structure bound to the agonist peptide KGCHM07 (PDB code: 6PT2) [65]. The standard Peptide docking protocol of Schrodinger [66] was applied, using default settings and MM-GBSA scoring, centering the grid on the crystal peptide ligand. Poses were analyzed and selected among the most favorable docking scores. The starting complexes of Leu-enkephalin (YGGFL), B5 (YGGWL), and A4 (GYYP) were chosen with Y and F/W/Y orientation in common. Each complex was embedded in a 90:10 POPC CHOL membrane and solvated in a cubic box containing K + Cl- corresponding to 150 nM ionic concentration and a total of 103,000 atoms. Using NAMD version 2.10 [67] and CHARMM36m force field, the three systems were first subjected to the multi-stage equilibration protocol as in [68]. Production runs were performed with OpenMM 7.4 software [69] using PME for electrostatic interactions, at 310 K temperature, under NPT ensemble using semi-isotropic pressure coupling, and with 4fs integration time-step (with mass repartitioning). Monte Carlo barostat and Langevin thermostat were used to maintain constant pressure and temperature, respectively. The van der Waals interactions were calculated applying a cutoff distance of 12 Å and switching the potential from 10 Å. Six replicates of 1 µs each were generated for each system, leading to a total of 18 µs simulation time. Clustering analysis was carried out using the GROMACS clustering tool and the Gromos method [70] with cutoff 0.2 nm.

4.7. Statistical Analysis

The data were analyzed using the statistics functions of the MedCalc statistical software version 18.11.6. (http://www.medcalc.org (accessed on 3 November 2022)). The ANOVA-One Way test differences were considered statistically significant when $p < 0.05$.

Supplementary Materials: The following supporting information can be downloaded at: https://www.mdpi.com/article/10.3390/ijms24043912/s1.

Author Contributions: Conceptualization, F.M. and S.C.; methodology, F.M., S.M. (Samman Mansoor), S.M. (Stella Muscianisi) and S.C.; software, G.M. and S.M. (Samman Mansoor); investigation, F.M., L.Z., G.M., S.M. (Samman Mansoor) and F.C.; resources, F.M. and S.C.; writing—original draft preparation, F.M.; writing—review and editing, G.M., L.Z., E.B. and S.C.; supervision, F.M. and S.C.; project administration, F.M. and S.C.; funding acquisition, F.M. and S.C. All authors have read and agreed to the published version of the manuscript.

Funding: This research received no external funding.

Institutional Review Board Statement: Not applicable.

Informed Consent Statement: Peripheral blood mononuclear cells (PBMCs) were obtained from healthy donors after informed consent (Cell Factory, Policlinico S.Matteo, Pavia, Italy) in agreement with Local Ethical Committee.

Data Availability Statement: Not applicable.

Acknowledgments: This research was supported by the Italian Ministry of Education, University and Research (MIUR): Dipartimenti di Eccellenza Program (2018–2022), Dept. of Biology and Biotechnology "L. Spallanzani", University of Pavia. This work was also supported by Fondazione Celiachia Onlus (FC) Grant n° 001_FC_2018 and "Il Bambino e il suo pediatra" Onlus. Authors thank Patrizia Vaghi, Amanda Oldani and Alberto Azzalin (PASS-Bio Med, Centro Grandi Strumenti, University of Pavia, Pavia, 27100, Italy) for the microscope and flow cytometry acquisitions, and Raffaella Lolla for technical assistance.

Conflicts of Interest: The authors declare no conflict of interest.

References

1. Di Sabatino, A.; Corazza, G.R. Coeliac disease. *Lancet* **2009**, *373*, 1480–1493. [CrossRef] [PubMed]
2. Ciccocioppo, R.; Di Sabatino, A.; Corazza, G.R. The immune recognition of gluten in coeliac disease. *Clin. Exp. Immunol.* **2005**, *140*, 408–416. [CrossRef] [PubMed]

3. Ludvigsson, J.F.; Leffler, D.A.; Bai, J.C.; Biagi, F.; Fasano, A.; Green, P.H.; Hadjivassiliou, M.; Kaukinen, K.; Kelly, C.P.; Leonard, J.N.; et al. The Oslo definitions for coeliac disease and related terms. *Gut* **2013**, *62*, 43–52. [CrossRef] [PubMed]
4. Di Sabatino, A.; Corazza, G.R. Some clarification is necessary on the Oslo definitions for coeliac disease-related terms. *Gut* **2013**, *62*, 182. [CrossRef]
5. Mustalahti, K.; Catassi, C.; Reunanen, A.; Fabiani, E.; Heier, M.; McMillan, S.; Murray, L.; Metzger, M.H.; Gasparin, M.; Bravi, E.; et al. Coeliac EU Cluster, Project Epidemiology. The prevalence of celiac disease in Europe: Results of a centralized, international mass screening project. *Ann. Med.* **2010**, *42*, 587–595. [CrossRef] [PubMed]
6. Fukudome, S.; Jinsmaa, Y.; Matsukawa, T.; Sasaki, R.; Yoshikawa, M. Release of opioid peptides, gluten exorphins by the action of pancreatic elastase. *FEBS Lett.* **1997**, *412*, 475–479. [CrossRef]
7. Zioudrou, C.; Streaty, R.A.; Klee, W.A. Opioid peptides derived from food proteins. The exorphins. *J. Biol. Chem.* **1979**, *254*, 2446–2449. [CrossRef]
8. Pruimboom, L.; de Punder, K. The opioid effects of gluten exorphins: Asymptomatic celiac disease. *J. Health Popul. Nutr.* **2015**, *33*, 24. [CrossRef]
9. Schusdziarra, V.; Henrichs, I.; Holland, A.; Klier, M.; Pfeiffer, E.F. Evidence for an effect of exorphins on plasma insulin and glucagon levels in dogs. *Diabetes* **1981**, *30*, 362–364. [CrossRef]
10. Morley, J.E.; Levine, A.S.; Yamada, T.; Gebhard, R.L.; Prigge, W.F.; Shafer, R.B.; Goetz, F.C.; Silvis, S.E. Effect of exorphins on gastrointestinal function, hormonal release, and appetite. *Gastroenterology* **1983**, *84*, 1517–1523. [CrossRef]
11. Fukudome, S.; Yoshikawa, M. Opioid peptides derived from wheat gluten: Their isolation and characterization. *FEBS Lett.* **1992**, *296*, 107–111. [CrossRef] [PubMed]
12. Fukudome, S.; Yoshikawa, M. Gluten exorphin C. A novel opioid peptide derived from wheat gluten. *FEBS Lett.* **1993**, *316*, 17–19. [CrossRef] [PubMed]
13. Gendron, L.; Cahill, C.M.; von Zastrow, M.; Schiller, P.W.; Pineyro, G. Molecular Pharmacology of δ-Opioid Receptors. *Pharmacol Rev.* **2016**, *68*, 631–700. [CrossRef] [PubMed]
14. Stuknyte, M.; Maggioni, M.; Cattaneo, S.; De Luca, P.; Fiorilli, A.; Ferraretto, A.; De Noni, I. Release of wheat gluten exorphins A5 and C5 during in vitro gastrointestinal digestion of bread and pasta and their absorption through an in vitro model of intestinal epithelium. *Food Res. Intern.* **2015**, *72*, 208–214. [CrossRef]
15. Maggioni, M.; Stuknyte, M.; De Luca, P.; Cattaneo, S.; Fiorilli, A.; De Noni, I.; Ferraretto, A. Transport of wheat gluten exorphins A5 and C5 through an in vitro model of intestinal epithelium. *Food Res. Intern.* **2016**, *88*, 319–326. [CrossRef]
16. DiCello, J.J.; Saito, A.; Rajasekhar, P.; Eriksson, E.M.; McQuade, R.M.; Nowell, C.J.; Sebastian, B.W.; Fichna, J.; Veldhuis, N.A.; Canals, M.; et al. Inflammation-associated changes in DOR expression and function in the mouse colon. *Am. J. Physiol. Gastrointest. Liver Physiol.* **2018**, *315*, G544–G559. [CrossRef]
17. Cahill, C.M.; Morinville, A.; Hoffert, C.; O'Donnell, D.; Beaudet, A. Up-regulation and trafficking of delta opioid receptor in a model of chronic inflammation: Implications for pain control. *Pain* **2003**, *101*, 199–208. [CrossRef]
18. Pol, O.; Palacio, J.R.; Puig, M.M. The expression of delta- and kappa-opioid receptor is enhanced during intestinal inflammation in mice. *J. Pharmacol. Exp. Ther.* **2003**, *306*, 455–462. [CrossRef]
19. Pol, O.; Puig, M.M. Expression of opioid receptors during peripheral inflammation. *Curr. Top. Med. Chem.* **2004**, *4*, 51–61. [CrossRef]
20. Singleton, P.A.; Mirzapoiazova, T.; Hasina, R.; Salgia, R.; Moss, J. Increased μ-opioid receptor expression in metastatic lung cancer. *Br. J. Anaesth.* **2014**, *113*, i103–i108. [CrossRef]
21. Chen, D.; Chen, Y.; Yan, Y.; Pan, J.; Xing, W.; Li, Q.; Zeng, W. Down-regulation of the tumour suppressor κ-opioid receptor predicts poor prognosis in hepatocellular carcinoma patients. *BMC Cancer* **2017**, *17*, 553. [CrossRef] [PubMed]
22. Wei, Y.C.; Zhang, B.; Li, X.; Liu, X.M.; Zhang, J.; Lei, B.; Li, B.; Zhai, R.; Chen, Q.; Li, Y. Upregulation and activation of δ-opioid receptors promotes the progression of human breast cancer. *Oncol. Rep.* **2016**, *36*, 2579–2586. [CrossRef] [PubMed]
23. Tang, B.; Li, Y.; Yuan, S.; Tomlinson, S.; He, S. Upregulation of the δ opioid receptor in liver cancer promotes liver cancer progression both in vitro and in vivo. *Int. J. Oncol.* **2013**, *43*, 1281–1290. [CrossRef]
24. Debruyne, D.; Leroy, A.; De Wever, O.; Vakaet, L.; Mareel, M.; Bracke, M. Direct effects of delta opioid receptor agonists on invasion-associated activities of HCT-8/E11 colon cancer cells. *Anticancer Res.* **2010**, *30*, 9–17.
25. Szczepaniak, A.; Fichna, J.; Zielińska, M. Opioids in Cancer Development, Progression and Metastasis: Focus on Colorectal Cancer. *Curr. Treat. Options Oncol.* **2020**, *21*, 6. [CrossRef] [PubMed]
26. Chander, U.; Leeman-Neill, R.J.; Bhagat, G. Pathogenesis of enteropathy-associated T cell lymphoma. *Curr. Hematol. Malig. Rep.* **2018**, *13*, 308–317. [CrossRef]
27. Marafini, I.; Monteleone, G.; Stolfi, C. Association Between Celiac Disease and Cancer. *Int. J. Mol. Sci.* **2020**, *21*, 4155. [CrossRef] [PubMed]
28. Bayani, J.; Squire, J.A. Preparation of cytogenetic specimens from tissue samples. *Current Protoc. Cell. Biol.* **2004**, *23*, 1–15. [CrossRef] [PubMed]
29. Grundmann, M.; Kostenis, E. Temporal Bias: Time-Encoded Dynamic GPCR Signaling. *Trends Pharmacol. Sci.* **2017**, *38*, 1110–1124. [CrossRef]
30. Ruvolo, P.P.; Deng, X.; May, W.S. Phosphorylation of Bcl2 and regulation of apoptosis. *Leukemia* **2001**, *4*, 515–522. [CrossRef]

31. Klionsky, D.J.; Abdel-Aziz, A.K.; Abdelfatah, S.; Abdellatif, M.; Abdoli, A.; Abel, S.; Abeliovich, H.; Abildgaard, M.H.; Abudu, Y.P.; Acevedo-Arozena, A.; et al. Guidelines for the use and interpretation of assays for monitoring autophagy (4th edition). *Autophagy* **2021**, *17*, 1–382. [PubMed]
32. Han, J.; Theiss, A.L. Stat3: Friend or foe in colitis and colitis-associated cancer? *Inflamm. Bowel Dis.* **2014**, *20*, 2405–2411. [CrossRef] [PubMed]
33. Katritch, V.; Cherezov, V.; Stevens, R.C. Structure-function of the G protein-coupled receptor superfamily. *Annual Rev Pharmacol. Toxicol.* **2013**, *53*, 531–556. [CrossRef] [PubMed]
34. Audet, N.; Paquin-Gobeil, M.; Landry-Paquet, O.; Schiller, P.W.; Piñeyro, G. Internalization and Src activity regulate the time course of ERK activation by delta opioid receptor ligands. *J. Biol. Chem.* **2005**, *280*, 7808–7816. [CrossRef]
35. Eisinger, D.A.; Schulz, R. Extracellular signal-regulated kinase/mitogen-activated protein kinases block internalization of delta-opioid receptors. *J. Pharmacol. Exp. Ther.* **2004**, *309*, 776–785. [CrossRef] [PubMed]
36. Xu, C.; Hong, M.H.; Zhang, L.S.; Hou, Y.Y.; Wang, Y.H.; Wang, F.F.; Chen, Y.J.; Xu, X.J.; Chen, J.; Xie, X.; et al. Serine 363 of the {delta}-opioid receptor is crucial for adopting distinct pathways to activate ERK1/2 in response to stimulation with different ligands. *J. Cell. Sci.* **2010**, *123*, 4259–4270. [CrossRef]
37. Heiss, A.; Ammer, H.; Eisinger, D.A. delta-Opioid receptor-stimulated Akt signaling in neuroblastoma x glioma (NG108-15) hybrid cells involves receptor tyrosine kinase-mediated PI3K activation. *Exp. Cell. Res.* **2009**, *315*, 2115–2125. [CrossRef]
38. Wilson, M.A.; Burt, A.R.; Milligan, G.; Anderson, N.G. Mitogenic signalling by delta opioid receptors expressed in rat-1 fibroblasts involves activation of the p70s6k/p85s6k S6 kinase. *Biochem. J.* **1997**, *325*, 217–222. [CrossRef]
39. Berven, L.A.; Willard, F.S.; Crouch, M.F. Role of the p70(S6K) pathway in regulating the actin cytoskeleton and cell migration. *Exp. Cell. Res.* **2004**, *296*, 183–195. [CrossRef]
40. Malamut, G.; El Machhour, R.; Montcuquet, N.; Martin-Lannerée, S.; Dusanter-Fourt, I.; Verkarre, V.; Mention, J.J.; Rahmi, G.; Kiyono, H.; Butz, E.A.; et al. IL-15 triggers an antiapoptotic pathway in human intraepithelial lymphocytes that is a potential new target in celiac disease-associated inflammation and lymphomagenesis. *J. Clin. Invest.* **2010**, *120*, 2131–2143. [CrossRef]
41. Fairlie, W.D.; Tran, S.; Lee, E.F. Crosstalk between apoptosis and autophagy signaling pathways. *Int. Rev. Cell. Mol. Biol.* **2020**, *352*, 115–158. [PubMed]
42. Manai, F.; Azzalin, A.; Gabriele, F.; Martinelli, C.; Morandi, M.; Biggiogera, M.; Bozzola, M.; Comincini, S. The in vitro effects of enzymatic digested gliadin on the functionality of the autophagy process. *Int. J. Mol. Sci.* **2018**, *19*, 635. [CrossRef]
43. Manai, F.; Azzalin, A.; Morandi, M.; Riccardi, V.; Zanoletti, L.; Dei Giudici, M.; Gabriele, F.; Martinelli, C.; Bozzola, M.; Comincini, S. Trehalose modulates autophagy process to counteract gliadin cytotoxicity in an in vitro celiac disease model. *Cells* **2019**, *8*, 348. [CrossRef] [PubMed]
44. Anand, P.K.; Tait, S.W.; Lamkanfi, M.; Amer, A.O.; Nunez, G.; Pagès, G.; Pouysségur, J.; McGargill, M.A.; Green, D.R.; Kanneganti, T.D. TLR2 and RIP2 pathways mediate autophagy of Listeria monocytogenes via extracellular signal-regulated kinase (ERK) activation. *J. Biol. Chem.* **2011**, *286*, 42981–42991. [CrossRef] [PubMed]
45. Kim, J.; Kundu, M.; Viollet, B.; Guan, K.L. AMPK and mTOR regulate autophagy through direct phosphorylation of Ulk1. *Nat. Cell. Biol.* **2011**, *13*, 132–141. [CrossRef] [PubMed]
46. Pickert, G.; Neufert, C.; Leppkes, M.; Zheng, Y.; Wittkopf, N.; Warntjen, M.; Lehr, H.A.; Hirth, S.; Weigmann, B.; Wirtz, S.; et al. STAT3 links IL-22 signaling in intestinal epithelial cells to mucosal wound healing. *J. Exp. Med.* **2009**, *206*, 1465–1472. [PubMed]
47. Neufert, C.; Pickert, G.; Zheng, Y.; Wittkopf, N.; Warntjen, M.; Nikolaev, A.; Ouyang, W.; Neurath, M.F.; Becker, C. Activation of epithelial STAT3 regulates intestinal homeostasis. *Cell Cycle* **2010**, *9*, 652–655. [CrossRef]
48. Wittkopf, N.; Pickert, G.; Billmeier, U.; Mahapatro, M.; Wirtz, S.; Martini, E.; Leppkes, M.; Neurath, M.F.; Becker, C. Activation of intestinal epithelial Stat3 orchestrates tissue defense during gastrointestinal infection. *PLoS ONE* **2015**, *10*, e0118401. [CrossRef]
49. Pang, L.; Huynh, J.; Alorro, M.G.; Li, X.; Ernst, M.; Chand, A.L. STAT3 Signalling via the IL-6ST/gp130 Cytokine Receptor Promotes Epithelial Integrity and Intestinal Barrier Function during DSS-Induced Colitis. *Biomedicines* **2021**, *9*, 187. [CrossRef] [PubMed]
50. Shahabi, N.A.; Sharp, B.M. Delta opioid agonists inhibit proliferation of highly purified murine CD4+ and CD8+ T-cells. *Adv Exp. Med. Biol.* **1995**, *373*, 29–36.
51. Janković, B.D.; Radulović, J. Enkephalins, brain and immunity: Modulation of immune responses by methionine-enkephalin injected into the cerebral cavity. *Int. J. Neurosci.* **1992**, *67*, 241–270. [CrossRef] [PubMed]
52. Plotnikoff, N.P.; Miller, G.C. Enkephalins as immunomodulators. *Int. J. Immunopharmacol.* **1983**, *5*, 437–441. [CrossRef] [PubMed]
53. Roscetti, G.; Ausiello, C.M.; Palma, C.; Gulla, P.; Roda, L.G. Enkephalin activity on antigen-induced proliferation of human peripheral blood mononucleate cells. *Int. J. Immunopharmacol.* **1988**, *10*, 819–823. [CrossRef]
54. Li, W.; Chen, W.; Herberman, R.B.; Plotnikoff, N.P.; Youkilis, G.; Griffin, N.; Wang, E.; Lu, C.; Shan, F. Immunotherapy of cancer via mediation of cytotoxic T lymphocytes by methionine enkephalin (MENK). *Cancer Lett.* **2014**, *344*, 212–222. [CrossRef]
55. Moro-García, M.A.; Mayo, J.C.; Sainz, R.M.; Alonso-Arias, R. Influence of Inflammation in the Process of T Lymphocyte Differentiation: Proliferative, Metabolic, and Oxidative Changes. *Front. Immunol.* **2018**, *9*, 339. [CrossRef] [PubMed]
56. Shahabi, N.A.; McAllen, K.; Sharp, B.M. delta opioid receptors stimulate Akt-dependent phosphorylation of c-jun in T cells. *J. Pharmacol. Exp. Ther.* **2006**, *316*, 933–939. [CrossRef]
57. Nguyen, K.; Miller, B.C. CD28 costimulation induces delta opioid receptor expression during anti-CD3 activation of T cells. *J. Immunol.* **2002**, *168*, 4440–4445. [CrossRef] [PubMed]

58. Li, M.D.; McAllen, K.; Sharp, B.M. Regulation of delta opioid receptor expression by anti-CD3-epsilon, PMA, and ionomycin in murine splenocytes and T cells. *J. Leukoc. Biol.* **1999**, *65*, 707–714. [CrossRef]
59. Rittié, L.; Fisher, G.J. Isolation and culture of skin fibroblasts. *Methods Mol. Med.* **2005**, *117*, 83–98.
60. Minkiewicz, P.; Iwaniak, A.; Darewicz, M. BIOPEP-UWM database of bioactive peptides: Current opportunities. *Int. J. Mol. Sci.* **2019**, *20*, 5978. [CrossRef]
61. Sbalchiero, E.; Azzalin, A.; Palumbo, S.; Barbieri, G.; Arias, A.; Simonelli, L.; Ferretti, L.; Comincini, S. Altered cellular distribution and sub-cellular sorting of doppel (Dpl) protein in human astrocytoma cell lines. *Cell. Oncol.* **2008**, *30*, 337–347. [CrossRef]
62. Ormerod, M.G.; Tribukait, B.; Giaretti, W. Consensus report of the task force on standardisation of DNA flow cytometry in clinical pathology. DNA Flow Cytometry Task Force of the European Society for Analytical Cellular Pathology. *Anal. Cell. Pathol.* **1998**, *17*, 103–110. [CrossRef] [PubMed]
63. Slivinschi, B.; Manai, F.; Martinelli, C.; Carriero, F.; D'Amato, C.; Massarotti, M.; Bresciani, G.; Casali, C.; Milanesi, G.; Artal, L.; et al. Enhanced Delivery of Rose Bengal by Amino Acids Starvation and Exosomes Inhibition in Human Astrocytoma Cells to Potentiate Anticancer Photodynamic Therapy Effects. *Cells* **2022**, *11*, 2502. [CrossRef]
64. Barbieri, G.; Palumbo, S.; Gabrusiewicz, K.; Azzalin, A.; Marchesi, N.; Spedito, A.; Biggiogera, M.; Sbalchiero, E.; Mazzini, G.; Miracco, C.; et al. Silencing of cellular prion protein (PrPC) expression by DNA-antisense oligonucleotides induces autophagy-dependent cell death in glioma cells. *Autophagy* **2011**, *7*, 840–853. [CrossRef] [PubMed]
65. Claff, T.; Yu, J.; Blais, V.; Patel, N.; Martin, C.; Wu, L.; Han, G.W.; Holleran, B.J.; Van der Poorten, O.; White, K.L.; et al. Elucidating the active δ-opioid receptor crystal structure with peptide and small-molecule agonists. *Sci. Adv.* **2019**, *5*, eaax9115. [CrossRef] [PubMed]
66. Friesner, R.A.; Banks, J.L.; Murphy, R.B.; Halgren, T.A.; Klicic, J.J.; Mainz, D.T.; Repasky, M.P.; Knoll, E.H.; Shaw, D.E.; Shelley, M.; et al. Glide: A New Approach for Rapid, Accurate Docking and Scoring. 1. Method and Assessment of Docking Accuracy. *J. Med. Chem.* **2004**, *47*, 1739–1749. [CrossRef]
67. Phillips, J.C.; Hardy, D.J.; Maia, J.D.C.; Stone, J.E.; Ribeiro, J.V.; Bernardi, R.C.; Buch, R.; Fiorin, G.; Henin, J.; Jiang, W.; et al. Scalable molecular dynamics on CPU and GPU architectures with NAMD. *J. Chem. Physics* **2020**, *153*, 044130. [CrossRef]
68. Plante, A.; Shore, D.M.; Morra, G.; Khelashvili, G.; Weinstein, H. A Machine Learning Approach for the Discovery of Ligand-Specific Functional Mechanisms of GPCRs. *Molecules* **2019**, *24*, 2097.
69. Eastman, P.; Swails, J.; Chodera, J.D.; McGibbon, R.T.; Zhao, Y.; Beauchamp, K.A.; Wang, L.P.; Simmonett, A.C.; Harrigan, M.P.; Stern, C.D.; et al. OpenMM 7: Rapid development of high performance algorithms for molecular dynamics. *PLoS Comp. Biol.* **2017**, *13*, e1005659. [CrossRef]
70. Daura, X.; Gademann, K.; Jaun, B.; Seebach, D.; van Gunsteren, W.F.; Mark, A.E. Peptide Folding: When Simulation Meets Experiment. *Angewandte Chemie Int.* **1999**, *38*, 236–240. [CrossRef]

Title: IL-1R signaling drives enteric glia-macrophage interactions in colorectal cancer

Lies van Baarle[1,12], Veronica De Simone[1,12], Linda Schneider[2,12], Sneha Santhosh[1,7], Saeed Abdurahiman[1], Francesca Biscu[1,8], Reiner Schneider[2], Lisa Zanoletti[1,9], Sara Verbandt[3], Zedong Hu[3], Michelle Stakenborg[1], Bo-Jun Ke[1], Balbina García-Reyes[2,10], Jonas Henn[2], Marieta Toma[4], Maxime Vanmechelen[5,11], Frederik De Smet[5,11], Sales Ibiza[6], Sabine Tejpar[3], Sven Wehner[2,13,*] and Gianluca Matteoli[1, 11, 13,14,*]

[1]Department of Chronic Diseases, Metabolism and Ageing (CHROMETA), Translational Research Center for Gastrointestinal Disorders (TARGID), KU Leuven, Leuven, Belgium

[2]Department of Surgery, University Hospital Bonn, Medical Faculty, Bonn, Germany

[3]Digestive Oncology, Department of Oncology, KU Leuven, Leuven, Belgium

[4]Department of Pathology, University Hospital Bonn, Medical Faculty, Bonn, Germany

[5]Laboratory for Precision Cancer Medicine, Translational Cell and Tissue Research Unit, Department of Imaging & Pathology, KU Leuven, Leuven, Belgium

[6]Laboratory of Cell Biology & Histology, Department of Veterinary Sciences, University of Antwerp, Antwerp, Belgium

[7]Department of Anatomy and Physiology, University of Melbourne, Parkville, VIC, 3010, Australia

[8]Centre for Inflammation Research, University of Edinburgh, Edinburgh, United Kingdom

[9]Department of Biology and Biotechnology “L. Spallanzani”, University of Pavia, Pavia, Italy

[10]Mildred Scheel School of Oncology, Aachen Bonn Cologne Düsseldorf (MSSO ABCD), University Hospital Bonn, Medical Faculty, Bonn, Germany

[11]Leuven Institute for Single-cell Omics (LISCO), KU Leuven, Leuven, Belgium

[12]These authors contributed equally

[13]Senior authors

[14]Lead contact

*Correspondence: sven.wehner@ukbonn.de (S.W.), gianluca.matteoli@kuleuven.be (G.M.)

ABSTRACT

Enteric glial cells (EGCs) have been implicated in colorectal cancer (CRC) pathogenesis. However, their precise mechanisms of interaction with the CRC immune cell compartment and pro-tumorigenic role remain unclear. This study aimed to investigate the immunomodulatory effects of EGCs on tumor-associated macrophages (TAMs) and their involvement in CRC progression. Using EGC depletion and supplementation models, we assessed the impact of EGCs on the immunomodulation of orthotopic murine CRC. Furthermore, by making use of Bulk RNA-sequencing of CRC EGCs and single-cell sequencing of the tumor microenvironment, we identified the factors involved in the EGC-TAM crosstalk. Findings demonstrate that EGCs acquire a reactive and immunomodulatory phenotype in both murine CRC models and patients, influencing TAM differentiation. Mechanistically, secretion of IL-1 by tumor-infiltrating monocytes and macrophages triggers the phenotypic and functional switch of CRC EGCs via IL-1R. Consequently, tumor EGCs secrete IL-6, promoting the differentiation of monocytes into pro-tumorigenic SPP1^{+} TAMs. Importantly, the reactive tumor EGCs phenotype correlates with worse disease outcomes in preclinical models and CRC patients. Here we uncover a previously unexplored neuroimmune interaction between EGCs and TAMs within the colorectal tumor microenvironment, informing potential therapeutic strategies and enhancing our understanding of CRC progression.

KEYWORDS: Colorectal Cancer; Enteric glial cells; Tumor Associated Macrophages; tumor microenvironment; neuroimmune crosstalk; IL-1R/IL-6 axis; SPP1^{+} TAMs; IL-1R signaling

Running title: EGC-TAM crosstalk in CRC

eTOC Summary: Our study unveils a novel neuroimmune interaction between enteric glia and TAMs in colon carcinoma. Monocyte/Macrophage-derived IL-1 activates enteric glia, leading to the differentiation of pro-tumorigenic SPP1^{+} TAMs via glial-derived IL-6. Blocking glial IL-1R-signaling reduces colonic tumor lesions, highlighting IL-1R as a potential therapeutic target.

INTRODUCTION

Identified as the world's third most common cancer, colorectal cancer (CRC) represents one of the preeminent causes of cancer-associated deaths worldwide. Although innovative technologies have significantly impacted the diagnosis, surgery, and treatment of CRC, patients with advanced disease still have a very poor prognosis. In fact, while the 5-year survival rates of patients with early-stage CRC can reach up to 90%, the survival rate plummets dramatically to as low as 10% for patients diagnosed with advanced metastasis (Kuipers et al., 2015). Hence, a better understanding of the pathogenesis of CRC is crucial to develop new therapeutic strategies along with advanced patient stratification for precision medicine. CRC consists of rapidly evolving neoplasms where acquired mutations in oncogenes and tumor-suppressor genes lead to increasing complexity of the tumor microenvironment (TME), unleashing interaction of the tumor cells with the stroma and the immune system, including fibroblasts, tumor-infiltrating immune cells, and cells of the enteric nervous system (AlMusawi et al., 2021; Albo et al., 2011). This process contributes to the formation of a complex network of cell types within the TME, which is leading to increase tumor fitness.

In recent years, enteric glial cells (EGCs) have also been identified as a new constituent of the colon carcinoma microenvironment (Valès et al., 2019; Yuan et al., 2020). EGCs, once regarded as merely supportive and accessory cells for neurons within the enteric nervous system (Neunlist et al., 2014), have now gained increased attention for their more complex roles in both health and disease (Seguella and Gulbransen, 2021). In homeostasis, EGCs regulate intestinal reflexes and support neurotransmission via communication with enteric neurons. However, accumulating evidence highlights EGCs as crucial mediators of interactions not only among enteric neurons but also intestinal epithelium, enteroendocrine cells, and immune cells (Thomasi and Gulbransen, 2023; Prochera and Rao, 2023; Bohórquez et al., 2014; Seguella and Gulbransen, 2021). Of particular interest is their significant role in modulating immune responses in various intestinal diseases (Ibiza et al., 2016; Progatzky et al., 2021; Grubišić et al., 2020, 2022). Being highly responsive to inflammatory mediators, including ATP, IL-1 cytokines, or LPS, EGCs are rapidly activated during intestinal diseases. Upon activation during intestinal pathologies, EGCs contribute to the shaping of the inflammatory milieu through the secretion of a plethora of cytokines and chemokines (Schneider et al., 2021; Brown et al., 2016; Schneider et al., 2022; Rosenbaum et al., 2016). In this regard, we recently demonstrated the profound influence EGCs exert on macrophage dynamics in the setting of acute intestinal inflammation, promoting the recruitment of monocytes and their differentiation into pro-resolving macrophages (Stakenborg et al., 2022; Schneider et al., 2022).

So far, in the context of CRC, a few studies suggested that EGCs exert a pro-tumorigenic effect during tumor development (Yuan et al., 2020; Valès et al., 2019), however, their influence on the tumor

immune microenvironment has not been addressed. In a study by Yuan *et al.*, glial cell depletion led to reduced tumor burden in a CRC mouse model (Yuan et al., 2020), indicating a central role of EGCs in CRC development. A xenograft model confirmed this role, and *in vitro* work suggested that EGC activation by IL-1 resulted in a pro-tumorigenic EGC phenotype (Valès et al., 2019), pointing to a direct interaction of EGCs with the TME. However, the mechanisms by which EGCs interact with the different components of the colorectal cancer TME to exert their pro-tumorigenic role remain poorly understood. Especially the molecular and cellular communication pathways involved are so far insufficiently explored and display a substantial lack of *in vivo* evidence.

In this study, we demonstrated, using *in vitro* and *in vivo* models, that upon exposure to the colorectal TME, EGCs undergo a reactive phenotypic switch, leading to the activation of immunomodulatory processes that promote the differentiation of tumor-associated macrophages (TAMs). Intriguingly, tumor-infiltrating monocytes were found to influence the phenotype and function of CRC EGCs through the IL-1 signaling pathway. In turn, EGC-derived IL-6 promoted the differentiation of these monocytes towards $SPP1^{+}$ TAMs. Importantly, this IL-1R/IL-6 axis was found to be essential for the tumor-supportive functions of EGCs.

Together, our findings uncover a novel neuroimmune interaction in the colon cancer microenvironment. This deepens our understanding and may facilitate the development of novel therapeutic approaches to treat this devastating disease.

MATERIAL AND METHODS

Animals. WT C57BL/6J (JAX:000664), $CCR2^{-/-}$ (JAX: 004999), $PLP1^{CreERT2}$iDTR (JAX:005975 and JAX:007900), $GFAP^{Cre}$IL-$1R1^{fl/fl}$ (JAX:012886 and JAX:028398), $GFAP^{Cre}Ai14^{fl/fl}$ (JAX:012886 and JAX:007908) and $Sox10^{CreERT2}Ai14^{fl/fl}$ [$Sox10^{CreERT2}$ (kindly provided by Dr. Vassilis Pachnis (Laranjeira et al., 2011), ($Ai14^{fl/fl}$ JAX:007908)] mice were originally purchased from Jackson Laboratory and bred in our animal facilities. All mice were housed in temperature-controlled specific pathogen–free facilities with ad libitum access to standard chow diet and water under 12-h light–dark cycles at the KU Leuven or University of Bonn. All experimental procedures were approved by the Animal Care and Animal Experiments Ethical Committee of KU Leuven (208/2018 and 213/2018) or by the appropriate authorities of North-Rhine-Westphalia, Germany (81-02.04.2021.A424).

Specific recombination of $Sox10^{CreERT2}$ in enteric glia was confirmed via confocal microscopy by the overlapping tdtomato signal with GFAP immunostaining (Figure S4B). In the case of $GFAP^{Cre}IL1R1^{fl/fl}$ mice, following recommendation by The Jackson Laboratory (JAX:012886), we used a strict mating scheme using only Cre^{+} carrying female with Cre^{-} males to overcome any issues of germline Cre-expression and to produce only litters with a GFAP-promotor-driven Cre-expression. Specific GFAP-Cre

recombination was confirmed in the reporter mouse line GFAP^{Cre}Ai14$^{fl/fl}$ showing in a strong overlap of tdtomato signal with immunolabelled GFAP and SOX10 cells in colonic tissue, confirming Cre activity exclusively in enteric glia (Figure S4E).

***In vitro* tumor EGCs model**. Both orthotopic tumors and healthy colons of C57BL/6J, CCR2$^{+/+}$ or CCR2$^{-/-}$ mice were digested for 30 min in DMEM with 2.5% FBS, 100 µg/mL Penicillin and Streptomycin, 200 U/mL collagenase IV (Gibco, ThermoFisher Scientific) and 125 µg/mL type II dispase (Gibco, ThermoFisher Scientific) to obtain a single-cell suspension. Tumor microenvironment conditioned medium (TME-CM) and healthy colon conditioned medium (H-CM) were generated by culturing 5 x 10^5 cells/mL in DMEM-complete medium overnight. Next, primary murine embryonic neurosphere-derived EGCs were stimulated with the TME-CM or H-CM for 6, 12 or 24 hours. For IL-1R blocking experiments, primary embryonic neurosphere-derived EGCs were incubated for 24h with TME-CM together with 5 µg/mL isotype IgG (BioXCell) or 5 µg/mL anti-IL-1R (BioXCell).

Orthotopic CRC model. Orthotopic colonic sub-mucosal implantation of CRC cells was performed as previously described (Zigmond et al., 2011). Briefly, MC38 cells (Corbett et al., 1975) were intracolonic (i.c.) injected via endoscopy as a single-cell suspension containing between 75 000 - 750 000 MC38 cells/ 100 µL PBS depending on the susceptibility of the mouse strain. For the EGCs supplementation model, primary embryonic neurosphere-derived EGCs were isolated with 0.05% Trypsin-EDTA (Gibco, ThermoFisher Scientific) and treated with HBSS (Gibo, ThermoFisher Scientific) supplemented with 100 µg/mL DNAse I (Roche) and 5 mM $MgCl_2$ (Sigma-Aldrich) for 30 min at RT. Subsequently, EGCs were first washed with HBSS with 5 mM $MgCl_2$ and then with PBS. Finally, EGCs were resuspended in PBS together with MC38 cells in a ratio of 1:1 and orthotopically co-injected in C57BL/6J WT mice. Two weeks prior to the start of each experiment, PLP1^{CreERT2}iDTR mice were injected intraperitoneally (i.p.) 2 times every other day with 100 mg/kg Tamoxifen (Sigma-Aldrich) dissolved in 100 µL MIGLYOL®812 (Sigma-Aldrich). For EGCs *in vivo* depletion experiments, PLP1^{CreERT2}iDTR mice were injected i.c. with 2 mg/kg Diphtheria toxin (DT) (Merck, Sigma) dissolved in 100 µL of saline, three and five days prior to the start of the tumor implantation. Tumor volume was determined by caliper measurements and calculated based on the height (h), length (l) and width (w) of the tumor, according to the formula: (π/6)*h*l*w.

AOM-DSS model. Female GFAP^{Cre}IL-1R1$^{fl/fl}$ and GFAP^{Wt}IL-1R1$^{fl/fl}$ littermate mice (10-14 weeks of age) were injected i.p. with azoxymethane (AOM; 10 mg/kg; Sigma-Aldrich) a week prior starting 3 cycles of DSS colitis using 1.5% DSS in drinking water (MP Biomedicals) for 5 days followed by 16 days of

recovery with normal drinking water (Parang et al., 2016). On day 70 colonic tumor development was determined.

RESULTS

EGCs shape the CRC immune compartment

Recent studies identified EGCs as an important component of the colon TME. However, their contribution to CRC pathogenesis and their possible interaction with the tumor immune compartment remains largely unexplored. Hence, to address the pro-tumorigenic and immunomodulatory role of EGCs, MC38 murine colorectal cancer cells were orthotopically injected into the colonic submucosa (Figure 1A and Figures S1A-S1B) of PLP1^{CreERT2}iDTR mice allowing temporal and local depletion of enteric glia during colon tumor development. Following tamoxifen exposure, diphtheria toxin (DT) was delivered by colonoscopy-guided injections into the colonic wall on days -5 and -3 before submucosal MC38 injection (Figure 1B). Mucosal injection of DT resulted in local EGC depletion, as indicated by decreased GFAP protein level at the injection site while normal GFAP protein levels were observed 1.5 cm adjacent to the DT injection site, with overall discernible impact on the total colon length (Figures S1C-S1E). However, PLP1 reporter-guided EGCs depletion only leads to a temporary depletion, as EGCs have been reported to repopulate the gut within 2 weeks following the initial depletion (Baghdadi et al., 2021). Taking advantage of the orthotopic CRC model, which confers precise control of tumor location and growth rate (Zigmond et al., 2011), the endpoint of our orthotopic depletion experiment was chosen 7 days post-tumor induction (a total of 12 days after the first DT injection). Seven days after colonic MC38 cells injection, a significant reduction of tumor size was observed in DT pre-treated mice compared to the vehicle group (Figure 1C). Interestingly, during this early phase of tumor growth (7 days), the depletion of EGCs resulted also in a decreased number of TAMs (Figure 1D and S1F). Furthermore, a decrease in the numbers of monocytes and eosinophils was observed in tumors after enteric glia depletion, whereas no differences were observed for neutrophils, T and B cells (Figures 1D and S1G).

To further validate the effect of EGCs on the CRC immune compartment, we established a co-injection model of MC38 cells together with primary EGCs (Figure 1E). Co-injection of MC38 and EGCs resulted in increased tumor growth together with higher numbers of TAMs, as well as CD4$^+$ T cell, CD8$^+$ T cell, and T_{reg} cells compared to mice orthotopically injected with MC38 cells alone (Figures 1F-1G and S1H). No differences were observed in the numbers of monocytes, eosinophils, neutrophils, and B cells (Figures 1G and S1H).

Spatial tissue mapping via confocal microscopy conformed close proximity between EGCs (GFAP$^+$) and TAMs (F4/80$^+$) within orthotopic colonic tumors injected in WT mice (Figure 1H), further suggesting the existence of a glial-immune interplay within the TME.

Overall, these findings suggest that EGCs participate in shaping the CRC immune microenvironment, by expanding the TAM population.

EGCs display an activated and immunomodulatory phenotype in CRC

To examine the molecular mechanisms by which EGCs influence the immune CRC compartment with particular regard to the TAMs, we first investigated their transcriptional adaptations upon CRC onset. To this end, we established an *in vitro* tumor EGC model, able to mimic the response of enteric glia to the factors secreted by the colonic tumor microenvironment (TME). To this end, primary embryonic-derived EGCs were treated with conditioned medium (CM) of digested murine MC38 orthotopic tumors, from now onwards, defined as TME-CM EGCs (Figure 2A). In this model, EGCs stimulated with supernatants derived from healthy colonic tissue (H-CM) and naïve unstimulated EGCs were used as controls. At 6 hours, 12 hours, and 24 hours post-stimulation bulk RNA sequencing (RNA-seq) was analyzed uncovering strong transcriptional differences among the various EGC groups. Principal component analysis (PCA) demonstrated a significant similarity between the H-CM and unstimulated EGC samples (Figure 2B). In contrast, TME-CM EGCs exhibited a distinct separation from both H-CM and unstimulated EGCs, suggesting a noticeable difference in their transcriptional programs. Next, using weighted gene correlation network analysis (WGCNA) we identified 12 gene co-expression modules. TME-CM EGCs showed specific correlation to modules 7 and 8 and an inverse correlation to module 4 (Figure 2C; Table S1). Here, module 7 showed a functional association with glial reactivity, indicated by the upregulation of genes such as *Lcn2* and *Timp1*, which are typical markers for pan-reactive astrocytes (Clarke et al., 2018) (Figure 2D). Module 8 consisted of genes, including *Ccl2* and *Il6,* that are associated with immunomodulatory functions of EGCs, mimicking a state of enteric gliosis (Schneider et al., 2022). Conversely, the genes of module 4, such as *Ntsr1* and *Sparlc1,* were associated with the homeostatic functions of EGCs (Drokhlyansky et al., 2020). In line, gene set enrichment analysis of the 24h TME-CM EGCs signature revealed impairment for functions previously ascribed to healthy EGCs, including GO terms like "*Positive regulation of stem cell differentiation", "Regulation of glial cell differentiation and gliogenesis", "Neuron projection guidance",* and *"Positive regulation of neurogenesis"* (Baghdadi et al., 2021; Seguella and Gulbransen, 2021) (Figure 2E; Table S2). Notably, in line with the previous *in vitro* findings of Valès *et al.*, TME-CM EGCs were also enriched for the GO terms such as "*Positive regulation of prostaglandin biosynthetic process",* and "*Interleukin 1 receptor activity"*, supporting the possible paracrine effect of IL-1/PGE_2 signaling (Valès et al., 2019). Lastly, gene set enrichment analysis predicted a direct interaction of CRC EGCs with TAMs, reflected by functional enrichment for the GO terms "*Macrophage differentiation"* and *"Positive regulation of macrophage activation* and *migration"* (Figure 2E). Taken together, upon

exposure to the CRC TME, EGCs undergo a phenotypic switch associated with the activation of immunomodulatory programs related to macrophage interplay.

Tumor EGC-derived IL-6 favors SPP1$^+$ TAM differentiation

Considering that tissue location and transcriptomic data suggest direct communication between EGCs and TAMs in the CRC microenvironment, we aim to decipher the molecular mechanisms underpinning their interaction. Firstly, single-cell transcriptomics was used to characterize the immune landscape of colorectal MC38 orthotopic tumors (Figure S2A). Interestingly, among the identified immune populations, monocytes and macrophages accounted for 60% of the tumor-infiltrating immune cells. Unsupervised clustering of the myeloid cells (*Lyz2, Cd68, H2-Ab1, Mrc1, C1qa, Ly6c2, Ccr2,* and *Fn1*) revealed 1 monocyte and 4 distinct macrophage sub-populations (Figures 3A and 3B). The macrophage cluster that was most abundant was characterized by marker genes both for monocytes (Ccr2 and Ly6c2) and for differentiated macrophages (H2-Ab1 and Nlrp3). This suggests a possible transitional state, which we have termed 'Intermediate Macrophages' (Figure 3B). Additionally, we identified two clusters of TAMs, 'SPP1$^+$ TAMs' co-expressing of *Spp1* and *Arg1,* together with genes involved in angiogenesis (*Vegfa*) and extracellular matrix remodeling (*Spp1* and *Tnf*) (Figures 3B and S2B) together with 'C1Q$^+$ TAMs' characterized by genes involved in phagocytosis (*Nr1h3*), antigen presentation (*H2-Ab1*) and the complement cascade (*C1qa*) (Figures 3B and S2B). A second C1Q$^+$ TAM cluster, characterized by high expression of cell cycle genes, including *Mki67* and *Top2a,* was classified as 'Cycling C1Q$^+$ TAMs' (Figure 3B).

Overall, our findings are in line with the study of Zhang *et al.*, which reported very similar dichotomous functional phenotypes of TAMs in CRC patients (Zhang et al., 2020). Additionally, Zhang and colleagues predicted a dichotomic differentiation trajectory of monocytes towards SPP1$^+$ TAMs or C1QC$^+$ TAMs in CRC patients. In line, we identified a strong directional flow from tumor-infiltrating monocytes towards intermediate macrophages, which in turn further branched into two opposite paths, ending either in SPP1$^+$ TAMs or C1Q$^+$ TAMs (Figure 3C).

SPP1$^+$ macrophages represent a significant cell population within the CRC immune cell compartment and are considered potential prognostic markers in CRC. However, the current knowledge regarding the microenvironmental cues, promoting the differentiation of tumor-infiltrating monocytes towards SPP1$^+$ TAMs or C1Q$^+$ TAMs, remains limited. Thus, we explored the possible role of EGCs in promoting monocyte to SPP1$^+$ TAM or C1Q$^+$ TAM differentiation using our EGC co-injection CRC model (Figures 3D and S2C). Strikingly, supplementation of EGCs within the CRC TME resulted in more than a twofold increase in SPP1$^+$ TAMs, while no significant difference was found for C1Q$^+$ TAMs.

Next, to identify key EGC-derived mediators accountable for SPP1$^+$ TAM differentiation in CRC, we applied NicheNet, a computational tool designed to infer relationships between signaling

molecules and their target gene expression (Browaeys et al., 2020). By using the genes differentially expressed between SPP1$^+$ TAMs and monocytes [data extracted from our single-cell RNA-seq (scRNAseq) murine orthotopic CRC dataset] as target genes, we prioritized candidate ligands derived from TME-CM EGCs (data extracted from bulk RNAseq *in vitro* CRC EGCs dataset) as potential drivers of this differentiation process (Figure 3E). Here, TME-CM EGC-derived IL-6 was identified as the top predicted candidate factor involved in driving the SPP1$^+$ TAM phenotype (Figures 3E and 3F).

In line with our prediction, IL-6 neutralization in TME-CM EGC supernatant (Figure 3G) attenuated the differentiation of monocytes into SPP1$^+$ TAMs, further reflected by reduced *Spp1* and *Arg1* expression (Figures 3H and 3I). Of note, TME-CM EGCs did not promote C1Q expression in monocytes, suggesting that CRC EGCs specifically favor SPP1$^+$ over C1Q$^+$ TAM differentiation (Figures 3H and 3I). Consistent with this, quantification of IL-6 revealed elevated levels in the supernatant of TME-CM EGCs compared to H-CM EGCs (Figure 3J).

Altogether, our data highlight an important and previously overlooked interaction between EGCs and TAMs in the CRC TME, where EGC-derived IL-6 might be a key regulator for driving SPP1$^+$ TAM differentiation.

Monocyte-derived IL-1 promotes the CRC EGC phenotype

Given the evidence that EGCs modulate their functions based on microenvironmental cues (Progatzky et al., 2021; Stakenborg et al., 2022; Schneider et al., 2021), we aimed at defining the factors driving the EGC phenotypic switch in CRC. Considering the heavy infiltration of the colon TME by immune cells, which recent studies have pinpointed as sources of EGC-activating factors (Progatzky et al., 2021), we investigated the possibility of immune cells driving CRC EGC transition, potentially creating a reinforcing neuroimmune feedback loop. To investigate the cellular circuits coordinating this interaction we used NicheNet (Browaeys et al., 2020) linking ligands derived from immune cells within the TME (from the scRNAseq murine orthotopic CRC dataset) to target genes differentially expressed between H-CM EGCs and TME-CM EGCs (data extracted from Bulk RNAseq *in vitro* CRC EGCs dataset) (Figure 4A). In this analysis, IL-1β and IL-1α emerged as the top-ranked ligands driving the transcriptional transition from H-CM EGCs to TME-CM EGCs (Figure 4A and 4B). Notably, we could confirm elevated levels of IL-1 in the TME samples compared to healthy colon cells, both at as RNA and protein (Figure 4C and S3A). Consistent with our prediction, treating primary EGCs with IL-1β markedly activated the CRC EGC phenotype, with induction of Lcn2 and Timp1, and immunomodulatory factors Ccl2 and Il6, both at RNA and protein levels (Figures 4D-4E, Figures S3B-S3C; Table S2). Conversely, inhibiting IL-1R signaling in EGCs during stimulation with the TME-CM, completely abrogated the induction of the CRC EGC key markers (Figure 4F and 4G). Taken together, these findings underscore the pivotal role of IL-1 in the reprogramming of EGCs upon exposure to the colonic TME.

Next, to identify the cellular source of IL-1 within the TME, we quantified IL-1 expression across epithelial, stromal, and immune cells (Figures 4H and S3D-S3F). While Valés *et al.* concluded that *in vitro* IL-1 is released by the tumor epithelial cells, we herein demonstrate that *in vivo* in the TME IL-1 secretion is restricted to myeloid cells, while no expression could be found in epithelial, nor in stromal cells (Figure S3F). Further analyses identified tumor monocytes as the principal producers of both IL-1β and IL-1α at the RNA and protein levels (Figures 4H and S3G).

To define the possible effect of tumor monocyte-derived IL-1 on the transcriptional reprogramming of EGCs, we isolated tumor- and bone marrow (BM)-derived monocytes from mice bearing orthotopic colon tumors and exposed primary enteric glia to their supernatant with or without IL-1R blockade (Figure 5A). Remarkably, the supernatant of tumor monocytes was able to induce a higher expression of CRC EGC marker genes (*Lcn2*, *Timp1*, *Ccl2*, and *Il6*) compared to control BM-derived monocytes in an IL-1R-dependent manner (Figure 5B).

To further verify the monocyte origin of IL-1 signaling, we examined the effects on primary EGCs of orthotopic TME-CM, sourced from tumors induced in both monocyte-deficient [C-C chemokine receptor type 2 deficient ($CCR2^{-/-}$)] and monocyte-competent mice ($CCR2^{+/+}$) (Figure 5C). Consistent with previous findings (Afik et al., 2016), the volume of orthotopic tumors grown in the colonic mucosa of $CCR2^{-/-}$ mice was significantly reduced (Figures 5D) as consequence of the reduce number of recruited monocyte and monocyte-derived macrophage in $CCR2^{-/-}$ tumors as confirmed by flow cytometry (Figure 5E). Consistently, *Il1b* and *Il1a* expressions were significantly decreased in the tumor tissue of CCR2-deficient mice compared to WT mice (Figure 5F), further corroborating that monocytes and monocyte-derived macrophages are the major source of IL-1 ligands in the colon TME. As expected, TME-CM isolated from the $CCR2^{-/-}$ mice failed to induce CRC EGC reprogramming as reflected by the reduced expression of *Lcn2, Ccl2,* and *Il6* when compared with EGCs treated with $CCR2^{+/+}$ TME-CM (Figure 5G). A similar trend, although not significant, was observed for *Timp1*. Overall, our findings strongly support the concept that IL-1, derived from tumor-infiltrating monocytes- and monocyte-derived macrophages, provides remodeling of the neighboring enteric glia into activated and immunomodulatory CRC EGCs.

IL-1R signaling in EGCs promotes $SPP1^{+}$ TAM differentiation and tumor progression

Next, we assessed whether IL-1R blocking in CRC EGCs might directly affect TAM differentiation. For this purpose, EGC cultures were exposed to TME-CM or H-CM in the presence of an IL-1R blocking antibody and subsequently their supernatant was used to treat naive monocytes (Figure 6A). The blockade of IL-1R reduced the differentiation of monocytes into $SPP1^{+}$ TAMs in the context of TME-CM EGCs, as evidenced by the reduced expression of SPP1 and ARG1 (Figures 6B and S4A). As a result, IL-6 levels were markedly reduced in the supernatant of TME-CM-exposed EGCs

following IL-1R inhibition (Figure 6C). These findings further corroborate our hypothesis regarding the critical role of the IL-1R/IL-6 axis in CRC EGCs in directing monocyte differentiation towards the $SPP1^{+}$ TAM phenotype.

To further analyze the role of IL-1R/IL-6 axis in this novel enteric glia and TAMs neuroimmune interaction *in vivo*, we utilized an inflammation-triggered CRC model induced by AOM/DSS (Figure 6D). Firstly, using the glia reporter mouse line $Sox10^{CreERT2}Ai14^{fl/fl}$, we confirmed spatial proximity of EGCs ($tdtomato^{+}$) and TAMs ($IBA1^{+}$) in the tumor regions as we previously observed in the orthotopic model (Figure 6E and Figure S4B). Transcriptomic analysis comparing AOM/DSS-induced tumors to naive tissue in wild-type mice additionally supports the involvement of the IL-1R/IL-6 pathway in EGC-TAM crosstalk within this model. In particular, transcriptomic differences highlighted an increase expression of CRC EGC markers, as well as TAM signature genes together with increase IL-1 signaling (Figure S4C and S4D).

To conclusively establish the role of IL-1-activated EGCs in *in vivo* CRC development, we subjected mice with a glial-specific knockout of IL-1R1 ($GFAP^{Cre}$IL-$1R1^{fl/fl}$) and their wild-type littermates ($GFAP^{Wt}$IL-$1R1^{fl/fl}$) to AOM/DSS (Figure S4E). Consistent with the role of enteric glia in the orthotopic CRC model, the number of colonic tumors was diminished in AOM/DSS-treated $GFAP^{Cre}$IL-$1R1^{fl/fl}$ compared to littermate $GFAP^{Wt}$IL-$1R1^{fl/fl}$ mice (Figure 6F), while no difference in weight loss were detectable between the two genotypes (Figure S4F). Interestingly, glial-specific IL-1R deficiency correlated with a decline in $SPP1^{+}$ TAMs, but $C1Q^{+}$ TAM levels remained unchanged (Figure 6G). Importantly, glial-specific IL-1R deficiency was further associated with a reduce *Il6* gene expression in tumor tissues of $GFAP^{Cre}$IL-$1R1^{fl/fl}$ compared to control $GFAP^{Wt}$IL-$1R1^{fl/fl}$ tumor lesions (Figure 6H). Consistently, IL-6 staining in tumor sections from the EGC reporter mouse line, $Sox10^{CreERT2}Ai14^{fl/fl}$, revealed that IL-6 protein co-localized with $tdtomato^{+}$ glial cells in AOM/DSS tumors, confirming enteric glia as important source of IL-6 in the colonic TME (Figure 6I and S4G).

In conclusion, these results provide additional *in vivo* evidence highlighting the IL-1-dependent interplay between EGCs and $SPP1^{+}$ TAMs in CRC.

IL-1R induced-CRC EGC phenotype in patients affected by CRC

After identifying enteric glia-immune interactions in pre-clinical models of CRC, we investigated whether a similar process might influence disease progression in CRC patients. Initially, spatial tissue co-localization of EGCs and TAMs was confirmed in patient-derived CRC samples (Figure 7A). Next, the possible contribution of EGCs in disease outcome was defined using the colon and rectal cancer datasets from The Cancer Genome Atlas (TCGA- COAD and READ). Here, we observed that CRC patients with a higher enteric glia transcriptomic signature (Supplementary Methods Table 3), consisting of genes highly expressed by EGCs as in previously published CRC scRNA-seq datasets (Lee

et al., 2020; Drokhlyansky et al., 2020; Kinchen et al., 2018), presented with a decreased overall survival probability compared to patient with low EGC signature (Figures 7B, S5A and S5B;). In-depth characterization of the patients with high EGC gene signature revealed 79% of this group belonging to the mesenchymal consensus molecular subtype 4 (CMS4) (Guinney et al., 2015), defined by the stromal invasion phenotype (Figure S5C). In comparison, only minor differences were identified when divided based on stage, microsatellite stability, or intrinsic CMS (iCMS) (Figure S5C). Interestingly, CRC patients with pronounced EGC involvement also exhibit higher expression of $SPP1^{+}$ TAM signature genes (Figure 7C; Supplementary Methods Table 3).

Next, to assess if the murine CRC EGC transcriptional signature was conserved also in human CRC EGCs, we analyzed EGCs identified in a scRNA-seq dataset containing both CRC lesions and unaffected colonic tissues (Lee et al., 2020) (Figure S5D and S5E). By comparing gene expression profiles of tumor and healthy EGCs, we identified 589 genes specifically expressed in human CRC EGCs (Figures 7D; Table S2). Strikingly, among the top differentially expressed CRC EGC genes, we identified the two key murine CRC EGC marker genes *Lcn2* and *Timp1*. Using gene set enrichment analysis, we found that human EGC populations differentiate along the same homeostatic and tumor pathogenesis pathway transcriptomic signatures (Figure 7E) as seen in our murine EGCs (Figure 2E). Importantly, the significance of IL-1 signaling in the differentiation of patient CRC EGC was further confirmed by the increase transcriptomic signatures for "*Interleukin-1 signaling*" and "*Gliosis*" as well as "*Regulation of macrophage differentiation, activation and migration*" compared to healthy colonic EGCs (Figure 7E). In alignment with our pre-clinical findings, cell-population profiling of human CRC samples identified tumor-infiltrating monocytes as the primary source to IL-1β production (Figures 7F and S5F). Lastly, the activated tumor EGC state was also indicative of disease outcome, as patients with a more pronounced gliosis gene signature (Supplementary Methods Table 3) (Schneider et al., 2022), have a less favorable prognosis with decreased overall survival (Figure 7G). This indicates that both the presence of EGCs (Figure 7B) and their distinct IL-1 induced CRC EGC phenotype play roles in determining CRC prognosis.

DISCUSSION

Using a variety of *in vitro* and *in vivo* models we uncover a previously unknown positive feedback loop between EGCs and TAMs in CRC. More specifically, we found that monocytes and monocyte-derived macrophages within the TME are the main producers of IL-1, inducing a pro-tumorigenic reactive phenotype in EGCs. IL-1 activated CRC EGCs via IL-6, in turn, directly promote the differentiation of tumor-infiltrating monocytes towards $SPP1^+$ TAMs. Importantly, the unique reactive phenotype of tumor EGCs correlates with worse disease outcomes, as observed in both pre-clinical CRC mouse models and in patients with CRC. Here we provide new insights into the CRC pathogenesis, uncovering a previously unidentified neuroimmune interaction between EGCs and TAMs.

EGCs are a highly plastic cells that can rapidly adapt their functions under the influence of microenvironmental cues (Seguella and Gulbransen, 2021). Recent studies have identified specific immunomodulatory factors, including IFN-γ, IL-1, and ATP, as triggers of enteric glia phenotypic and functional reprogramming in both homeostasis and diseased conditions (Progatzky et al., 2021; Schneider et al., 2022, 2021). In particular, IL-1-mediated EGC reactivity and its effects on immune cell modulation have been extensively studied in the context of intestinal inflammation (Schneider et al., 2022; Stoffels et al., 2014). However, the mechanisms underlying these processes in CRC were not yet understood. Using an unbiased approach combining murine bulk and human scRNA-seq, our investigation pinpointed TME-derived IL-1 as the principal initiator of EGC reactivity. Furthermore, we found that this IL-1-triggered EGC activation coincides with a profoundly immunomodulatory transcriptional signature in CRC EGCs. Of note, IL-1R signaling in EGCs may hold relevance for additional functions of CRC EGCs, as *in vitro* studies indicated the significance of IL-1 in EGC-cancer stem cell interactions (Valès et al., 2019). Interestingly, we identified tumor-infiltrating monocytes and macrophages as the main source of IL-1 within the tumor. Nevertheless, although our *in vivo* data and scRNAseq studies could not verify epithelial cells as a significant IL-1 source in CRC, low amounts of tumor epithelial IL-1 might also contribute to EGC activation during CRC (Valès et al., 2019).

Our study utilizes single-cell and bulk RNA-seq techniques to better understand and predict the interactions between EGCs and TAMs within the colonic TME. In our murine orthotopic CRC model, we identified two distinct subsets of TAMs with different ontogeny and properties. The $C1Q^+$ TAMs, which preferentially express genes involved in phagocytosis and antigen presentation, coexist in the TME with $SPP1^+$ TAMs that are enriched for factors regulating angiogenesis and extracellular matrix, suggesting their key role in colon tumorigenesis. This dichotomy recently also identified in patients with colorectal cancer (Zhang et al., 2020), supports the relevance of our findings to human disease. Importantly, our findings underscore a novel EGC-TAM interaction, showing that IL-1 activated EGCs drive monocyte differentiation into pro-tumorigenic $SPP1^+$ macrophages through IL-6. Thereby, our

study identified EGCs as an additional important regulator of SPP1$^+$ TAM differentiation that, together with other cancer-associated stromal cells, may contribute to tumor progression (Qi et al., 2022; Luo et al., 2022). Consistent with this, pan-cancer transcriptome analysis has pinpointed SPP1$^+$ TAMs as the most pro-tumorigenic macrophage subset across various cancers, including CRC (Cheng et al., 2021). Hence, inhibiting the differentiation of SPP1$^+$ TAMs by blocking IL-1R signaling in EGCs may significantly impede tumor progression.

Furthermore, our data also point to a functional associated between CRC EGCs and monocyte migration, as reflected by increased *Ccl2* expression in CRC glia. Considering that the tumor monocyte population decreased upon EGC depletion, we speculate that CRC EGC-derived chemokines (i.e., CCL2 and CXCL5) could also promote the infiltration of monocytes in the colonic tumor site. This would be in line with our recent findings showing early expression of CCL2 by reactive EGCs in the context of intestinal inflammation (Stakenborg et al., 2022). However, further research will need to determine whether the pro-tumorigenic role of EGCs is exerted solely on the SPP1$^+$ TAMs or whether EGCs also affect other immune or stromal cells via glial-derived factors. Recent work by Progatzky et al. provides supportive evidence for this, demonstrating that EGCs are involved in a protective immune and stromal response to control parasitic insult in the gut (Progatzky et al., 2021).

Consistent with the identification of a pro-tumorigenic EGC phenotype in mice, we found that also in patients the reactive EGC transcriptomic signature was associated with reduced overall survival. Therefore, we could speculate that our newly identified CRC EGC gene signature might be used as a potential biomarker to predict disease outcomes. In line with the stromal nature of EGCs, we demonstrated that the vast majority of patients with high EGC involvement belonged to the consensus molecular subtype 4 (CMS4), which is characterized by a mesenchymal-like phenotype, a strong stromal infiltration and the worst overall and relapse-free survival compared to the other CMS subtypes (Guinney et al., 2015). Gene ontology analysis revealed that also the human tumor glial cells were enriched for immunomodulatory transcriptional programs related to macrophage differentiation, leading to the assumption that CRC EGC-derived signals modulate TAMs also in patients. In line, human tumor EGCs also displayed enriched GO terms for “Interleukin-1 signalling” and “Gliosis”, hinting at a similar EGC activation in CRC as in our preclinical models. Moreover, various studies demonstrated increased IL-6 levels in both tumor tissues and serum samples of human CRC patients compared to healthy controls (Komoda et al., 1998; Galizia et al., 2002). Consistently, immune-related pathways, including IL-6 signalling, were enriched in CRC EGCs in a human single-cell data set published by Qi et al. (Qi et al., 2022).

Our research elucidates the role of the IL-1/IL-6 axis in glial-immune communication in CRC, which could potentially be of relevance to various other tumors exhibiting neuronal infiltration, a features often associated with less favorable disease outcomes (Pundavela et al., 2015; Renz et al.,

2018; Hayakawa et al., 2017; Albergotti et al., 2017; Zhu et al., 2018; Murakami et al., 2013; Magnon et al., 2013). Apart from EGCs, peripheral glial cells, including Schwann cells, are known to play a crucial role in cancer pathophysiology, as demonstrated in pancreatic ductal adenocarcinoma, lung cancer, and melanoma (Deborde et al., 2022; Zhou et al., 2020; Shurin et al., 2019). Consistent with the pro-tumorigenic functions of EGCs in CRC, studies in melanoma models have shown that tumor Schwann cells favor the differentiation of pro-tumorigenic macrophages enhancing tumor growth (Shurin et al., 2019). Overall, glial-immune crosstalk might be an overlooked critical component of tumor pathophysiology in many cancer types beyond CRC.

In conclusion, our study reveals a critical role for IL-1R signaling in driving enteric glia-macrophage interactions in CRC pathogenesis. Our research provides essential insight into the complex neuroimmune mechanisms underlying the development of this disease, shedding light on potential novel biomarkers and specific therapeutic targets that hold the promise of transforming the management of this devastating disease.

ACKNOWLEDGMENTS

We acknowledge all members of Prof. Matteoli's laboratory and Prof. Wehner´s laboratory for the support and scientific discussions. We would like to thank Tine Gomers, Karlien Vranken and Renata Siqueira de Mello (TARGID, KU Leuven) and Patrik Efferz and Bianca Schneiker (Department of Surgery, University Hospital Bonn) for technical assistance during experiments. Furthermore, we would like to thank Ally Peddle and Yourae Hong (Molecular Digestive Oncology, Department, KU Leuven), Lukas Ferreira Maciel (Laboratory for Molecular Cancer Biology, VIB-KU Leuven) and Florent Petitprez (MRC Centre for Reproductive Health, University of Edinburgh) for their scientific support on bio-informatic analysis. Within KU Leuven we would like to acknowledge the following core facilities: FACS Core, Genomics Core (UZ Leuven), LiMoNe VIB Bioimaging Core and VIB Center for Brain & Disease Research. We would like to thank the Cell and Tissue Imaging Cluster (KU Leuven) for the usage of the Zeiss LSM 880 – Airyscan (supported by Hercules AKUL/15/ 37_GOH1816N and FWO G.0929.15 to Prof. Pieter Vanden Berghe). We would like to thank the support from the Core Facilities of the Medical Faculty, University of Bonn, specifically, the Analytical Proteomics Core, funded by the Deutsche Forschungsgemeinschaft (DFG) – project 386936527, the Bioinformatics Data Analysis Core, the Microscopy Core Facility funded by the DFG – project 266686698, and the Next Generation Sequencing Core. We thank Dr. Vassilis Pachnis for sharing the Sox10^{CreERT2} mice with us. BioRender was used for creating graphical images.

V.D.S. was supported by a Stichting tegen Kanker postdoctoral fellowship. S.S. was supported by KU Leuven-University of Melbourne Global PhD (GPUM/22/020). F.B. was supported by the KU Leuven-University of Edinburgh Global PhD (GPUE/20/003). B.K. was supported by the Taiwan - KU Leuven PhD Scholarship. M.V. was supported by a Fonds voor Wetenschappelijk Onderzoek Vlaanderen (FWO, 11L0822N) PhD fellowship. S.I. was supported by a MSCA-IF (79756–GLIAMAC) and a fellowship from the European Crohn's and Colitis Organization (ECCO). S.V. and S.T. were supported by the FWO grant G067821N and Stichting tegen Kanker grant F/2020/1512. G.M.'s lab was supported by FWO grants G0D8317N, G0A7919N, G086721N, G088816N and S008419N, KU Leuven Internal Funds (C12/15/016 and C14/17/097). S.W. and L.S. were supported by the DFG-funded Immunosensation^2 cluster of excellence EXC2151-190873048. S.W. and R.S. received funding from BONFOR. B.G.R. received funding from the Deutsche Krebshilfe through a Mildred Scheel Nachwuchszentrum Grant (70113307).

AUTHOR CONTRIBUTIONS

Conceptualization, L.V.B., V.D.S., L.S., R.S., S.W. and G.M.; Methodology, L.V.B., V.D.S., L.S., S.W. and G.M.; Software, S.S., S.A., Z.H., J.H., L.V.B. and L.S.; Validation, L.V.B., V.D.S. and L.S.; Formal Analysis, L.V.B., V.D.S., L.S., S.S. and S.A.; Investigation, L.V.B., V.D.S., L.S., S.S., S.A., F.B., L.Z., S.V., B.K., B.G.R., M.T., M.V. and S.I.; Resources, G.M., S.W., S.T. and F.D.S.; Data Curation, L.V.B., V.D.S., L.S., S.S., S.A.,

S.V., Z.H. and J.H.; Writing – original draft, L.V.B., V.D.S. and L.S.; Writing – review & editing, all; Visualization, L.V.B., V.D.S., L.S., S.S., S.A., and Z.H.; Supervision, G.M., S.W., S.T., F.D.S., R.S., M.S. and V.D.S.; Project administration, L.V.B., V.D.S., L.S., R.S., S.W. and G.M.; Funding acquisition, V.D.S., S.I., G.M. and S.W..

DECLARATION OF INTERESTS

The authors declare no competing interests.

INCLUSION AND DIVERSITY

We support inclusive, diverse, and equitable conduct of research.

REFERENCES

Afik, R., E. Zigmond, M. Vugman, M. Klepfish, E. Shimshoni, M. Pasmanik-Chor, A. Shenoy, E. Bassat, Z. Halpern, T. Geiger, I. Sagi, and C. Varol. 2016. Tumor macrophages are pivotal constructors of tumor collagenous matrix. *J. Exp. Med.* 213:2315–2331. doi:10.1084/jem.20151193.

Albergotti, W.G., H.L. Schwarzbach, S. Abberbock, R.L. Ferris, J.T. Johnson, U. Duvvuri, and S. Kim. 2017. Defining the prevalence and prognostic value of perineural invasion and angiolymphatic invasion in human papillomavirus-positive oropharyngeal carcinoma. *JAMA Otolaryngol. - Head Neck Surg.* 143:1236–1243. doi:10.1001/jamaoto.2017.2019.

Albo, D., C.L. Akay, C.L. Marshall, J.A. Wilks, G. Verstovsek, H. Liu, N. Agarwal, D.H. Berger, and G.E. Ayala. 2011. Neurogenesis in colorectal cancer is a marker of aggressive tumor behavior and poor outcomes. *Cancer*. 117:4834–4845. doi:10.1002/cncr.26117.

AlMusawi, S., M. Ahmed, and A.S. Nateri. 2021. Understanding cell-cell communication and signaling in the colorectal cancer microenvironment. *Clin. Transl. Med.* 11:e308. doi:10.1002/ctm2.308.

Baghdadi, M.B., A. Ayyaz, S. Coquenlorge, C. Streutker, J.L. Wrana, T. Kim, M.B. Baghdadi, A. Ayyaz, S. Coquenlorge, B. Chu, S. Kumar, and C. Streutker. 2021. Enteric glial cell heterogeneity regulates intestinal stem cell niches. *Cell Stem Cell*. 29:1–15. doi:10.1016/j.stem.2021.10.004.

Bohórquez, D. V., L.A. Samsa, A. Roholt, S. Medicetty, R. Chandra, and R.A. Liddle. 2014. An enteroendocrine cell - Enteric glia connection revealed by 3D electron microscopy. *PLoS One*. 9:e89881. doi:10.1371/journal.pone.0089881.

Browaeys, R., W. Saelens, and Y. Saeys. 2020. NicheNet: modeling intercellular communication by linking ligands to target genes. *Nat. Methods*. 17:159–162. doi:10.1038/s41592-019-0667-5.

Brown, I.A.M., J.L. McClain, R.E. Watson, B.A. Patel, and B.D. Gulbransen. 2016. Enteric Glia Mediate Neuron Death in Colitis Through Purinergic Pathways That Require Connexin-43 and Nitric Oxide. *Cmgh*. 2:77–91. doi:10.1016/j.jcmgh.2015.08.007.

Cheng, S., Z. Li, R. Gao, B. Xing, Y. Gao, Y. Yang, S. Qin, L. Zhang, H. Ouyang, P. Du, L. Jiang, B. Zhang, Y. Yang, X. Wang, X. Ren, J. Bei, X. Hu, Z. Bu, J. Ji, and Z. Zhang. 2021. A pan-cancer single-cell transcriptional atlas of tumor infiltrating myeloid cells. *Cell*. 184:792–809. doi:10.1016/j.cell.2021.01.010.

Clarke, L.E., S.A. Liddelow, C. Chakraborty, A.E. Münch, M. Heiman, and B.A. Barres. 2018. Normal aging induces A1-like astrocyte reactivity. *Proc. Natl. Acad. Sci. U. S. A.* 115:E1896–E1905. doi:10.1073/pnas.1800165115.

Corbett, T.H., D.P. Griswold, B.J. Roberts, J.C. Peckham, and F.M. Schabel. 1975. Tumor Induction Relationships in Development of Transplantable Cancers of the Colon in Mice for Chemotherapy Assays, with a Note on Carcinogen Structure. *Cancer Res.* 35:2434–2439.

Deborde, S., L. Gusain, A. Powers, A. Marcadis, Y. Yu, C.H. Chen, A. Frants, E. Kao, L.H. Tang, E. Vakiani, M. Amisaki, V.P. Balachandran, A. Calo, T. Omelchenko, K.R. Jessen, B. Reva, and R.J. Wong. 2022. Reprogrammed Schwann Cells Organize into Dynamic Tracks that Promote Pancreatic Cancer Invasion. *Cancer Discov.* 12:2454–2473. doi:10.1158/2159-8290.CD-21-1690.

Drokhlyansky, E., C.S. Smillie, N. Van Wittenberghe, M. Ericsson, G.K. Griffin, G. Eraslan, D. Dionne, M.S. Cuoco, M.N. Goder-Reiser, T. Sharova, O. Kuksenko, A.J. Aguirre, G.M. Boland, D. Graham, O. Rozenblatt-Rosen, R.J. Xavier, and A. Regev. 2020. The Human and Mouse Enteric Nervous System at Single-Cell Resolution. *Cell*. 182:1606–1622. doi:10.1016/j.cell.2020.08.003.

Galizia, G., M. Orditura, C. Romano, E. Lieto, P. Castellano, L. Pelosio, V. Imperatore, G. Catalano, C.

Pignatelli, and F. De Vita. 2002. Prognostic significance of circulating IL-10 and IL-6 serum levels in colon cancer patients undergoing surgery. *Clin. Immunol.* 102:169–178. doi:10.1006/clim.2001.5163.

Grubišić, V., V. Bali, D.E. Fried, H.K. Eltzschig, S.C. Robson, M.S. Mazei-Robison, and B.D. Gulbransen. 2022. Enteric glial adenosine 2B receptor signaling mediates persistent epithelial barrier dysfunction following acute DSS colitis. *Mucosal Immunol.* 15:964–976. doi:10.1038/s41385-022-00550-7.

Grubišić, V., J.L. Mcclain, D.E. Fried, S.C. Robson, F.L. Christofi, and B.D. Gulbransen. 2020. Enteric Glia Modulate Macrophage Phenotype and Visceral Sensitivity following Inflammation. *Cell Rep.* 32:108100. doi:10.1016/j.celrep.2020.108100.

Guinney, J., R. Dienstmann, X. Wang, A. De Reyniès, A. Schlicker, C. Soneson, L. Marisa, P. Roepman, G. Nyamundanda, P. Angelino, B.M. Bot, J.S. Morris, I.M. Simon, S. Gerster, E. Fessler, F. De Sousa .E Melo, E. Missiaglia, H. Ramay, D. Barras, K. Homicsko, D. Maru, G.C. Manyam, B. Broom, V. Boige, B. Perez-Villamil, T. Laderas, R. Salazar, J.W. Gray, D. Hanahan, J. Tabernero, R. Bernards, S.H. Friend, P. Laurent-Puig, J.P. Medema, A. Sadanandam, L. Wessels, M. Delorenzi, S. Kopetz, L. Vermeulen, and S. Tejpar. 2015. The consensus molecular subtypes of colorectal cancer. *Nat. Med.* 21:1350–1356. doi:10.1038/nm.3967.

Hayakawa, Y., K. Sakitani, M. Konishi, S. Asfaha, R. Niikura, H. Tomita, B.W. Renz, Y. Tailor, M. Macchini, M. Middelhoff, Z. Jiang, T. Tanaka, Z.A. Dubeykovskaya, W. Kim, X. Chen, A.M. Urbanska, K. Nagar, C.B. Westphalen, M. Quante, C.S. Lin, M.D. Gershon, A. Hara, C.M. Zhao, D. Chen, D.L. Worthley, K. Koike, and T.C. Wang. 2017. Nerve Growth Factor Promotes Gastric Tumorigenesis through Aberrant Cholinergic Signaling. *Cancer Cell*. 31:21–34. doi:10.1016/j.ccell.2016.11.005.

Ibiza, S., B. García-Cassani, H. Ribeiro, T. Carvalho, L. Almeida, R. Marques, A.M. Misic, C. Bartow-Mckenney, D.M. Larson, W.J. Pavan, G. Eberl, E.A. Grice, and H. Veiga-Fernandes. 2016. Glial-cell-derived neuroregulators control type 3 innate lymphoid cells and gut defence. *Nature*. 535:440–443. doi:10.1038/nature18644.

Kinchen, J., H.H. Chen, K. Parikh, A. Antanaviciute, M. Jagielowicz, D. Fawkner-Corbett, N. Ashley, L. Cubitt, E. Mellado-Gomez, M. Attar, E. Sharma, Q. Wills, R. Bowden, F.C. Richter, D. Ahern, K.D. Puri, J. Henault, F. Gervais, H. Koohy, and A. Simmons. 2018. Structural Remodeling of the Human Colonic Mesenchyme in Inflammatory Bowel Disease. *Cell*. 175:372–386. doi:10.1016/j.cell.2018.08.067.

Komoda, H., Y. Tanaka, M. Honda, Y. Matsuo, K. Hazama, and T. Takao. 1998. Interleukin-6 levels in colorectal cancer tissues. *World J. Surg.* 22:895–898. doi:10.1007/s002689900489.

Kuipers, E.J., W.M. Grady, D. Lieberman, T. Seufferlein, J.J. Sung, P.G. Boelens, C.J.H. Van De Velde, and T. Watanabe. 2015. Colorectal cancer. *Nat. Rev. Dis. Prim.* 1:1–25. doi:10.1038/nrdp.2015.65.

Laranjeira, C., K. Sandgren, N. Kessaris, W. Richardson, A. Potocnik, P. Vanden Berghe, and V. Pachnis. 2011. Glial cells in the mouse enteric nervous system can undergo neurogenesis in response to injury. *J. Clin. Invest.* 121:3412–3424. doi:10.1172/JCI58200.

Lee, H.O., Y. Hong, H.E. Etlioglu, Y.B. Cho, V. Pomella, B. Van den Bosch, J. Vanhecke, S. Verbandt, H. Hong, J.W. Min, N. Kim, H.H. Eum, J. Qian, B. Boeckx, D. Lambrechts, P. Tsantoulis, G. De Hertogh, W. Chung, T. Lee, M. An, H.T. Shin, J.G. Joung, M.H. Jung, G. Ko, P. Wirapati, S.H. Kim, H.C. Kim, S.H. Yun, I.B.H. Tan, B. Ranjan, W.Y. Lee, T.Y. Kim, J.K. Choi, Y.J. Kim, S. Prabhakar, S. Tejpar, and W.Y. Park. 2020. Lineage-dependent gene expression programs influence the immune landscape of colorectal cancer. *Nat. Genet.* 52:594–603. doi:10.1038/s41588-020-

0636-z.

Luo, H., X. Xia, L.-B. Huang, H. An, M. Cao, G.D. Kim, H.-N. Chen, W.-H. Zhang, Y. Shu, X. Kong, Z. Ren, P.-H. Li, and Y. Lio. 2022. Pan-cancer single-cell analysis reveals the heterogeneity and plasticity of cancer- associated fibroblasts in the tumor microenvironment. *Nat. Commun.* 13:6619. doi:10.1038/s41467-022-34395-2.

Magnon, C., S. Hall, J. Lin, X. Xue, L. Gerber, S. Freedland, and P. Frenette. 2013. Autonomic Nerve Development Contributes to Prostate Cancer Progression. *Science.* 341:1236361. doi:10.1038/aja.2013.113.

Murakami, Y., K. Uemura, T. Sudo, Y. Hashimoto, N. Kondo, N. Nakagawa, T. Muto, H. Sasaki, K. Urabe, and T. Sueda. 2013. Perineural Invasion in Extrahepatic Cholangiocarcinoma: Prognostic Impact and Treatment Strategies. *J. Gastrointest. Surg.* 17:1429–1439. doi:10.1007/s11605-013-2251-0.

Neunlist, M., M. Rolli-Derkinderen, R. Latorre, L. Van Landeghem, E. Coron, P. Derkinderen, and R. De Giorgio. 2014. Enteric glial cells: Recent developments and future directions. *Gastroenterology*. 147:1230–1237. doi:10.1053/j.gastro.2014.09.040.

Parang, B., C.W. Barrett, and C.S. Williams. 2016. AOM/DSS Model of Colitis-Associated Cancer. *In* Methods Mol Biol. 297–307.

Prochera, A., and M. Rao. 2023. Mini-Review: Enteric glial regulation of the gastrointestinal epithelium. *Neurosci. Lett.* 805:137215. doi:10.1016/j.neulet.2023.137215.

Progatzky, F., M. Shapiro, S.H. Chng, B. Garcia-Cassani, C.H. Classon, S. Sevgi, A. Laddach, A.C. Bon-Frauches, R. Lasrado, M. Rahim, E.M. Amaniti, S. Boeing, K. Shah, L.J. Entwistle, A. Suárez-Bonnet, M.S. Wilson, B. Stockinger, and V. Pachnis. 2021. Regulation of intestinal immunity and tissue repair by enteric glia. *Nature*. 599:125–130. doi:10.1038/s41586-021-04006-z.

Pundavela, J., S. Roselli, S. Faulkner, J. Attia, R.J. Scott, R.F. Thorne, J.F. Forbes, R.A. Bradshaw, M.M. Walker, P. Jobling, and H. Hondermarck. 2015. Nerve fibers infiltrate the tumor microenvironment and are associated with nerve growth factor production and lymph node invasion in breast cancer. *Mol. Oncol.* 9:1626–1635. doi:10.1016/j.molonc.2015.05.001.

Qi, J., H. Sun, Y. Zhang, Z. Wang, Z. Xun, Z. Li, X. Ding, R. Bao, L. Hong, W. Jia, F. Fang, H. Liu, L. Chen, J. Zhong, D. Zou, L. Liu, L. Han, F. Ginhoux, Y. Liu, Y. Ye, and B. Su. 2022. Single-cell and spatial analysis reveal interaction of FAP+ fibroblasts and SPP1+ macrophages in colorectal cancer. *Nat. Commun.* 13:1742. doi:10.1038/s41467-022-29366-6.

Renz, B.W., R. Takahashi, T. Tanaka, M. Macchini, Y. Hayakawa, Z. Dantes, H.C. Maurer, X. Chen, Z. Jiang, C.B. Westphalen, M. Ilmer, G. Valenti, S.K. Mohanta, A.J.R. Habenicht, M. Middelhoff, T. Chu, K. Nagar, Y. Tailor, R. Casadei, M. Di Marco, A. Kleespies, R.A. Friedman, H. Remotti, M. Reichert, D.L. Worthley, J. Neumann, J. Werner, A.C. Iuga, K.P. Olive, and T.C. Wang. 2018. β2 Adrenergic-Neurotrophin Feedforward Loop Promotes Pancreatic Cancer. *Cancer Cell*. 33:75–90. doi:10.1016/j.ccell.2017.11.007.

Rosenbaum, C., M.A. Schick, J. Wollborn, A. Heider, C.J. Scholz, A. Cecil, B. Niesler, J. Hirrlinger, H. Walles, and M. Metzger. 2016. Activation of myenteric glia during acute inflammation in vitro and in vivo. *PLoS One*. 11:1–20. doi:10.1371/journal.pone.0151335.

Schneider, R., P. Leven, T. Glowka, I. Kuzmanov, M. Lysson, B. Schneiker, A. Miesen, Y. Baqi, C. Spanier, I. Grants, E. Mazzotta, E. Villalobos-Hernandez, J.C. Kalff, C.E. Müller, F.L. Christofi, and S. Wehner. 2021. A novel P2X2-dependent purinergic mechanism of enteric gliosis in intestinal inflammation. *EMBO Mol. Med.* 13:1–20. doi:10.15252/emmm.202012724.

Schneider, R., P. Leven, S. Mallesh, M. Breßer, L. Schneider, E. Mazzotta, P. Fadda, T. Glowka, T.O. Vilz, P. Lingohr, J.C. Kalff, F.L. Christofi, and S. Wehner. 2022. IL-1-dependent enteric gliosis guides intestinal inflammation and dysmotility and modulates macrophage function. *Commun. Biol.* 5:1–16. doi:10.1038/s42003-022-03772-4.

Seguella, L., and B.D. Gulbransen. 2021. Enteric glial biology, intercellular signalling and roles in gastrointestinal disease. *Nat. Rev. Gastroenterol. Hepatol.* 18:571–587. doi:10.1038/s41575-021-00423-7.

Shurin, G. V., O. Kruglov, F. Ding, Y. Lin, X. Hao, A.A. Keskinov, Z. You, A.E. Lokshin, W.A. LaFramboise, L.D. Falo, M.R. Shurin, and Y.L. Bunimovich. 2019. Melanoma-induced reprogramming of schwann cell signaling aids tumor growth. *Cancer Res.* 79:2736–2747. doi:10.1158/0008-5472.CAN-18-3872.

Stakenborg, M., S. Abdurahiman, V. De Simone, G. Goverse, N. Stakenborg, L. Van Baarle, Q. Wu, D. Pirottin, J. Kim, L. Chappell-maor, I. Pintelon, E. Pollenus, L. Boon, P. Van Den Steen, M. Hao, J.A. Van Ginderachter, G.E. Boeckxstaens, J. Timmermans, and S. Jung. 2022. Enteric glial cells favor accumulation of anti-inflammatory macrophages during the resolution of muscularis in flammation. *Mucosal Immunol.* 15:1296–1308. doi:10.1038/s41385-022-00563-2.

Stoffels, B., K.J. Hupa, S.A. Snoek, S. Van Bree, K. Stein, T. Schwandt, T.O. Vilz, M. Lysson, C.V.T. Veer, M.P. Kummer, V. Hornung, J.C. Kalff, W.J. De Jonge, and S. Wehner. 2014. Postoperative ileus involves interleukin-1 receptor signaling in enteric glia. *Gastroenterology*. 146:176–187. doi:10.1053/j.gastro.2013.09.030.

Thomasi, B., and B. Gulbransen. 2023. Mini-review: Intercellular communication between enteric glia and neurons. *Neurosci. Lett.* 806:137263. doi:10.1016/j.neulet.2023.137263.

Valès, S., G. Bacola, M. Biraud, M. Touvron, A. Bessard, F. Geraldo, K.A. Dougherty, S. Lashani, C. Bossard, M. Flamant, E. Duchalais, S. Marionneau-Lambot, T. Oullier, L. Oliver, M. Neunlist, F.M. Vallette, and L. Van Landeghem. 2019. Tumor cells hijack enteric glia to activate colon cancer stem cells and stimulate tumorigenesis. *EBioMedicine*. 49:172–188. doi:10.1016/j.ebiom.2019.09.045.

Yuan, R., N. Bhattacharya, J.A. Kenkel, J. Shen, M.A. Dimaio, S. Bagchi, T.R. Prestwood, A. Habtezion, and E.G. Engleman. 2020. Enteric Glia Play a Critical Role in Promoting the Development of Colorectal Cancer. *Front. Oncol.* 10:1–12. doi:10.3389/fonc.2020.595892.

Zhang, L., Z. Li, K.M. Skrzypczynska, Q. Fang, W. Zhang, S.A. O'Brien, Y. He, L. Wang, Q. Zhang, A. Kim, R. Gao, J. Orf, T. Wang, D. Sawant, J. Kang, D. Bhatt, D. Lu, C.M. Li, A.S. Rapaport, K. Perez, Y. Ye, S. Wang, X. Hu, X. Ren, W. Ouyang, Z. Shen, J.G. Egen, Z. Zhang, and X. Yu. 2020. Single-Cell Analyses Inform Mechanisms of Myeloid-Targeted Therapies in Colon Cancer. *Cell*. 181:442–459. doi:10.1016/j.cell.2020.03.048.

Zhou, Y., J. Li, B. Han, R. Zhong, and H. Zhong. 2020. Schwann cells promote lung cancer proliferation by promoting the M2 polarization of macrophages. *Cell. Immunol.* 357:104211. doi:10.1016/j.cellimm.2020.104211.

Zhu, Y., G. Zhang, Y. Yang, L. Cui, S. Jia, Y. Shi, S. Song, and S. Xu. 2018. Perineural invasion in early-stage cervical cancer and its relevance following surgery. *Oncol. Lett.* 15:6555–6561. doi:10.3892/ol.2018.8116.

Zigmond, E., Z. Halpern, E. Elinav, E. Brazowski, S. Jung, and C. Varol. 2011. Utilization of murine colonoscopy for orthotopic implantation of colorectal cancer. *PLoS One*. 6:1–7. doi:10.1371/journal.pone.0028858.

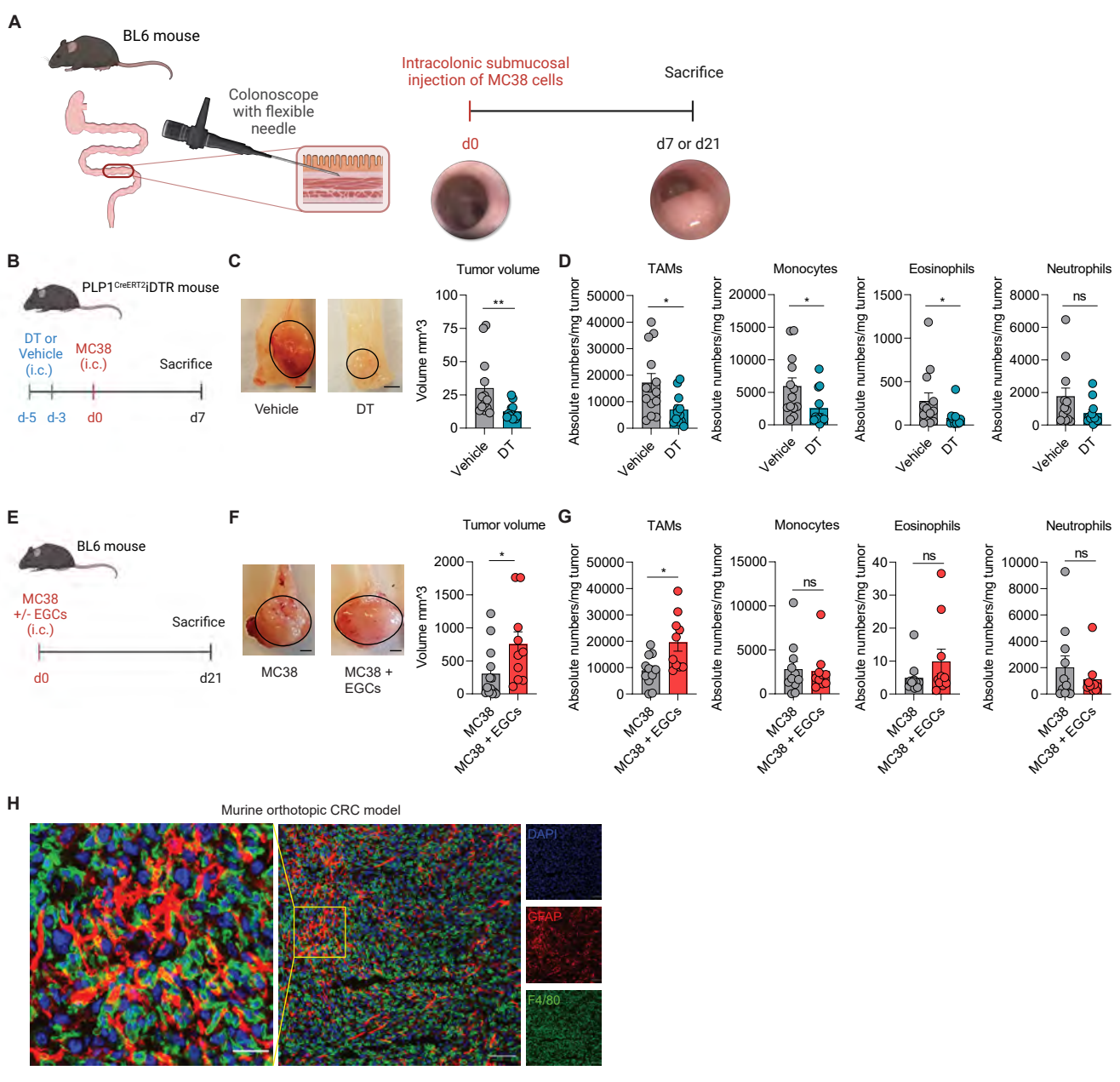
A
BL6 mouse
Colonoscope with flexible needle
Intracolonic submucosal injection of MC38 cells
Sacrifice
d0
d7 or d21
B
PLP1CreERT2iDTR mouse
DT or Vehicle (i.c.)
MC38 (i.c.)
Sacrifice
d-5
d-3
d0
d7
C
Vehicle
DT
Tumor volume
Volume mm^3
Vehicle
DT
D
TAMs
Monocytes
Eosinophils
Neutrophils
Absolute numbers/mg tumor
ns
E
BL6 mouse
MC38 +/- EGCs (i.c.)
Sacrifice
d0
d21
F
MC38
MC38 + EGCs
Tumor volume
Volume mm^3
G
TAMs
Monocytes
Eosinophils
Neutrophils
Absolute numbers/mg tumor
MC38
MC38 + EGCs
H
Murine orthotopic CRC model
DAPI
GFAP
F4/80

Figure 1. EGCs shape the CRC immune compartment

(A) BL6 mice were injected endoscopically in the colonic submucosa at day(d)0 with MC38 cells. Tumors were assessed at d7 or d21. Schematic representation of the murine orthotopic CRC model.

(B-D) PLP1^{CreERT2}iDTR mice were intracolonic (i.c.). at d-5 and d-3 with 40 ng Diphtheria toxin (DT) or saline (Vehicle). At d0, MC38 cells were i.c. injected in both groups. Tumor growth and myeloid immune infiltration were assessed at d7. Schematic representation of EGCs depletion mouse model (B) with representative pictures (scale bar 2 mm) and quantitative comparison of tumor volume (C). Data show absolute tumor-infiltrating myeloid immune cell numbers per mg tumor tissue (D) (*n = 13* Vehicle, *n = 12* DT).

(E-G) BL6 mice were intracolonic injected at d0 with MC38 cells with or without embryonic neurosphere-derived EGCs (1:1 ratio). Tumor growth and myeloid immune infiltration were assessed at d21. Schematic representation of EGCs co-injection mouse model (E) with representative pictures (scale bar 2 mm) and quantitative comparison of tumor volume (F). Data show absolute tumor-infiltrating myeloid immune cell numbers per mg tumor tissue (G) (*n = 11* MC38, *n = 10* MC38 + EGCs).

(H) Representative image showing GFAP (red), F4/80 (green) and DAPI (blue) in orthotopic murine tumor sections, (scale bar 70 µm and 25 µm).

Data show mean ± SEM. Statistical analysis: unpaired Mann-Whitney test (C-D,F-G) *p < 0.05, **p < 0.005, ns not significant. See also Figure S1.

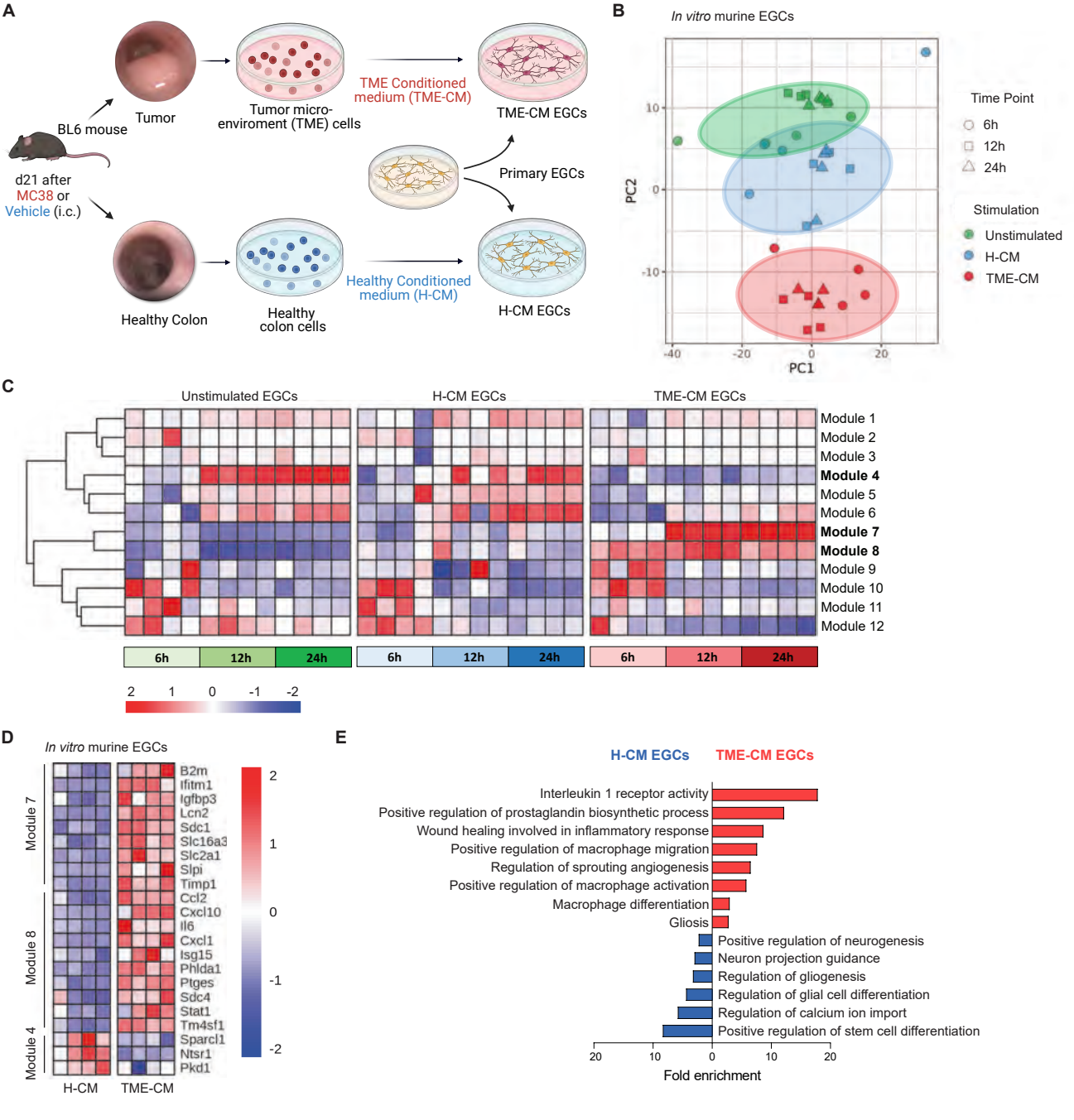
A
Tumor
Tumor micro-enviroment (TME) cells
TME Conditioned medium (TME-CM)
TME-CM EGCs
BL6 mouse
d21 after MC38 or Vehicle (i.c.)
Primary EGCs
Healthy Colon
Healthy colon cells
Healthy Conditioned medium (H-CM)
H-CM EGCs
B
In vitro murine EGCs
PC2
PC1
Time Point
6h
12h
24h
Stimulation
Unstimulated
H-CM
TME-CM
C
Unstimulated EGCs
H-CM EGCs
TME-CM EGCs
Module 1
Module 2
Module 3
Module 4
Module 5
Module 6
Module 7
Module 8
Module 9
Module 10
Module 11
Module 12
6h
12h
24h
2
1
0
-1
-2
D
In vitro murine EGCs
Module 7
Module 8
Module 4
B2m
Ifitm1
Igfbp3
Lcn2
Sdc1
Slc16a3
Slc2a1
Slpi
Timp1
Ccl2
Cxcl10
Il6
Cxcl1
Isg15
Phlda1
Ptges
Sdc4
Stat1
Tm4sf1
Sparcl1
Ntsr1
Pkd1
H-CM
TME-CM
E
H-CM EGCs
TME-CM EGCs
Interleukin 1 receptor activity
Positive regulation of prostaglandin biosynthetic process
Wound healing involved in inflammatory response
Positive regulation of macrophage migration
Regulation of sprouting angiogenesis
Positive regulation of macrophage activation
Macrophage differentiation
Gliosis
Positive regulation of neurogenesis
Neuron projection guidance
Regulation of gliogenesis
Regulation of glial cell differentiation
Regulation of calcium ion import
Positive regulation of stem cell differentiation
Fold enrichment

Figure 2. EGCs display an activated and immunomodulatory phenotype in CRC

Transcriptome analysis of *in vitro* primary embryonic neurosphere-derived EGCs alone or stimulated with healthy conditioned medium (H-CM) or tumor microenvironment conditioned medium (TME-CM) at different time points (6h, 12h, and 24h, *n = 4*).

(A) Schematic representation of the *in vitro* tumor EGCs model.

(B) Principal component analysis (PCA) plot of EGCs gene signature identified by 3´mRNA bulk RNA-seq. Each dot represents an individual sample.

(C) Heatmap showing the transcriptional modules identified by weighted gene correlation network analysis (WGCNA).

(D) Heatmap of differentially expressed genes in modules 4, 7, and 8 of *in vitro* murine EGCs stimulated for 24h with H- or TME-CM.

(E) Gene set enrichment analysis for the differentially up- and down-regulated genes in TME-CM versus H-CM stimulated EGCs after 24h (*n = 4*). See also Table S1 and S2.

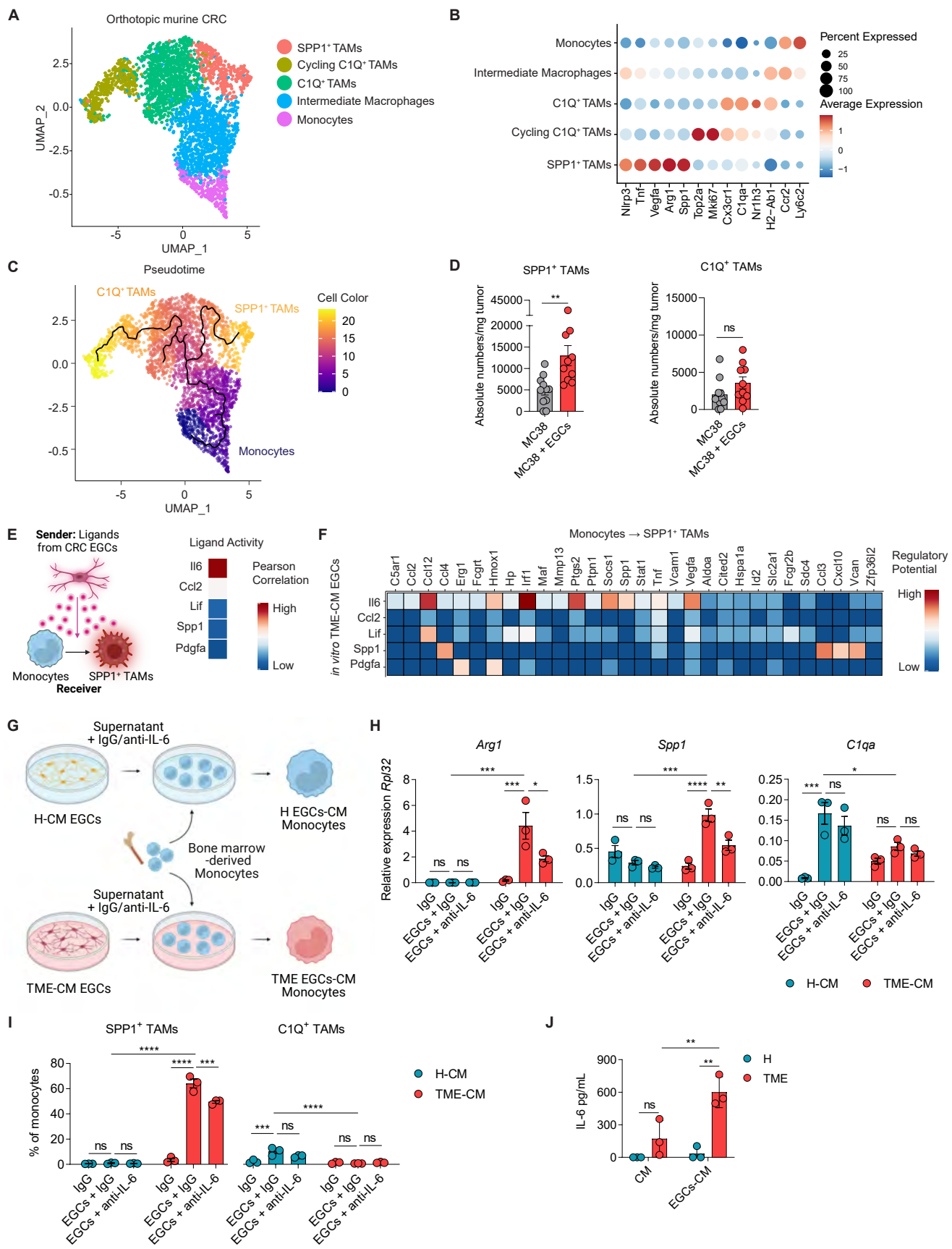
A
Orthotopic murine CRC
SPP1⁺ TAMs
Cycling C1Q⁺ TAMs
C1Q⁺ TAMs
Intermediate Macrophages
Monocytes
UMAP_2
UMAP_1
B
Monocytes
Intermediate Macrophages
C1Q⁺ TAMs
Cycling C1Q⁺ TAMs
SPP1⁺ TAMs
Percent Expressed
Average Expression
Nlrp3
Tnf
Vegfa
Arg1
Spp1
Top2a
Mki67
Cx3cr1
C1qa
Nr1h3
H2−Ab1
Ccr2
Ly6c2
C
Pseudotime
C1Q⁺ TAMs
SPP1⁺ TAMs
Monocytes
Cell Color
UMAP_1
D
SPP1⁺ TAMs
C1Q⁺ TAMs
Absolute numbers/mg tumor
MC38
MC38 + EGCs
ns
E
Sender: Ligands from CRC EGCs
Monocytes
SPP1⁺ TAMs
Receiver
Ligand Activity
Il6
Ccl2
Lif
Spp1
Pdgfa
Pearson Correlation
High
Low
F
Monocytes → SPP1⁺ TAMs
in vitro TME-CM EGCs
C5ar1
Ccl2
Ccl12
Ccl4
Erg1
Fcgrt
Hmox1
Hp
Irf1
Maf
Mmp13
Ptgs2
Ptpn1
Socs1
Spp1
Stat1
Tnf
Vcam1
Vegfa
Aldoa
Cited2
Hspa1a
Id2
Slc2a1
Fcgr2b
Sdc4
Ccl3
Cxcl10
Vcan
Zfp36l2
Il6
Ccl2
Lif
Spp1
Pdgfa
Regulatory Potential
High
Low
G
Supernatant + IgG/anti-IL-6
H-CM EGCs
H EGCs-CM Monocytes
Bone marrow -derived Monocytes
Supernatant + IgG/anti-IL-6
TME-CM EGCs
TME EGCs-CM Monocytes
H
Arg1
Spp1
C1qa
Relative expression Rpl32
IgG
EGCs + IgG
EGCs + anti-IL-6
H-CM
TME-CM
I
SPP1⁺ TAMs
C1Q⁺ TAMs
% of monocytes
H-CM
TME-CM
J
IL-6 pg/mL
H
TME
CM
EGCs-CM

Figure 3. Tumor EGC-derived IL-6 favors SPP1$^+$ TAM differentiation.

(A-C) scRNA-seq analysis of monocytes and macrophages from the scRNA-seq data of tumors from BL6 mice bearing orthotopic MC38 tumors, 21 days(d) after tumor induction *(n = 3)*. UMAP of tumor-infiltrating monocyte and macrophage subclusters (A) and dot plot of differentially expressed marker genes used for their annotation (B). Differentiation trajectory of murine CRC-infiltrating monocyte and macrophage subsets inferred by Monocle (C).

(D) BL6 mice were intracolonic injected with MC38 cells and with or without embryonic neurosphere-derived EGCs (1:1 ratio). SPP1$^+$ TAMs and C1Q$^+$ TAMs infiltration was assessed on d21. Data represents absolute numbers per mg tumor tissue (*n = 11* MC38, *n = 10* MC38 + EGCs).

(E-F) Nichenet analysis was performed considering the ligands expressed by 24h TME-CM EGCs, data extracted from *in vitro* CRC EGCs bulk RNAseq dataset (See Figure 2) and considering the differentially expressed genes between monocytes and SPP1$^+$ TAMs as target genes, data extracted from CRC orthotopic murine CRC dataset (See Figure 3A). Top ligands from *in vitro* tumor microenvironment conditioned medium (TME-CM) EGCs and their Pearson correlation, predicted to be inducing monocytes to SPP1$^+$ TAM differentiation according to NicheNet (E). Heatmap of ligand-target pairs showing regulatory potential scores between top positively correlated prioritized ligands of *in vitro* TME-CM EGCs and their target genes among the differentially expressed genes between monocytes and SPP1$^+$ TAMs (F).

(G-I) *In vitro* murine bone marrow-derived monocytes cultured for 48h with supernatant of healthy (H)-CM, TME-CM, H EGCs-CM, and TME EGCs-CM in the presence of IgG or anti-IL-6 (both 5 µg/mL) *(n = 3)*. Experimental design (G). Relative mRNA levels for *Arg1, Spp1,* and *C1qa* normalized to the housekeeping gene *Rpl32* in monocytes after stimuli (H). Percentages of SPP1$^+$ and C1Q$^+$ TAMs in monocyte cultures after stimuli (I).

(J) IL-6 concentration in the H-CM, TME-CM, H EGCs-CM, and TME EGCs-CM *(n = 3)*.

All data are represented as mean ± SEM. Statistical analysis: unpaired t-test (D), two-way ANOVA test with correction for multiple comparisons (H-J). * $p < 0.05$, ** $p < 0.005$, *** $p < 0.0005$, **** $p < 0.00005$, ns not significant. See also Figure S2.

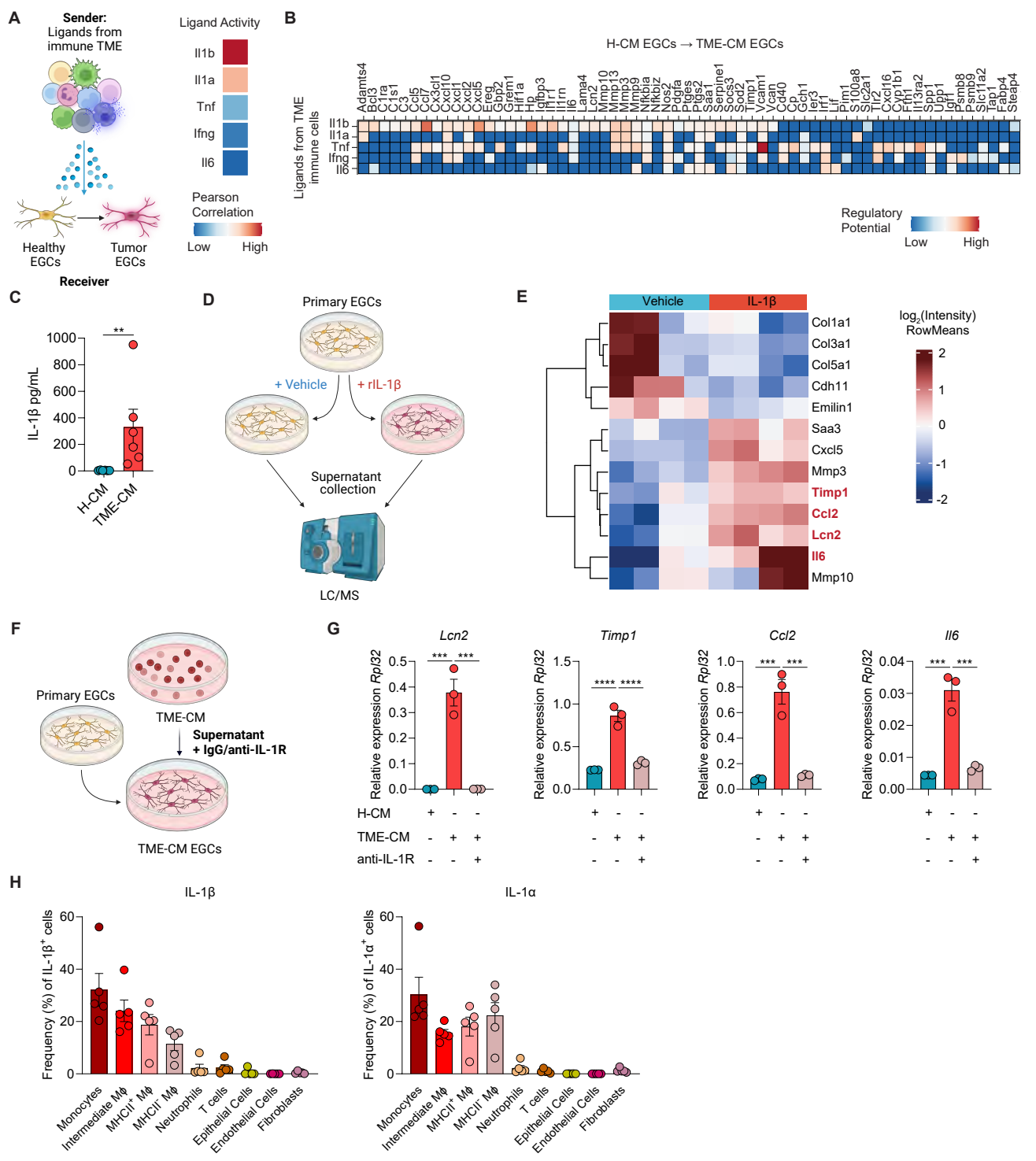
A
Sender:
Ligands from immune TME
Ligand Activity
Il1b
Il1a
Tnf
Ifng
Il6
Pearson Correlation
Low
High
Healthy EGCs
Tumor EGCs
Receiver
B
H-CM EGCs → TME-CM EGCs
Ligands from TME immune cells
Il1b
Il1a
Tnf
Ifng
Il6
Adamts4 Bcl3 C1ra C1s1 C3 Ccl5 Ccl7 Cx3cl1 Cxcl10 Cxcl1 Cxcl2 Cxcl5 Ereg Gbp2 Grem1 Hif1a Ifnb Igfbp3 Irf1 Il1rn Il6 Lama4 Lcn2 Mmp10 Mmp13 Mmp3 Mmp9 Nfkbia Nfkbiz Nos2 Pdgfa Ptges Ptgs2 Saa1 Serpine1 Socs3 Sod2 Timp1 Vcam1 Ccl20 Cd40 Gch1 Ier3 Irf1 Lif Pim1 S100a8 Slc2a1 Tlr2 Cxcl16 Cyp1b1 Fth1 Il13ra2 Spp1 Ubp1 Igf1 Fsmb8 Fsmb9 Slc11a2 Tap1 Fabp4 Steap4
Regulatory Potential
Low
High
C
IL-1β pg/mL
1000
800
600
400
200
0
**
H-CM
TME-CM
D
Primary EGCs
+ Vehicle
+ rIL-1β
Supernatant collection
LC/MS
E
Vehicle
IL-1β
log2(Intensity) RowMeans
2
1
0
-1
-2
Col1a1
Col3a1
Col5a1
Cdh11
Emilin1
Saa3
Cxcl5
Mmp3
Timp1
Ccl2
Lcn2
Il6
Mmp10
F
Primary EGCs
TME-CM
Supernatant + IgG/anti-IL-1R
TME-CM EGCs
G
Lcn2
Timp1
Ccl2
Il6
Relative expression Rpl32
***
****
H-CM
TME-CM
anti-IL-1R
H
IL-1β
IL-1α
Frequency (%) of IL-1β+ cells
Frequency (%) of IL-1α+ cells
Monocytes
Intermediate Mϕ
MHCII+ Mϕ
MHCII- Mϕ
Neutrophils
T cells
Epithelial Cells
Endothelial Cells
Fibroblasts

Figure 4. IL-1R activation drives the CRC EGC phenotype

(A-B) Top ligands from orthotopic CRC tumor-infiltrating immune cells predicted by NicheNet to be inducing CRC EGC signature. Nichenet analysis was performed considering the ligands expressed by murine orthotopic CRC tumor-infiltrating immune cells, data extracted from CRC orthotopic murine CRC dataset (See Figure S2A) and considering the differentially expressed genes between 24h Healthy conditioned medium (H-CM) EGCs and tumor microenvironment (TME)-CM EGCs as target genes, data extracted from *in vitro* CRC EGCs bulk RNAseq dataset (See Figure 2). Schematic representation of TME-derived ligand-EGC interplay (left) and top 5 predicted ligands with their Pearson correlation (right) (A). Heatmap of ligand-target pairs showing regulatory potential scores between top ligands and target genes among the differentially expressed genes between *in vitro* H-CM EGCs and TME-CM EGCs (B).

(C) Protein level of IL-1β in H-CM and TME-CM *(n = 6)*.

(D-E) Primary adult neurosphere-derived EGCs were isolated from BL6 mice and treated with or without rIL-1β (10 ng/mL) for 24h. Protein concentration in the culture supernatants was determined by liquid chromatography/mass spectrometry (*n = 4*). Schematic experimental representation (D) and heatmap of differentially expressed proteins between Vehicle and IL-1β-treated EGCs (E).

(F-G) Primary embryonic neurosphere-derived EGCs were stimulated for 24h with H-CM or TME-CM in the presence or absence of IgG or anti-IL-1R (5 µg/mL each) *(n = 3)*. Schematic representation of experimental setup (F). Relative mRNA levels for *Lcn2, Timp1, Ccl2,* and *Il6* normalized to the housekeeping gene *Rpl32* (G).

(H) BL6 mice were intracolonic injected at day(d)0 with MC38 cells, and both stromal and immune cells were assessed for IL-1β and IL-1α expression at d21. Data are presented as the frequency of total live IL-1β^+ or IL-1α^+ cells *(n = 5).*

All data are represented as mean ± SEM (C, G-H). Statistical analysis: unpaired Mann-Whitney test (C), unpaired t-test (G). ** p <0.005, *** p<0.0005, **** p <0.00005 See also Figure S3 and Table S2.

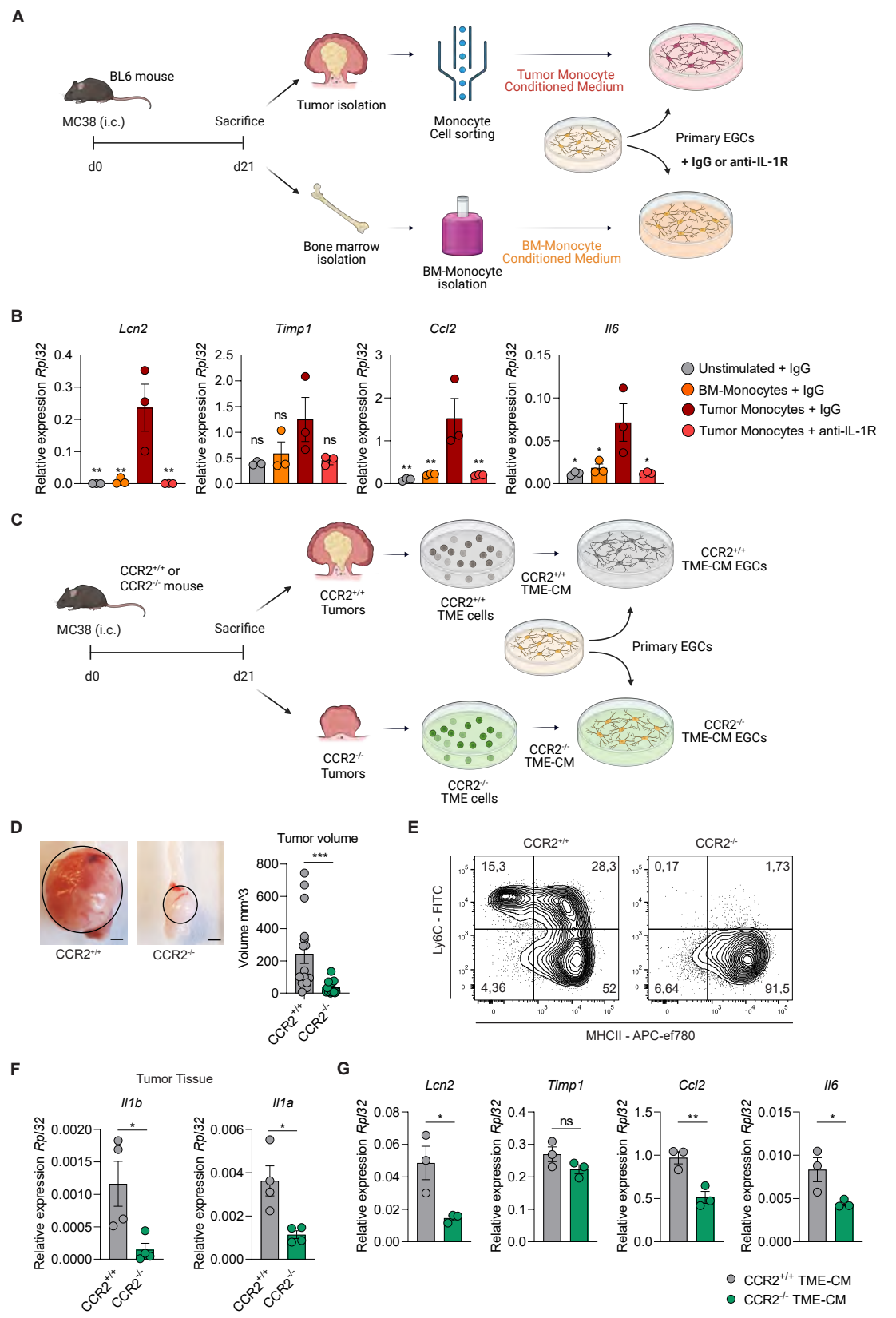
A
BL6 mouse
MC38 (i.c.)
d0
Sacrifice
d21
Tumor isolation
Monocyte
Cell sorting
Tumor Monocyte
Conditioned Medium
Primary EGCs
+ IgG or anti-IL-1R
Bone marrow
isolation
BM-Monocyte
isolation
BM-Monocyte
Conditioned Medium
B
Lcn2
Timp1
Ccl2
Il6
Relative expression Rpl32
Unstimulated + IgG
BM-Monocytes + IgG
Tumor Monocytes + IgG
Tumor Monocytes + anti-IL-1R
C
CCR2+/+ or
CCR2-/- mouse
MC38 (i.c.)
d0
Sacrifice
d21
CCR2+/+
Tumors
CCR2+/+
TME cells
CCR2+/+
TME-CM
CCR2+/+
TME-CM EGCs
Primary EGCs
CCR2-/-
Tumors
CCR2-/-
TME cells
CCR2-/-
TME-CM
CCR2-/-
TME-CM EGCs
D
CCR2+/+
CCR2-/-
Tumor volume
Volume mm^3
E
CCR2+/+
CCR2-/-
Ly6C - FITC
MHCII - APC-ef780
15,3
28,3
4,36
52
0,17
1,73
6,64
91,5
F
Tumor Tissue
Il1b
Il1a
Relative expression Rpl32
G
Lcn2
Timp1
Ccl2
Il6
Relative expression Rpl32
CCR2+/+ TME-CM
CCR2-/- TME-CM

Figure 5. Monocyte-derived IL-1 promotes the CRC EGC phenotype

(A-B) Primary embryonic neurosphere-derived EGCs were stimulated for 24h with IgG or anti-IL-1R (5 µg/mL each) with or without the supernatant of sorted tumor monocytes or bone marrow (BM)-derived monocytes from BL6 mice bearing orthotopic CRC tumors. Schematic representation of experimental setup (A). Relative mRNA levels of *Lcn2, Timp1, Ccl2,* and *Il6,* normalized to the housekeeping gene *Rpl32,* in primary embryonic neurosphere-derived EGCs were compared between EGCs stimulated with tumor monocyte supernatant and all other conditions *(n = 3)* (B).

(C-G) $CCR2^{+/+}$ and $CCR2^{-/-}$ mice were intracolonic injected at day(d)0 with MC38 cells, tumor tissue was collected at d21. Then, *in vitro* embryonic neurosphere-derived EGCs were cultured for 24h with the tumor microenvironment-conditioned medium (TME-CM) of $CCR2^{+/+}$ and $CCR2^{-/-}$ tumors. Schematic representation of experimental setup (C). Representative pictures (left, scale bar 2 mm) and quantitative comparison of tumor volume (right) (*n = 16* $CCR2^{+/+}$, *n = 17* $CCR2^{-/-}$) (D). Representative contour plots of tumor-infiltrating monocytes and macrophages gated on live-$CD45^{+}$-$CD11b^{+}$-$Ly6G^{-}$-$CD64^{+}$ cells (E). Relative mRNA levels of *Il1b* and *Il1a* normalized to the housekeeping gene *Rpl32* in $CCR2^{+/+}$ and $CCR2^{-/-}$ CRC tumors *(n = 3)* (F). Relative mRNA levels of *Lcn2, Timp1, Ccl2,* and *Il6* in EGCs stimulated with TME-CM of $CCR2^{+/+}$ and $CCR2^{-/-}$ mice, normalized to the housekeeping gene *Rpl32 (n = 3)* (G).

Data represented as mean ± SEM (B, D, F-G). Statistical analysis: One-way ANOVA test with correction for multiple comparisons, compared to tumor monocyte supernatant + IgG condition (B), Mann Whitney test (D) or unpaired t-test (F-G). *$p < 0.05$, ** $p < 0.005$, *** $p < 0.0005$, ns not significant.

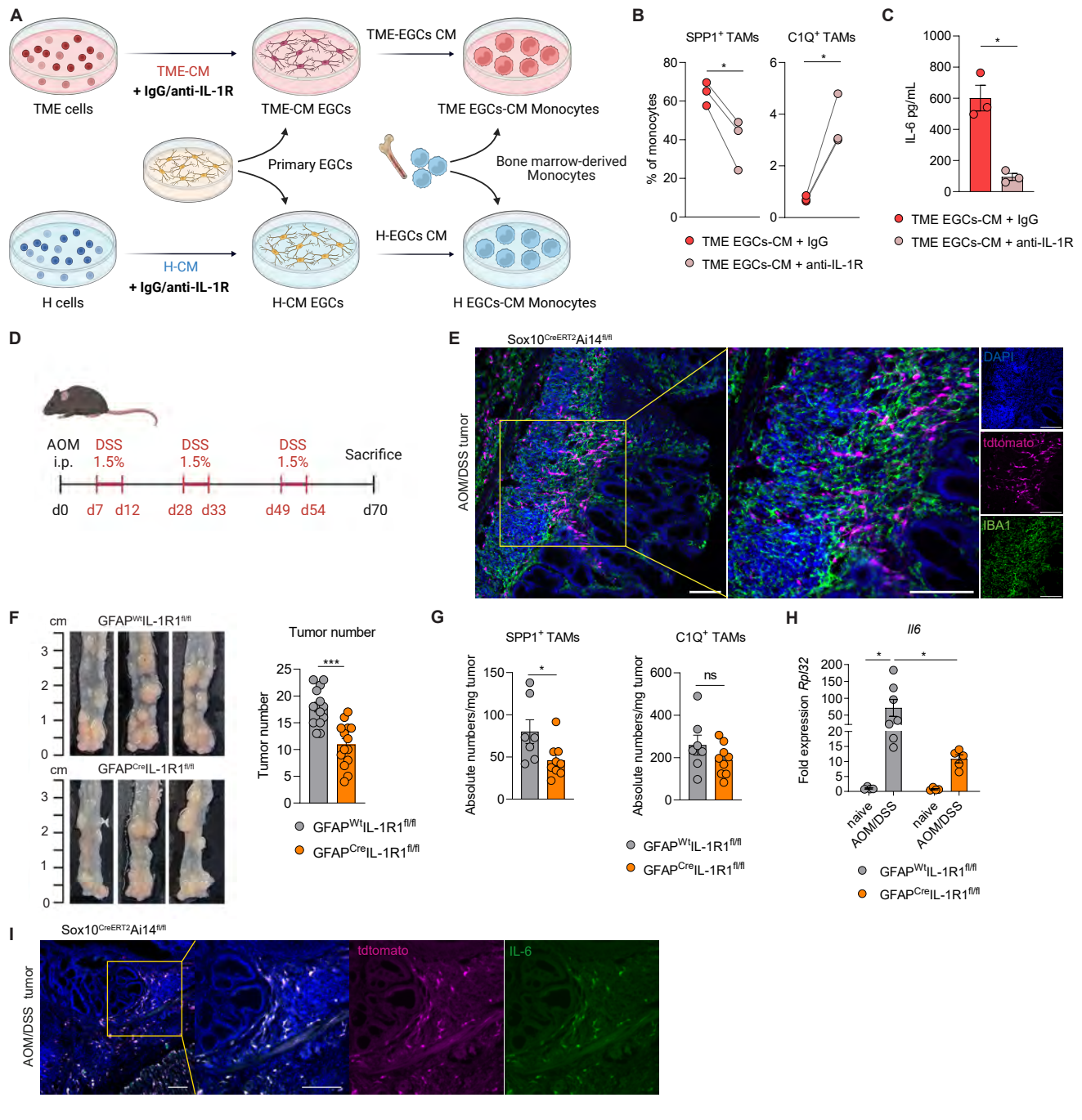
A
TME cells
TME-CM
+ IgG/anti-IL-1R
TME-CM EGCs
TME-EGCs CM
TME EGCs-CM Monocytes
Primary EGCs
Bone marrow-derived Monocytes
H cells
H-CM
+ IgG/anti-IL-1R
H-CM EGCs
H-EGCs CM
H EGCs-CM Monocytes
B
SPP1+ TAMs
C1Q+ TAMs
% of monocytes
TME EGCs-CM + IgG
TME EGCs-CM + anti-IL-1R
C
IL-6 pg/mL
TME EGCs-CM + IgG
TME EGCs-CM + anti-IL-1R
D
AOM
i.p.
DSS
1.5%
DSS
1.5%
DSS
1.5%
Sacrifice
d0
d7
d12
d28
d33
d49
d54
d70
E
Sox10CreERT2Ai14fl/fl
AOM/DSS tumor
DAPI
tdtomato
IBA1
F
cm
GFAPWtIL-1R1fl/fl
GFAPCreIL-1R1fl/fl
Tumor number
Tumor number
GFAPWtIL-1R1fl/fl
GFAPCreIL-1R1fl/fl
G
SPP1+ TAMs
C1Q+ TAMs
Absolute numbers/mg tumor
ns
GFAPWtIL-1R1fl/fl
GFAPCreIL-1R1fl/fl
H
Il6
Fold expression Rpl32
naive
AOM/DSS
naive
AOM/DSS
GFAPWtIL-1R1fl/fl
GFAPCreIL-1R1fl/fl
I
Sox10CreERT2Ai14fl/fl
AOM/DSS tumor
tdtomato
IL-6

Figure 6. IL-1R signaling in EGCs promotes SPP1^{+} TAM differentiation and tumor progression

(A-C) Murine bone marrow-derived monocytes were cultured for 48h with supernatant of primary embryonic neurosphere-derived EGCs, which were pre-incubated for 24h with tumor microenvironment conditioned medium (TME-CM) together with isotype IgG or anti-IL-1R (5 µg/mL each) *(n = 3).* Experimental design (A). FACS quantification of SPP1^{+} TAMs and C1Q^{+} TAMs gated on monocytes after stimuli (B). IL-6 concentration in the conditioned medium of TME EGCs (C).

(D) Schematic representation of experimental set-up of the murine AOM/DSS CRC model. Mice were subjected to an intraperitoneal (i.p.) injection with azoxymethane (AOM, 10 mg/kg body weight) at day(d)0. Starting from d7, mice underwent 3 repetitive cycles of 1.5% dextran sodium sulfate (DSS) (or 2% for Sox10^{CreERT2}Ai14$^{fl/fl}$ mice) in drinking water as indicated.

(E) Sox10^{CreERT2}Ai14$^{fl/fl}$ mice were i.p. injected with Tamoxifen (1 mg in 100 µL sterile corn oil) on d-7, -6, and -5. Subsequently, mice were subjected to the AOM/DSS model as described in Figure 6D. Representative image showing tdtomato (magenta), IBA1 (green), and DAPI (blue) in a tumor section at d70 (scale bar 100 µm).

(F-H) GFAP^{Wt}IL-1R1$^{fl/fl}$ and GFAP^{Cre}IL-1R1$^{fl/fl}$ mice were subjected to the AOM/DSS model as described in Figure 6D. Tumor number, tumor tissue, and TAMs infiltration were collected or assessed at d70. Tumor numbers of GFAP^{Wt}IL-1R1$^{fl/fl}$ and GFAP^{Cre}IL-1R1$^{fl/fl}$ littermates with representative images (left) and quantitative comparison of the tumor numbers (right) *(n = 14)* (F). Corresponding absolute numbers of SPP1^{+} and C1Q^{+} TAMs per mg tumor tissue (*n = 7* GFAP^{Wt}IL-1R1$^{fl/fl}$, *n = 9* GFAP^{Cre}IL-1R1$^{fl/fl}$) (G). Relative mRNA levels for *Il6*, normalized to the housekeeping gene *Rpl32* in naive (*n = 4)* and AOM/DSS treated mice (*n = 7* GFAP^{Wt}IL-1R1$^{fl/fl}$, *n = 5* GFAP^{Cre}IL-1R1$^{fl/fl}$) (H).

(I) Sox10^{CreERT2}Ai14$^{fl/fl}$ mice were subjected to the AOM/DSS model as described in Figure 6D. Representative image of tdtomato (magenta), IL-6 (green), and DAPI (blue) in tumor section at d70 (scale bar 100 µm).

Data are represented as mean ± SEM (C, F-H). Statistical analysis: paired t-test for (B-C), unpaired t-test (F), unpaired Mann-Whitney test (G), and two-way ANOVA test with correction for multiple comparisons (H). *p < 0.05, *** p <0.0005, ns not significant. See also Figure S4 and Table S3.

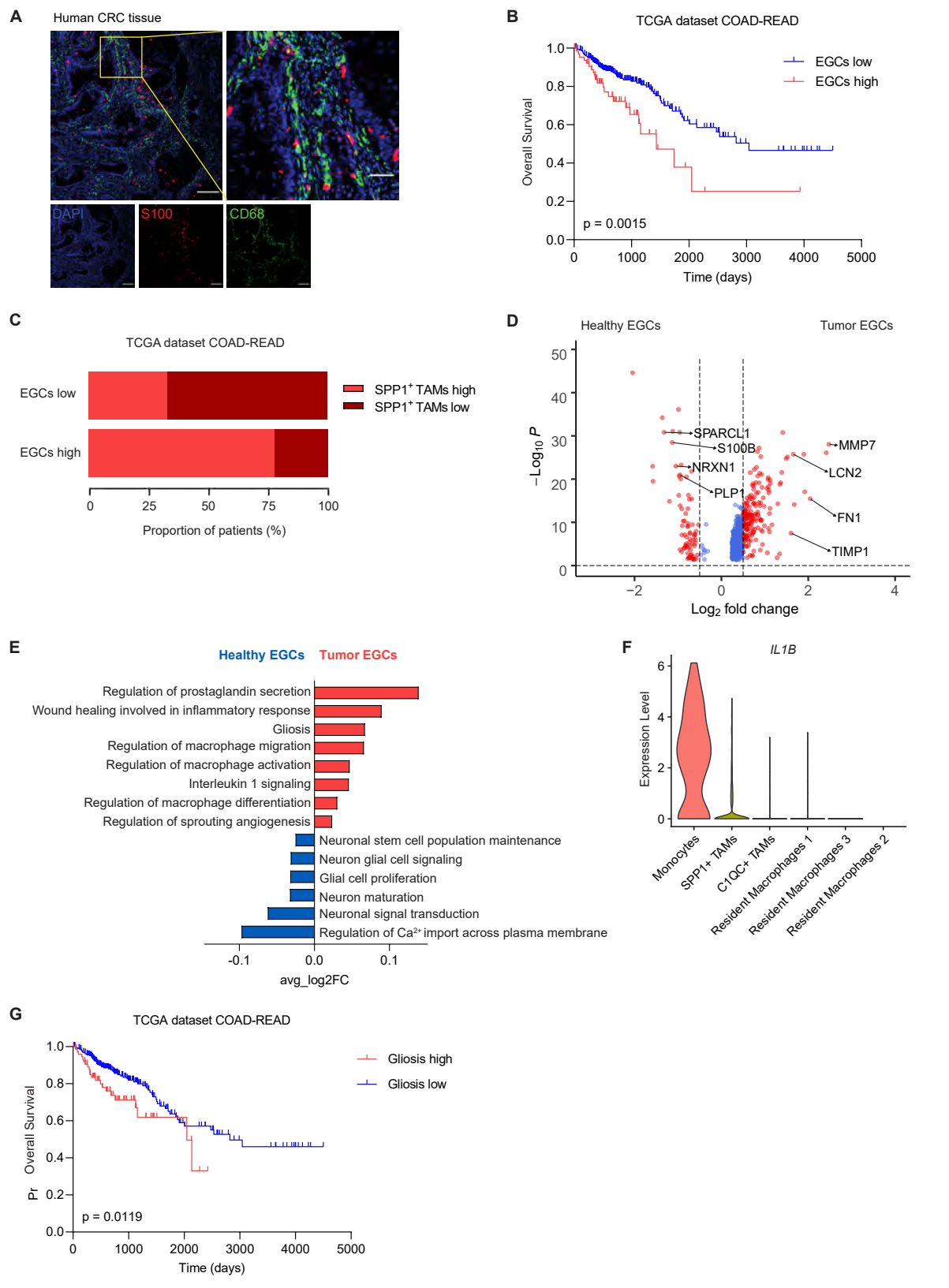
A
Human CRC tissue
DAPI
S100
CD68
B
TCGA dataset COAD-READ
EGCs low
EGCs high
Overall Survival
p = 0.0015
Time (days)
C
TCGA dataset COAD-READ
EGCs low
EGCs high
SPP1+ TAMs high
SPP1+ TAMs low
Proportion of patients (%)
D
Healthy EGCs
Tumor EGCs
SPARCL1
S100B
NRXN1
PLP1
MMP7
LCN2
FN1
TIMP1
Log2 fold change
E
Healthy EGCs
Tumor EGCs
Regulation of prostaglandin secretion
Wound healing involved in inflammatory response
Gliosis
Regulation of macrophage migration
Regulation of macrophage activation
Interleukin 1 signaling
Regulation of macrophage differentiation
Regulation of sprouting angiogenesis
Neuronal stem cell population maintenance
Neuron glial cell signaling
Glial cell proliferation
Neuron maturation
Neuronal signal transduction
Regulation of Ca2+ import across plasma membrane
avg_log2FC
F
IL1B
Expression Level
Monocytes
SPP1+ TAMs
C1QC+ TAMs
Resident Macrophages 1
Resident Macrophages 3
Resident Macrophages 2
G
TCGA dataset COAD-READ
Gliosis high
Gliosis low
Overall Survival
p = 0.0119
Time (days)

Figure 7. IL-1R induced-CRC EGC phenotype is conserved in patients affected by CRC

(A) Representative image showing S100 (red), CD68 (green) and DAPI (blue) in a human CRC tissue section (scale bar 200 µm and 50 µm).

(B-C) TCGA COAD and READ patients stratified based on their expression of the EGCs signature genes. Heatmap of patients clustering (*n = 309* EGCs low, *n = 67* EGCs high). Kaplan-Meier overall survival curve for EGCs high and low patients (B). The proportion of EGCs high and low patients classified based on high or low $SPP1^{+}$ TAMs gene signature expression (C).

(D-E) Transcriptome analysis of tumor EGCs in CRC patients (KUL3 Dataset, Lee H. O. et al. 2020, *n = 5*). Volcano plot of differentially expressed genes between healthy and tumor EGCs (D), highlighting genes defining the tumor EGCs signature. Gene Set Enrichment Analysis presenting GO terms of interest (E).

(F) Violin plot showing expression of *IL1B* in the tumor-infiltrating myeloid cell clusters of human CRC in the KUL3 Dataset, Lee H. O. et al. 2020 (*n = 5*).

(G) Kaplan-Meier overall survival curve for TCGA dataset COAD-READ patients stratified based on their expression of the gliosis signature genes. (*n = 299* gliosis low, *n = 77* gliosis high).

Statistical analysis: Mantel cox test (B, G). See also Figure S5 and Table S2.

International Journal of
Molecular Sciences

MDPI

Review

Dimethyl Fumarate and Intestine: From Main Suspect to Potential Ally against Gut Disorders

Federico Manai [1], Lisa Zanoletti [1,2], Davide Arfini [1], Simone Giorgio De Micco [1], Arolda Gjyzeli [1], Sergio Comincini [1] and Marialaura Amadio [3,*]

[1] Department of Biology and Biotechnology "L. Spallanzani", University of Pavia, 27100 Pavia, Italy; federico.manai01@universitadipavia.it (F.M.); lisa.zanoletti01@universitadipavia.it (L.Z.); davide.arfini01@universitadipavia.it (D.A.); simonegiorgio.demicco01@universitadipavia.it (S.G.D.M.); arolda.gjyzeli01@universitadipavia.it (A.G.); sergio.comincini@unipv.it (S.C.)
[2] Department of Chronic Diseases and Metabolism (CHROMETA), Katholieke Universiteit Leuven, 3000 Leuven, Belgium
[3] Department of Drug Sciences, University of Pavia, 27100 Pavia, Italy
* Correspondence: amadio@unipv.it

Abstract: Dimethyl fumarate (DMF) is a well-characterized molecule that exhibits immuno-modulatory, anti-inflammatory, and antioxidant properties and that is currently approved for the treatment of psoriasis and multiple sclerosis. Due to its Nrf2-dependent and independent mechanisms of action, DMF has a therapeutic potential much broader than expected. In this comprehensive review, we discuss the state-of-the-art and future perspectives regarding the potential repurposing of DMF in the context of chronic inflammatory diseases of the intestine, such as inflammatory bowel disorders (i.e., Crohn's disease and ulcerative colitis) and celiac disease. DMF's mechanisms of action, as well as an exhaustive analysis of the in vitro/in vivo evidence of its beneficial effects on the intestine and the gut microbiota, together with observational studies on multiple sclerosis patients, are here reported. Based on the collected evidence, we highlight the new potential applications of this molecule in the context of inflammatory and immune-mediated intestinal diseases.

Keywords: dimethyl fumarate; intestine; inflammation; inflammatory bowel diseases; Crohn's disease; ulcerative colitis; celiac disease; gut disorders; Nrf2; repurposing

Citation: Manai, F.; Zanoletti, L.; Arfini, D.; Micco, S.G.D.; Gjyzeli, A.; Comincini, S.; Amadio, M. Dimethyl Fumarate and Intestine: From Main Suspect to Potential Ally against Gut Disorders. *Int. J. Mol. Sci.* **2023**, *24*, 9912. https://doi.org/10.3390/ijms24129912

Academic Editors: Jose E. Mesonero, Eva Latorre and Elena Layunta

Received: 20 May 2023
Revised: 4 June 2023
Accepted: 6 June 2023
Published: 8 June 2023

1. Dimethyl Fumarate Pharmacokinetics and Mechanisms of Action

Dimethyl fumarate (DMF; IUPAC name: dimethyl (*E*′)-but-2enedioate) is an α,β-unsaturated carboxylic ester with a molecular weight of 144.13 g/mol derived from fumarate (or fumaric acid, FA), an organic compound found in *Fumaria officinalis*, *Boletus fomentarius*, and *Cetraria islandica*. The synthesis of DMF can be performed following two different approaches: one based on the isomerization of dimethyl maleate through reversible addition of an amine catalyzed by a Lewis acid, and another involving a Fisher esterification of FA. DMF and its active metabolite monomethyl fumarate (MMF) exert a wide range of biological functions, in particular as anti-inflammatory and immune-modulatory agents [1–6]. According to its high tolerability as well as its well-studied mechanisms of action, DMF is currently approved by the US Food and Drug Administration (FDA) as the commercial products Fumaderm® and Tacfidera® for the treatment of psoriasis and relapsing-remitting multiple sclerosis (RRMS) [7–10].

The pharmacokinetics of DMF has been thoroughly characterized: specifically, after oral administration, DMF is normally undetectable in the bloodstream [11] and urine [12], while its main metabolite MMF is present and shows a systemic peak after 2.5–3.5 h [11,13]. In vitro studies clarified the turnover of DMF in the gastrointestinal (GI) tract and its pre-systemic metabolism. Particularly, in permeation experiments with intestinal mucosa, Werdenberg and colleagues [14] demonstrated that DMF was rapidly hydrolyzed when

in contact with intestinal homogenates and perfusates compared with those derived from pancreatic tissues (used as control), due to the high concentration of carboxylesterases (present in perfusate) and carboxyl-/cholinesterases (in homogenate). Moreover, intestinal homogenates show a higher efficiency in DMF catabolism with respect to the perfusates. The reaction catalyzed by intestinal esterases in the lumen and mucosa generates, in a 1:1 ratio, MMF and methanol; the latter is then converted into formic acid by intestinal alcohol dehydrogenases (e.g., ADH1A and ADH4). The in situ levels of methanol and formic acid are the main factors responsible for DMF-related GI symptoms and ailments experienced by some patients (e.g., nausea, diarrhea, abdominal pain, cramps) [15]. The pharmacokinetics of DMF is also influenced by its instability in biological fluids and lipophilicity (10-fold higher vs. MMF), the latter likely explaining its rapid penetration in the tissues and its potent biological effects compared with the relative monoester [14]. In particular, permeability experiments with intestinal mucosa in an Ussing-type chamber further suggested that DMF is completely metabolized in the intestine, given that only MMF was detected in the lower chamber. Additionally, the environmental pH plays a role in DMF pharmacokinetics since this molecule is preferentially hydrolyzed at alkaline pH (as in the intestine) instead of acidic pH [16]. In vivo studies using adult male rats demonstrated that soon after DMF is given directly into the small intestine, it reacts with glutathione (GSH) to form the adduct *S*-(1,2-dimethoxycarbonylethyl)glutathione (GS-DMS), as confirmed by the absence of free DMF and the presence of MMF and GS-DMS in the plasma of the portal vein blood. Moreover, in the mucosa of the small intestine, DMF and MMF are mainly detected as adducts with GSH (i.e., GS-DMS and GS-MMS) [17]. Notably, in vitro evidence shows that DMF is hardly hydrolyzed to MMF in a buffer of pH 7.4, but it is rapidly hydrolyzed is human serum at the same pH, indicating the need for enzymatic reactions. More specifically, compared to serum, the half-life of DMF in whole blood samples is drastically reduced, mainly for the metabolization promoted by monocytes/lymphocytes, and also, the concentrations of MMF and monoethyl fumarate decrease over time [16]. Figure 1 shows a schematic representation of DMF's fate in the intestine:

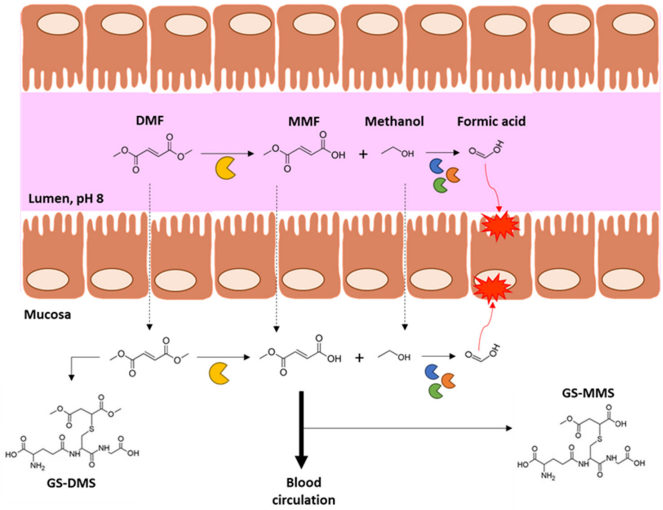

Figure 1. Schematic representation of DMF metabolism in the gut. Briefly, DMF is metabolized by intestinal esterases in MMF, the main DMF metabolite, and methanol, a well-known gut irritant. Methanol is converted into formic acid due to the action of several enzymes (e.g., dehydrogenases, or oxidases and dismutases). Once in the mucosa, both DMF and MMF can react with GSH to form adducts. According to the physico-chemical properties of DMF and the high presence of enzymes, this molecule is completely metabolized in the intestine. Only MMF enters in the blood circulation, from which it is then distributed to the target tissues. GS-DMS and GS-MMS indicate the glutathione adducts with DMF and MMF, respectively.

The main and best-studied mechanism of action of DMF/MMF relies on activation, at low concentrations, of the translocation of the nuclear factor erythroid 2 [NF-E2]-related factor 2 (Nrf2, Nfe2l2). At basal conditions, Nrf2 is retained in the cytoplasm, inhibited, and catabolized after ubiquitination and proteasomal degradation through the binding with its repressor, Kelch-like ECH-associated protein 1 (Keap1) [18]. Specifically, DMF's mechanism of action is mainly based on the reaction of succination exerted on cysteine residues on Keap1, thus leading to Keap1 conformational change and release of Nrf2, although other binding sites within the Keap1 structure have been identified as contributors to DMF's pharmacological activity [19,20]. The consequent translocation of Nrf2 into the nucleus promotes the transcription of target genes carrying in their promoter regions cis-regulatory enhancers, the so-called antioxidant response elements (AREs), which encode for cytoprotective and detoxifying enzymes. Among others, some Nrf2 target genes are *Heme Oxygenase-1* (*HO-1*), *NAD(P)H Quinone Dehydrogenase 1* (*HQO1*), and *γ-Glutamylcysteine Synthetase* (*GCLC*) [21–23] (Figure 2). Notably, Nrf2 can induce also the DNA damage signaling pathway through *TP53* transcription, whose promoter contains three AREs [24], thus connecting Nrf2 with the autophagy pathway, which is in turn regulated by p53 in oxidative stress contexts [25]. Importantly, in vivo experiments using a mouse model with *Atg5*$^{-/-}$ hepatocytes demonstrated that autophagy dysregulation leads to a prolonged Nrf2 activation as a compensatory mechanism [26]. However, the crosstalk between Nrf2 and autophagy mainly occurs through sequestosome1 (SQSTM1/p62). This autophagy adaptor protein promotes the autophagy-mediated degradation of Keap1, thus leading to the activation of Nrf2. The regulation of Keap1 cytoplasmic levels by SQSTM1/p62 has been demonstrated through both *SQSTM1/p62* overexpression and knockdown experiments [27]. The SQSTM1/p62-mediated degradation of Keap1 is also dependent on Sestrin1 and Sestrin2 [28]. The positive feedback loop between Nrf2 and autophagy is further strengthened by the regulation of the SQSTM1/p62 expression levels by Nrf2 itself [29]. *Nrf2* knockdown is accompanied by impaired SQSTM1/p62 levels and, similarly, *SQSTM1/p62* knockdown leads to a decrease in Nrf2, HO-1, and NQO1 levels [30]. In addition, in the presence of high reactive oxygen species (ROS) levels, 5′AMP-activated protein kinase (AMPK) also induces Nrf2 activation and sustains autophagy due to its negative effects on the mammalian target of rapamycin (mTOR); thus, as a regulatory triangle, AMPK, Nrf2 and mTOR guarantee a dynamic and precise control of autophagy under oxidative stress [31,32]. In agreement, AMPK can facilitate Nrf2 nuclear translocation [33] and boost the antioxidant Nrf2/HO-1 signaling pathway [34].

The pharmacological action of DMF is not limited to the Nrf2 pathway; it is performed also by Nrf2-indepenent mechanisms. For example, Nrf2 inhibits aerobic glycolysis through glyceraldehyde 3-phosphate dehydrogenase (GAPDH) succination in myeloid and lymphoid cells [35]; inhibition of the nuclear translocation of nuclear factor kappa-light-chain-enhancer of activated B cells (NF-κB) protein mediated by hydroxycarboxylic acid receptor 2 (HCAR2) represents another biological mechanism that contributes to the anti-inflammatory properties of DMF. Particularly, DMF-mediated HCAR2 activation leads to the induction of the AMPK-SIRT1 pathway, which promotes NF-κB deacetylation and, as a consequence, its inhibition [36–39]. Notably, some evidence suggests that DMF inhibits the expression and function of the hypoxia-inducible factor-1α (HIF-1α), by promoting its misfolding and consequently its proteasome-dependent degradation [40]. Indeed, DMF interferes with the interaction between HIF-1α and chaperone heat shock protein 90 (Hsp90) and promotes HIF-1α binding to the receptor for activated C kinase 1 (Rack1), which is able to induce HIF-1α degradation. Notably, a decrease in caspase-1 and NLR family pyrin domain containing 3 (NLRP3) has been described as another effect of DMF [41,42].

heat shock protein 90 (Hsp90) and promotes HIF-1α binding to the receptor for activated C kinase 1 (Rack1), which is able to induce HIF-1α degradation. Notably, a decrease in caspase-1 and NLR family pyrin domain containing 3 (NLRP3) has been described as another effect of DMF [41,42].

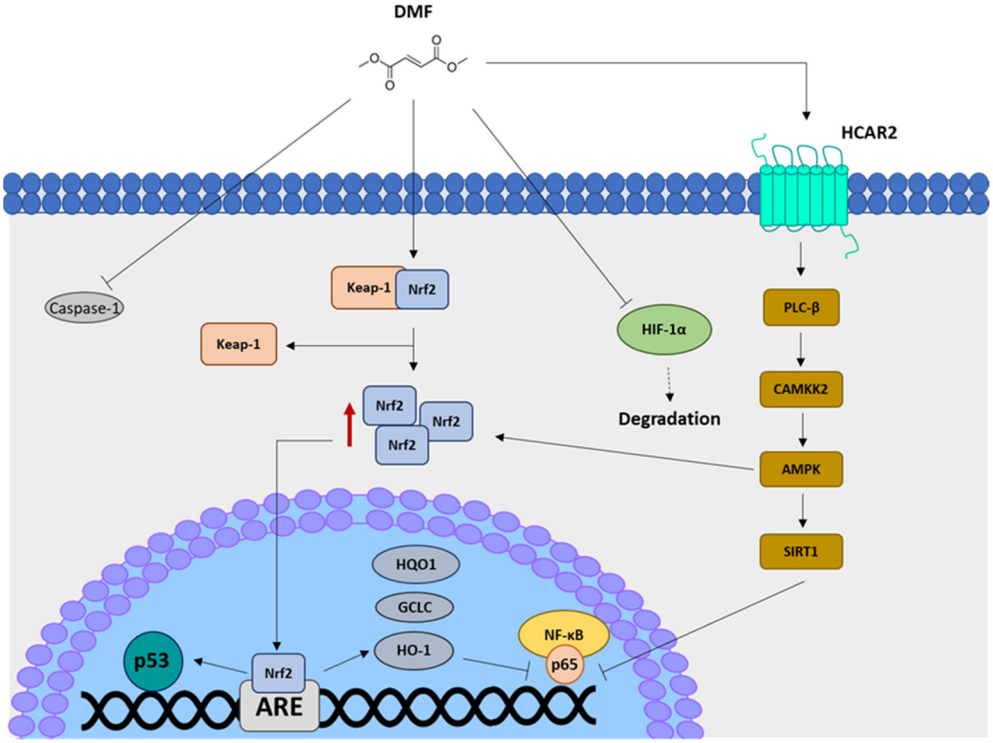

Figure 2. Schematic representation of DMF mechanisms of action. Briefly, once entered into the cytoplasm, DMF induces the dissociation of Keap-1 from Nrf2, thus allowing its translocation into the nucleus and the binding of target genes containing ARE sequences in their promoter (*e.g., TP53, HQO1, GCLC,* and *HO-1*). DMF can also inhibit caspase-1, thus alleviating the NLRP3-mediated inflammatory response, and HIF-1α, promoting its degradation. Another target of DMF is the NF-κB pathway, which is inhibited by the effects mediated by HO-1 or SIRT1, the latter interfering with NF-κB nuclear translocation.

2. Dimethyl Fumarate and Intestine: State of the Art

Starting from 1994, the number of publications regarding the beneficial effects of DMF in intestinal tissues gradually increased. Indeed, gut inflammatory disorders (e.g., inflammatory bowel diseases and celiac disease) are still characterized by a high socio-economic burden and a consistent impact in the patient's overall quality of life [43,44]. The number of entries in PubMed obtained by searching "Dimethyl fumarate AND intestine", 40, is very similar to those of other tissues (*e.g.*, heart = 44; eye = 26) and associated disorders, in which the repurposing of DMF has been already postulated [45–51]. In the following paragraphs, the state of the art regarding the effects exerted by DMF on intestine and gut microbiota will be highlighted. The search was performed on PubMed using "Dimethyl fumarate AND intestine" as keywords to isolate the relevant research articles focused on this topic. Additionally, synonyms of intestine (i.e., gut and bowel) were used. Reviews were excluded.

2.1. Dimethyl Fumarate's Effects on Intestinal Mucosa

The first evidence regarding DMF's effects in the intestine came from comparative studies with other molecules published starting from the mid-1990s. It was demonstrated that DMF was able to reduce the foci of aberrant crypts induced by azoxymethane in the colon of male Fisher rats [52]. Moreover, rats pre-treated with DMF and challenged with a toxic dose of naphthoquinones showed a higher increase in the DT-diaphorase levels in the intestine compared with those obtained with other inducers and, as a consequence, a higher amount of activated 2-hydroxy-1,4-naphthoquinone. In addition, pre-treatment with DMF decreased the renal lesions in these rats [53]. Several papers demonstrated that DMF exerted its beneficial effects in the intestinal tissue mainly through the activation of Nrf2

and inhibition of NF-κB. The Nrf2-dependent response and protective effects of DMF were first described in an aberrant crypt foci (ACF) model of colon carcinogenesis. As reported, DMF significantly induced the activity of both NQO1 and glutathione S-transferases (GST) in colon, the former being indicated by authors as relevant to inhibiting the initiation of carcinogenesis [54]. Another, more recent, study proved the anti-proliferative impact of DMF in vitro in human colon cancer cells by arresting the cell cycle in G0/G1 phase as well as activating both autophagy and apoptosis [55]. DMF can also promote colon cancer cell death through glutathione depletion and consequent apoptosis/necroptosis [56,57]. Using in vitro Caco-2 cells, another study demonstrated that DMF is able to protect against H_2O_2-caused barrier dysfunction by promoting HO-1-mediated zonulin-1 (ZO-1) induction [58].

In different in vivo models of intestinal disorders, DMF leads to the activation of Nrf2 and the downstream effectors, such as HO-1, GCLC, and GPX. Specifically, DMF induced an increase in GSH content as well as levels of Nrf2 and its target genes (i.e., HO-1 and HQO1) in a murine model of dextran sulphate sodium (DSS)-induced colitis [41]. The DMF-mediated increases in Nrf2 and HO-1 levels were also observed in the ileum of a rat model of experimental autoimmune neuritis [59] and in the intestine of an ischemia/reperfusion injury rat model [60], respectively. Additionally, oral administration of DMF in the DSS-induced colitis model led also to a reduction in weight loss, colon length shortening and tissue damage. Furthermore, DMF promoted an increase in GSH levels, as well as suppression of interleukin-1β (IL-1β), tumor necrosis factor-α (TNF-α), and IL-6 at both the mRNA and protein level. The described decrease in caspase-1 and NLR family pyrin domain containing 3 (NLRP3) seems to be caused by the reduction of mitochondrial ROS (mROS) and mitochondrial DNA (mtDNA) release [41], all consistent with DMF's antioxidant properties. In the experimental autoimmune neuritis model, DMF was able to reduce mRNA levels of Toll-like receptor 4 (TLR4), interferon-γ (IFN-γ), and forkhead fox P3 (FoxP3) in the intestinal lamina propria. Moreover, the authors described an increase in CD4+CD25+ regulatory T-cells in Peyer's patches [59]. Similar results were also obtained in the intestinal ischemia/reperfusion model, in which the DMF reduced the levels of IL-1β, TNF-α, MPO, iNOS, P-selectin, caspase-3, and glycogen synthase kinase-3β (GSK-3β). A decrease in NF-κB was also detected, suggesting a concomitant Nrf2-independent mechanism of DMF in this model [60]. Protection against hemorrhagic diarrhea and weight loss was demonstrated also in a model of colitis induced by dinitrobenzene sulphuric acid (DNBS). Again, DMF prevents the increase in MPO, TNF-α, and intercellular adhesion molecule-1 (ICAM-1) [58]. Similar outcomes were reported also in two additional studies, one based on DSS-induced colitis and the other one on necrotizing enterocolitis induced by hypoxia and lipopolysaccharide (LPS). Particularly, in the former study, DMF reduced the weight loss and the abdominal distension associated with diarrhea. The intestinal damage reduction relied mainly on the decrease in IL-1β, TNF-α, IL-6, NF-κB, TLR-4, Bcl-2-associated X protein (BAX), and effector caspases [61]. The latter study described the beneficial effects of DMF oral administration, which led to a reduction in intestinal length shortening and cyclooxygenase-2 (COX-2) levels as well as an increase in the antioxidant enzymes glutamate-cysteine ligase catalytic subunit (GCLC) and glutathione peroxidase (GPX) [62].

The Nrf2-independent beneficial effects of DMF were observed in a murine model of postoperative ileus obtained through intestinal manipulation (IP). In this experiment, either intragastric or intraperitoneal DMF administration prevented the delay in transit after IP, lymphocyte infiltration, activation of NF-κB and extracellular signal-regulated kinases 1/2 (Erk1/2), and it reduced IL-6 levels [63]. The anti-inflammatory effect of DMF due to impairment of NF-κB signaling was observed also in the DNBS-induced colitis model together with a substantial increase in Mn-superoxide dismutase [58]. Ethyl pyruvate, a redox analog of DMF, exerted similarly beneficial effects in a murine model of colitis, leading to the improvement of symptoms and a decrease in high mobility group box 1 (HMGB1), a key mediator of inflammation [64]. These results were also corroborated in a murine model of MS, in which ethyl fumarate reduced the number of active T cells, antigen presenting

cells (APCs), and Th1/Th17-related molecules in mesenteric lymph nodes and Peyer's patches [65]. DMF's beneficial effects were also demonstrated in other pathological contexts featured by the presence of mycotoxins or intestinal infections. Specifically, DMF promoted the growth and morphology of the intestinal mucosa of BALB/c mice, also improving the intestinal barrier and microbiota [66]. Furthermore, DMF reduced intestinal inflammation in a mouse model of DSS-induced colitis infected with Citrobacter rodentium [67]. Despite the encouraging results in animal models, in a study by Buscarinu and colleagues [68] conducted on 25 RRMS patients, the effects of DMF on gut alterations were variable and characterized by no longitudinal pattern.

Notably, DMF was able to protect gastric mucosa in a dose-dependent manner in a model of ethanol-induced gastric ulcers, suggesting possible applications also for the treatment of stomach disorders. The effect was similar to that exerted by omeprazole [69]. These findings were also corroborated by Sangineto and colleagues [70].

Table 1 reports all of the cited papers and their most relevant findings.

Table 1. Published papers (in chronological order) reporting the beneficial effects of DMF and related molecules in different models of GI disorders.

Author and Year	Molecule	Type of Study	Model	Described Effects
Pereira et al., 1994 [52]	DMF	In vitro	Fisher rats (ACF model)	↓ ACF
Munday et al., 1999 [53]	DMF	In vivo	Sprague-Dawley rats (treated with naphthoquinone)	↑ DT-diaphorase
Kirlin et al., 1999 [56]	DMF	In vitro	HT-29 cells	↑ Apoptosis
Begleiter et al., 2003 [54]	DMF	In vivo	Sprague-Dawley rats (ACF model)	↑ NQO1, GST; No effects on UGT
Davé et al., 2009 [64]	EP	In vivo/in vitro	Murine IL-10 KO chronic colitis model, murine macrophages	↑ HMGB1, HO-1; ↓ RAGE, IL-12p40, NO, NF-κB DNA binding
Xie et al., 2015 [57]	DMF	In vitro	CT-26, HT-29, HCT-116, and SGC-7901 cells	↓ GSH, viability; ↑ JNK, p38, Erk1/2, autophagy markers
Liu et al., 2016 [41]	DMF	In vivo/in vitro	DSS-induced colitis model (wt or *Nrf2*$^{-/-}$ C57BL/J mice) Bone marrow cells Human THP-1 cells	↓ Body weight loss, colon shortening, MPO, iNOS, IL-1β, TNF-α, IL-6, caspase-1, NLRP3, mROS, mtDNA release; ↑ GSH, Nrf2
Casili et al., 2016 [58]	DMF	In vivo/in vitro	Experimental colitis (IL-10KO and wt mice, CD-1 mice treated with DNBS)	↓ Body weight loss, diarrhea, colon damage, MPO, TNF-α, ICAM-1; ↑ Mn-SOD, ZO-1, HO-1 impairment of NF-κB
Djedović et al., 2017 [65]	EP	In vivo	EAE mouse model	↓ T cells, APCs, Th1/Th17-related molecules in mesenteric lymph nodes and Peyer patches
Ma et al., 2017 [66]	DMF	In vivo	BALB/c mice	↑ Growth and morphology of intestinal mucosa; ↓ IEB permeability, mycotoxins
Kaluzki et al., 2019 [55]	DMF	In vitro	HT-29 and T84 cells	↓ Proliferation, cyclin D1, CDK4; ↑ p21, autophagy and apoptotic markers
Pitarokoili et al., 2019 [59]	DMF	In vivo/ex vivo	Experimental autoimmune neuritis (Lewis rats)	↓ *TLR-4* and *IFN-γ* mRNA; ↑ *Nrf2*, *HO-1*, and *FoxP3* mRNA; regulatory T cells in Peyer patches
Li et al., 2020 [62]	DMF	In vivo	DSS-induced colitis model	↓ Colon shortening, inflammation, COX-2; ↑GCLC, GPX

Table 1. *Cont.*

Author and Year	Molecule	Type of Study	Model	Described Effects
Van Dingenen et al., 2020 [63]	DMF	In vivo	Post-operative ileus model (C57BL/J mice under IM)	↓ Delayed transit; ↓ IL-6, lymphocyte infiltration, Erk-1/2, NF-κB
Sangineto et al., 2020 [70]	DMF	In vivo	Ethanol-induced gastric ulcer model	Protection against gut barrier dysfunction and LPS translocation
Gendy et al., 2021 [60]	DMF	In vivo	Ischemia/reperfusion model (Wistar rats)	↑ Nrf2, HO-1, Bcl-2; ↓ GSK-3β, MDA, iNOS, NF-κB, MPO, TNF-α, IL-1β, P-selectin, caspase-3
Buscarinu et al., 2021 [68]	DMF	Observational study	MS patients	Variable effects on gut barrier alterations
Patel et al., 2022 [69]	DMF	In vivo	Ethanol-induced gastric ulcer model	↓ Thiobarbituric acid reactive substance levels; protection against ulcers
Mi et al., 2023 [61]	DMF	In vivo	Necrotizing enterocolitis (C57BL/J mice treated with hypoxia and LPS)	↓ Weight loss, diarrhea, IL-6, IL-1β, TNF-α, TLR-4, NF-κB, Bax, caspase 3/9; ↑ Bcl-2
Chen et al., 2023 [67]	DMF	In vivo	DSS-induced colitis or *C. rodentium* infection	↓ Intestinal inflammation, gasdermin D-induced pyroptosis of IELs

2.2. Dimethyl Fumarate's Effects on Gut Microbiota

It is well known that, before its use as a drug in clinics, DMF was employed as a fungicide in the textile industry. Of interest, DMF is able to positively modulate the intestinal flora. One of the first pieces of evidence regarding the effects of DMF on the gut microbiota came from a study by Eppinga and colleagues [71]. Specifically, the authors demonstrated that DMF treatment in psoriasis patients was able to increase the levels of *Saccharomyces cerevisiae* in the intestine, as revealed by the analysis of fecal samples. Notably, DMF promotes the growth of this yeast also in vitro. Accordingly, DMF-related GI side effects may be induced by alterations in intestinal microbiota caused by the treatment itself. Indeed, an abnormal increase in *S. cerevisiae* levels may contribute to GI symptoms associated with DMF treatment. Yeast/fungal overgrowth can lead to infection and, in the worst cases, fungemia. Although *S. cerevisiae* is a safe yeast, its increase can generate opportunistic infections of the intestine, which are characterized by symptoms resembling those occurring after DMF treatment (e.g., abdominal pain, diarrhea, vomiting) [72–75]. The biological action of DMF on microorganisms was also demonstrated through in vitro experiments using *Clostridium perfringens*. This bacterium is associated with MS, inducing new lesions due to the tropism for the blood–brain barrier and myelin of the CNS. DMF, like other Michael acceptors (e.g., α,β-unsaturated carbonyl compounds and their derivatives), is able to inhibit C. perfringens and the release of the associated toxin [76]. Gene sequence analysis of 16 rRNA in BALB/c mice demonstrated that DMF increased the amount and diversity of the intestinal bacteria, thus promoting micro-ecologic stability as well as a positive impact on intestinal biodiversity. Notably, DMF promoted bacteria belonging to taxa associated with intestinal health, such as those producing short chain fatty acids (e.g., *Bacillus* and *Bacteroides*) [66]. In another murine model, DMF-induced gut microbiota alterations led to an increase in some bacteria (e.g., butyrate-producing *Faecalibacterium*), an effect that is associated with an improvement in memory performance due to Nrf2/ARE system induction in the hippocampus [77]. Conversely, this molecule seemed not to alter the mycobiome, although there is only one paper demonstrating no effects, however, with a limited sampling size [78]. A study conducted on 168 RRMS patients showed that DMF altered the microbiota composition: particularly, the treatment led to a decrease in *Clostridiales*, *Lachnospiraceae*, and *Veillonellacease* as well as in the phyla Firmucutes and Fusobacteria. Conversely, an increase in the phylum Bacterioidetes was

detected [79]. Another study based on 36 RRMS patients showed no differences in human gut microbiota after delayed-release DMF treatment; however, a decreasing trend in Actinobacteria was observed after 2 weeks, whereas an increasing trend in Firmicutes (i.e., *Faecalibacterium*) was detected after 12 weeks [80]. The decrease in Clostridium after DMF treatment was confirmed by another study even at 6 months after drug suspension [81]. Again, DMF-related GI side effects were associated with concomitant intestinal dysbiosis. Specifically, patients that experienced GI symptoms were characterized by an increase in *Streptococcus, Haemophilus, Clostridium* and other bacteria as well as by a reduction in *Bacteroidetes*, *Akkermansia* and other Proteobacteria families [81]. Notably, DMF treatment led to a decrease in MS-associated pro-inflammatory taxa, such as *Akkermansia muciniphilia* and *Coprococcus eutactus*, and an increase in anti-inflammatory species, such as *Lactobacillus pentosus*. Interestingly, lymphopenia that developed in patients during DMF treatment was associated with the presence of *A. muciniphilia* and the concomitant absence of *Prevotella copri*, suggesting a crosstalk between these two taxa, with *P. copri* able to mitigate the effects of *A. muciniphilia* [82].

Table 2 reports literature regarding DMF-mediated gut microbiota alterations.

Table 2. Literature studies (in chronological order) reporting the effects of DMF on gut micro- and mycobiota.

Author and Year	Molecule	Type of Study	Model	Described Effects
Eppinga et al., 2017 [71]	DMF	In vivo/in vitro	Fecal samples from psoriasis patients; *S. cerevisiae*	↑ *S. cerevisiae* in DMF-treated patients
Rumah et al., 2017 [76]	DMF	In vitro	*C. perfringens*	↓ Growth
Ma et al., 2017 [66]	DMF	In vivo	BALB/c mice	↑ Growth and morphology of intestinal mucosa; ↓ IEB permeability, mycotoxins
Katz Sand et al., 2018 [79]	DMF	Observational study	MS patients	↓ *Lachnospiraceae*, *Veillonellaceae*, Firmicutes, Fusobacteria, Clostridiales; ↑ Bacteroidetes
Storm-Larsen et al., 2019 [80]	DMF	Observational study	MS patients	Reduced trend of Actinobacteria, ↑ Firmicutes (*Faecalibacterium*)
Sadnovnikova et al., 2021 [77]	DMF	In vivo	C57BL/J mice	↑ Mitochondrial biogenesis, mitophagy, Nrf2/ARE pathway; modification of gut microbiota
Shah et al., 2021 [78]	DMF	Observational study	MS patients	No changes in gut mycobiota
Diebold et al., 2022 [82]	DMF	Observational study	MS patients	↓ *Akkermansia muciniphilia* and *Coprococcus eutactus*; ↑ *Lactobacillus pentosus*
Ferri et al., 2023 [81]	DMF	Observational study	MS patients	↓ Clostridium; ↑ *Streptococcus*, *Haemophilus*, *Clostridium*, *Lachnospira*, *Blautia*, *Subdoligranulum* and ↓ *Bacteroidetes*, *Barnesiella*, *Odoribacter*, *Akkermansia* in patients with side effects

3. Intestinal Disorders as Targets of DMF

In accordance with the findings summarized in the previous sections, we hypothesized that DMF administration might represent a valuable approach to counteract inflammatory bowel diseases (IBDs) and celiac disease (CeD). The repurposing of DMF in the treatment

of these intestinal pathologies relies on their pathogenetic mechanisms, involving cellular types in which beneficial effects of DMF have been already described.

3.1. Inflammatory Bowel Diseases (IBDs)

Inflammatory bowel disease is a general term that refers to two chronic and systemic disorders mainly affecting the intestine, specifically Crohn's disease (CD) and ulcerative colitis (UC). Since 1990, the incidence of IBDs has increased worldwide, with a frequency in Western countries of 0.3% [83]. Despite the similarities in their clinical manifestations, CD and UC involve different parts of the human gut, with CD affecting intestine, stomach and/or esophagus, and UC being localized primarily in the colon. Furthermore, the histopathological hallmarks of these two disorders are different: CD is characterized by damaged mucosa, granulomas, and transmural inflammation, and UC by mucosal and submucosal inflammation, mainly localized in the crypts (e.g., cryptitis and abscesses) [84–88]. The differences in the clinical manifestations of CD and UC are still unclear; however, it has been hypothesized that they may rely on distinct molecular triggers (antigens/dietary particles for CD and bacteria for UC, respectively) as well as on the different immune cells recruited in the affected area (macrophages for CD and neutrophils for UC) [89]. IBD is a syndrome characterized by a plethora of symptoms ranging from abdominal pain, diarrhea, and weight loss to infiltration of neutrophils and macrophages with consequent production of pro-inflammatory cytokines [85,86]. The onset of IBDs depends on different genetic, epigenetic, and environmental factors. Genome-wide association studies (GWAS) as well as next-generation sequencing studies (NGS) led to the identification of up to 200 genes specifically associated with CD and UC. These susceptibility genes are involved in epithelial barrier homeostasis, innate and adaptive immune modulation, cell migration, autophagy, and other relevant cellular pathways [87,90,91]. Notably, both CD and UC are associated with gut microbiota alterations, which seem to contribute to the onset of IBDs [85,86]. The relevance of intestinal dysbiosis in the pathogenesis of CD and UC has been confirmed also by the potential of fecal microbiota transplantation (FMT) as a therapeutic approach [92–94].

CD and UC pathogeneses present both similarities and differences. Briefly, CD comprises a persistent immune response against luminal antigens produced by both micro- and mycobiota. One of the key leading events is the altered secretion of mucus by Paneth cells; indeed, changes in the expression of genes involved in mucus production, such as *the nucleotide-binding oligomerization domain-containing protein 2* (*NOD2*, also known *CARD15*), the *authophagy related 16 like 1* (*ATG16L1*), *the immunity related GMPase M* (*IRGM*), and the *leucine rich repeat kinase 2* (*LRRK2*) [91,92], have been reported. Polymorphisms in *NOD2* as well as in genes belonging to NF-κB promote epithelial barrier dysfunction, thus leading the luminal content to reach the *lamina propria*. Consequently, antigen presenting cells (APCs) release cytokines (e.g., IL-12, IL-23, and IFN-γ) that lead to the hyperactivation of pro-inflammatory T cells, inducing mainly a Th1 phenotype. These cytokines are also able to activate natural killer (NK) cells, which contribute to sustained intestinal inflammation. In this scenario, IL-4, IL-6 and IL-21 also play key roles in maintaining the inflammatory response [95,96]. Conversely, UC is characterized by a Th2-mediated inflammatory response after intestinal mucosal damage. Moreover, recently, a novel subset of T cells, Th9, was identified; Th9 cells are responsible for the release of IL-9, thus interfering with the mechanisms of tissue repair and intestinal barrier functionality [86]. The current IBD treatments are based on aminosalicylates, corticosteroids, and immunomodulators [97].

3.2. Celiac Disease

Celiac disease (CeD), also referred to as celiac sprue or gluten-sensitive enteropathy, is a serious immune-mediated condition belonging to the family of gluten-related disorders (GRDs). CeD affects genetically predisposed individuals in which the ingestion of gluten leads to several intestinal and extra-intestinal symptoms (e.g., anemia, fatigue, infertility, osteoporosis, neurologic disorders, and dermatitis herpetiformis). Currently,

it is estimated that CeD affects 1% of people worldwide, although only one in 6 people are correctly diagnosed. CeD is associated with several comorbidities, and untreated or undiagnosed forms are usually characterized by severe long-term effects and consequences for the general health of diseased individuals [98]. CeD is triggered by the ingestion of gluten, a complex mixture of protein storage present in the mature seed endosperm of grains of the Triticeae group (i.e., wheat, barley and rye) and all of their hybrids (i.e., spelt, Kamut and triticale) [99]. Specifically, the pathogenic mechanism is linked to gliadin, the cytotoxic alcohol-soluble component of gluten [98]. In CD patients, ingestion of gluten leads to an abnormal response of the innate and adaptive immune system and, therefore, to the generation of an inflammatory environment characterized by the presence of lymphocyte infiltration in the epithelium and villous atrophy. The first effect of gliadin at the intestinal level is the increase in gut permeability through the zonulin release [100]. Once in the lamina propria, gluten peptides are modified by the enzymatic activity of extracellular transglutaminase 2 (TG2, TGM2), whose levels and activity are raised after tissue injury, thus increasing their binding affinity to HLA-DQ2/DQ8 molecules [101,102]. Dendritic cells (DCs) present gliadin peptides to CD4+ naïve T cells, thus promoting the repertoire expansion of gluten-specific Th1/Th17 pro-inflammatory T cells, with a concomitant production of IFN-γ, TNF-α, IL-18 and IL-21 [103–105]. INF-γ production increases the number of CD8+ TRC$\alpha\beta$+ and TCR$\gamma\delta$+ intraepithelial lymphocytes (IELs) with innate-like lymphokine-activated killer (LAK) activities. At the same time, intestinal epithelial cells (IECs) over-express the ligands of these receptors, respectively MICA and HLA-E, in response to the stress caused by IL-15 release. The interaction between IELs and IECs mediated by their receptors and ligands produces the release of IFN-γ and cytolysis, thus leading to tissue damage. CD4+ T cells can also interact with B cells, promoting their maturation, thus favoring the production of specific anti-TG2 and anti-gliadin antibodies [104]. Currently, the only effective therapy is a gluten-free diet (GFD) [98].

4. Rationale for DMF Repurposing in Intestinal Pathologies

The repurposing of DMF in the treatment of intestinal disorders firstly relies on its Nrf2-dependent mechanism of action. Indeed, Nrf2 plays a key role in enterogenesis, as demonstrated by in vivo studies [106,107]. As already reviewed by Piotrowska and colleagues [108], the Nrf2 pathway is involved in intestinal protection and in the maintenance of intestinal epithelial barrier homeostasis [109,110]. In vivo experiments demonstrate that Nrf2 knockout leads to an increased susceptibility to inflammation and oxidative stress damage in DSS-induced colitis mouse models [111]. The importance of a fine modulation of Nrf2 for gut homeostasis was confirmed by another in vivo study in which Nrf2 overexpression led to a worsening of the inflammatory status in a model of acute colitis [112]. The protective role of Nrf2 was also demonstrated in the context of CeD. Particularly, wheat germ peptides exerted a beneficial role in an in vitro model of CeD through the activation of the Nrf2 pathway [113]; moreover, resveratrol, a well-known Nrf2 inducer, led to a reduction in oxidative stress and epithelial cell damage in in vitro and in vivo CeD models [114]. Similar results were also obtained in a gliadin-induced enteropathy mouse model using conjugated linoleic acid [115]. Notably, 5-aminosalicylic acid (5-ASA), a drug used for the treatment of IBDs, in its oxidized form is able to induce the Nrf2 pathway, thus promoting an anti-inflammatory response [116]. Considering the pathogenesis of IBDs and CeD, the immunomodulatory properties of DMF (reviewed by [117]) or similar compounds might play a beneficial role by reducing inflammation, promoting a more tolerogenic phenotype in APCs [118], or inhibiting T cell maturation and activation [119].

Gut homeostasis is strongly affected by the enteric nervous system (ENS), in particular through the functions of enteric neurons (ENs) and enteric glial cells (EGCs). Considering the beneficial modulatory effects exerted by DMF in these two cell types (i.e., neurons and glial cells), the rationale for DMF repurposing in gut diseases may rely on enteric neuron/glia neuroprotection. As widely discussed in the literature, the ENS plays an essential role in the maintenance of intestinal health. Particularly, under physiological conditions, the

crosstalk among IEC, EGCs, and ENs regulates the correct intestinal epithelial barrier function as follows: (1) EGCs secrete pro-epidermal growth factor (pro-EGF), glial-derived neurotrophic factor (GDNF), S-nitrosoglutathione (GSNO), TGF-β, 15-Hydroxyeicosatetraenoic acid (15-HETE), and 15-deoxy-delta-12,14-prostaglandin J2 (15d-PGJ2); (2) ENs release acetylcholine (ACh), vasoactive intestinal peptide (VIP), neuropeptide Y (NPY) and other factors; (3) IECs secrete mucus and antimicrobial peptides (AMPs) as protection. Inflammatory conditions or environmental stressors lead to the induction of reactive glia, with the consequent secretion of nitric oxide (NO), S100 calcium-binding protein B (S100β), nerve growth factor (NGF), IL-1β and IL-6. Under stress (i.e., inflammation, oxidative stress, infection), neurons also contribute to dysfunction of the intestinal epithelial barrier, for example, through the corticotropin-releasing factor (CRF) [120,121]. Due to the plethora of cellular functions exerted by EGCs, some disorders have been reconsidered by placing these cells at the center of attention, as in the case of CD, which can be classified as a gliopathy, as suggested by Pochard and colleagues [122]. A possible involvement of EGCs in the pathogenesis of CeD was also hypothesized by Esposito and colleagues [123], who demonstrated that CeD patients are characterized by an increased number of EGCs in the duodenum, showing an up-regulation of S100β, iNOS gene expression and NO. Furthermore, this enteric glia response, compatible with a reactive phenotype, seems to be directly induced by gliadin.

Enteric glia may represent the principal target for DMF-mediated modulation of the ENS. Indeed, the induction of the ARE elements in the central nervous system (CNS) is restricted to astroglial cells instead of neurons [124]; furthermore, DMF leads to a decrease in inflammatory mediators after Nrf2 activation, as demonstrated in vitro and in vivo [125–128].

DMF-mediated modulation of the gut microbiota/mycobiota in IBDs or CeD may be attractive, considering that dysbiosis is associated with these intestinal disorders [129–134]. Beneficial effects of DMF in gut micro- and mycobiota may contribute to the resolution of dysbiosis and the rescue of taxa involved in intestinal health. Figure 3 summarizes the beneficial effects of DMF in different cellular targets in the context of intestinal disorders (e.g., CD).

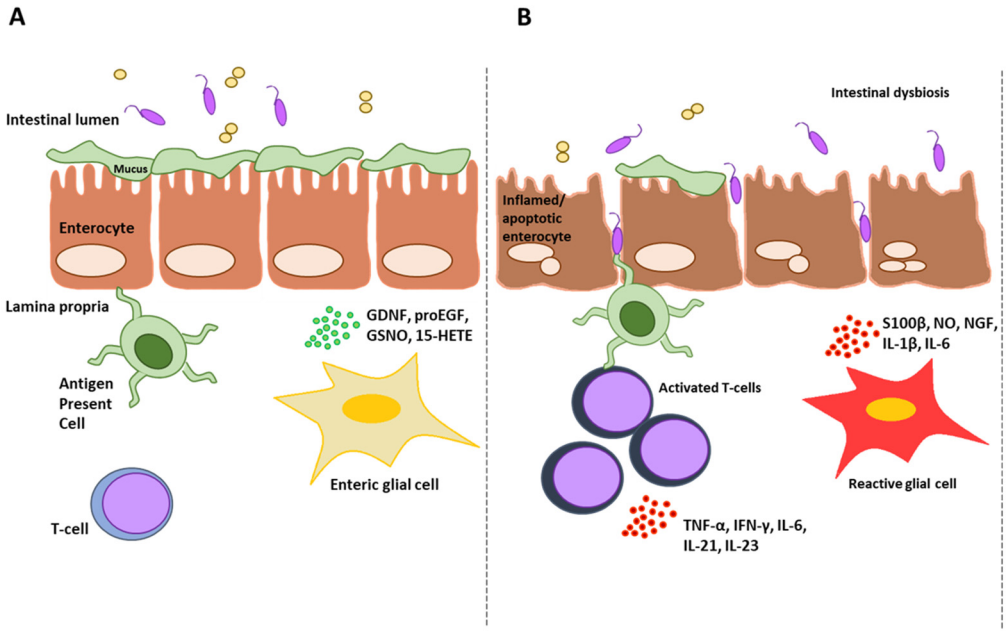

Figure 3. Cont.

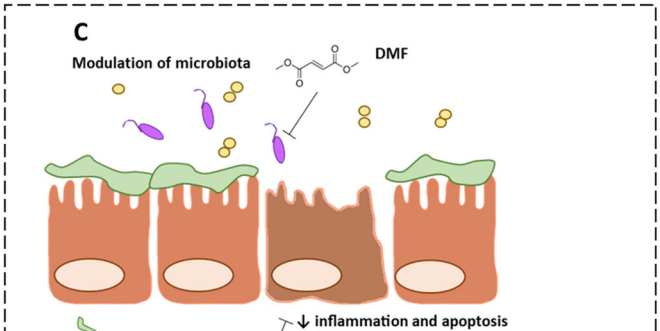

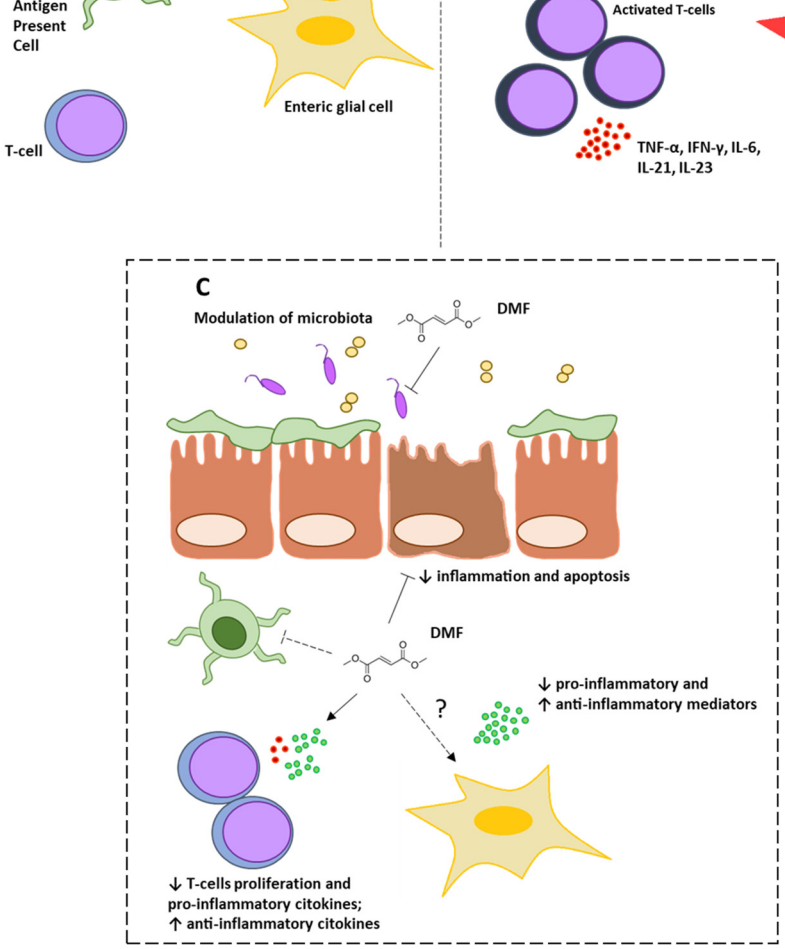

Figure 3. Schematic representation of DMF's beneficial effects in the context of intestinal disorders (e.g., CD). Panels (**A**) and (**B**) show the physiological and pathological intestinal mucosa with the main cellular protagonists. Panel (**C**) summarizes the beneficial effects of DMF on the different cellular targets. Briefly, DMF can modulate the gut microbiota, favoring an increase in taxa associated with healthy intestinal mucosa. Moreover, DMF is also able to induce a more tolerogenic phenotype in antigen presenting cells (APCs). The anti-inflammatory effects of this molecule target enterocytes as well as T-cells, whose proliferation and secretion of pro-inflammatory cytokines are inhibited. As hypothesized in the previous paragraph, DMF could exert positive effects also on the cellular components of the enteric nervous system (ENS), specifically enteric glial cells (EGCs).

5. Other Considerations for DMF-Based Approaches in Intestinal Disorders

All of the evidence collected in this review highlighted that DMF might be useful in treating intestinal disorders. In recent years, modulation of the Nrf2 pathway has received more and more attention, especially regarding IBDs. Different studies described the beneficial effects of Nrf2/Keap1/ARE signaling modulation in some models of gut diseases. Particularly, it has been reported that mesenchymal stem cells (MSCs) promote intestinal healing by regulating Nrf2 [135]. Notably, other molecules also exert similar effects, such as epoxymicheliolide (EMCL) [136], carnosic acid [137], melianodiol [138], miconazole [139], sulphorafane (SFN), polyphenols and proanthocyanidin extracts [140–142]. However, compared to all of these molecules, DMF has the advantage of being well characterized and already approved by the FDA for clinical applications. The adverse effects described for DMF (e.g., nausea, vomiting, abdominal pain, and diarrhea) are caused by the levels of methanol produced during its metabolism as well as possible alterations in gut microbiota. These symptoms are common and attributable to many intestinal diseases; considering these premises, monitoring by physicians is needed to avoid the risk of misdiagnosis. A case report by Wilkinson described a patient affected by psoriasis experiencing several GI disorders that were initially ascribed to Fumaderm®. The onset of microcytic anemia led to the correct diagnosis of colon cancer and partial obstruction [143], thus underling the importance of accurate patient follow-up and management, especially considering the wide spectrum of GI side effects characterizing DMF treatment. Despite these concerns, it is necessary to underline that the GI symptoms caused by DMF are reversible and can be managed through the modulation of therapeutic doses/timing of administration, without necessarily compromising its beneficial effects, as demonstrated in a case report by Kofler

and colleagues [144] involving an 88-year-old woman affected by cystoid macular edema. Considering the fact that DMF is completely metabolized in the intestine, treating gut disorders using lower doses of DMF compared to those commonly used for other pathologies may represent a good strategy, since the effect would be local. In addition, a low dose of DMF may lead to a sub-toxic amount of methanol, the main cause of DMF-induced gut irritation. Another strategy might be the direct use of MMF, which is characterized by better GI tolerability and exerts protective effects against gastric ulcerations [145,146], although several studies in the literature in different contexts underline the higher efficacy of DMF compared to MMF [147,148]. DMF seems to be stable from hydrolysis at low pH. This likely means that in the stomach (~1.5/2 pH), DMF may exert its beneficial effects directly, in the absence of conversion into MMF. This aspect may represent an advantage since, as mentioned, methanol is produced after DMF catabolism. However, it is necessary to remember that, currently, the available formulations of DMF are gastro-resistant tablets. Derivatives of DMF, such as diroximel fumarate (DRF) or HYCO-3, which showed a reduced GI toxicity [149,150], might represent additional alternative strategies to avoid the onset of GI symptoms in susceptible individuals without reducing the immunomodulating and anti-inflammatory response. Notably, considering the role of trefoil factor (TFF) peptides and tight junctions (TJs) in intestinal mucosa homeostasis and damage response [151–153], DMF might restore the physiological levels of these molecules in GI inflammatory contexts. Particularly, the levels of TFF peptides (mainly expressed in the gastric glands and goblet cells) are dysregulated in pathological conditions: for instance, TFF3 is up-regulated in gastric ulcers, and *tff3*$^{-/-}$ mice are more susceptible to colitis after DSS administration [152]. Up-regulation of TFF3 is associated with many gastric and colon cancers; accordingly, the possible rescue of its physiological levels by DMF might also exert long-term protection, thus preventing the onset of these pathologies. Considering that Nrf2-inducing phytochemicals are able to increase the levels of hepcidin [154], DMF might also affect the expression of this important factor.

6. Conclusions

DMF is an effective drug already approved for psoriasis and RRMS. The growing evidence of the beneficial effects of DMF in vivo on the intestine encourages its repurposing for the treatment of GI disorders.

In conclusion, the conceptualization of novel DMF-based therapeutic approaches in intestinal diseases merits more consideration and a careful analysis by the scientific community.

Author Contributions: Conceptualization, F.M. and M.A.; writing—original draft preparation, F.M.; writing—review and editing, L.Z., D.A., S.G.D.M., A.G., S.C. and M.A.; supervision, S.C. and M.A. All authors have read and agreed to the published version of the manuscript.

Funding: This research received no external funding.

Institutional Review Board Statement: Not applicable.

Informed Consent Statement: Not applicable.

Data Availability Statement: Not applicable.

Acknowledgments: This research was supported by the Italian Ministry of Education, University and Research (MIUR): Dipartimenti di Eccellenza Program (2018–2022), Dept. of Biology and Biotechnology "L. Spallanzani", University of Pavia.

Conflicts of Interest: The authors declare no conflict of interest.

References

1. Saidu, N.E.B.; Kavian, N.; Leroy, K.; Jacob, C.; Nicco, C.; Batteux, F.; Alexandre, J. Dimethyl fumarate, a two-edged drug: Current status and future directions. *Med. Res. Rev.* **2019**, *39*, 1923–1952. [CrossRef] [PubMed]
2. Eleni, K.; Michalis, S.C.; Patrickios, C.S. Group transfer polymerization of biobased monomers. *Eur. Polym. J.* **2013**, *49*, 761–767.
3. Love, B.E.; Bennett, L.J. Two approaches to the synthesis of dimethyl fumarate that demonstrate fundamental principles of organic chemistry. *J. Chem. Educ.* **2017**, *94*, 1543–1546. [CrossRef]

4. Kees, F. Dimethyl fumarate: A Janus-faced substance? *Expert. Opin. Pharm.* **2013**, *14*, 1559–1567. [CrossRef] [PubMed]
5. Schulze-Topphoff, U.; Varrin-Doyer, M.; Pekarek, K.; Spencer, C.M.; Shetty, A.; Sagan, S.A.; Cree, B.A.; Sobel, R.A.; Wipke, B.T.; Steinman, L.; et al. Dimethyl fumarate treatment induces adaptive and innate immune modulation independent of Nrf2. *Proc. Natl. Acad. Sci. USA* **2016**, *113*, 4777–4782. [CrossRef]
6. Peng, H.; Li, H.; Sheehy, A.; Cullen, P.; Allaire, N.; Scannevin, R.H. Dimethyl fumarate alters microglia phenotype and protects neurons against proinflammatory toxic microenvironments. *J. Neuroimmunol.* **2016**, *299*, 35–44. [CrossRef]
7. Zhovtis Ryerson, L.; Green, R.; Confident, G.; Pandey, K.; Richter, B.; Bacon, T.; Sammarco, C.; Laing, L.; Kalina, J.; Kister, I. Efficacy and tolerability of dimethyl fumarate in White-, African- and Hispanic- Americans with multiple sclerosis. *Ther. Adv. Neurol. Disord.* **2016**, *9*, 454–461. [CrossRef]
8. Ochi, H.; Niino, M.; Onizuka, Y.; Hiramatsu, K.; Hase, M.; Yun, J.; Matta, A.; Torii, S. 72-Week Safety and Tolerability of Dimethyl Fumarate in Japanese Patients with Relapsing-remitting Multiple Sclerosis: Analysis of the Randomised, Double Blind, Placebo-Controlled, Phase III APEX Study and its Open-Label Extension. *Adv. Ther.* **2018**, *35*, 1598–1611. [CrossRef]
9. Sabin, J.; Urtiaga, S.; Pilo, B.; Thuissard, I.; Galan, V.; Sainz de la Maza, S.; Costa-Frossard, L.; Gómez-Moreno, M.; Díaz-Díaz, J.; Oreja-Guevara, C.; et al. Tolerability and safety of dimethyl fumarate in relapsing multiple sclerosis: A prospective observational multicenter study in a real-life Spanish population. *J. Neurol.* **2020**, *267*, 2362–2371. [CrossRef]
10. Mallucci, G.; Annovazzi, P.; Miante, S.; Torri-Clerici, V.; Matta, M.; La Gioia, S.; Cavarretta, R.; Mantero, V.; Costantini, G.; D'Ambrosio, V.; et al. Two-year real-life efficacy, tolerability and safety of dimethyl fumarate in an Italian multicentre study. *J. Neurol.* **2018**, *265*, 1850–1859. [CrossRef]
11. Litjens, N.H.; Burggraaf, J.; van Strijen, E.; van Gulpen, C.; Mattie, H.; Schoemaker, R.C.; van Dissel, J.T.; Thio, H.B.; Nibbering, P.H. Pharmacokinetics of oral fumarates in healthy subjects. *Br. J. Clin. Pharm.* **2004**, *58*, 429–432. [CrossRef] [PubMed]
12. Rostami-Yazdi, M.; Clement, B.; Schmidt, T.J.; Schinor, D.; Mrowietz, U. Detection of metabolites of fumaric acid esters in human urine: Implications for their mode of action. *J. Investig. Derm.* **2009**, *129*, 231–234. [CrossRef] [PubMed]
13. Rostami-Yazdi, M.; Clement, B.; Mrowietz, U. Pharmacokinetics of anti-psoriatic fumaric acid esters in psoriasis patients. *Arch. Derm. Res.* **2010**, *302*, 531–538. [CrossRef] [PubMed]
14. Werdenberg, D.; Joshi, R.; Wolffram, S.; Merkle, H.P.; Langguth, P. Presystemic metabolism and intestinal absorption of antipsoriatic fumaric acid esters. *Biopharm. Drug. Dispos.* **2003**, *24*, 259–273. [CrossRef]
15. Palte, M.J.; Wehr, A.; Tawa, M.; Perkin, K.; Leigh-Pemberton, R.; Hanna, J.; Miller, C.; Penner, N. Improving the Gastrointestinal Tolerability of Fumaric Acid Esters: Early Findings on Gastrointestinal Events with Diroximel Fumarate in Patients with Relapsing-Remitting Multiple Sclerosis from the Phase 3, Open-Label EVOLVE-MS-1 Study. *Adv. Ther.* **2019**, *36*, 3154–3165. [CrossRef]
16. Litjens, N.H.; van Strijen, E.; van Gulpen, C.; Mattie, H.; van Dissel, J.T.; Thio, H.B.; Nibbering, P.H. In vitro pharmacokinetics of anti-psoriatic fumaric acid esters. *BMC Pharm.* **2004**, *4*, 22. [CrossRef]
17. Dibbert, S.; Clement, B.; Skak-Nielsen, T.; Mrowietz, U.; Rostami-Yazdi, M. Detection of fumarate-glutathione adducts in the portal vein blood of rats: Evidence for rapid dimethylfumarate metabolism. *Arc. Derm. Res.* **2013**, *305*, 447–451. [CrossRef]
18. Canning, P.; Sorrell, F.J.; Bullock, A.N. Structural basis of Keap1 interactions with Nrf2. *Free Radic. Biol. Med.* **2015**, *88 Pt B*, 101–107. [CrossRef]
19. Takaya, K.; Suzuki, T.; Motohashi, H.; Onodera, K.; Satomi, S.; Kensler, T.W.; Yamamoto, M. Validation of the multiple sensor mechanism of the Keap1-Nrf2 system. *Free Radic. Biol. Med.* **2012**, *53*, 817–827. [CrossRef]
20. Unni, S.; Deshmukh, P.; Krishnappa, G.; Kommu, P.; Padmanabhan, B. Structural insights into the multiple binding modes of Dimethyl Fumarate (DMF) and its analogs to the Kelch domain of Keap1. *FEBS J.* **2021**, *288*, 1599–1613. [CrossRef]
21. Kensler, T.W.; Wakabayashi, N.; Biswal, S. Cell survival responses to environmental stresses via the Keap1-Nrf2-ARE pathway. *Annu. Rev. Pharm. Toxicol.* **2007**, *47*, 89–116. [CrossRef] [PubMed]
22. Yamamoto, M.; Kensler, T.W.; Motohashi, H. The KEAP1-NRF2 System: A Thiol-Based Sensor-Effector Apparatus for Maintaining Redox Homeostasis. *Physiol. Rev.* **2018**, *98*, 1169–1203. [CrossRef] [PubMed]
23. Raghunath, A.; Sundarraj, K.; Nagarajan, R.; Arfuso, F.; Bian, J.; Kumar, A.P.; Sethi, G.; Perumal, E. Antioxidant response elements: Discovery, classes, regulation and potential applications. *Redox Biol.* **2018**, *17*, 297–314. [CrossRef] [PubMed]
24. Kim, S.B.; Pandita, R.K.; Eskiocak, U.; Ly, P.; Kaisani, A.; Kumar, R.; Cornelius, C.; Wright, W.E.; Pandita, T.K.; Shay, J.W. Targeting of Nrf2 induces DNA damage signaling and protects colonic epithelial cells from ionizing radiation. *Proc. Natl. Acad. Sci. USA* **2012**, *109*, E2949–E2955. [CrossRef]
25. Jin, S. p53, Autophagy and tumor suppression. *Autophagy* **2005**, *1*, 171–173. [CrossRef]
26. Ni, H.M.; Boggess, N.; McGill, M.R.; Lebofsky, M.; Borude, P.; Apte, U.; Jaeschke, H.; Ding, W.X. Liver-specific loss of Atg5 causes persistent activation of Nrf2 and protects against acetaminophen-induced liver injury. *Toxicol. Sci.* **2012**, *127*, 438–450. [CrossRef]
27. Copple, I.M.; Lister, A.; Obeng, A.D.; Kitteringham, N.R.; Jenkins, R.E.; Layfield, R.; Foster, B.J.; Goldring, C.E.; Park, B.K. Physical and functional interaction of sequestosome 1 with Keap1 regulates the Keap1-Nrf2 cell defense pathway. *J. Biol. Chem.* **2010**, *285*, 16782–16788. [CrossRef]
28. Bae, S.H.; Sung, S.H.; Oh, S.Y.; Lim, J.M.; Lee, S.K.; Park, Y.N.; Lee, H.E.; Kang, D.; Rhee, S.G. Sestrins activate Nrf2 by promoting p62-dependent autophagic degradation of Keap1 and prevent oxidative liver damage. *Cell. Metab.* **2013**, *17*, 73–84. [CrossRef]

29. Jain, A.; Lamark, T.; Sjøttem, E.; Larsen, K.B.; Awuh, J.A.; Øvervatn, A.; McMahon, M.; Hayes, J.D.; Johansen, T. p62/SQSTM1 is a target gene for transcription factor NRF2 and creates a positive feedback loop by inducing antioxidant response element-driven gene transcription. *J. Biol. Chem.* **2010**, *285*, 22576–22591. [CrossRef]
30. Liao, W.; Wang, Z.; Fu, Z.; Ma, H.; Jiang, M.; Xu, A.; Zhang, W. p62/SQSTM1 protects against cisplatin-induced oxidative stress in kidneys by mediating the cross talk between autophagy and the Keap1-Nrf2 signalling pathway. *Free Radic. Res.* **2019**, *53*, 800–814. [CrossRef]
31. Kapuy, O.; Papp, D.; Vellai, T.; Bánhegyi, G.; Korcsmáros, T. Systems-Level Feedbacks of NRF2 Controlling Autophagy upon Oxidative Stress Response. *Antioxidants* **2018**, *7*, 39. [CrossRef]
32. Sun, W.; Yi, Y.; Xia, G.; Zhao, Y.; Yu, Y.; Li, L.; Hua, C.; He, B.; Yang, B.; Yu, C.; et al. Nrf2-miR-129-3p-mTOR Axis Controls an miRNA Regulatory Network Involved in HDACi-Induced Autophagy. *Mol. Ther.* **2019**, *27*, 1039–1050. [CrossRef] [PubMed]
33. Joo, M.S.; Kim, W.D.; Lee, K.Y.; Kim, J.H.; Koo, J.H.; Kim, S.G. AMPK Facilitates Nuclear Accumulation of Nrf2 by Phosphorylating at Serine 550. *Mol. Cell. Biol.* **2016**, *36*, 1931–1942. [CrossRef]
34. Zimmermann, K.; Baldinger, J.; Mayerhofer, B.; Atanasov, A.G.; Dirsch, V.M.; Heiss, E.H. Activated AMPK boosts the Nrf2/HO-1 signaling axis--A role for the unfolded protein response. *Free Radic. Biol. Med.* **2015**, *88 Pt B*, 417–426. [CrossRef] [PubMed]
35. Kornberg, M.D.; Bhargava, P.; Kim, P.M.; Putluri, V.; Snowman, A.M.; Putluri, N.; Calabresi, P.A.; Snyder, S.H. Dimethyl fumarate targets GAPDH and aerobic glycolysis to modulate immunity. *Science* **2018**, *360*, 449–453. [CrossRef] [PubMed]
36. Gillard, G.O.; Collette, B.; Anderson, J.; Chao, J.; Scannevin, R.H.; Huss, D.J.; Fontenot, J.D. DMF, but not other fumarates, inhibits NF-κB activity in vitro in an Nrf2-independent manner. *J. Neuroimmunol.* **2015**, *283*, 74–85. [CrossRef]
37. Loewe, R.; Holnthoner, W.; Gröger, M.; Pillinger, M.; Gruber, F.; Mechtcheriakova, D.; Hofer, E.; Wolff, K.; Petzelbauer, P. Dimethylfumarate inhibits TNF-induced nuclear entry of NF-kappa B/p65 in human endothelial cells. *J. Immunol.* **2002**, *168*, 4781–4787. [CrossRef]
38. Chen, H.; Assmann, J.C.; Krenz, A.; Rahman, M.; Grimm, M.; Karsten, C.M.; Köhl, J.; Offermanns, S.; Wettschureck, N.; Schwaninger, M. Hydroxycarboxylic acid receptor 2 mediates dimethyl fumarate's protective effect in EAE. *J. Clin. Investig.* **2014**, *124*, 2188–2192. [CrossRef]
39. Parodi, B.; Rossi, S.; Morando, S.; Cordano, C.; Bragoni, A.; Motta, C.; Usai, C.; Wipke, B.T.; Scannevin, R.H.; Mancardi, G.L.; et al. Fumarates modulate microglia activation through a novel HCAR2 signaling pathway and rescue synaptic dysregulation in inflamed CNS. *Acta Neuropathol.* **2015**, *130*, 279–295. [CrossRef]
40. Zhao, G.; Liu, Y.; Fang, J.; Chen, Y.; Li, H.; Gao, K. Dimethyl fumarate inhibits the expression and function of hypoxia-inducible factor-1α (HIF-1α). *Biochem. Biophys. Res. Commun.* **2014**, *448*, 303–307. [CrossRef]
41. Liu, X.; Zhou, W.; Zhang, X.; Lu, P.; Du, Q.; Tao, L.; Ding, Y.; Wang, Y.; Hu, R. Dimethyl fumarate ameliorates dextran sulfate sodium-induced murine experimental colitis by activating Nrf2 and suppressing NLRP3 inflammasome activation. *Biochem. Pharm.* **2016**, *112*, 37–49. [CrossRef]
42. Tastan, B.; Arioz, B.I.; Tufekci, K.U.; Tarakcioglu, E.; Gonul, C.P.; Genc, K.; Genc, S. Dimethyl Fumarate Alleviates NLRP3 Inflammasome Activation in Microglia and Sickness Behavior in LPS-Challenged Mice. *Front. Immunol.* **2021**, *12*, 737065. [CrossRef] [PubMed]
43. Zhao, M.; Gönczi, L.; Lakatos, P.L.; Burisch, J. The Burden of Inflammatory Bowel Disease in Europe in 2020. *J. Crohns Colitis* **2021**, *15*, 1573–1587. [CrossRef] [PubMed]
44. Makharia, G.K.; Singh, P.; Catassi, C.; Sanders, D.S.; Leffler, D.; Ali, R.A.R.; Bai, J.C. The global burden of coeliac disease: Opportunities and challenges. *Nat. Rev. Gastroenterol. Hepatol.* **2022**, *19*, 313–327. [CrossRef] [PubMed]
45. Booth, L.; Malkin, M.; Dent, P. Repurposing Tecfidera for cancer. *Aging* **2016**, *8*, 1289–1290. [CrossRef]
46. Lastres-Becker, I.; García-Yagüe, A.J.; Scannevin, R.H.; Casarejos, M.J.; Kügler, S.; Rábano, A.; Cuadrado, A. Repurposing the NRF2 Activator Dimethyl Fumarate as Therapy Against Synucleinopathy in Parkinson's Disease. *Antioxid. Redox Signal.* **2016**, *25*, 61–77. [CrossRef]
47. Ahmadi-Beni, R.; Najafi, A.; Savar, S.M.; Mohebbi, N.; Khoshnevisan, A. Role of dimethyl fumarate in the treatment of glioblastoma multiforme: A review article. *Iran. J. Neurol.* **2019**, *18*, 127–133. [CrossRef]
48. Garcia-Mesa, Y.; Xu, H.N.; Vance, P.; Gruenewald, A.L.; Garza, R.; Midkiff, C.; Alvarez-Hernandez, X.; Irwin, D.J.; Gill, A.J.; Kolson, D.L. Dimethyl Fumarate, an Approved Multiple Sclerosis Treatment, Reduces Brain Oxidative Stress in SIV-Infected Rhesus Macaques: Potential Therapeutic Repurposing for HIV Neuroprotection. *Antioxidants* **2021**, *10*, 416. [CrossRef]
49. Thomas, S.D.; Jha, N.K.; Sadek, B.; Ojha, S. Repurposing Dimethyl Fumarate for Cardiovascular Diseases: Pharmacological Effects, Molecular Mechanisms, and Therapeutic Promise. *Pharmaceuticals* **2022**, *15*, 497. [CrossRef]
50. Manai, F.; Govoni, S.; Amadio, M. The Challenge of Dimethyl Fumarate Repurposing in Eye Pathologies. *Cells* **2022**, *11*, 4061. [CrossRef]
51. Majkutewicz, I. Dimethyl fumarate: A review of preclinical efficacy in models of neurodegenerative diseases. *Eur. J. Pharm.* **2022**, *926*, 175025. [CrossRef] [PubMed]
52. Pereira, M.A.; Barnes, L.H.; Rassman, V.L.; Kelloff, G.V.; Steele, V.E. Use of azoxymethane-induced foci of aberrant crypts in rat colon to identify potential cancer chemopreventive agents. *Carcinogenesis* **1994**, *15*, 1049–1054. [CrossRef] [PubMed]
53. Munday, R.; Smith, B.L.; Munday, C.M. Effect of inducers of DT-diaphorase on the toxicity of 2-methyl- and 2-hydroxy-1,4-naphthoquinone to rats. *Chem. Biol. Interact.* **1999**, *123*, 219–237. [CrossRef] [PubMed]

54. Begleiter, A.; Sivananthan, K.; Curphey, T.J.; Bird, R.P. Induction of NAD(P)H quinone: Oxidoreductase1 inhibits carcinogen-induced aberrant crypt foci in colons of Sprague-Dawley rats. *Cancer Epidemiol. Biomark. Rev.* **2003**, *12*, 566–572.
55. Kaluzki, I.; Hailemariam-Jahn, T.; Doll, M.; Kaufmann, R.; Balermpas, P.; Zöller, N.; Kippenberger, S.; Meissner, M. Dimethylfumarate Inhibits Colorectal Carcinoma Cell Proliferation: Evidence for Cell Cycle Arrest, Apoptosis and Autophagy. *Cells* **2019**, *8*, 1329. [CrossRef]
56. Kirlin, W.G.; Cai, J.; DeLong, M.J.; Patten, E.J.; Jones, D.P. Dietary compounds that induce cancer preventive phase 2 enzymes activate apoptosis at comparable doses in HT29 colon carcinoma cells. *J. Nutr.* **1999**, *129*, 1827–1835. [CrossRef]
57. Xie, X.; Zhao, Y.; Ma, C.Y.; Xu, X.M.; Zhang, Y.Q.; Wang, C.G.; Jin, J.; Shen, X.; Gao, J.L.; Li, N.; et al. Dimethyl fumarate induces necroptosis in colon cancer cells through GSH depletion/ROS increase/MAPKs activation pathway. *Br. J. Pharm.* **2015**, *172*, 3929–3943. [CrossRef]
58. Casili, G.; Cordaro, M.; Impellizzeri, D.; Bruschetta, G.; Paterniti, I.; Cuzzocrea, S.; Esposito, E. Dimethyl Fumarate Reduces Inflammatory Responses in Experimental Colitis. *J. Crohns Colitis* **2016**, *10*, 472–483. [CrossRef]
59. Pitarokoili, K.; Bachir, H.; Sgodzai, M.; Grüter, T.; Haupeltshofer, S.; Duscha, A.; Pedreiturria, X.; Motte, J.; Gold, R. Induction of Regulatory Properties in the Intestinal Immune System by Dimethyl Fumarate in Lewis Rat Experimental Autoimmune Neuritis. *Front. Immunol.* **2019**, *10*, 2132. [CrossRef]
60. Gendy, A.; Soubh, A.; Al-Mokaddem, A.; Kotb El-Sayed, M. Dimethyl fumarate protects against intestinal ischemia/reperfusion lesion: Participation of Nrf2/HO-1, GSK-3β and Wnt/β-catenin pathway. *Biomed. Pharm.* **2021**, *134*, 111130. [CrossRef]
61. Mi, Y.; Xie, X.; Bao, Z.; Xiong, X.; Wang, X.; Zhang, H. Dimethyl fumarate protects against intestine damage in necrotizing enterocolitis by inhibiting the Toll-like receptor (TLR) inflammatory signaling pathway. *Tissue Cell* **2023**, *81*, 102003. [CrossRef] [PubMed]
62. Li, S.; Takasu, C.; Lau, H.; Robles, L.; Vo, K.; Farzaneh, T.; Vaziri, N.D.; Stamos, M.J.; Ichii, H. Dimethyl Fumarate Alleviates Dextran Sulfate Sodium-Induced Colitis, through the Activation of Nrf2-Mediated Antioxidant and Anti-inflammatory Pathways. *Antioxidants* **2020**, *9*, 354. [CrossRef] [PubMed]
63. Van Dingenen, J.; Pieters, L.; Van Nuffel, E.; Lefebvre, R.A. Hemin reduces postoperative ileus in a heme oxygenase 1-dependent manner while dimethyl fumarate does without heme oxygenase 1-induction. *Neurogastroenterol. Motil.* **2020**, *32*, e13624. [CrossRef] [PubMed]
64. Davé, S.H.; Tilstra, J.S.; Matsuoka, K.; Li, F.; DeMarco, R.A.; Beer-Stolz, D.; Sepulveda, A.R.; Fink, M.P.; Lotze, M.T.; Plevy, S.E. Ethyl pyruvate decreases HMGB1 release and ameliorates murine colitis. *J. Leukoc. Biol.* **2009**, *86*, 633–643. [CrossRef] [PubMed]
65. Djedović, N.; Stanisavljevic, S.; Jevtić, B.; Momčilović, M.; Lavrnja, I.; Miljković, D. Anti-encephalitogenic effects of ethyl pyruvate are reflected in the central nervous system and the gut. *Biomed. Pharm.* **2017**, *96*, 78–85. [CrossRef]
66. Ma, N.; Wu, Y.; Xie, F.; Du, K.; Wang, Y.; Shi, L.; Ji, L.; Liu, T.; Ma, X. Dimethyl fumarate reduces the risk of mycotoxins via improving intestinal barrier and microbiota. *Oncotarget* **2017**, *8*, 44625–44638. [CrossRef]
67. Chen, H.; Wu, X.; Sun, R.; Lu, H.; Lin, R.; Gao, X.; Li, G.; Feng, Z.; Zhu, R.; Yao, Y.; et al. Dysregulation of $CD177^{+}$ neutrophils on intraepithelial lymphocytes exacerbates gut inflammation via decreasing microbiota-derived DMF. *Gut Microbes* **2023**, *15*, 2172668. [CrossRef]
68. Buscarinu, M.C.; Gargano, F.; Lionetto, L.; Capi, M.; Morena, E.; Fornasiero, A.; Reniè, R.; Landi, A.C.; Pellicciari, G.; Romano, C.; et al. Intestinal Permeability and Circulating CD161+CCR6+CD8+T Cells in Patients With Relapsing-Remitting Multiple Sclerosis Treated With Dimethylfumarate. *Front. Neurol.* **2021**, *12*, 683398. [CrossRef]
69. Patel, V.; Joharapurkar, A.; Kshirsagar, S.; Patel, M.; Savsani, H.; Patel, A.; Ranvir, R.; Jain, M. Repurposing dimethyl fumarate for gastric ulcer and ulcerative colitis: Evidence of local efficacy without systemic side effect. *Med. Drug. Discov.* **2022**, *16*, 100142. [CrossRef]
70. Sangineto, M.; Grabherr, F.; Adolph, T.E.; Grander, C.; Reider, S.; Jaschke, N.; Mayr, L.; Schwärzler, J.; Dallio, M.; Moschen, A.R.; et al. Dimethyl fumarate ameliorates hepatic inflammation in alcohol related liver disease. *Liver Int.* **2020**, *40*, 1610–1619. [CrossRef]
71. Eppinga, H.; Thio, H.B.; Schreurs, M.W.J.; Blakaj, B.; Tahitu, R.I.; Konstantinov, S.R.; Peppelenbosch, M.P.; Fuhler, G.M. Depletion of *Saccharomyces cerevisiae* in psoriasis patients, restored by Dimethylfumarate therapy (DMF). *PLoS ONE* **2017**, *12*, e0176955. [CrossRef] [PubMed]
72. Herbrecht, R.; Nivoix, Y. *Saccharomyces cerevisiae* fungemia: An adverse effect of Saccharomyces boulardii probiotic administration. *Clin. Infect. Dis.* **2005**, *40*, 1635–1637. [CrossRef] [PubMed]
73. Pérez-Torrado, R.; Querol, A. Opportunistic Strains of *Saccharomyces cerevisiae*: A Potential Risk Sold in Food Products. *Front. Microbiol.* **2016**, *6*, 1522. [CrossRef]
74. Rannikko, J.; Holmberg, V.; Karppelin, M.; Arvola, P.; Huttunen, R.; Mattila, E.; Kerttula, N.; Puhto, T.; Tamm, Ü.; Koivula, I.; et al. Fungemia and Other Fungal Infections Associated with Use of Saccharomyces boulardii Probiotic Supplements. *Emerg. Infect. Dis.* **2021**, *27*, 2090–2096. [CrossRef] [PubMed]
75. Lamps, L.W.; Lai, K.K.; Milner, D.A., Jr. Fungal infections of the gastrointestinal tract in the immunocompromised host: An update. *Adv. Anat. Pathol.* **2014**, *21*, 217–227. [CrossRef] [PubMed]
76. Rumah, K.R.; Vartanian, T.K.; Fischetti, V.A. Oral Multiple Sclerosis Drugs Inhibit the In vitro Growth of Epsilon Toxin Producing Gut Bacterium, *Clostridium perfringens*. *Front. Cell. Infect. Microbiol.* **2017**, *7*, 11. [CrossRef] [PubMed]

77. Sadovnikova, I.S.; Gureev, A.P.; Ignatyeva, D.A.; Gryaznova, M.V.; Chernyshova, E.V.; Krutskikh, E.P.; Novikova, A.G.; Popov, V.N. Nrf2/ARE Activators Improve Memory in Aged Mice via Maintaining of Mitochondrial Quality Control of Brain and the Modulation of Gut Microbiome. *Pharmaceuticals* **2021**, *14*, 607. [CrossRef]
78. Shah, S.; Locca, A.; Dorsett, Y.; Cantoni, C.; Ghezzi, L.; Lin, Q.; Bokoliya, S.; Panier, H.; Suther, C.; Gormley, M.; et al. Alterations of the gut mycobiome in patients with MS. *EBioMedicine* **2021**, *71*, 103557. [CrossRef]
79. Katz Sand, I.; Zhu, Y.; Ntranos, A.; Clemente, J.C.; Cekanaviciute, E.; Brandstadter, R.; Crabtree-Hartman, E.; Singh, S.; Bencosme, Y.; Debelius, J.; et al. Disease-modifying therapies alter gut microbial composition in MS. *Neurol. Neuroimmunol. Neuroinflamm.* **2018**, *6*, e517. [CrossRef]
80. Storm-Larsen, C.; Myhr, K.M.; Farbu, E.; Midgard, R.; Nyquist, K.; Broch, L.; Berg-Hansen, P.; Buness, A.; Holm, K.; Ueland, T.; et al. Gut microbiota composition during a 12-week intervention with delayed-release dimethyl fumarate in multiple sclerosis—A pilot trial. *Mult. Scler. J. Exp. Transl. Clin.* **2019**, *5*, 2055217319888767. [CrossRef]
81. Ferri, C.; Castellazzi, M.; Merli, N.; Laudisi, M.; Baldin, E.; Baldi, E.; Mancabelli, L.; Ventura, M.; Pugliatti, M. Gut Microbiota Changes during Dimethyl Fumarate Treatment in Patients with Multiple Sclerosis. *Int. J. Mol. Sci.* **2023**, *24*, 2720. [CrossRef] [PubMed]
82. Diebold, M.; Meola, M.; Purushothaman, S.; Siewert, L.K.; Pössnecker, E.; Roloff, T.; Lindberg, R.L.; Kuhle, J.; Kappos, L.; Derfuss, T.; et al. Gut microbiota composition as a candidate risk factor for dimethyl fumarate-induced lymphopenia in multiple sclerosis. *Gut Microbes* **2022**, *14*, 2147055. [CrossRef] [PubMed]
83. Ng, S.C.; Shi, H.Y.; Hamidi, N.; Underwood, F.E.; Tang, W.; Benchimol, E.I.; Panaccione, R.; Ghosh, S.; Wu, J.C.Y.; Chan, F.K.L.; et al. Worldwide incidence and prevalence of inflammatory bowel disease in the 21st century: A systematic review of population-based studies. *Lancet* **2017**, *390*, 2769–2778. [CrossRef] [PubMed]
84. Abraham, C.; Cho, J.H. Inflammatory bowel disease. *N. Eng. J. Med.* **2009**, *361*, 2066–2078. [CrossRef] [PubMed]
85. Baumgart, D.C.; Sandborn, W.J. Crohn's disease. *Lancet* **2012**, *380*, 1590–1605. [CrossRef]
86. Ungaro, R.; Mehandru, S.; Allen, P.B.; Peyrin-Biroulet, L.; Colombel, J.F. Ulcerative colitis. *Lancet* **2017**, *389*, 1756–1770. [CrossRef]
87. Khor, B.; Gardet, A.; Xavier, R.J. Genetics and pathogenesis of inflammatory bowel disease. *Nature* **2011**, *474*, 307–317. [CrossRef]
88. Gajendran, M.; Loganathan, P.; Catinella, A.P.; Hashash, J.G. A comprehensive review and update on Crohn's disease. *Dis. Mon.* **2018**, *64*, 20–57. [CrossRef]
89. Qin, X. Why is damage limited to the mucosa in ulcerative colitis but transmural in Crohn's disease? *World J. Gastrointest. Pathophysiol.* **2013**, *4*, 63–64. [CrossRef]
90. Huang, H.; Fang, M.; Jostins, L.; Umićević Mirkov, M.; Boucher, G.; Anderson, C.A.; Andersen, V.; Cleynen, I.; Cortes, A.; Crins, F.; et al. Fine-mapping inflammatory bowel disease loci to single-variant resolution. *Nature* **2017**, *547*, 173–178. [CrossRef]
91. Peters, L.A.; Perrigoue, J.; Mortha, A.; Iuga, A.; Song, W.M.; Neiman, E.M.; Llewellyn, S.R.; Di Narzo, A.; Kidd, B.A.; Telesco, S.E.; et al. A functional genomics predictive network model identifies regulators of inflammatory bowel disease. *Nat. Genet.* **2017**, *49*, 1437–1449. [CrossRef] [PubMed]
92. Zhou, S.; Cui, Y.; Zhang, Y.; Zhao, T.; Cong, J. Fecal microbiota transplantation for induction of remission in Crohn's disease: A systematic review and meta-analysis. *Int. J. Color. Dis.* **2023**, *38*, 62. [CrossRef] [PubMed]
93. van Lingen, E.E.; Baunwall, S.S.M.D.; Lieberknecht, S.S.C.; Benech, N.N.; Ianiro, G.G.; Sokol, H.H.; Gasbarrini, A.A.; Cammarota, G.G.; Eriksen, M.M.K.; van der Meulen-de Jong, A.A.E.; et al. Short- and long-term follow-up after fecal microbiota transplantation as treatment for recurrent *Clostridioides difficile* infection in patients with inflammatory bowel disease. *Ther. Adv. Gastroenterol.* **2023**, *16*, 17562848231156285. [CrossRef] [PubMed]
94. Saleh, A.; Parsa, S.; Garza, M.; Quigley, E.M.M.; Abraham, B.P. The Role of Fecal Microbiota Transplantation in the Induction of Remission in Ulcerative Colitis. *Dig. Dis.* **2023**. [CrossRef]
95. Roda, G.; Chien Ng, S.; Kotze, P.G.; Argollo, M.; Panaccione, R.; Spinelli, A.; Kaser, A.; Peyrin-Biroulet, L.; Danese, S. Crohn's disease. *Nat. Rev. Dis. Prim.* **2020**, *6*, 22. [CrossRef] [PubMed]
96. Petagna, L.; Antonelli, A.; Ganini, C.; Bellato, V.; Campanelli, M.; Divizia, A.; Efrati, C.; Franceschilli, M.; Guida, A.M.; Ingallinella, S.; et al. Pathophysiology of Crohn's disease inflammation and recurrence. *Biol. Direct* **2020**, *15*, 23. [CrossRef] [PubMed]
97. Cai, Z.; Wang, S.; Li, J. Treatment of Inflammatory Bowel Disease: A Comprehensive Review. *Front. Med.* **2021**, *8*, 765474. [CrossRef]
98. Di Sabatino, A.; Corazza, G.R. Coeliac disease. *Lancet* **2009**, *373*, 1480–1493. [CrossRef]
99. Yan, D.; Duermeyer, L.; Leoveanu, C.; Nambara, E. The functions of the endosperm during seed germination. *Plant. Cell. Physiol.* **2014**, *55*, 1521–1533. [CrossRef]
100. Drago, S.; El Asmar, R.; Di Pierro, M.; Grazia Clemente, M.; Tripathi, A.; Sapone, A.; Thakar, M.; Iacono, G.; Carroccio, A.; D'Agate, C.; et al. Gliadin, zonulin and gut permeability: Effects on celiac and non-celiac intestinal mucosa and intestinal cell lines. *Scand. J. Gastroenterol.* **2006**, *41*, 408–419. [CrossRef]
101. Siegel, M.; Strnad, P.; Watts, R.E.; Choi, K.; Jabri, B.; Omary, M.B.; Khosla, C. Extracellular transglutaminase 2 is catalytically inactive, but is transiently activated upon tissue injury. *PLoS ONE* **2008**, *3*, e1861. [CrossRef] [PubMed]
102. Molberg, O.; Mcadam, S.N.; Körner, R.; Quarsten, H.; Kristiansen, C.; Madsen, L.; Fugger, L.; Scott, H.; Norén, O.; Roepstorff, P.; et al. Tissue transglutaminase selectively modifies gliadin peptides that are recognized by gut-derived T cells in celiac disease. *Nat. Med.* **1998**, *4*, 713–717. [CrossRef] [PubMed]

103. Bernardo, D. Human intestinal dendritic cells as controllers of mucosal immunity. *Rev. Esp. Enferm. Dis.* **2013**, *105*, 279–290. [CrossRef] [PubMed]
104. Escudero-Hernández, C.; Peña, A.S.; Bernardo, D. Immunogenetic Pathogenesis of Celiac Disease and Non-celiac Gluten Sensitivity. *Curr. Gastroenterol. Rep.* **2016**, *18*, 36. [CrossRef] [PubMed]
105. Tjon, J.M.; van Bergen, J.; Koning, F. Celiac disease: How complicated can it get? *Immunogenetics* **2010**, *62*, 641–651. [CrossRef]
106. Kopacz, A.; Kloska, D.; Klimczyk, D.; Kopec, M.; Jozkowicz, A.; Piechota-Polanczyk, A. Nrf2 Transcriptional Activity Governs Intestine Development. *Int. J. Mol. Sci.* **2022**, *23*, 6175. [CrossRef]
107. Yagishita, Y.; McCallum, M.L.; Kensler, T.W.; Wakabayashi, N. Constitutive Activation of Nrf2 in Mice Expands Enterogenesis in Small Intestine Through Negative Regulation of Math1. *Cell. Mol. Gastroenterol. Hepatol.* **2021**, *11*, 503–524. [CrossRef]
108. Piotrowska, M.; Swierczynski, M.; Fichna, J.; Piechota-Polanczyk, A. The Nrf2 in the pathophysiology of the intestine: Molecular mechanisms and therapeutic implications for inflammatory bowel diseases. *Pharm. Res.* **2021**, *163*, 105243. [CrossRef]
109. Wen, Z.; Liu, W.; Li, X.; Chen, W.; Liu, Z.; Wen, J.; Liu, Z. A Protective Role of the NRF2-Keap1 Pathway in Maintaining Intestinal Barrier Function. *Oxid. Med. Cell. Longev.* **2019**, *2019*, 1759149. [CrossRef]
110. Yanaka, A. Contribution of NRF2 in Gastrointestinal Protection from Oxidative Injury. *Curr. Pharm. Des.* **2018**, *24*, 2023–2033. [CrossRef]
111. Khor, T.O.; Huang, M.T.; Kwon, K.H.; Chan, J.Y.; Reddy, B.S.; Kong, A.N. Nrf2-deficient mice have an increased susceptibility to dextran sulfate sodium-induced colitis. *Cancer Res.* **2006**, *66*, 11580–11584. [CrossRef] [PubMed]
112. Gerstgrasser, A.; Melhem, H.; Leonardi, I.; Atrott, K.; Schäfer, M.; Werner, S.; Rogler, G.; Frey-Wagner, I. Cell-specific Activation of the Nrf2 Antioxidant Pathway Increases Mucosal Inflammation in Acute but Not in Chronic Colitis. *J. Crohns Colitis* **2017**, *11*, 485–499. [CrossRef] [PubMed]
113. Wang, C.; Cui, C.; Li, N.; Sun, X.; Wen, L.; Gao, E.; Wang, F. Antioxidant activity and protective effect of wheat germ peptides in an in vitro celiac disease model via Keap1/Nrf2 signaling pathway. *Food Res. Int.* **2022**, *161*, 111864. [CrossRef] [PubMed]
114. Yu, T.; Xie, Y.; Yuan, J.; Gao, J.; Xiao, Z.; Wu, Y.; Chen, H. The Nutritional Intervention of Resveratrol Can Effectively Alleviate the Intestinal Inflammation Associated with Celiac Disease Induced by Wheat Gluten. *Front. Immunol.* **2022**, *13*, 878186. [CrossRef]
115. Bergamo, P.; Palmieri, G.; Cocca, E.; Ferrandino, I.; Gogliettino, M.; Monaco, A.; Maurano, F.; Rossi, M. Adaptive response activated by dietary cis9, trans11 conjugated linoleic acid prevents distinct signs of gliadin-induced enteropathy in mice. *Eur. J. Nutr.* **2016**, *55*, 729–740. [CrossRef]
116. Kang, S.; Kim, W.; Jeong, S.; Lee, Y.; Nam, J.; Lee, S.; Jung, Y. Oxidized 5-aminosalicylic acid activates Nrf2-HO-1 pathway by covalently binding to Keap1: Implication in anti-inflammatory actions of 5-aminosalicylic acid. *Free Radic. Biol. Med.* **2017**, *108*, 715–724. [CrossRef]
117. Hosseini, A.; Masjedi, A.; Baradaran, B.; Hojjat-Farsangi, M.; Ghalamfarsa, G.; Anvari, E.; Jadidi-Niaragh, F. Dimethyl fumarate: Regulatory effects on the immune system in the treatment of multiple sclerosis. *J. Cell. Physiol.* **2019**, *234*, 9943–9955. [CrossRef]
118. Djedovic, N.; Mansilla, M.J.; Jevtić, B.; Navarro-Barriuso, J.; Saksida, T.; Martínez-Cáceres, E.M.; Miljković, Đ. Ethyl Pyruvate Induces Tolerogenic Dendritic Cells. *Front. Immunol.* **2019**, *10*, 157. [CrossRef]
119. Mazzola, M.A.; Raheja, R.; Regev, K.; Beynon, V.; von Glehn, F.; Paul, A.; Pierre, I.; Kivisakk, P.; Weiner, H.L.; Gandhi, R. Monomethyl fumarate treatment impairs maturation of human myeloid dendritic cells and their ability to activate T cells. *Mult. Scler.* **2019**, *25*, 63–71. [CrossRef]
120. Neunlist, M.; Van Landeghem, L.; Mahé, M.M.; Derkinderen, P.; des Varannes, S.B.; Rolli-Derkinderen, M. The digestive neuronal-glial-epithelial unit: A new actor in gut health and disease. *Nat. Rev. Gastroenterol. Hepatol.* **2013**, *10*, 90–100. [CrossRef]
121. Vergnolle, N.; Cirillo, C. Neurons and Glia in the Enteric Nervous System and Epithelial Barrier Function. *Physiology* **2018**, *33*, 269–280. [CrossRef] [PubMed]
122. Pochard, C.; Coquenlorge, S.; Freyssinet, M.; Naveilhan, P.; Bourreille, A.; Neunlist, M.; Rolli-Derkinderen, M. The multiple faces of inflammatory enteric glial cells: Is Crohn's disease a gliopathy? *Am. J. Physiol. Gastrointest. Liver Physiol.* **2018**, *315*, G1–G11. [CrossRef] [PubMed]
123. Esposito, G.; Cirillo, C.; Sarnelli, G.; De Filippis, D.; D'Armiento, F.P.; Rocco, A.; Nardone, G.; Petruzzelli, R.; Grosso, M.; Izzo, P.; et al. Enteric glial-derived S100B protein stimulates nitric oxide production in celiac disease. *Gastroenterology* **2007**, *133*, 918–925. [CrossRef] [PubMed]
124. Murphy, T.H.; Yu, J.; Ng, R.; Johnson, D.A.; Shen, H.; Honey, C.R.; Johnson, J.A. Preferential expression of antioxidant response element mediated gene expression in astrocytes. *J. Neurochem.* **2001**, *76*, 1670–1678. [CrossRef]
125. Graber, D.J.; Hickey, W.F.; Stommel, E.W.; Harris, B.T. Anti-inflammatory efficacy of dexamethasone and Nrf2 activators in the CNS using brain slices as a model of acute injury. *J. Neuroimmune Pharm.* **2012**, *7*, 266–278. [CrossRef]
126. Kalinin, S.; Polak, P.E.; Lin, S.X.; Braun, D.; Guizzetti, M.; Zhang, X.; Rubinstein, I.; Feinstein, D.L. Dimethyl fumarate regulates histone deacetylase expression in astrocytes. *J. Neuroimmunol.* **2013**, *263*, 13–19. [CrossRef]
127. Paraiso, H.C.; Kuo, P.C.; Curfman, E.T.; Moon, H.J.; Sweazey, R.D.; Yen, J.H.; Chang, F.L.; Yu, I.C. Dimethyl fumarate attenuates reactive microglia and long-term memory deficits following systemic immune challenge. *J. Neuroinflammation* **2018**, *15*, 100. [CrossRef]
128. Liu, L.; Vollmer, M.K.; Ahmad, A.S.; Fernandez, V.M.; Kim, H.; Doré, S. Pretreatment with Korean red ginseng or dimethyl fumarate attenuates reactive gliosis and confers sustained neuroprotection against cerebral hypoxic-ischemic damage by an Nrf2-dependent mechanism. *Free Radic. Biol. Med.* **2019**, *131*, 98–114. [CrossRef]

129. Pascal, V.; Pozuelo, M.; Borruel, N.; Casellas, F.; Campos, D.; Santiago, A.; Martinez, X.; Varela, E.; Sarrabayrouse, G.; Machiels, K.; et al. A microbial signature for Crohn's disease. *Gut* **2017**, *66*, 813–822. [CrossRef]
130. Breton, J.; Tanes, C.; Tu, V.; Albenberg, L.; Rowley, S.; Devas, N.; Hwang, R.; Kachelries, K.; Wu, G.D.; Baldassano, R.N.; et al. A Microbial Signature for Paediatric Perianal Crohn's Disease. *J. Crohns Colitis* **2022**, *16*, 1281–1292. [CrossRef]
131. Nistal, E.; Caminero, A.; Herrán, A.R.; Arias, L.; Vivas, S.; de Morales, J.M.; Calleja, S.; de Miera, L.E.; Arroyo, P.; Casqueiro, J. Differences of small intestinal bacteria populations in adults and children with/without celiac disease: Effect of age, gluten diet, and disease. *Inflamm. Bowel Dis.* **2012**, *18*, 649–656. [CrossRef] [PubMed]
132. Di Cagno, R.; De Angelis, M.; De Pasquale, I.; Ndagijimana, M.; Vernocchi, P.; Ricciuti, P.; Gagliardi, F.; Laghi, L.; Crecchio, C.; Guerzoni, M.E.; et al. Duodenal and faecal microbiota of celiac children: Molecular, phenotype and metabolome characterization. *BMC Microbiol.* **2011**, *11*, 219. [CrossRef]
133. Schippa, S.; Iebba, V.; Barbato, M.; Di Nardo, G.; Totino, V.; Checchi, M.P.; Longhi, C.; Maiella, G.; Cucchiara, S.; Conte, M.P. A distinctive 'microbial signature' in celiac pediatric patients. *BMC Microbiol.* **2010**, *10*, 175. [CrossRef] [PubMed]
134. Caminero, A.; Galipeau, H.J.; McCarville, J.L.; Johnston, C.W.; Bernier, S.P.; Russell, A.K.; Jury, J.; Herran, A.R.; Casqueiro, J.; Tye-Din, J.A.; et al. Duodenal Bacteria From Patients With Celiac Disease and Healthy Subjects Distinctly Affect Gluten Breakdown and Immunogenicity. *Gastroenterology* **2016**, *151*, 670–683. [CrossRef] [PubMed]
135. Liu, P.; Xie, X.R.; Wu, H.; Li, H.; Chi, J.S.; Liu, X.M.; Luo, J.; Tang, Y.; Xu, C.X. Mesenchymal Stem Cells Promote Intestinal Mucosal Repair by Positively Regulating the Nrf2/Keap1/ARE Signaling Pathway in Acute Experimental Colitis. *Dig. Dis. Sci.* **2023**, *68*, 1835–1846. [CrossRef] [PubMed]
136. He, J.; Liu, L.; Liu, X.; Chen, H.; Liu, K.; Huang, N.; Wang, Y. Epoxymicheliolide prevents dextran sulfate sodium-induced colitis in mice by inhibiting TAK1-NF-κB pathway and activating Keap1-NRF2 signaling in macrophages. *Int. Immunopharmacol.* **2022**, *113 Pt A*, 109404. [CrossRef]
137. Yang, N.; Xia, Z.; Shao, N.; Li, B.; Xue, L.; Peng, Y.; Zhi, F.; Yang, Y. Carnosic acid prevents dextran sulfate sodium-induced acute colitis associated with the regulation of the Keap1/Nrf2 pathway. *Sci. Rep.* **2017**, *7*, 11036. [CrossRef]
138. Shen, J.; Ma, X.; He, Y.; Wang, Y.; Zhong, T.; Zhang, Y. Anti-inflammatory and anti-oxidant properties of Melianodiol on DSS-induced ulcerative colitis in mice. *PeerJ* **2022**, *10*, e14209. [CrossRef]
139. Alsharif, I.A.; Fayed, H.M.; Abdel-Rahman, R.F.; Abd-Elsalam, R.M.; Ogaly, H.A. Miconazole Mitigates Acetic Acid-Induced Experimental Colitis in Rats: Insight into Inflammation, Oxidative Stress and Keap1/Nrf-2 Signaling Crosstalk. *Biology* **2022**, *11*, 303. [CrossRef]
140. Guo, F.; Tsao, R.; Li, C.; Wang, X.; Zhang, H.; Jiang, L.; Sun, Y.; Xiong, H. Green Pea (*Pisum sativum* L.) Hull Polyphenol Extracts Ameliorate DSS-Induced Colitis through Keap1/Nrf2 Pathway and Gut Microbiota Modulation. *Foods* **2021**, *10*, 2765. [CrossRef]
141. Wang, X.; Quan, S.; Li, J.; Liu, Y.; Sun, H.; Zhang, J.; Liu, D. Protective Effects of Grape Seed Proanthocyanidin Extract in Preventing DSS Induced Ulcerative Colitis Based on Pharmacodynamic, Pharmacokinetic and Tissue Distribution. *Curr. Drug. Metab.* **2022**, *23*, 496–505. [PubMed]
142. Wang, N.; Cui, C.; Xu, C.; Ren, H.; Wang, F.; Yu, Q.; Zhang, G. Effect and mechanism of peanut skin proanthocyanidins on gliadin-induced Caco-2 celiac disease model cells. *Clin. Immunol.* **2022**, *245*, 109100. [CrossRef] [PubMed]
143. Ng, S.Y.; Wilkinson, J. A salutary case of Fumaderm potentially masking the symptoms of bowel cancer and partial bowel obstruction. *Br. J. Derm.* **2007**, *157*, 825–826. [CrossRef] [PubMed]
144. Kofler, L.; Kathrein-Schneider, S.; Schweinzer, K.; Kofler, H. Fumaric acid: A possible new therapy for macular edema? *Int. Ophthalmol.* **2019**, *39*, 1627–1631. [CrossRef] [PubMed]
145. Wynn, D.; Lategan, T.W.; Sprague, T.N.; Rousseau, F.S.; Fox, E.J. Monomethyl fumarate has better gastrointestinal tolerability profile compared with dimethyl fumarate. *Mult. Scler. Relat. Disord.* **2020**, *45*, 102335. [CrossRef]
146. Shakya, A.; Soni, U.K.; Rai, G.; Chatterjee, S.S.; Kumar, V. Gastro-protective and Anti-stress Efficacies of Monomethyl Fumarate and a Fumaria indica Extract in Chronically Stressed Rats. *Cell. Mol. Neurobiol.* **2016**, *36*, 621–635. [CrossRef]
147. Brennan, M.S.; Matos, M.F.; Li, B.; Hronowski, X.; Gao, B.; Juhasz, P.; Rhodes, K.J.; Scannevin, R.H. Dimethyl fumarate and monoethyl fumarate exhibit differential effects on KEAP1, NRF2 activation, and glutathione depletion in vitro. *PLoS ONE* **2015**, *10*, e0120254. [CrossRef]
148. Wipke, B.T.; Hoepner, R.; Strassburger-Krogias, K.; Thomas, A.M.; Gianni, D.; Szak, S.; Brennan, M.S.; Pistor, M.; Gold, R.; Chan, A.; et al. Different Fumaric Acid Esters Elicit Distinct Pharmacologic Responses. *Neurol. Neuroimmunol. Neuroinflamm.* **2021**, *8*, e950. [CrossRef]
149. Naismith, R.T.; Wundes, A.; Ziemssen, T.; Jasinska, E.; Freedman, M.S.; Lembo, A.J.; Selmaj, K.; Bidollari, I.; Chen, H.; Hanna, J.; et al. EVOLVE-MS-2 Study Group Diroximel Fumarate Demonstrates an Improved Gastrointestinal Tolerability Profile Compared with Dimethyl Fumarate in Patients with Relapsing-Remitting Multiple Sclerosis: Results from the Randomized, Double-Blind, Phase III EVOLVE-MS-2 Study. *CNS Drugs* **2020**, *34*, 185–196.
150. Motterlini, R.; Nikam, A.; Manin, S.; Ollivier, A.; Wilson, J.L.; Djouadi, S.; Muchova, L.; Martens, T.; Rivard, M.; Foresti, R. HYCO-3, a dual CO-releaser/Nrf2 activator, reduces tissue inflammation in mice challenged with lipopolysaccharide. *Redox Biol.* **2019**, *20*, 334–348. [CrossRef]
151. Aihara, E.; Engevik, K.A.; Montrose, M.H. Trefoil Factor Peptides and Gastrointestinal Function. *Annu. Rev. Physiol.* **2017**, *79*, 357–380. [CrossRef] [PubMed]

152. Yang, Y.; Lin, Z.; Lin, Q.; Bei, W.; Guo, J. Pathological and therapeutic roles of bioactive peptide trefoil factor 3 in diverse diseases: Recent progress and perspective. *Cell. Death Dis.* **2022**, *13*, 62. [CrossRef] [PubMed]
153. Chelakkot, C.; Ghim, J.; Ryu, S.H. Mechanisms regulating intestinal barrier integrity and its pathological implications. *Exp. Mol. Med.* **2018**, *50*, 1–9. [CrossRef] [PubMed]
154. Bayele, H.K.; Balesaria, S.; Srai, S.K. Phytoestrogens modulate hepcidin expression by Nrf2: Implications for dietary control of iron absorption. *Free Radic. Biol. Med.* **2015**, *89*, 1192–1202. [CrossRef]